IntechOpen

Abrasive Technology
Characteristics and Applications

Edited by Anna Rudawska

ABRASIVE TECHNOLOGY - CHARACTERISTICS AND APPLICATIONS

Edited by **Anna Rudawska**

Abrasive Technology - Characteristics and Applications
http://dx.doi.org/10.5772/intechopen.72364
Edited by Anna Rudawska

Contributors

Pavel Kovac, Marin Gostimirovic, Ngoc Pi Vu, Quoc Hung Tran, Zhiyong Gao, Chengwei Li, Hong Jin Kim, Babak Alinejad, Yazdan Zare, H.-T. (Peter) Liu, Vanessa Cutler, Chidambaram Raghavan, Peter Miles, Ernst Schubert, Nathan Webers, Jingsi Wang, Łukasz Klapiszewski, Artur Jamrozik, Beata Strzemiecka, Adam Voelkel, Teofil Jesionowski, Erika Sohn, Elfego Ruiz, Esteban Luna, Luis Salas, Joel Herrera, Anton Nurkenov, Viktor Guzeev, Xinping Long, Qi Liu

Notice

First published in London, United Kingdom, 2018 by IntechOpen
eBook (PDF) Published by IntechOpen, 2019
IntechOpen is the global imprint of INTECHOPEN LIMITED, registered in England and Wales, registration number: 11086078, The Shard, 25th floor, 32 London Bridge Street
London, SE19SG – United Kingdom
Printed in Croatia

British Library Cataloguing-in-Publication Data
A catalogue record for this book is available from the British Library

Additional hard and PDF copies can be obtained from orders@intechopen.com

Abrasive Technology - Characteristics and Applications
Edited by Anna Rudawska

p. cm.

Print ISBN 978-1-78984-193-0

Online ISBN 978-1-78984-194-7

eBook (PDF) ISBN 978-1-83881-680-3

Meet the editor

Anna Rudawska, PhD, DSc, Eng, Assoc Prof, is the head of the Technological Processes and Systems Design Chair, and since September 1, 2012, she has been the vice dean of the Faculty of Mechanical Engineering at Lublin University of Technology, Poland. She has authored or coauthored 200 scientific publications and several patents in the adhesive field. She is a member of many international and national organizations and a reviewer and a member of editorial boards of international journals. Her research focuses on the issues of analysis of the influence of technological and structural factors on the adhesive joint strength of polymers and metals, design of bonding technology, adhesive properties research, as well as issues related to receiving the appropriate adhesive properties to increase the strength of the adhesive joint.

Contents

Preface

The aim of this book is to present information on the characteristics and applications of abrasive technology, abrasive tools, and tests, as well as the innovative methods of this technology. This book presents information regarding the abrasive technology methods, the characteristics of the methods (for example, the technological parameters, tools, and machines), innovative methods, characteristics of surface structure and surface properties after this type of mechanical process, the tests of various issues of abrasive technology, and also the application in various industrial branches and other technical and technological domains.

Abrasive technology is becoming increasingly important in precision manufacturing. It covers the mechanics and mechanisms of abrasive processes, characteristics of abrasive tools, their structure, materials, and wear, as well as the grinding, finishing, sanding, deburring, hybrid super-finishing, and the abrasive-jet and flow machining processes, among others. Moreover, this book includes the issues on high-speed machining, eco-machining, nano-machining, and laser micro-machining technologies.

There are a lot of factors, which influence the abrasive process—abrasive tools, technological parameters of the abrasive process, the type of machining methods, the type of machines and their characteristics, and the type of machining materials.

One of the important factors, which has a significant influence on the abrasive process and the surface roughness, is the type, structure, and properties of the abrasive material. Abrasives generally rely on a difference in hardness between the abrasive and the material being worked upon, the abrasive being the harder of the two substances. The shape, size, and nature of the workpiece and the desired finish will influence the choice of the abrasive used. For example, a much harder abrasive will cut faster and deeper. The adhesion between grains, between grains and backing, between grains and matrix determines how quickly grains are lost from the abrasive and how soon fresh grains, if present, are exposed. Moreover, there are lots of abrasive materials. In the past, abrasive grains were derived from natural minerals, such as emery, quartz sand, and so on. Today, the industry is almost entirely dependent upon synthetic grains, which are far more consistent and cost-effective.

The book was divided into two parts: the first part: *Characteristics and Applications of Abrasive Technology and Abrasive Methods* and the second part: *Characteristics of Abrasive Tools, Materials, and Machines*.

The aim of such a presentation was to present the usage of characteristics and application of the abrasive methods (also innovative methods and tests) as well as the abrasive tools in very different aspects. These issues are very important in precision manufacturing in many branches of industry, as well as in dentistry and medical applications.

This information enables scientists, engineers, and designers to ensure the soundness and integrity of the fabricated components and to develop new techniques effectively. I would like to express my gratitude to all the contributors for high-quality manuscripts. I hope that the open-access format of this book will help researchers and engineers.

Anna Rudawska
Lublin University of Technology
Faculty of Mechanical Engineering
Department of Production Engineering
Poland

Section 1

Characteristics and Application of Abrasive Technology and Abrasive Methods

Chapter 1

Numerical Analysis of the Liquid-Gas-Solid Three Phase Flow Inside AWJ Nozzle

Xinping Long and Qi Liu

Additional information is available at the end of the chapter

http://dx.doi.org/10.5772/intechopen.75938

Abstract

The multiphase flows inside the two abrasive waterjet (AWJ) nozzles with different abrasive inlet tube angles are simulated using the standard k-ε turbulence model based on the Euler-Lagrangian approach. The volume of fluid (VOF) method is employed to simulate the water-air multiphase flows. And, the abrasive particles are treated as dilute dispersed phase and tracked with the discrete particle method (DPM). The results indicate that the abrasive inlet tube angle has little impact on the water-phase flows. Further analysis shows that a larger abrasive inlet tube angle can enhance the particle accelerations. The particle number independence analysis is conducted, and the results indicate that sufficient particles should be tracked in order to obtain statistically representative results. The effects of particle initial velocities, particle shape factors, and the restitution coefficients on the predicted particle movements are further analyzed for the two nozzles with abrasive inlet tube angles of 45° and 60°. The results reveal that at the current velocity range, the particle initial velocities have little impact on the predicted particle velocities. However, both the shape factors and the restitution coefficients play an important role on the calculated particle velocities. The results provide a deeper understanding of particle acceleration performance inside the AWJ nozzles with different abrasive inlet tube angles.

Keywords: abrasive waterjet, multiphase flow, DPM, VOF

1. Introduction

The abrasive waterjet (AWJ) is originally developed to improve the cutting ability of the pure waterjet (PWJ). As a new type of cold cutting technology, the AWJ is performed to cut target materials with water-containing abrasive particles at high pressures. Generally, the AWJ is capable of cutting or manufacturing both brittle and ductile materials without imposing thermal

impact on the target materials. It also has the advantages of high machining versatility, small machining force, and high flexibility compared with other manufacturing methods. Therefore, the AWJ has been widely applied in numerous fields [1–4]. Recently, the potential of the AWJ technology for high precision cutting or manufacturing of hard-to-machine materials has made the AWJ again receive much attention [5, 6].

It should be mentioned that the AWJ is different from the abrasive slurry jet (ASJ). And, the definition of the two types is mainly based on the mixing process of abrasive particles with fluid. For the ASJ, in the high-pressure tank, the abrasive particles are premixed with water to produce the so-called slurry which is directly ejected from the nozzle. However, for the AWJ, as illustrated in **Figure 1**, the high-pressure pure water is firstly ejected from the orifice into the mixing chamber where the abrasive particles and the air are simultaneously entrained to mix with the high-speed water, and then the AWJ is generated in the focus tube. Therefore, there are only two phases of flows (particle and water) in ASJ nozzle but three phases of flows (particle, water, and air) in AWJ nozzle. The operating pressure of AWJ is much higher than that of the ASJ, and the energy utilization of AWJ is comparatively lower. Thus, extensive efforts have already been made to investigate the cutting, machining, and energy transfer efficiency of the so-called AWJ technology [7, 8]. Momber investigated the energy transfer during the high-speed waterjet formation process and also the abrasive particle mixing and

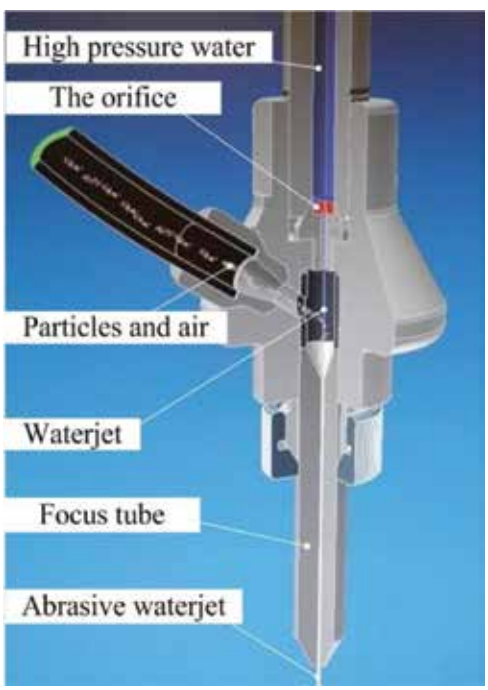

Figure 1. The AWJ cutting system and AWJ nozzle [6].

acceleration processes by conducting impact-force measurements [7]. Lee et al. studied the material removal mechanisms of AWJ with micro-sized abrasive particles [9]. Shanmugam and Masood experimentally investigated the effects of AWJ operating parameters on the kerf taper angle of two types of layered composites [10]. Coray et al. tested a 5:1 scale AWJ equipment models to study the kinetic energy distributions of the abrasive particles together with the jet structure. They reported that due to the strong interactions among the three phases the signal differences between water phase and abrasive particles could not yet be distinguished experimentally [11].

It is already well known that the AWJ nozzle, as an important component of the AWJ equipment, has a significant impact on the overall manufacturing performances and is crucial for improving machining quality and reducing energy consumption. Thus, a better understanding of the effects of nozzle parameters on the jet structure and abrasive particle movements is essential to develop high-performance AWJ equipment. However, due to the small dimensions of the AWJ nozzle and the highly aggressiveness of abrasive particles, conducting experiments to study the three phases of flows inside the AWJ nozzle is still very challenging. And, the accurate measurement of the complex multiphase flows which involves ultrahigh-speed water, air, and abrasive particles inside the extremely small nozzle space may even impossible at present. With the rapid development of computational fluid dynamics (CFD) and computing ability, numerical simulations of this complex internal flows have been made possible, which provides an effective way to gain a better understanding of the multiphase interaction mechanisms. Long et al. conducted numerical simulations to investigate the particle movement inside the AWJ nozzle using different particle shape factors. The results revealed that a smaller particle shape factor could enhance the overall particle acceleration process [6]. Yang et al. numerically studied the abrasive particle motions and the corresponding erosion rate inside the AWJ nozzle at the pressures beyond 300 MPa. It was revealed that the proposed numerical model provided a reliable way to investigate the AWJ nozzle internal multiphase flows [12]. Basha et al. simulated the internal multiphase flows inside an AWJ nozzle and investigated the jet flow dynamic characteristics. It was confirmed that the numerical simulations could accurately capture the AWJ nozzle performance [13].

Despite the abovementioned efforts, the complex interactions between the fluid phases and the particles inside the AWJ nozzle are not yet fully understood, and the effects of numerical model parameters on the simulation results are not well investigated. Also, the effects of nozzle structure on the multiphase flows are not well studied. Inspired by the mentioned work, the present paper is devoted to investigating the liquid-gas-solid multiphase flows in AWJ nozzles with different abrasive inlet tube angles at a given high operating pressure under different model parameters based on three-dimensional Euler-Lagrangian numerical simulations. The effects of particle initial velocities, particle shape factors, and particle-wall restitution coefficients on the predicted particle velocities are discussed. The effects of abrasive inlet tube angles on the multiphase flows are further analyzed. The results can help to provide guidance for future CFD-aided AWJ nozzle optimization.

2. Governing equations and numerical method

As illustrated in **Figure 1**, the high-pressure water is firstly ejected from the orifice, and the resulted high-speed water jet then enters into the mixing chamber. By the high-speed jet entraining effects, the air phase together with the abrasive particles is entrained into the mixing chamber where strong interactions are expected. The abrasive particles are mixed and accelerated by the high-speed fluid phase and finally ejected through the long focus tube to impact on the workpiece. The present study is performed by simulating the steady-state multiphase flows in AWJ nozzles based on the time-averaged Navier-Stokes equations. It was reported that the volume fractions of the abrasive particles in the AWJ nozzle was normally less than 10% [14]. Thus, the Euler-Lagrangian method is finally utilized for all the present simulations. Both the water phase and the air phase are treated as continuums and are computed in Eulerian reference frame using the finite volume method. However, the abrasive particles are considered as discrete phase and are solved in Lagrangian reference frame using the discrete particle method (DPM).

2.1. Governing equations for continuous phases

The water-air multiphase flows are modeled using the volume of fluid (VOF) model. The volume fraction-based composition of AWJ is approximately 0.2–0.5% abrasive particles, 4–6% water phase, and 93–95% air phase [15]. The air phase is finally chosen as the primary phase in the present simulations, and thus the continuity equation for the volume fraction of the water phase can be written as

$$\frac{\partial(\alpha_w u_i)}{\partial x_i} = 0 \tag{1}$$

where α_w is the volume fraction of water and u_i is velocity. The volume fraction of the primary phase α_a can be directly obtained by the simple equation:

$$\alpha_a = 1.0 - \alpha_w \tag{2}$$

As the VOF is based upon the single fluid assumption, the air phase and the water phase share the same velocity field, and a single momentum equation is solved throughout the computational domain. Therefore, the governing equation for the conservation of momentum can be given as

$$\frac{\partial(\rho u_i u_j)}{\partial x_j} = -\frac{\partial p}{\partial x_i} + \frac{\partial}{\partial x_j}\left[(\mu + \mu_t)\left(\frac{\partial u_i}{\partial x_j} + \frac{\partial u_j}{\partial x_i} - \frac{2}{3}\frac{\partial u_k}{\partial u_k}\delta_{ij}\right)\right] \tag{3}$$

where u_i and u_j are the velocities in the x_i and x_j coordinate directions, respectively. p and ρ stand for the pressure and the mixture density. μ is the laminar viscosity of the fluid mixture.

http://dx.doi.org/10.5772/intechopen.75938

It should be noted that the one-way coupling method is applied indicating that the particle movement is influenced by the continuous phase, but the flow phase is not influenced by the particle motion. So, there are no additional source terms in Eq. (3).

The fluid mixture properties of water and air in Eq. (3) are calculated as

$$\begin{aligned} \mu &= \alpha_a \cdot \mu_a + \alpha_w \cdot \mu_w \\ \rho &= \alpha_a \cdot \rho_a + \alpha_w \cdot \rho_w \end{aligned} \tag{4}$$

where subscripts *a* and *w* represent air and water, respectively.

To predict the turbulent viscosity μ_t, the standard *k*-*ε* turbulence model is used. The transport equations of turbulence kinetic energy *k* and the turbulence dissipation rate ε can be given as

$$\frac{\partial(\rho k)}{\partial t} + \frac{\partial\left(\rho k u_j\right)}{\partial u_j} = \frac{\partial}{\partial x_j}\left[\left(\mu + \frac{\mu_t}{\sigma_k}\right)\frac{\partial k}{\partial x_j}\right] + P_t - \rho\varepsilon \tag{5}$$

$$\frac{\partial(\rho\varepsilon)}{\partial t} + \frac{\partial(\rho\varepsilon\, u_j)}{\partial u_j} = \frac{\partial}{\partial x_j}\left[\left(\mu + \frac{\mu_t}{\sigma_\varepsilon}\right)\frac{\partial \varepsilon}{\partial x_j}\right] + C_{\varepsilon 1} P_t \frac{\varepsilon}{k} - C_{\varepsilon 2}\rho\frac{\varepsilon^2}{k} \tag{6}$$

where μ_t is computed by $\mu_t = C_\mu \rho k^2/\varepsilon$ with $C_\mu = 0.09$, σ_k and σ_ε are the turbulent Prandtl number for *k* and *ε*, and their values are set as 1.3 and 1.0, respectively. The other two empirical constants are given as $C_{\varepsilon 1} = 1.44$ and $C_{\varepsilon 2} = 1.92$.

2.2. Disperse-phase tracking method

The interactions among the particles are neglected as the volume-based concentration of abrasive particles in the present cases is less than 10%. The so-called one-way coupling method is adopted to track the abrasive particles. As the diameters of the particles are small, the rotation motions of the abrasive particles are neglected. The forces acting on each particle include the drag force, the virtual mass force, and the pressure gradient force. The governing equation for each abrasive particle in the Cartesian coordinate form can be given as

$$\frac{du_p}{dt} = F_d(u - u_p) + F_{vm} + F_p \tag{7}$$

where u_p is the particle velocity and F_d is the drag force per unit particle mass, which can be calculated as

$$F_d = \frac{18\mu}{\rho_p d_p^2}\frac{C_D Re_p}{24} \tag{8}$$

where Re_p stands for the particle Reynolds number which defined as

$$Re_{\mathrm{p}} = \frac{\rho\, d_{\mathrm{p}} |u - u_p|}{\mu} \tag{9}$$

where d_{p} represents the particle diameter and ρ_p stands for the particle density. The drag coefficient C_{D} is predicted by the following equation [16]:

$$C_{\mathrm{D}} = \frac{24}{Re_{\mathrm{p}}}\left(1 + b_1 Re_{\mathrm{p}}^{\,b_2}\right) + \frac{b_3 Re_{\mathrm{p}}}{b_4 + Re_{\mathrm{p}}} \tag{10}$$

where

$$\begin{cases} b_1 = \exp\left(2.3288 - 6.4581\varphi + 2.4486\,\varphi^2\right) \\ b_2 = 0.0964 + 0.5565\varphi \\ b_3 = \exp\left(4.905 - 13.8944\varphi + 18.4222\,\varphi^2 - 10.2599\,\varphi^3\right) \\ b_4 = \exp\left(1.4681 + 12.2584\varphi - 20.7322\,\varphi^2 + \mathrm{T}\ 15.8855\,\varphi^3\right) \end{cases} \tag{11}$$

where φ is termed as the shape factor to take the particle sphericity into consideration as shown in **Figure 2**. According to its definition, $\varphi = s/S$, where s represents the nominal surface area of a sphere particle which has the same volume as the real particle and S is the actual surface area of the particle; $\varphi = 1$ indicates that the particle is spherical, where φ is smaller than unity indicating that the particle is nonspherical. A smaller value of the shape factor represents an increase of the particle irregularity.

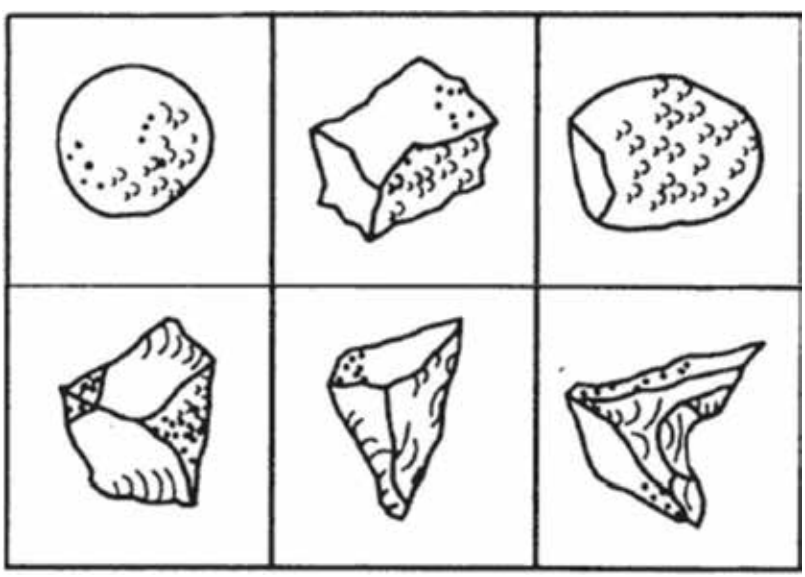

Figure 2. Typical shapes of abrasive particle [17].

http://dx.doi.org/10.5772/intechopen.75938

The virtual mass force acting on each abrasive particle can be calculated as

$$F_{\mathrm{vm}} = \frac{1}{2}\frac{\rho}{\rho_{\mathrm{p}}}\frac{d}{dt}(u - u_{\mathrm{p}}) \tag{12}$$

The effect of virtual mass is significant when the particle density ρ_{p} is much smaller than the fluid phase density ρ.

The pressure gradient force is caused by a pressure difference and can be modeled as

$$F_{\mathrm{p}} = \frac{\rho}{\rho_{\mathrm{p}}}\nabla p \tag{13}$$

The diameters of abrasive particles used in the present simulations are very small, and the pressure difference over one particle diameter distance can be ignored. Therefore, only the drag force is taken into consideration in the current study.

For turbulent flows, the fluid velocity can be divided into the mean velocity and the random fluctuation velocity. To predict the effect of turbulent flow velocity fluctuations on the particle movement, the random walk model (RWM) is used. The turbulent fluctuating velocity is modeled as

$$u' = \varsigma\sqrt{\frac{2k}{3}} \tag{14}$$

where k is the calculated turbulence kinetic energy and ζ is a Gaussian distributed random number.

A reflecting boundary condition is adopted to consider the interactions between the abrasive particles and the wall boundaries. The particles reach the wall and change directions after the collisions. Two famous parameters, namely, the normal restitution coefficient e_{n} and the tangential coefficient e_{τ}, are defined as follows:

$$\begin{aligned} e_n &= \frac{v_{p2}}{v_{p1}} \\ e_\tau &= \frac{u_{p2}}{u_{p1}} \end{aligned} \tag{15}$$

where v_{p} is the particle velocity normal to the wall and the corresponding subscript 1 and 2 represent before and after the collision, respectively. Likely, the tangential coefficient accounts for the momentum changes in the direction tangential to the wall boundary. The restitution coefficients for both directions equal to unity indicate a fully elastic collision which means that there is no energy loss during the collision.

2.3. Computational model and numerical setup

A typical geometry of the three-dimensional AWJ nozzle is illustrated in **Figure 3**. The high-pressure water tube diameter is 4 mm, the orifice diameter is 0.4 mm, the mixing chamber

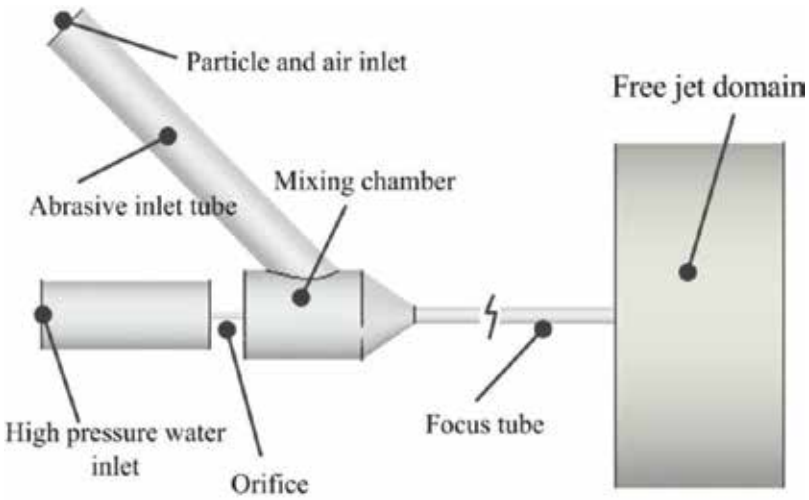

Figure 3. Geometry of the AWJ nozzle for the 3D simulation.

diameter is 5 mm, and the abrasive particle inlet tube diameter is 3 mm. The focus tube has a diameter of 1 mm with the length of 60 mm. Two AWJ nozzles with different abrasive inlet tube angles are modeled in the present study as illustrated in **Figure 4**. Model 1 represents the AWJ nozzle with the abrasive inlet tube angle of 45°, and model 2 stands for the AWJ nozzle with the abrasive inlet tube angle of 60°. The computational domains of the two models are meshed as shown in **Figures 5** and **6**. In order to ensure the accurate tracking of VOF surface, a mesh refinement is conducted around the orifice and the water-air interface regions. Both tetrahedral and hexahedral meshes are generated inside the computational domains, and high-density mesh regions are located where large gradients are expected. The grid independence analysis for both the two models indicate that the results predicted with the meshes with about 900,000 nodes will not change with further refinement of mesh resolution. The meshes used in the subsequent simulations are given in **Figures 5** and **6**.

The pressure inlet boundary condition with a given pressure of 300 MPa is specified at the water inlet, while atmospheric pressure is fixed at the air inlet boundary. At the free jet domain boundary region, the outlet boundary condition is applied with a pressure fixed at

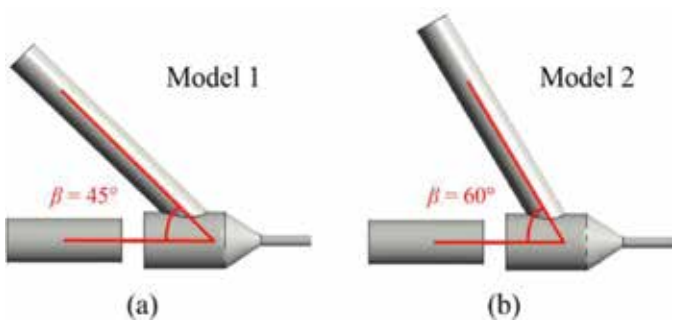

Figure 4. AWJ nozzles with different abrasive inlet tube angles.

http://dx.doi.org/10.5772/intechopen.75938

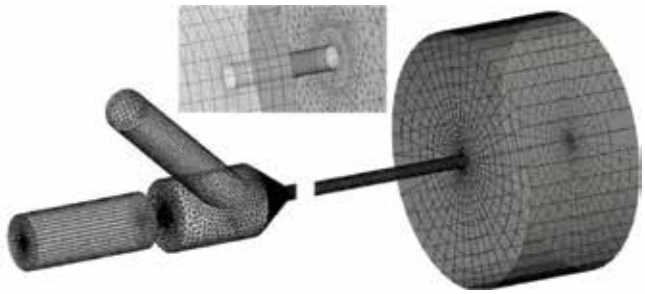

Figure 5. Computational mesh used in the simulations (model 1).

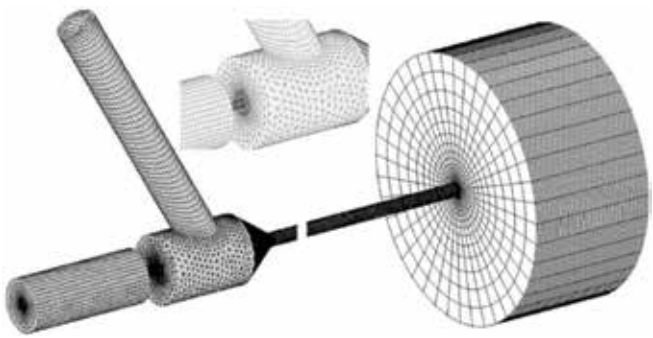

Figure 6. Computational mesh used in the simulations (model 2).

the atmospheric pressure. The no-slip wall boundary condition is specified at the walls. The abrasive particles are injected into the computational domains with uniform velocity with a given mass flow rate of 5 g/s. And, the density of abrasive particle is 2600 kg/m^3. The interactions between the wall and particles are modeled by specifying the restitution coefficients. The abovementioned steady-state governing equations for air and water phases are finally discretized in space domain using the finite volume method (FVM) with SIMPLE algorithm. The QUICK scheme is used to approximate the phase volume fraction. The second-order accurate central differential scheme is adopted to discretize the diffusion terms. And, the second-order accurate upwind scheme is implemented to discretize the other convective terms. The convergence criterions for all the cases are specified as that the residuals for each equation drop below 10^{-4}. Once the steady-state simulations of continuous phases are completed, the abrasive particles are released, and the particle trajectories are correspondingly predicted. All the simulations are performed with commercial software Ansys Fluent 15.0.

3. Results and discussion

3.1. Flow field inside AWJ nozzle

Figure 7 shows the predicted flow patterns inside the two AWJ nozzles at the same operating pressure of 300 MPa. The typical free jet structures are captured by the present model in the

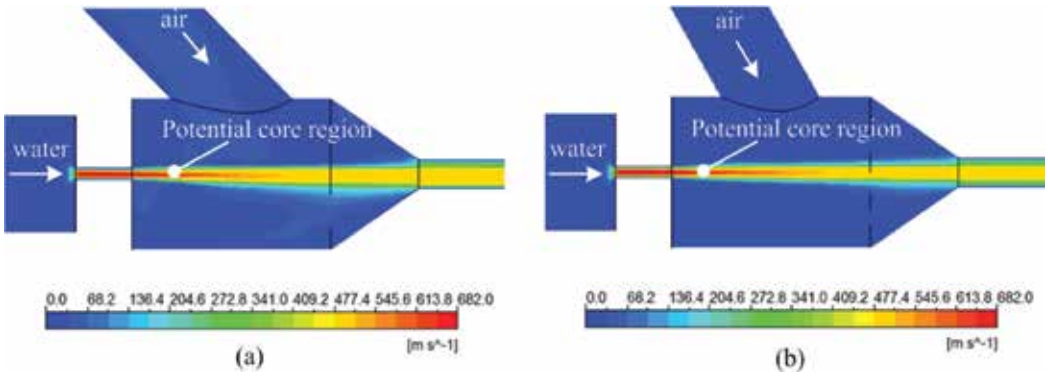

Figure 7. Velocity contour inside (**a**) model 1 and (**b**) model 2 AWJ nozzles.

mixing chamber. It can be seen that the high-pressure water ejected from the orifice produces a high-speed water jet. The predicted potential core region has the maximum velocity, and the axial velocity begins to decay significantly further downstream. Due to the high-speed region in the chamber, a comparatively low-pressure region is generated, and thus the air is entrained into the nozzle by the water jet entraining effect. The predicted area-weighted average velocity at the air inlet is about 37 m/s. It is noted that the comparatively low-velocity region in the velocity is slightly asymmetric, which is mainly caused by the presence of the particle inlet tube. The velocity distributions in the axial lines of the two types of nozzles are shown in **Figure 8**. There is a small gap between the velocity profiles in the mixing chamber. However, the two lines are almost collapsed together in the focus tubes. Generally, the impact of abrasive inlet tube angle on the fluid flow is not significant.

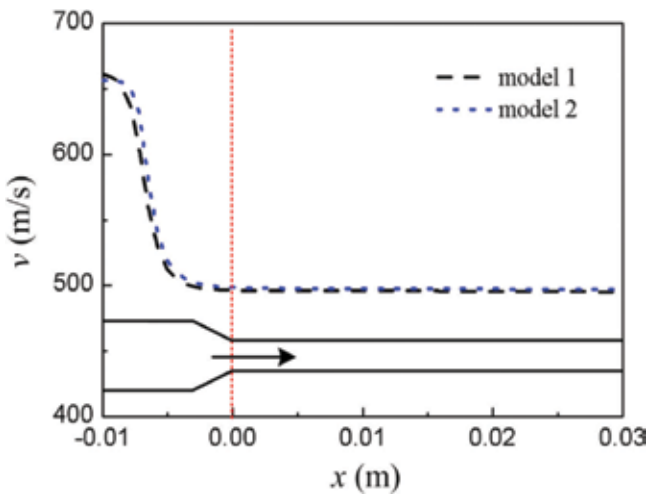

Figure 8. Velocity distributions in the axial lines of the two nozzles.

3.2. Independence analysis of particle number

As the abrasive particle concentrations on the volume fraction basis are less than 1% in the present simulations, the one-way coupling method is utilized to predict the particle trajectories, and the effects of particle movements on the continuous phases are not considered. Thus, the integration of particle paths is a post-process, which is performed after the fluid field is obtained. Since the effect of turbulent velocity on the particle paths has been accounted, the independence analysis of particle number should be conducted in order to obtain statistically representative results.

Four different particle numbers are sampled at about 60 different cross sections along the focus tube, and the results are shown in **Figure 9**. It should be noted that the particles are assumed to be spherical, and the energy loss due to particle-wall interactions is also neglected. As illustrated in **Figure 9**, the sampled particle velocities tend to collapse together with the increasing of sampled particle numbers. It is noted that when the sampled particle number is greater than 10,500, the resulted velocities do not change with further increase of sampled particles. Thus, the tracked particle number is maintained at about 10,500 in the subsequent calculations.

3.3. Effect of particle initial velocity

The particle initial velocities at the abrasive particle inlet tube are hard to determine experimentally, and thus in the abovementioned simulations, the initial velocity is set as zero uniformly, and the particles are accelerated by the entrained air phase. In order to ensure that the boundary condition for the inlet abrasive particle is reasonable, the effects of particle initial velocities on the final predicted velocities need to be further investigated. Two

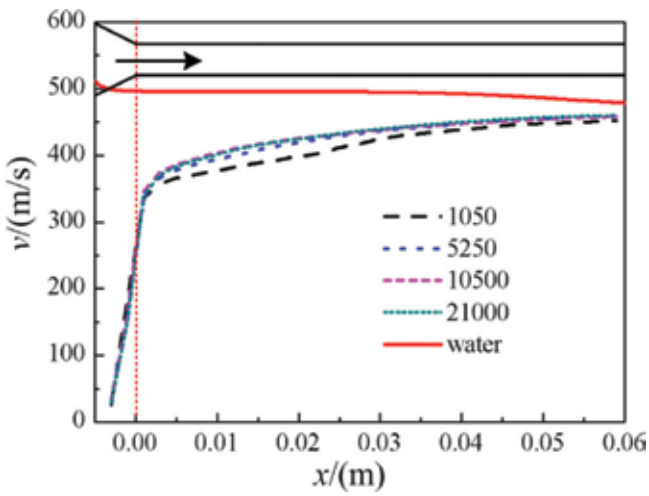

Figure 9. Velocity distribution with different particle sampling numbers (model 1).

different particle initial velocities for the two nozzles are discussed, and the sampled results are given in **Figure 10**. As it can be seen, the predicted velocities under the two different particle initial velocities coincide with each other for each model. Thus, it is confirmed that the simulated results are insensitive to the particle initial velocities within the discussed range of 0–2 m/s.

The results also indicate that the general particle accelerations for both the two AWJ nozzle models are similar. In the convergence section of the focus tubes, the particle velocities are increased linearly with the increase of the axial distance, and the velocity rises sharply from a low-level value to a high-level value. In the initial straight part of the focus tubes, the accelerations of abrasive particles are gradually weakened, and the overall velocities are approaching a constant value which is always smaller than the corresponding water speed. As the particles move further downstream in the focus tube, the velocity differences between the water and the particle are further reduced, which means that the particles are continuously accelerated by the high-speed jet flow. As shown in **Figure 10**, the velocity profiles of model 1 and model 2 have a gap in the initial section of the focus tube. The particle acceleration of model 2 is faster than that of model 1, which indicates that a larger abrasive particle inlet tube angle can enhance the particle accelerations.

3.4. Effect of shape factor

The shape factor in the drag coefficient model is introduced to account for the effects of particle shape on the drag force predictions. Two different shape factors are defined for both the two nozzle models to investigate the shape factor value on the calculated particle velocities. As given in **Figure 11**, the particle velocities under with the two different shape factors show obvious differences for both model 1 and model 2. At the convergence part of the focus tube, the corresponding two velocity curves for each nozzle model collapse together. However, at

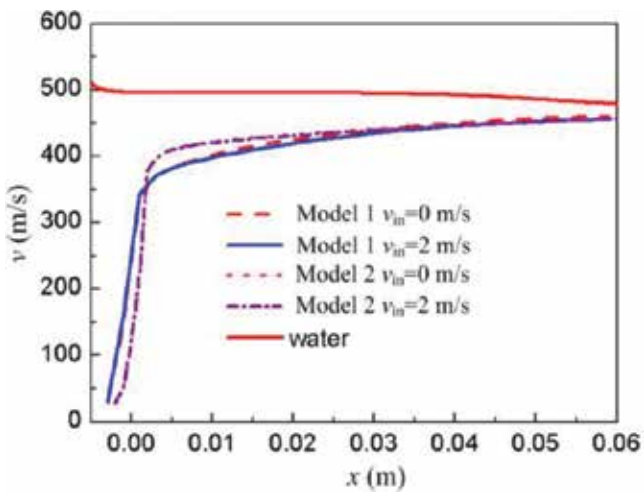

Figure 10. Velocity distributions with different particle initial velocities.

http://dx.doi.org/10.5772/intechopen.75938

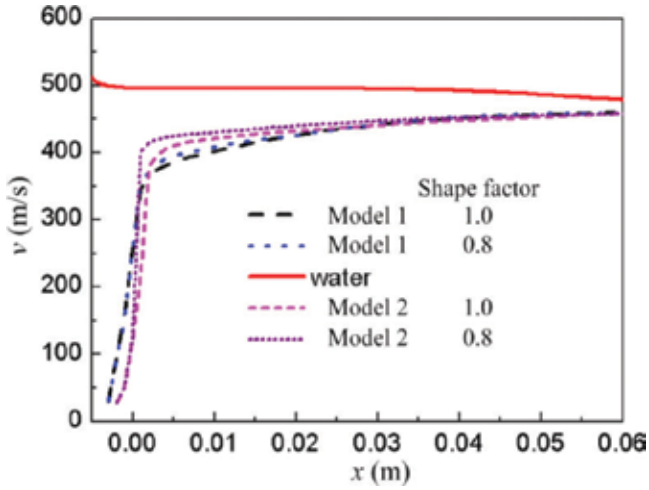

Figure 11. Velocity distributions with different shape factors.

the straight part between 0.0 and 0.04 m, the curves begin to separate, and the velocity with smaller shape factor is comparatively larger. It can be explained by the fact that the drag forces acting on the abrasive particles are larger at a smaller shape factor and thus the particles are accelerated much more quickly. At the following part, the curves again come together indicating that the particle velocities under the selected shaper factors are the same at the focus tube outlet. Thus, the results further reveal that the length of focus tube has an impact on the final particle velocities and a properly designed focus tube should be introduced to ensure that the abrasive particles are fully accelerated.

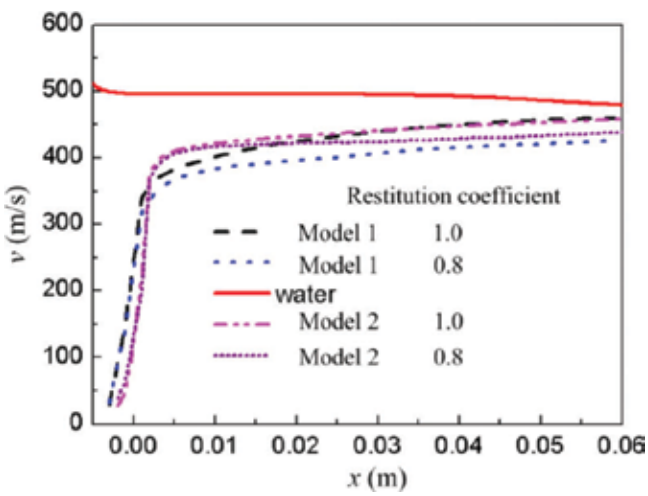

Figure 12. Velocity distributions with different restitution coefficients.

3.5. Effect of particle-wall restitution coefficient

The effects of restitution model accounting for the particle-wall interactions on the predicted velocities are studied to obtain an accurate prediction on the particle paths. When the restitution coefficients at normal and tangential directions are both set as unity, the particle energy loss upon collision is neglected. In real cases, the rebound velocity is lower than the incident velocity. In this work, two kinds of restitution coefficients for both the two AWJ nozzle models are adopted, and the predicted results are shown in **Figure 12**. With the decreased restitution coefficients, the sampled particle velocities at the straight section of the focus tube are lower for both the two models, which indicate that a proper rebound model should be introduced in order to consider the real behaviors of particle-wall interactions.

4. Conclusions

The multiphase flows inside the two AWJ nozzle models with different abrasive inlet tube angles at the same operating pressure are simulated using the standard k-ε turbulence model coupled with the VOF multiphase model based on the Euler-Lagrangian approach. The results indicate that sufficient particles should be sampled in order to obtain a statistically representative result. At the studied velocity range, the particle initial velocities for the two AWJ nozzles do not influence the predicted results. Further analysis shows that for both the two nozzles smaller particle shape factors enhance the process of particle accelerations and a proper length of the focus tube can guarantee that the particles will be fully accelerated. The restitution coefficients may have a significant influence on the particle paths as well as the predicted particle velocities. And, a proper rebound model should be introduced in order to capture the real particle behaviors in the AWJ nozzle. The abrasive inlet tube angle has little impact on the water-phase flows, while a larger abrasive inlet tube angle can enhance the particle accelerations.

Acknowledgements

This work was financially supported by the National High-Technology Research and Develop ment Program 863 (2015AA043401).

Author details

Xinping Long[1]* and Qi Liu[2]

*Address all correspondence to: xplong@whu.edu.cn

1 School of Power and Mechanical Engineering, Wuhan University, Wuhan, Hubei, China

2 China Ship Development and Design Center, Wuhan, China

References

[1] Matsumura T, Muramatsu T, Fueki S. Abrasive water jet machining of glass with stagnation effect. CIRP Annals – Manufacturing Technology. 2011;**60**:355-358

[2] Wang J, Shanmugam DK. Cutting meat with bone using an ultrahigh pressure abrasive waterjet. Meat Science. 2009;**81**:671-677

[3] Henning A, Liu HT, Olsen C. Economic and technical efficiency of high performance abrasive waterjet cutting. Journal of Pressure Vessel Technology. 2012;**134**:021405-021405

[4] Haghbin N, Ahmadzadeh F, Spelt JK, Papini M. Effect of entrained air in abrasive water jet micro-machining: Reduction of channel width and waviness using slurry entrainment. Wear. 2015;**344-345**:99-109

[5] Axinte DA, Srinivasu DS, Kong MC, Butler-Smith PW. Abrasive waterjet cutting of polycrystalline diamond: A preliminary investigation. International Journal of Machine Tools and Manufacture. 2009;**49**:797-803

[6] Long X, Ruan X, Liu Q, Chen Z, Xue S, Wu Z. Numerical investigation on the internal flow and the particle movement in the abrasive waterjet nozzle. Powder Technology. 2017;**314**:635-640

[7] Momber AW. Energy transfer during the mixing of air and solid particles into a high-speed waterjet: An impact-force study. Experimental Thermal and Fluid Science. 2001; **25**:31-41

[8] Liu H, Wang J, Kelson N, Brown RJ. A study of abrasive waterjet characteristics by CFD simulation. Journal of Materials Processing Technology. 2004;**153-154**:488-493

[9] Lee J-H, Park K-S, Kang MC, Kang BS, Shin BS. Experiments and computer simulation analysis of impact behaviors of micro-sized abrasive in waterjet cutting of thin multiple layered materials. Transactions of Nonferrous Metals Society of China. 2012; **22**(3):s864-s869

[10] Shanmugam DK, Masood SH. An investigation on kerf characteristics in abrasive waterjet cutting of layered composites. Journal of Materials Processing Technology. 2009;**209**:3887-3893

[11] Coray PS, Jurisevic B, Junkar M, Heiniger KC. Measurements on 5:1 scale abrasive water jet cutting head models, In: Proceedings of the 6th International Conference on Management of Innovative Technologies MIT 2003 – post-conference edition. Ljubljana: University of Ljubljana; 2003. pp. 87-102

[12] Yang M, Wang Y, Kang C, Feng YU. Multiphase flow and wear in the cutting head of ultra-high pressure abrasive water jet. Chinese Journal of Mechanical Engineering. 2009;**22**:729-734

[13] Basha AT, Annoni M, Monno M, et al. Investigation of the hydrodynamic characteristics of abrasive water jet cutting head[J]. International Journal of Machining & Machinability of Materials. 2013;**14**(1):105-122

[14] Tazibt A, Parsy F, Abriak N. Theoretical analysis of the particle acceleration process in abrasive water jet cutting. Computational Materials Science. 1996;**5**:243-254

[15] Ahmed SE, Naser J, et al. Numerical Simulation of Abrasive Water Jet for Different Taper Inlet Angles, [C]//14th Australasian Fluid Mechanics Conference, Australia. 2001:645-648

[16] Haider A, Levenspiel O. Drag coefficient and terminal velocity of spherical and non-spherical particles. Powder Technology. 1989;**58**:63-70

[17] Momber AW, Kovacevic R. Principles of Abrasive Water Jet Machining. London: Springer; 1998

Chapter 2

Ultrasonic Machining: A Total Mechanical Machining Technology Using Loose Abrasive Particles

Jingsi Wang

Additional information is available at the end of the chapter

http://dx.doi.org/10.5772/intechopen.75170

Abstract

Although manufacturing technologies are well developed for materials like metals and their alloys, considerable problems still exist in the fabrication of hard and brittle materials including ceramics and glass. Their superior physical and mechanical properties lead to long machining cycle and high production cost. Ultrasonic machining (USM) using loose abrasive particles suspended in a liquid slurry for material removal is considered an effective method for manufacturing these materials. This work gives a brief overview of USM first and then mainly addresses the development of a simulation model of this process using a mesh-free numerical technique, the smoothed particle hydrodynamics (SPH). The crack formation on the work surface impacted by two abrasive particles is studied for understanding the material removal and the interaction of abrasive particles in USM. Experiments are also conducted to verify the simulation results. The SPH model is proven useful for studying USM and is capable of predicting the machining performance.

Keywords: ultrasonic machining, smoothed particle hydrodynamics (SPH), hard and brittle materials, material removal mechanism, hole drilling

1. Introduction

Hard and brittle materials, such as glass, ceramics, and quartz crystal, are getting more and more attention in the recent years due to their superior properties like high hardness, high strength, chemical stability, and low density. High-performance products made of these materials play an important role in various industrial fields including semiconductor, optical components, aerospace, and automotive industries [1, 2]. However, considerable problems such as long machining cycle and high production cost still exist in the fabrication of hard and brittle materials. Particular difficulties are the production of micro−/nanostructures with

high machining efficiency, high aspect ratios, and good surfaces possessing no residual stress and microcracks. Hence, there is a crucial need for developing precision and efficient micro-machining techniques for these materials.

Nontraditional machining techniques such as electric discharge machining and laser beam machining have been proposed to machine hard and brittle materials. However, even these processes have prominent limitations that the machined surfaces are always subjected to heat-induced damages like recast layer and thermal stress. Ultrasonic machining (USM) is another alternative method for manufacturing both conductive and nonconductive hard and brittle materials. It is known as a total mechanical process without suffering from heat or chemical effects, so USM would not thermally damage the machining objects or appear to cause significant levels of residual stress and chemical alterations.

However, not much research has been conducted to clarify the mechanism of USM up to date, and the knowledge for the process is far from sufficient to provide a complete understanding and instructive rules for practical use. Therefore, no further developments of micro-USM happened in recent years. In this work, a brief overview of USM is given first in Section 2. Then, a mesh-free numerical technique, the smoothed particle hydrodynamics (SPH), is introduced to simulate the USM process in Section 3, and its verification experiments are presented after that. The crack formation on the work surface impacted by two abrasive particles was studied in the simulation to reveal the material removal and the interaction of abrasive particles in USM. Finally, problems to be solved in order to put USM into an effective industrial micro-machining method are given. Further work should be conducted to clarify the nature of USM process for improving the machining performance.

2. Overview of ultrasonic machining (USM)

2.1. Principle of USM

Figure 1 shows a schematic of the basic elements of a USM apparatus used nowadays. High-frequency electrical energy can be converted into mechanical vibrations with resonant frequency via the transducer. The excited vibration is subsequently transmitted through an energy-focusing horn to amplify the vibration amplitude and finally delivered to the tool tip. Thus, the tool which locates directly above the workpiece can vibrate along its longitudinal axis with a desired high amplitude. A slurry comprising hard abrasive particles (generally using silicon carbide, boron carbide, and alumina) in water or oil is provided constantly into the machining area. During the fabrication of hard and brittle materials, a large number of tiny fractures occur on the work surface and lead to the material removal.

2.2. Features and potentialities of USM

Markov [3] classified workpiece materials into three categories in consideration of the USM suitability: the materials belonging to the first group, such as glass, mica, and quartz, are quite brittle and easy for USM process. The materials are removed by the initiation and propagation

http://dx.doi.org/10.5772/intechopen.75170

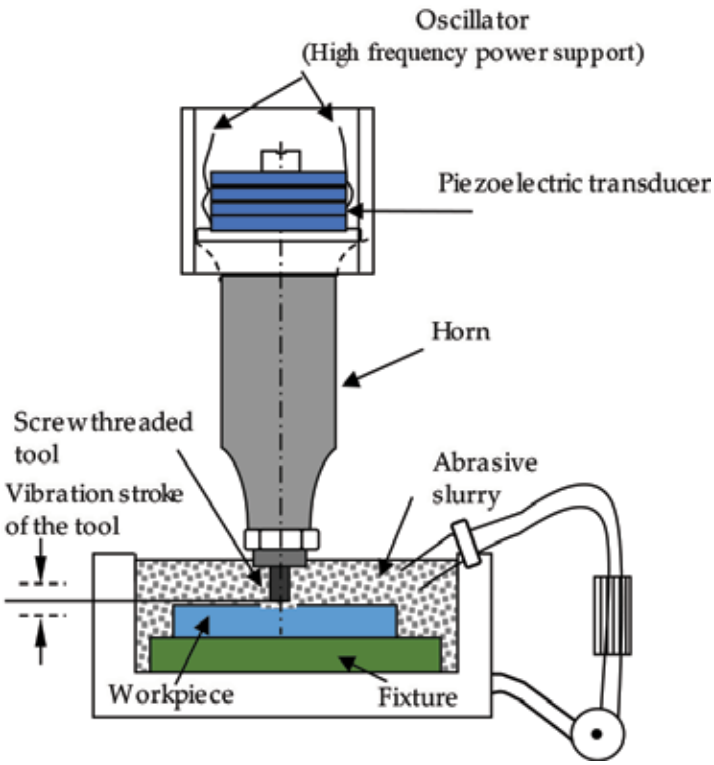

Figure 1. Schematic of basic elements in USM.

of tiny cracks of the workpiece in this situation. The second group includes the materials that exhibit some plastic deformation before fracture like titanium alloys, carburized, and nitrided steels. USM can machine these materials although with some difficulty. The last group consists of the ductile materials, such as soft steel and copper, and they are unsuitable in principle for USM. Note that a recent research reported that the ductile substrate materials are not really removed but are displaced, which also have been observed for some fine polishing operations [4]. The classification of the materials and fields of application for USM are given in **Table 1**.

USM has shown potentialities in many manufacturing uses; the most commonly ones are the fabricating structures of any shapes on hard and brittle materials. Hole drilling always stands as the most popular machining process for product manufacturing, and USM in particular shows a high potentiality in fabricating diverse holes either with large/small diameters or high aspect ratios. Masuzawa's group firstly proposed micro-USM as an effective micromachining process for hard and brittle materials. Holes with diameters as small as 5 μm and aspect ratios larger than 5 were successfully fabricated on quartz glass and silicon by micro-USM in one of their studies [6]. At the other extreme, tools with diameters as large as 85 mm were successfully employed for drilling holes with a high-capacity (2.5 kW) ultrasonic machine [7]. Besides, USM is playing an irreplaceable role in fabricating holes with a high

Group of material	Predominant type of deformation	Type of failure	Field of application of USM
I. Glass, mica, quartz, ceramic, diamond, germanium, silicon, ferrite, alsifer	Elastic	Brittle	Manufacturing parts of semiconducting materials
			Making industrial diamonds
			Fabricating special ceramics
			Manufacturing parts of glass quartz or minerals in the optical and jewelry industries
			Machining ferrite, alsifer, and other materials
II. Alloys tempered to high hardness carburized and nitrided steels, titanium alloys	Elastic–plastic	Brittle after work hardening by plastic deformation	Making and repairing hard alloy dies, press tools, and purchases
			Shaping or sharpening hard alloy tools
III. Lead, copper, soft steel	Plastic	No failure (or ductile failure)	Unsuitable for ultrasonic machining

Table 1. Classification of materials and fields of application for USM [3, 5].

aspect ratio. Micro-holes under 100 μm in diameter and aspect ratios of 10 on quartz glass were achieved by electrorheological fluid-assisted USM [8].

There also has been a heavy industrial demand for the fabrication of 3D microstructures on various hard and brittle materials. Two ways are used to achieve microstructures on hard and brittle materials via USM. One is by directly duplicating the tool shape on workpiece. In this way, complex 3D structures or multiple holes can be generated with a single pass of the machining tool. However, some problems including different machining rates over the whole working area and differential tool wear rate should be solved when using tools of complex form for keeping the product shape [9, 10]. Moreover, it is troublesome to fabricate micro-tools of complex shapes. The other one is to employ a simple "pencil" tool and contour the complex structures via a computerized numerical control (CNC) program. By using this method, machining any complex microstructures on hard and brittle materials accurately is possible. Sun et al. [11] have developed a 3D micro center-pin bearing air turbine using this method successfully, and the test results show that the turbine has a great reliability.

2.3. Involved material removal mechanism

The material removal mechanisms in basic USM were investigated quite intensively. Three well-recognized major removal actions were summarized by the previous researchers and include [5, 9, 12] (i) mechanical abrasion due to direct hammering of larger abrasive particles on the workpiece surface, (ii) microchipping resulted from the impact of free-moving abrasive particles, and (iii) cavitation erosion from the abrasive slurry. These mechanisms are schematically shown in **Figure 2**.

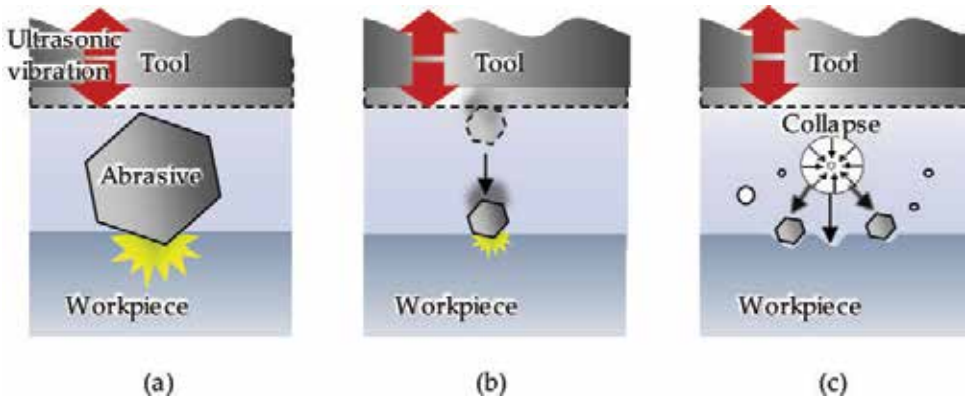

Figure 2. Schematic diagram of material removal mechanisms in USM: (a) hammering action, (b) impact action, and (c) cavitation erosion.

However, as it is difficult to observe the USM phenomena directly, a total understanding of the material removal is still not possible. Only qualitative evaluations according to experimental results were reported [13–15], except that an analysis model was established recently [16] based on the former study [17]. In other studies, the researchers concentrated on revealing the material removal mechanism [5, 18] by assuming the hammering of an abrasive particle in USM as an indentation process. However, the direct indentation process does not involve the actions including the tool vibration and abrasive fracture in USM; a more effective way for investigating and understanding the nature of material removal in USM is necessary.

The present author's group firstly proposed to study the influences of the hammering action and the impact action on material removal in USM process using a mesh-free numerical simulation method, smoothed particle hydrodynamics (SPH) [19]. The results are shown in **Figures 3** and **4**, respectively. One cycle of the tool vibration was simulated, and the fluid effect was not considered. Fractures occurred in both the abrasive and the workpiece after the hammering action as shown in **Figure 3(d)**. However, in the case of impact action, the accelerated abrasive due to the tool impact did not generate fractures and rebounded as depicted in **Figure 4(d)**, which means that the impact action is not effective for material removal on the raw work surface. The obtained results support the common view that hammering action plays a primary role in material removal of USM process [5].

2.4. Main process parameters

A large number of input parameters exist in USM process which would influence the machining performance. A cause and effect diagram to show the potential factors affecting USM is depicted in **Figure 5**. Influences of major process parameters on the material removal rate, machining precision, surface quality, and tool wear have been widely experimentally investigated.

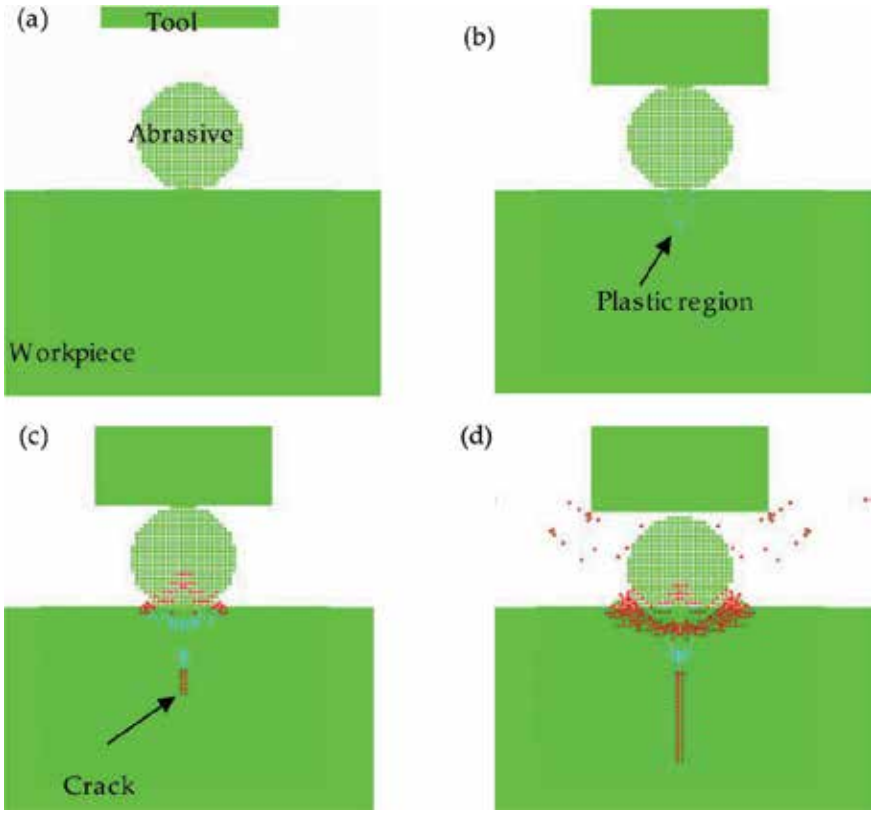

Figure 3. Simulation results of direct hammering action on the work surface: (a) before calculation, (b) after tool impact (0.1 μs calculation), (c) 1 μs calculation, and (d) after unloading.

Lee and Chan [18] investigated the influence of vibration amplitude, static load, and the particle size on the machining rate and surface roughness. They suggested that the material removal rate (MRR) would be increased, while the machined surface would be roughened with any increase in these parameters. Yu et al. [20] stated that the machining speed decreased with an increase in the static load beyond a certain level and the abrasive size was a dominant factor influencing the surface roughness in USM. Guzzo et al. [21] demonstrated an increase in material removal rate with larger abrasive particles due to the increase in the stress induced by the impact of these particles against the work surface. Komaraiah and Reddy [5] discussed the effects of mechanical properties of the workpiece on material removal rate and found that the hardness and fracture toughness of the workpiece material played an important role in ultrasonic machining. There was a reduction in material removal rate with the increase of the hardness and fracture toughness of the workpiece material. In another study of Komaraiah and Reddy [22], experiments were carried out to clarify the effect of tool materials on the material removal rate, tool wear, and surface quality. While a difficult-to-machine material can be machined effectively, the tool in USM was

http://dx.doi.org/10.5772/intechopen.75170

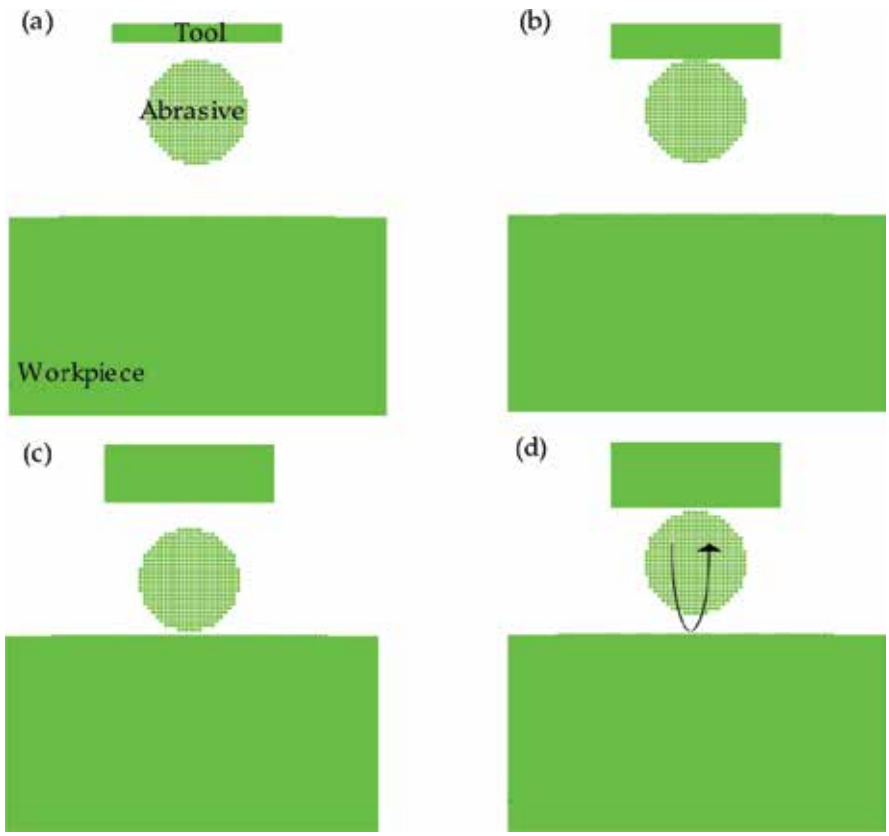

Figure 4. Simulation results of impact action: (a) before calculation, (b) after the tool impact on the abrasive particle, (c) after the particle impact on the work surface, and (d) rebound of the abrasive particle.

also worn. It was found that larger material removal rate, diametral tool wear resistance, and lower surface roughness can be obtained when using harder tool material. They also stated that both the hardness and the impact strength of the tool material would influence the longitudinal tool wear. Hocheng et al. [23] considered that large vibration amplitude increased the kinetic energy of abrasive particles, which wore the tool tip seriously, while a large static load depressed the free vibration of the abrasive particles and slowed down the tool wear.

Although many factors affect the machining performance of USM, it is believed that an optimum machining condition can be found to meet specific machining requirements. Further studies on the material removal mechanism in USM are extremely significant for understanding the influences of various process parameters on machining performance, which can provide a guidance in choosing suitable machining conditions and improve the machining performance.

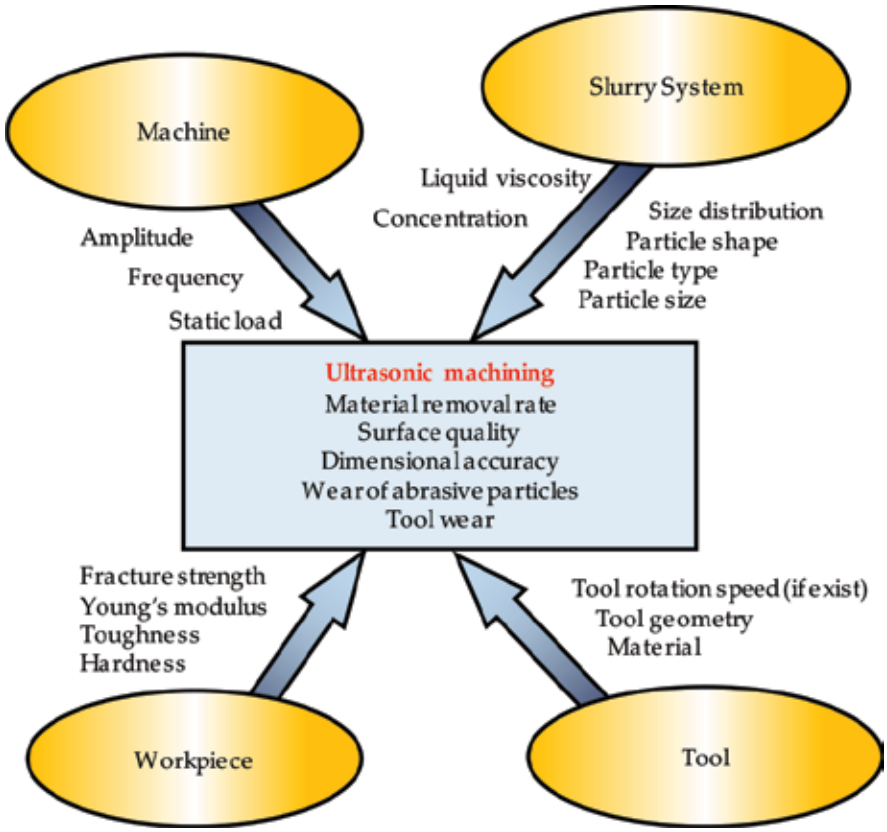

Figure 5. A cause and effect diagram for machining parameters in USM.

3. SPH simulation and experimental verification

3.1. Simulation method and results

3.1.1. Smoothed particle hydrodynamics (SPH)

SPH is a mesh-free numerical technique first introduced to solve astrophysics problems. In SPH, the system is represented by a set of particles that carry material properties and interact with each other according to the governing conservation equation. Problems involved in large deformation, which may cause errors due to mesh distortion and tangle with the grid-based method, can be effectively solved by the SPH. Thus, it is capable to simulate a USM process, in which material fracture occurs under repeated impacts of abrasive particles.

3.1.2. Material modeling

Glass, silicon carbide (SiC), and SS304 referred to stainless steel (AISI:304) were used for workpiece, abrasive, and tool material, respectively. Glass and SiC, which are hard and brittle, have

high compressive strength but low tensile strength; the Mie-Grüneisen polynomial equation of state was employed. On the other hand, the strength and damage behavior of these materials were modeled with Johnson-Holmquist material model [24, 25], in which fracturing occurs when the hydro tensile limit is reached. For SS304 material, the Shock equation of state was used, and the strength is formed by Steinberg-Guinan model. The constants related to the equations of the material models and material properties, for glass [26], SiC [27], and SS304 [28], are obtained from existing test data and summarized as shown in **Table 2**.

3.1.3. Modeling conditions and assumptions

In USM, a large number of abrasive particles act on the workpiece simultaneously by repeated impacts of the tool, and the hammering action dominates the main material removal. Therefore, the simulation model was built with two abrasive particles based on the direct hammering action to figure out influences of the interaction between adjacent abrasive particles on the process. **Figure 6** shows a snapshot of the model. The dimensions for each part is as defined in the figure. One half of the geometry was established with symmetric boundary conditions, and spherical abrasive particles were considered. The abrasive particle and the partial workpiece areas around the hammering site, where heavy deformation can occur, were built with SPH solver. The ultrasonically vibrated tool and the remaining parts of the workpiece were modeled by using the Lagrange finite element mesh. It is because that the SPH algorithm takes more time to find neighboring particles, which is usually more expensive in computation time. Materials in small deformation to be constructed with the grid-based Lagrange solver are helpful to reduce the calculation amount.

Figure 7 shows the moving conditions of the tool tip. The solid curve is the ideal condition given in the experiments: the tool tip vibrates sinusoidally with a frequency of 61 kHz and the total amplitude of 4 μm. Contrastingly, the dashed curve is the simplified condition for the calculation: the

	Float glass	**SiC**	**SS304**
Equation of state	Polynomial		Shock
Density (g/cm^3)	2.53	3.215	7.9
Bulk modulus (GPa)	45.4	220	None
Grüneisen coefficient (Γ)	None		1.93
Strength	Johnson-Holmquist		Steinberg-Guinan
Shear modulus (GPa)	30.4	193.5	77 (G_0)
Hugoniot elastic limit (GPa)	5.95	11.7	None
Yield stress (MPa)	None	None	340 (Y_0)
Failure	Johnson-Holmquist		None
Hydro tensile limit (MPa)	150	750	None

Table 2. Material models and relevant parameters.

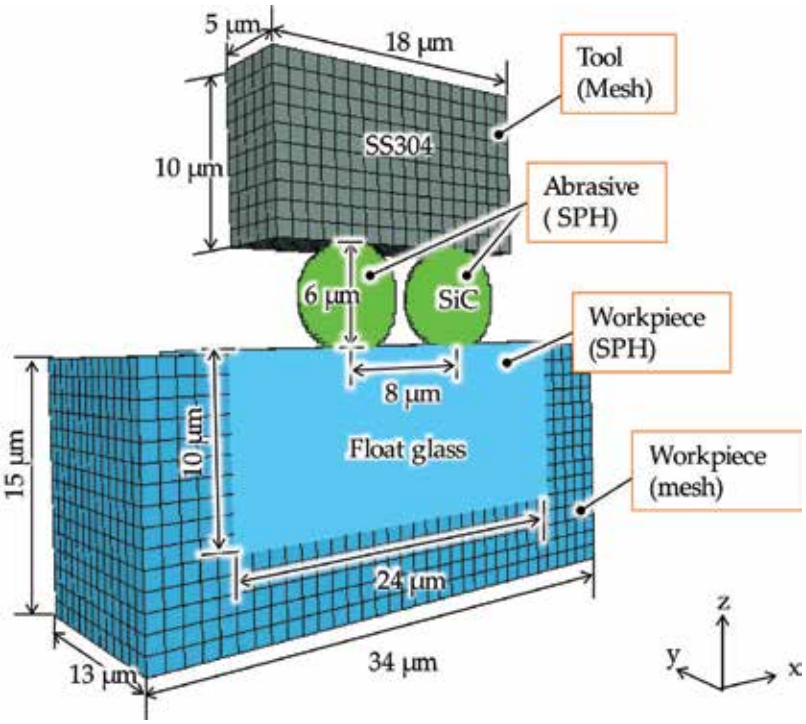

Figure 6. Snapshot of the initial state of the simulation model for two abrasive particles.

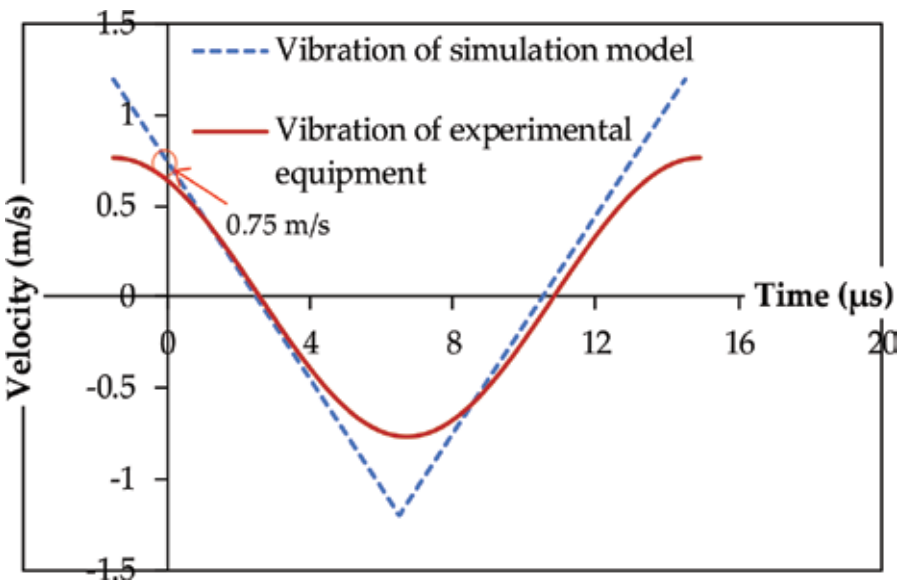

Figure 7. Velocity condition of the ultrasonically vibrated tool.

http://dx.doi.org/10.5772/intechopen.75170

condition is approximated to be linear variation in the simulation model. Even though the force between the tool and the abrasive particle may alter the tool motion, it is assumed that the velocity variation keeps linear in the whole calculation. The tool velocity condition was applied to nodes on the top surface of the tool, and the calculation starts with the velocity value of 0.75 m/s. All nodes on the bottom and side surfaces of the workpiece were constrained in the direction of z and x/y axes, respectively. Before calculation, the tool tip surface and the work surface are completely flat. As the tool starts to touch the abrasive and forces the abrasive to penetrate into the workpiece, all parts begin to deform or fracture. The contacts between the abrasive and the tool and the abrasive and the workpiece were assumed frictionless. Effect of the liquid in slurry and its flow on the material removal is negligible, which means that only the abrasive particle was considered.

3.1.4. Simulation results

The time-dependent simulation results along X-Z symmetric plane are shown in **Figure 8**. The colors shown in the figure represent the state of the material. The green, blue, and red

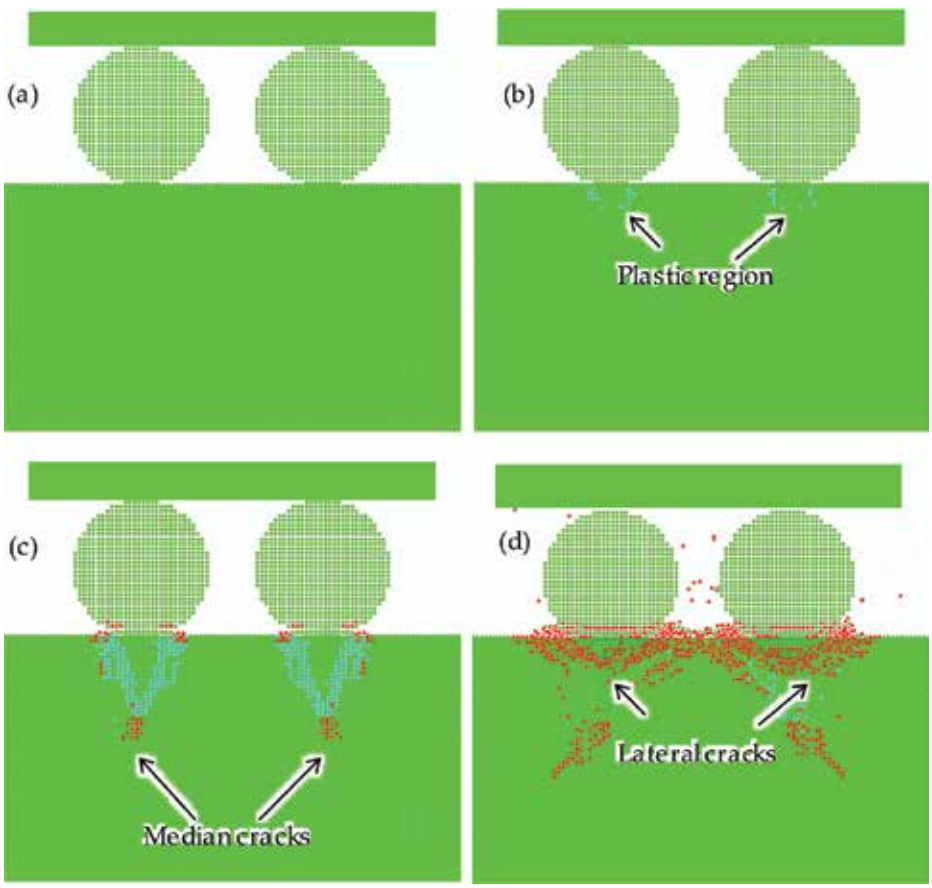

Figure 8. Simulation results of hammering actions by two adjacent abrasive particles: (a) initial condition, (b) after 0.1 μs, (c) after 0.25 μs, and (d) after unloading.

elements indicate elastic, plastic, and failure states, respectively. After 0.1 μs calculation, plastic zone induced by each of the two abrasive particles can be confirmed from the workpiece beneath the hammering location as shown in **Figure 8(b)**, which is the same as the result obtained from the single hammering calculation. With increase of the penetration of the tool, the median cracks initiate and propagate as shown in **Figure 8(c)**. A simultaneous fracture of the abrasives is also observed. With further penetration imposed by the tool, the cracks indicated in **Figure 8(c)** propagated into the surrounding material at an angle to the load axis instead of propagating parallel to the loading axis beneath the impact surface. In addition, the crushing of work material near the hammering site that is caused by each of the two abrasive particles became larger and larger as the loading displacement increases and finally coalesced. **Figure 8(d)** shows the final results after unloading. The lateral cracks also developed and propagated nearly parallel to the work surface after unloading.

3.1.5. Effect of the distance between impacts

Calculations were conducted by varying the distance between abrasive particles, and the results are shown in **Figure 9**. When the distance is within a specific range, the cracks are coalesced in the region between the impacts. With the increase of the distance between the two particles, the crack distribution becomes more similar to the one developed by a single impact, which means the interaction of the adjacent abrasive on the stresses in the region between two particles is decreased. The change of the material removal rate of the workpiece versus the distance between two adjacent abrasive particles is depicted in **Figure 10**. The material removal rate was defined as the mean volume of the materials removed by the mass of the two particles. It is noted that the interference between the two abrasive particles decreases when the distance between the two adjacent abrasive particles increases, which

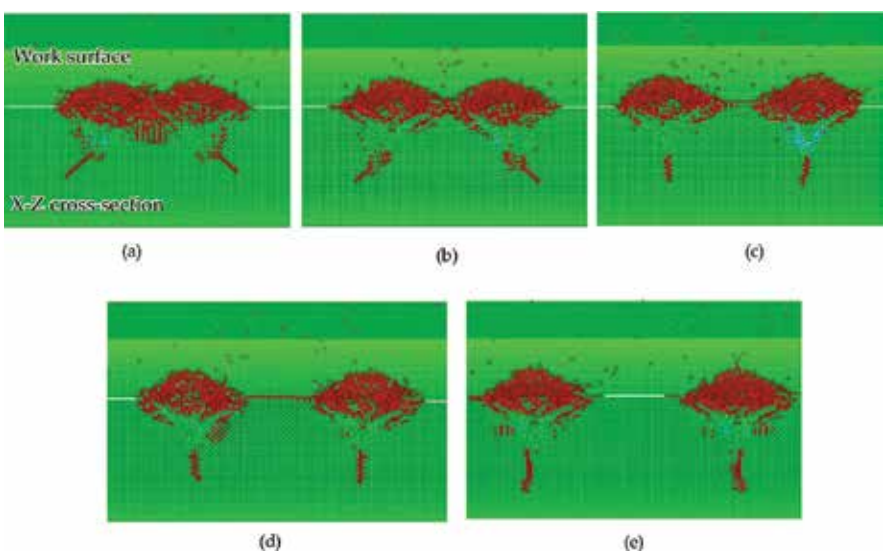

Figure 9. Effect of the distance between impacts: (a) 6.5 μm, (b) 8 μm, (c) 10 μm, (d) 12 μm, and (e) 14 μm.

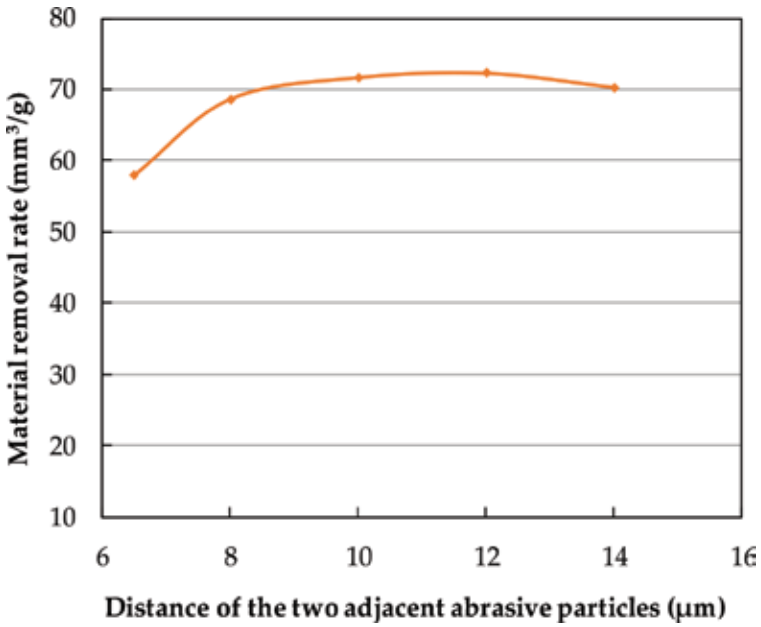

Figure 10. Effect of the distance between impacts on material removal of the workpiece.

increases the material removal rate. However, when a certain distance is exceeded, the interaction effect of the two adjacent abrasive particles is lost and the material removal would not be increased any more. The optimal distance for enhancing material removal rate was found to be 12 μm, twice the particle diameter.

3.2. USM experiments for verifying the simulation results

3.2.1. Experimental methods

USM experiments were conducted with different slurry concentrations for investigating the effect of the distance change among the abrasive particles. **Table 3** lists the experimental conditions. The machining was carried out with no circulation of slurry, and no tool feed was applied on the tool. A noncontact laser probe profilometer (Model: NH-3SP; Mitaka Kohki Co. Ltd., Japan) was used to scan across the machined area, and the volume of material removal was obtained by analyzing the three-dimensional surface topography. The cross sections of the machined surfaces were then created and examined using a scanning electron microscope (Model: SUI510; Hitachi Co. Ltd., Japan).

3.2.2. Experimental results

Figure 11 shows a schematic diagram of the experiment. In the simulation, only two particles were considered. However, there are a large number of abrasive particles worked on the workpiece in practical USM. Therefore, in order to verify the simulation results, the two parameters, i.e., material removal rate and distance of the two adjacent abrasive particles,

Vibration frequency (kHz)	61
Vibration amplitude (μm)	4 (peak to peak)
Tool material	SS304
Workpiece material	Glass
Abrasive (mesh size)	SiC #2000 (mean size, 8.4 μm)
Concentration of abrasive slurry	5, 10, 20, 30, 40, and 50 wt% mixed with water
Distance between workpiece and tool (μm)	10
Machining time (s)	30

Table 3. Experimental conditions.

were defined for comparison. The material removal rate was calculated as the volume of the materials removed from the workpiece divided by the mass of abrasive particles in the machining zone as shown in **Figure 11**. The distance between two adjacent abrasive particles in the slurry was calculated from the slurry concentration according to a formula taken from previous work [29]:

$$C = \frac{(\pi/6)\, d_0^3\, \eta \rho_g}{\lambda^2 d_0^3 \rho_g + (\pi/6)\, d_0^3\, \eta(\rho_g - \rho_e)} \times 100. \quad (1)$$

in which abrasive particles with the same diameter d_0 are supposed to be equally distributed in the machining area and schematically shown in **Figure 12**. λd_0 is the distance between the two adjacent abrasive particles, C is the slurry concentration, η is the volumetric efficiency of the abrasive particle, ρ_g is the density of the abrasive material, and ρ_e is the density of the slurry medium. In this work, the abrasive particle is SiC and the slurry medium is water; the corresponding densities are $\rho_g = 3.2$ g/cm^3 and $\rho_e = 1$ g/cm^3, respectively. Parameter $\eta = 90\%$, which

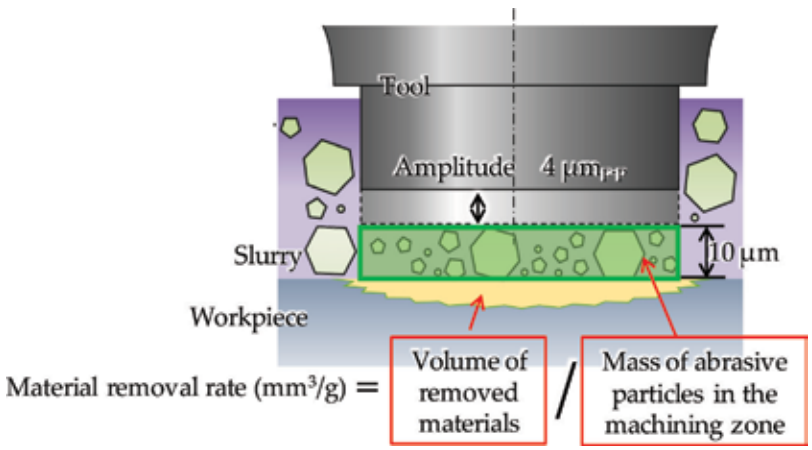

Figure 11. Schematic diagram of the experiment.

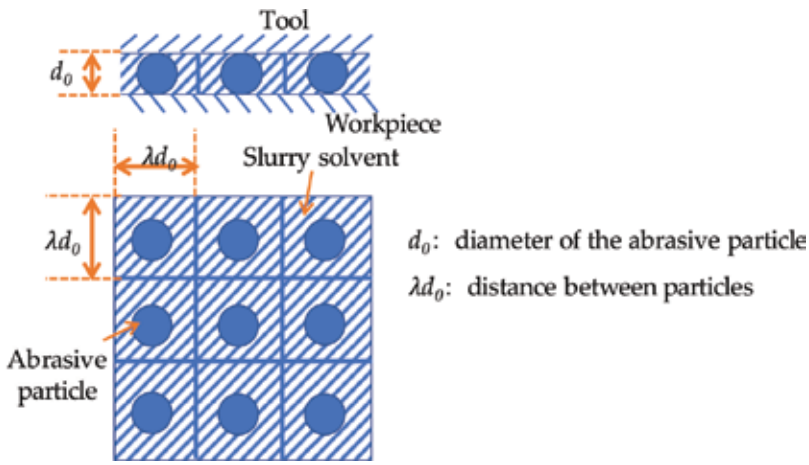

Figure 12. Distribution of abrasive particles in the machining area.

was determined by analyzing the abrasive particle shape using a particle analyzer (Model: Sysmex FPIA-3000; Malvern Instruments Ltd.). By substituting these values, λ under different slurry concentrations can be obtained. The relationship between the material removal rate and λ was determined and compared with the simulation results as shown in **Figure 13**. The simulation results were obtained from **Figure 10**, where the description of X axis was changed to λ by dividing the particle diameter 6 μm used in the model. The values obtained from

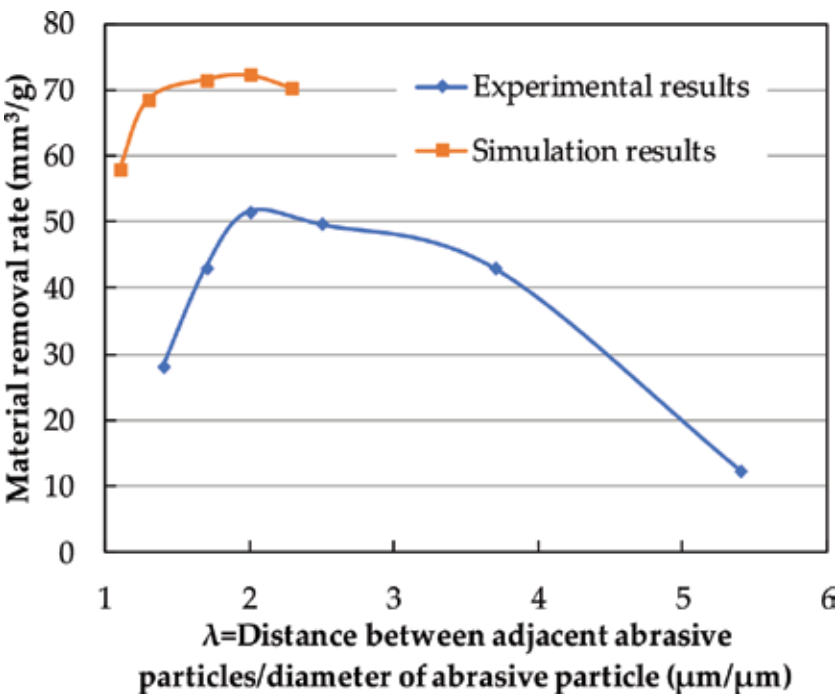

Figure 13. Effect of the distance between two adjacent abrasive particles on material removal rate.

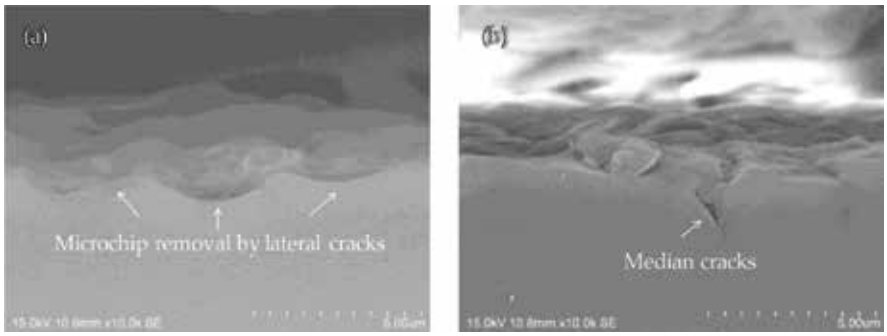

Figure 14. Cross sections of the machined surfaces: (a) microchip removal by lateral cracks, (b) example of median cracks.

the simulation results are constantly higher than those of experiments due to several factors including the nonuniformity of the abrasive particles in real machining process. However, both curves indicate that low material removal rate was obtained when the two adjacent abrasive particles are either very close or extremely far away. Maximum material removal was developed only when the distance between the impacting abrasive particles is optimal, which is found to be equal twice the diameter of abrasive particle from these results.

Although the material removal rate is influenced by slurry concentrations, the machined surfaces showed the same topography because materials are removed by the accumulation of cracks. **Figure 14** presents the SEM micrographs of cross sections of the surface machined by USM. From the micrographs, material removal via microchips which were occurred by the accumulation of lateral cracks can be confirmed. In **Figure 11(b)**, the median cracks remaining in the workpiece can also be observed. Both of the simulation and experimental results indicate that the material removal during USM is mainly caused by the accumulation of lateral cracks, while the median crack may play a less role. In addition, the median cracks that remain in the workpiece may cause subsurface defects and accordingly lower the quality of machined surface.

4. Summary and prospect

The current work introduced the background of the USM firstly. The importance of developing efficient micromachining technology for hard and brittle materials was stated. By comparing several machining processes, the potentiality of USM in micromachining of various hard and brittle materials was pointed out. Then, smoothed particle hydrodynamics method was proposed to study the material removal in USM and to reveal the influence of distance between two adjacent abrasive particles. The model was proven capable of simulating the crack generation in USM and helpful for predicting the machining results.

As the machining requirements of modern electronical, optical, and automotive components are getting stricter, there still exist many problems to be solved in the future for putting USM into practical industry. In micro-USM, the volume of material removed per stroke is very little due to the use of micrometer size abrasive particles. In fact, the corresponding machining speed is slowed down in order to obtain high form accuracy and superior surface finish

without large damages. However, with respect to a brittle material, microcracks are expected to be generated during this process and accordingly left on the machined surface. It is therefore important to find ways to remove these surface/subsurface cracks with no sacrifice of the machining speed, which means that the best balance machining conditions should be explored. A deep understanding of the mechanism and the effect of each machining parameter on USM needs to be given in future works.

Acknowledgements

The author gratefully acknowledges the support from Professor Tsunemoto Kuriyagawa, Associate Professor Masayoshi Mizutani, and Assistant Professor Keita Shimada at Tohoku University in Japan for their kind suggestions of my research work. The author would also like to thank Taga Electric Corporation in Japan with respect to the manufacture of USM tool and SmartDIYs Corporation for the provision of laser cutter parts for crack repair in the experiments.

The author would like to thank the financial support of "the Fundamental Research Funds for the Central Universities," China [Grant no. 3132018259].

Conflict of interest

The author(s) declared no potential conflicts of interest with respect to the research, authorship, and/or publication of this article.

Author details

Jingsi Wang

Address all correspondence to: jixiewangjingsi@hotmail.com

Marine Engineering College, Dalian Maritime University, Dalian, China

References

[1] Brow RK, Schmitt ML. A survey of energy and environmental applications of glass. Journal of the European Ceramic Society. 2009;**29**(7):1193-1201. DOI: 10.1016/j.jeurceramsoc.2008.08.011

[2] Tsuboi R, Kakinuma Y, Aoyama T, Ogawa H, Hamada S. Ultrasonic vibration and cavitation-aided micromachining of hard and brittle materials. Procedia CIRP. 2012;**1**:342-346. DOI: 10.1016/j.procir.2012.04.061

[3] Markov AI, Neppiras EA. Ultrasonic Machining of Intractable Materials. Iliffe: Scripta Technica, Inc.; 1966

[4] Klocke F, Dambon O, Capudi Filho GG. Influence of the polishing process on the near-surface zone of hardened and unhardened steel. Wear. 2005;**258**:1794-1803. DOI: 10.1016/j.wear.2004.12.015

[5] Komaraiah M, Reddy PN. A study on the influence of workpiece properties in ultrasonic machining. International Journal of Machine Tools and Manufacture. 1993;**33**(3):495-505. DOI: 10.1016/0890-6955(93)90055-Y

[6] Egashira K, Masuzawa T. Microultrasonic machining by the application of workpiece vibration. CIRP Annals – Manufacturing Technology. 1999;**48**(1):131-134. DOI: 10.1016/S0007-8506(07)63148-5

[7] Baek DK, Ko TJ, Yang SH. Enhancement of surface quality in ultrasonic machining of glass using a sacrificing coating. Journal of Materials Processing Technology. 2013;**213**(4):553-559. DOI: 10.1016/j.jmatprotec.2012.11.005

[8] Tateishi T, Yoshihara N, Kuriyagawa T. Fabrication of high-aspect ratio micro holes on hard brittle materials—Study on electrorheological fluid-assisted micro ultrasonic machining. In: The 4th International Conference on Leading Edge Manufacturing in 21th Century (LEM21); 2007

[9] Thoe TB, Aspinwall DK, Wise MLH. Review on ultrasonic machining. International Journal of Machine Tools and Manufacture. 1998;**38**(4):239-255. DOI: 10.1016/S0890-6955(97)00036-9

[10] Ghabrial SR. Trends towards improving surfaces produced by modern processes. Wear. 1986;**109**(1):113-118. DOI: 10.1016/0043-1648(86)90256-5

[11] Sun X, Masuzawa T, Fujino M. Micro ultrasonic machining and its applications in MEMS. Sensors and Actuators A: Physical. 1996;**57**:159-164. DOI: 10.1016/S0924-4247(97)80107-0

[12] Ichida Y, Sato R, Morimoto Y, Kobayashi K. Material removal mechanisms in non-contact ultrasonic abrasive machining. Wear. 2005;**258**(1):107-114. DOI: 10.1016/j.wear.2004.05.016

[13] Kumar J, Khamba JS. Modeling the material removal rate in ultrasonic machining of titanium using dimensional analysis. The International Journal of Advanced Manufacturing Technology. 2010;**48**:103-119. DOI: 10.1007/s00170-009-2287-1

[14] Zarepour H, Yeo SH. Predictive modeling of material removal modes in micro ultrasonic machining. International Journal of Machine Tools and Manufacture. 2012;**62**:13-23. DOI: 10.1016/j.ijmachtools.2012.06.005

[15] Singh R, Khamba JS. Taguchi technique for modeling material removal rate in ultrasonic machining of titanium. Materials Science and Engineering A. 2007;**460**:365-369. DOI: 10.1016/j.msea.2007.01.093

[16] Agarwal S. On the mechanism and mechanics of material removal in ultrasonic machining. International Journal of Machine Tools and Manufacture. 2015;**96**:1-14. DOI: 10.1016/j.ijmachtools.2015.05.006

[17] Kainth GS, Nandy A, Singh K. On the mechanics of material removal in ultrasonic machining. International Journal of Machine Tool Design and Research. 1979;**19**(1):33-41. DOI: 10.1016/0020-7357(79)90019-2

[18] Lee TC, Chan CW. Mechanism of the ultrasonic machining of ceramic composites. Journal of Materials Processing Technology. 1997;**71**(2):195-201. DOI: 10.1016/S0924-0136(97)00068-X

[19] Katahira T, Shimada K, Zhou T, Yan J, Kuriyagawa T. Material removal mechanism of ultrasonic machining. Journal of the Japan Society for Abrasive Technology. 2012;**56**(2):108-111. DOI: 10.11420/jsat.56.108

[20] Yu Z, Hu X, Rajurkar KP. Influence of debris accumulation on material removal and surface roughness in micro ultrasonic machining of silicon. CIRP Annals—Manufacturing Technology. 2006;**55**(1):201-204. DOI: 10.1016/S0007-8506(07)60398-9

[21] Guzzo PL, Shinohara AH, Raslan AA. A comparative study on ultrasonic machining of hard and brittle materials. Journal of the Brazilian Society of Mechanical Sciences and Engineering. 2004;**26**(1):56-61. DOI: 10.1590/S1678-58782004000100010

[22] Komaraiah M, Reddy PN. Relative performance of tool materials in ultrasonic machining. Wear. 1993;**161**:1-10. DOI: 10.1016/0043-1648(93)90446-S

[23] Hocheng H, Kuo KL, Lin JT. Machinability of zirconia ceramics in ultrasonic drilling. Materials and Manufacturing Processes. 1999;**14**(5):713-724. DOI: 10.1080/10426919908914864

[24] Johnson GR, Holmquist J. A computational constitutive model for brittle materials subjected to large strains, high strain rates and high pressures. In: Shock-Wave and High-Strain-Rate Phenomena in Materials. New York: Marcel Dekker; 1992. pp. 1075-1081

[25] Johnson GR, Holmquist TJ. An improved computational constitutive model for brittle materials. High-Pressure Science and Technology. 1994:981-984

[26] Holmquist TJ, Johnson GR, Grady DE, Lopatin CM, Hertel Jr ES. High strain rate properties and constitutive modeling of glass. In: Proceeding of the 15th International Symposium on Ballistics; 1995. p. 237

[27] Holmquist TJ, Johnson GR. Response of silicon carbide to high velocity impact. Journal of Applied Physics, Livermore. 2002;**91**(9):5858-5866. DOI: 10.1063/1.1468903

[28] Steinberg DJ. Equation of State and Strength Properties of Selected Materials. Livermore: Lawrence Livermore National Laboratories; 1996

[29] Sato K, Matsui M. Seimitsu Shiagehou (Precision Finishing). Kyoritsu Shuppan, Tokyo; 1958 (in Japanese)

Chapter 3

Advanced Abrasive Waterjet for Multimode Machining

H.-T. (Peter) Liu, Vanessa Cutler,
Chidambaram Raghavan, Peter Miles,
Ernst Schubert and Nathan Webers

Additional information is available at the end of the chapter

http://dx.doi.org/10.5772/intechopen.75313

Abstract

Abrasive waterjet (AWJ) possesses inherent technological and manufacturing advantages unmatched by most machine tools. Recent advancements in AWJ processes have enhanced those merits. Multidisciplinary advancements include process automation, position accuracy, cutting models, range of part dimensions, ergonomics, user and environmental friendliness, feature recognition, and others. Among the technological merits, AWJ is material independent and a cold cutting tool, capable of preserving the structural and chemical integrity of parent materials. For heat sensitive materials, AWJ often cuts over 10 times faster than thermal cutting tools such as lasers and electrode discharge machining. Unlike photochemical etching, AWJ is environmentally friendly, producing no toxic byproducts. Additionally, AWJ requires only a single tool assisted with accessories to qualify for multimode machining; it is cost effective with fast turnaround for small and large lots alike. Recent advancements together with relevant R&D, engineering, and industrial applications will be presented for precision multimode machining from macro to micro scales.

Keywords: high pressure pump, micro abrasive waterjet, multimode machining, cold cutting, material independence, heat affected zone, cutting model, multi-passes

1. Introduction

Abrasive waterjet (AWJ) is a machine tool that removes materials by an erosion process of abrasive particles impacting the workpiece at supersonic speeds [1–3]. In [1], the history and fundamentals of waterjet technology and the early stage of the development of micro abrasive waterjet (μAWJ) technology is described. This chapter is an update to report the

progresses in the evolution of μAWJ and its impact on the overall advancement of waterjet technology.

AWJ inherently possesses several technological and manufacturing merits unmatched by most other tools [1]. The ones that are most relevant for precision machining are revisited below and expanded throughout this article.

- Material independence – cuts virtually any material, thin and thick
- Cold cutting – induces no heat affected zone (HAZ) and preserves structural and chemical integrity of parent materials
- Low force exerted on workpiece
- One tool qualified for multimode machining
- Broad range of part size from macro to micro scales
- No tooling requirement - cost effective with fast turnaround

In a 2005 marketing report, Frost and Sullivan stated that waterjet machine tools emerged as the fastest growing segment of the overall machine tool industry in the last decade, and this trend is expected to continue.[1] The lack of awareness among potential end-users, however, posed a stiff challenge to market participants on increasing the end-user base. Since then, waterjet technology has made advancements to take full advantage of its inherent merits. Waterjet performance has been elevated to the degree that it competes on an equal footing with conventional tools such as lasers, electronic discharge machining (EDM), and photo-chemical etching. In some cases, its performance greatly exceeds those of its conventional counterparts. The lack of awareness of these merits, though, still presents a considerable challenge to a broader acceptance as a precision machine tool.

2. Technical approach

The evolution of waterjet technology has focused on the development of software, hardware, and machining processes to take advantage of technological and manufacturing benefits. These developments focused on automating machining processes, improving machining precision and efficiency, minimizing environmental impact, enhancing ergonomics, ensuring user friendliness, and broadening capabilities toward multimode machining. At OMAX Corporation, this included software development of the Intelli-MAX® Software Suite to upgrade to new generations of cutting models and add new machining features aimed at precision and automated machining; hardware development and commercialization of micro abrasive waterjet (μAWJ) for meso-micro machining and the development of novel processes concepts for machining various features.

[1]Frost and Sullivan – "The World Waterjet Cutting Tools Markets" Date Published: 30 Aug 2005 (www.frost.com)

3. Equipment

3.1. JetMachining Centers

AWJ machining was carried out on several models of JetMachining Centers® (JMCs), including the MicroMAX® and the 60120®, as illustrated in **Figure 1**. The MicroMAX is one of the newest JMCs developed and commercialized under the support of an NSF SBIR Phase II grant for precision meso-micro machining. With the NSF SBIR Phase IIB supplemental funding, the MicroMAX was upgraded to incorporate a Tilt-A-Jet® (TAJ) for taper compensation and a Rotary Axis® for facing, turning, grooving, trimming, and machining other 3D features. The 60120 with a 3200 mm by 1575 mm cutting envelope was designed for machining large parts.

Three key accessories, the TAJ for taper compensation, the Rotary Axis for machining features on rotating workpieces, and the A-Jet 5-axis articulate head are options available for most JMCs, as illustrated in **Figure 2**. The combined operation of the Rotary Axis and the A-Jet is capable of machining many complex 3D features. A camera can be mounted next to the cutting head for precision locating and aligning features on workpieces.

3.2. Abrasive waterjet nozzles

Four AWJ nozzles were used: 14/30, 10/21, 7/15, and 5/10, each with orifice ID/mixing tube ID (in thousandth of inch). The diameter ratios are 0.36 mm/0.76 mm, 0.25 mm/0.53 mm, 0.18 mm/0.38 mm, and 0.13 mm/0.25 mm, respectively. The 7/15 is the smallest production nozzle whereas the 5/10 nozzle is a beta nozzle. A water-only nozzle is available for cutting relatively soft materials. **Figure 3** illustrates these nozzles. Garnet with sizes from 80 to 320 mesh was used as the abrasives in this investigation to machine parts with a wide range of part size and thickness.

3.3. Software

The software for automating waterjet cutting is the Intelli-MAX Software Suite. It includes a specialized CAD package LAYOUT, a user friendly controller MAKE, and an OMAX Interactive Reference (OIR) (http://www.omax.com/waterjets/software).

Figure 1. (a) MicroMAX and (b) 60120 JMC.

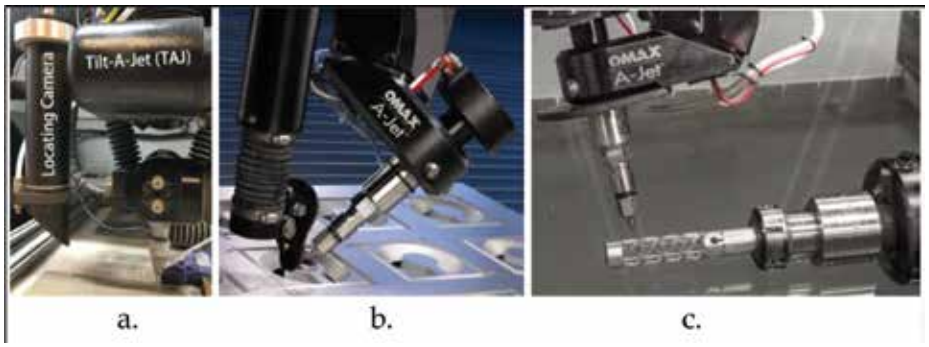

Figure 2. Accessories for 3D machining (a) TAJ (b) A-Jet (c) Rotary Axis.

Figure 3. Waterjet nozzles.

Intelligent software **–** The JMCs are controlled by a suite of software programs built around the patented motion control to automate the AWJ machining processes. Samples of the software suite are listed below.

3.3.1. Operational software

- **LAYOUT** is a full-featured CAD program created and designed to work with JMCs. Part drawings can be created by using a full set of drawing tools, importing a drawing from another CAD program in standard format such as DXF, or tracing a drawing or photograph. The toolpath of that part can then be created with LAYOUT.
- **MAKE** actually controls the JMC to create parts with several simple steps: (1) open a toolpath file created by LAYOUT (or another CAD/CAM drawing tool), (2) choose the material you want to use and its thickness (from which the exact nozzle motions required to make the part are calculated accurately, and (3) click on the "Begin Machining" to begin machining parts.

- **Intelli-MAX®** – a suite of new technologies integrated into the OMAX JMCs to enhance the performance of AWJ machining. It is designed to make higher tolerance parts faster – faster and with higher tolerance than any other AWJ systems. The suite has several software modules including Intelli-NEST for part nesting, Intelli-PIERCE for hole piercing, Intelli-TAPER to minimize edge taper, and Intelli-CORNER to corner compensation.

4. Results

One of the most recent advancements in waterjet technology was the development of micro abrasive waterjet (μAWJ) technology for meso-micro machining. The merits of cold cutting, material independence, and low side force exertion on workpieces are keys to elevate the μAWJ as a precision meso-micro machine tool.

For cutting heat-sensitive materials, waterjet is superior to thermally based machine tools such as lasers, electric discharge machining (EDM), plasma cutting, and others. The heat generated by these tools induces a heat-affected zone (HAZ) that alters the structural and chemical properties of the parent material. For thin materials, for example, the heat damage by CO_2 lasers results in considerable part warpage, formation of slag, or even vaporization of materials [2, 4]. The HAZ must be removed or minimized. Removal often requires grinding that is time consuming whereas minimization of the HAZ requires significant reduction in cutting power and therefore cutting speed.

Many machine tools are material limited. For example, lasers have difficulty cutting reflective materials such as copper; EDM cannot cut nonconductive materials; CNC hard tools meet with considerable challenges to cut hardened metals with large Rockwell indices. On the other hand, AWJ cuts most of these materials for a wide range of part size and thickness from macro to micro scales. In fact, AWJ cuts titanium 34% faster than stainless steel.

The low side force exertion on workpieces enables the AWJ to machine thin separations between features. Although the diameter of the μAWJ nozzle is only capable of machining features such as the kerf width of slots and the diameter of holes in the meso scale range (>200 μm), the separation or wall between these features is approaching the micro scale range (<100 μm) [5]. Such a meso-micro machining capability is unmatched by most machine tools that do not offer the combination of cold cutting and low side force exertion.

By adding the MicroMAX into its product line, OMAX has established the full capability of multimode machining of most materials from macro to micro scales – the "7 M" advantage [3]. Considerable efforts have been devoted to conducting cutting tests and presenting the samples to demonstrate the versatility of waterjet technology as a whole. Selected tests and samples are presented herein.

4.1. High pressure pump

The only method we have to produce these very high pressures is through reciprocating motion. There is no turbine or other "continuous" mechanism that can do this. The two

types of electrical prime movers are the electric motor that rotates and a coil or solenoid that can directly produce reciprocating motion. The other prime mover is an internal combustion engine that starts out producing exactly the kind of reciprocating motion we require but in most cases this is converted to rotary motion through a crankshaft. This is then converted back to reciprocating motion in the pump. Waterjet pumps for industrial use are run by electric motors. Pumps for field use tend to be powered by internal combustion engines.

1. Electric motor-intensifier: These are the earliest systems, with the first commercially viable system having been developed by McCartney MFG originally for pumping catalyst in the polyethelene industry.[2] The electric motor drives a hydraulic pump. This hydraulic pressure is routed through a four-way valve system to either side of a hydraulic intensifier that results in reciprocating action and high pressure.
2. Electric motor-direct drive pump: This approach eliminates the hydraulic circuit. An electric motor drives a crankshaft that converts rotary motion to reciprocating motion. These systems can also be run by an internal combustion engine for field applications.
3. Low speed electric servo motor – intensifier: This uses a ball screw to convert low speed rotary motion to low speed reciprocating motion.

Hydraulic horsepower (HP): This is the HP delivered at the nozzle. All the power consumed by the electric motor ends up either as hydraulic HP that is the useful power, or as wasted power in the form of heat.

Efficiency: The electric power delivered to the motor is used up in the following ways:

- **Resistance heating**
  - Losses in the electric motor windings are proportional to the square of the current (i^2R). Motors can be designed with various efficiencies depending on windings. A normal efficiency of an electric motor is in the 90% range.
- **Conversion of rotary to linear motion**
  - The crankshaft is the most efficient method of doing this, as the forces are transmitted between two cylindrical surfaces with a lubrication film between them. The crankcase oil in a direct drive pump should not generally require any cooling system.
  - The hydraulic intensifier is the least efficient as it first converts the rotary motion of the motor to reciprocating motion of the hydraulic pump plungers which then pump a flow rate of hydraulic fluid 20–33 times the cutting water flow rate through a loop. This consists of passages in four-way valves and relief valves, causing pressure drops and heating. This fluid then has to move a large diameter piston that is connected to a smaller diameter plunger, and then return to the holding tank from where it is recirculated. The heat accumulates in the oil and has to be removed by pumping cold water through a heat

[2]"KMT McCartney Products for the LDPE Industry". KMT McCartney Products. Retrieved 10 June 2012.

exchanger or a chiller. The cooling water flow rate may be 4–6 times the water used for cutting.

- In the low speed servo motor system, a servo motor drives a ball screw to convert rotary to linear motion. The ball screw is ideal for accurate position control of the XYZ axes but is highly inefficient at converting large amounts of power and huge forces from rotary to linear motion. These forces have to be conveyed across the small surface areas of the balls in the ball screw, creating a lubrication challenge. The lubrication system of the ball screw has to be separately cooled.

- **Friction** between the plungers and the guide bushings and dynamic seals create a small amount of heat in all pumps.
- **Check Valves** create heat when they leak and this is taken away by the cutting water that can also be used to cool the plungers and the dynamic seals.

Useful power/wasted power: This is the ratio of the two powers referred to above – the good vs. the bad. The lower the ratio, the worse the pump. The ratio for an intensifier can be one third that of an efficient direct drive pump.

Check valve design: A good seal requires high, even contact stress in the sealing zone. A ball on a cone does precisely this along a circle. A flat poppet on a flat seat is not the ideal way to seal a high pressure system. The probability of random debris getting between two flat surfaces is vastly higher than the probability of debris getting precisely on the ball-seat circle of contact. Second, if debris gets in between the flat surfaces it has no chance of escaping, whereas it gets pushed to one side or the other by the spherical surface of the ball and not cause damage. Third, the metal surfaces of the flat poppet and seat get eroded easily by high pressure water sneaking past on almost every stroke as the two surfaces cannot close in a manner precisely parallel to each other. These flat surfaces need frequent lapping, leading to more maintenance.

Constant and variable speed control: The bore of an orifice may vary by 2.5%. At a certain pressure, the difference in flow rate between these extreme sizes will be 5%. If a pump is set up to run at constant speed, producing a constant flow rate, the pressure drop across this range of orifice sizes will vary by 10%. In order to operate at a set pressure, a constant speed pump will have to be run at a higher speed to accommodate the larger size orifice and most of the time it will be dumping the extra water. Also, as the seals wear and the check valves erode, the output flow will drop and the pump will have to compensate for this and run constantly at an even higher speed. Constant speed pumps therefore run at about 10–13% higher speed than variable speed pumps and all this extra output is wasted. The variable frequency drive (VFD) adjusts the speed for the required pressure and avoids wastage.

When piercing holes, it is advantageous to drop the pressure to a piercing pressure. Doing this is easy with the VFD. An important application for waterjets is cutting composites and brittle piercing. Drilling starter holes in composites and in brittle materials requires the pump to shut off and start with the nozzle open. Direct Drive Pumps with a VFD can do this easily.

4.2. Micro AWJ technology

Under the support of an NSF SBIR Phase II grant, OMAX developed and commercialized μAWJ technology, culminating the MicroMAX JetMachining Center for precision meso-micro machining.[3] The MicroMAX was subsequently upgraded by incorporating the TAJ for taper compensation and the Rotary Axis for machining features on rotating workpieces. The MicroMAX was named a Finalist of the 2016 R&D 100 Award. The technological innovation and success in commercialization of the MicroMAX has led to OMAX's reception of the U.S. Small Business Administration (SBA) 2016 Tibbetts Award. NSF subsequently selected OMAX as a success story for its SBIR/STTR program (https://www.sbir.gov/node/1308555).

The MicroMAX takes advantage of most of the merits of waterjet technology. Success in making the MicroMAX available commercially has greatly broadened the waterjet machining applications. The meso-micro machining capability has led to penetrating several industrial sectors in which conventional waterjets are inadequate for R&D, prototyping, and production applications. These sectors include but are not limited to aerospace, biomedical, electronic/optic, engineering, and military applications.

For precision AWJ machining, consistent abrasive flow rate is essential. Garnet is mostly used for AWJ machining because of its low cost and superior performance as the abrasive. A rule of thumb to prevent nozzle clogging with abrasives is to use abrasives with mean particle size no larger than 1/3 of the bore diameter of the mixing tube. This is to avoid bridging of two large particles inside the bore. With the downsizing of AWJ nozzles, the particle size of the abrasive is proportionally reduced accordingly. It is well known that the finer the particle, the more difficult for it to flow under gravity feed. One of the common problems of feeding fine abrasive from a hopper is the formation of rat holes, resulting in unsteady mass flow [6]. As the rat holes are formed, flushing or flooding of fine abrasives would result when a positive pressure gradient builds up locally near the nozzle. Packing of fine abrasives also leads to positive pressure buildup. Under certain circumstances, a negative pressure gradient could build up just upstream of the nozzle. The presence of negative pressure gradient would reduce the flow rate of fine abrasives through the nozzle. In other words, fine abrasives flowing through the hopper would experience unsteady flow rate under the influence of buildups of positive and/or negative pressure gradients inside the hopper. The abrasive ceases to flow when the rate holes are fully developed. For the 5/10 nozzle, the finest abrasives can be used to assure consistent feeding is 240 mesh with a mean particle size of 60 μm. Since the surface roughness of AWJ-machined edges is proportional to the particle size, finer garnet such as 320 mesh with a mean particle size of 30 μm is often used to reduce surface roughness. Novel processes were developed to improve the flowabiliy of fine abrasive 320 mesh and finer (US Patent 8920213 B2). **Figure 4a** and **b** shows three photographs of the flow patterns of unprocessed and processed garnet, respectively. When examining flow patterns of 320-mesh garnet exiting the feed gate of the hopper, the unsteadiness and inconsistency of the flow patterns of the unprocessed garnet is evident. Cutting with unprocessed fine garnet would lead to wavy kerf width and even skipped cutting [7].

Figure 5 shows a display board highlighting μAWJ machined 2D and 3D parts cut from various materials such as metals (aluminum, steel, and titanium), nonmetal (glass, ceramics, carbon

[3]There are five US patents and one PCT patent application pending for μAWJ technology

Figure 4. Flow patterns of unprocessed and processed 320-mesh garnet [7] (a) Unprocessed (b) Processed.

Figure 5. Photographs of μAWJ-machined parts—An overview.

fiber, acrylic, polycarbonate, Garolite (G10), Poly-Ether-Ether-Ketone (PEEK), and honeycomb. Also, a simulated nanomaterial with large gradients of nonlinear material properties has been cut with AWJ [7]. These displays clearly demonstrate the merits of abrasive waterjet technology for material independence, no tooling requirements, and one single tool for multimode machining. There is simply no other machine tool capable of machining such a wide range of materials.

As a cold cutting tool that is materials independent, the μAWJ was demonstrated to machine large-aspect-ratio slots on a 2.2 mm thick 440C stainless steel sheet that was heat treated to a Rockwell index of R_c = 58. The part is a bonding extender for lapping thin-film ceramic substrates. This μAWJ machined part was cut on the MicroMAX using the 5/10 nozzle with 240-mesh garnet. **Figure 6** illustrates the μAWJ machined part; **Figure 6a** and **b** correspond to the photographs of the entry and exit surface of the part. Pockets and patterns were precut on the blank before waterjet machining. The slots consisted of widths as narrow as 0.3 mm and lengths as long as 260 mm. In the absence of the HAZ, it took a single pass of the waterjet to machine the part in 23 minutes.

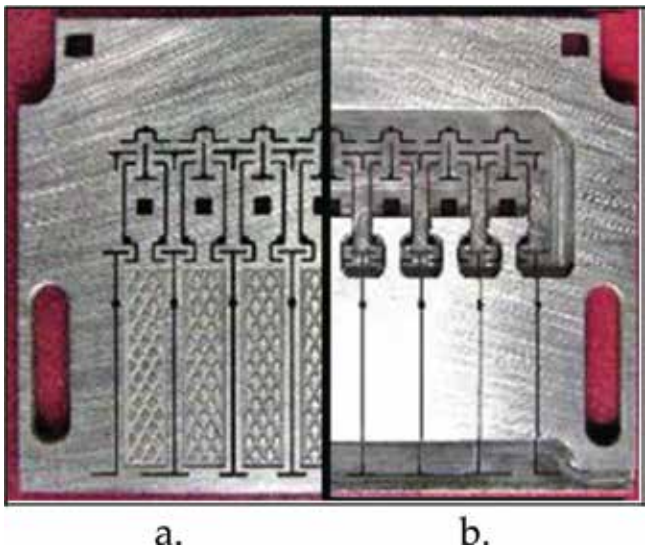

Figure 6. μAWJ-machined complex slot patterns on hardened steel (Courtesy of Competitive Engineering) [2] (a) Entry side (b) Exit side.

For such narrow slots with large aspect ratios machined on highly hardened steel, it is extremely difficult if not impossible to cut using CNC hard tools as they often do not have the stiffness and tend to wear too rapidly to achieve the required tolerance. The current method to machine the part is by wire EDM. The EDM process requires three passes to cut each slot in order to minimize the HAZ. As a result, it took over 6 hours to cut the part. In other words, the cutting speed of the waterjet is better than 15 times faster than the wire EDM for comparable cutting quality.

With the TAJ activated, nearly taperless or square edges can be readily machined with waterjets. Several precision devices critically rely on square edges to achieve their optimum performance. Mechanical flexures are often used for accurate force measurements, precision motion control, and mitigation of backlash. In collaborating with MIT Mechanical Engineering, OMAX used the MicroMAX to machine prototypes of nonlinear load cells with large-aspect-ratio of thin flexures [8]. The patented design was capable of five orders of force range and its superior performance was verified through laboratory experiments [9, 10]. The close agreement between the theory and the experimental results was attributed to the nearly taperless edges of the large-aspect-ratio flexures.

As a part of Asteroid Redirection Mission (ARM) program, the Jet Propulsion Laboratory (JPL) of NASA has been developing prototypes of flexure-based microsplines to serve as the asteroid gripping device. The flexures consisting of several spring-like elements were originally machined with the wire EDM that must be cut with multiple passes at low speeds to minimize the heat damage in the presence of the HAZ such as surface hardening on the cut edges and distortion of the spring-like flexure elements. In collaborating with JPL, OMAX conducted a series of tests to machine several 3.2-mm-thick aluminum flexures. The single-pass cutting tests were conducted on the MicroMAX with the 7/15 nozzle together with 240-mesh

garnet. **Figure 7** illustrates several flexure elements that were supported only at two ends. With the TAJ activated, the cold cutting with extremely low side force exertion is essential for cutting such flexure elements with nearly taperless edges and very little distortion. The performance of the MicroMAX also met NASA's precision requirements. Based on the times required to machine these parts, the cost ratio of the waterjet and wire EDM was 1:14, leading to a cost saving of 93%. JPL has adopted the MicroMAX as one of the primary tool to continue the development and refinement of microsplines for the asteroid gripping device.

The Rotary Axis facilitates machining of features on rotating workpieces. Initially the LAYOUT drawing is the same as that of the 2D part. The features along the Y-axis are then converted to those in the rotary axis via the X-data, an algorithm that lets one input "extra" data for any entity in a drawing. After the tool path of the drawing is created, MAKE cuts the part by controlling the motion of the Rotary Axis to machine 3D features on the part. **Figure 8a** illustrates an interlocking link structure in a tube machined with AWJ. Machining the interlocking feature would be challenging for other machine tools. **Figure 8b** illustrates a titanium mesh cage, an implant used in spinal surgery to replace and reinforce the anterior column. A sacrificial rod was inserted into the tube while machining to protect the opposite wall from damaged by the spent AWJ. a titanium mesh cage, an implant used in spinal surgery to replace and reinforce the anterior column. A sacrificial rod was inserted into the tube while machining to protect the opposite wall from damaged by the spent AWJ.

4.3. Versatility of AWJ technology

With four product lines of waterjet systems equipped with accessories for 2D/3D machining and nozzles for wide range of part size and thickness, OMAX has established the full capability for multimode machining of most materials from macro to micro scales – the "7 M" advantage [3]. Several publications have been devoted to demonstrating the versatility of waterjet in terms of material independence and precision meso-micro machining capability [2–5, 7–10]. Inside the Engineering and the Demonstration Laboratories, cutting tests continue taking place to look for new applications on new materials. A part of the tests was conducted

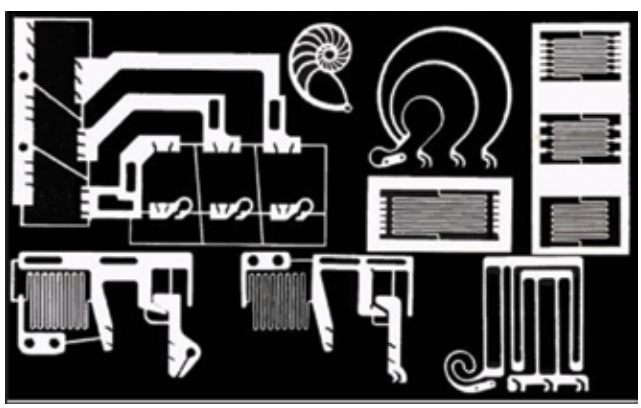

Figure 7. μAWJ-machined aluminum flexures with flimsy spring-like elements (courtesy of NASA/JPL).

Figure 8. Two cylindrical parts machined with the rotary axis.

by the in-house R&D and Engineering Group. Many of them were requested from prospective clients before committing to purchase one or more of the machines. In this subsection, several applications to demonstrate the versatility of waterjet technology are described, in particular, those applications that are unique to waterjet technology.

4.3.1. 3D machining

The spent AWJ still consists considerable erosion power, if "not tamed," could cause damage either to the operator or workpiece around the cutting nozzle. In other words, AWJs are not inherently suitable for 3D machining, particularly for parts with complex 3D features. Because the simplest and most effective means to dissipate the residual energy of spent abrasives is to let the spent AWJ shoot into a column of still water, most AWJ systems are built on top of a water tank that also serves to support the traversing mechanism. Such AWJ systems are generally designed for 2D machining. Novel methods and accessories were developed, within the constraints of operational safety, to machine 3D parts using 2D AWJ systems [11].

One of the simple methods to machine a 3D part on a 2D platform is to machine it multiple times in different orientations. As an example, **Figure 9** illustrates a model fighter plane machined on an aluminum rectangular block in three orientations.

Another example was to build a 3D assembly using many 2D components. **Figure 10** illustrates a model Boeing 777 aircraft (right half) that was assembled from AWJ-machined wing and nacelle cross sections, stabilizer, and rudders made from thin sheets of carbon fiber. Selected wing cross sections are shown in the upper left corner.

The Intelli-MAX Software Suite has incorporated several programs for machining parametric shapes, or pre-configured shapes that use equations to machine a shape without having to create the tool path first. One such program is the internal and external Gear, Rack and Sprocket Generator in both U.S. and metric standards. Using the 5/10 nozzle on the MicroMAX, several sets of miniature planetary gears made from titanium, PEEK (with and without fiber reinforce-

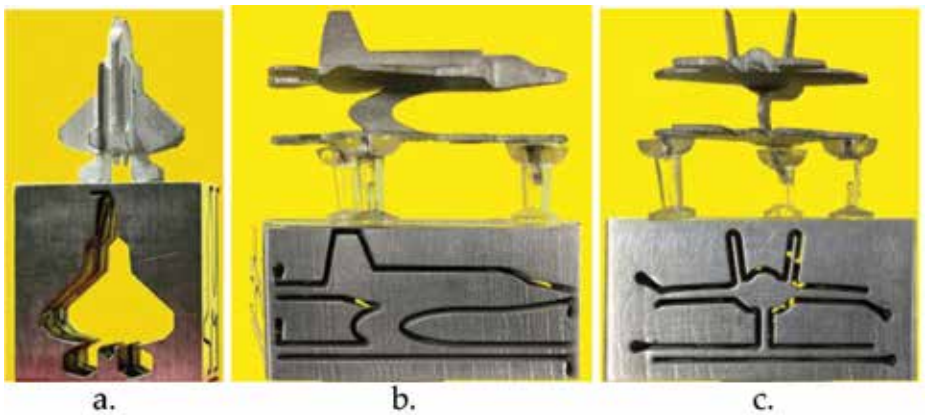

Figure 9. AWJ-cut 3D fighter aircraft—completed in three separate 2D cuts (a) Top view (b) Side view and (c) End view.

Figure 10. A Boeing 777 aircraft model assembled from AWJ-cut components made from carbon fiber [3].

ment) were machined and assembled into operating models [3]. One of the common gears is the cycloidal gear that is designed for watch making. **Figure 11** illustrates a set of miniature cycloidal gears cut with the 5/10 nozzle on the MicroMAX. The gears were made from titanium sheet 2.0 mm thick. They were assembled into two decks of gears driven by a micro motor (a 298:1 71 rpm micro spur gear head motor manufactured by Solarobotics, Model GM14a). The lower deck consists of a large gear (19.3 mm OD) and two small gears (5.4 mm OD). The upper deck consists of a large gear (12.7 mm OD) and three small gears (3.61 mm OD). The two decks of gears were separated by an acrylic plate. The two large gears were mounted on a common shaft that is driven by the micro motor powered by a 3 V button battery (Panasonic CR2477). The assembled AWJ as-cut gears run quite smoothly, demonstrating the adequacy of the precision of the MicroMAX. Our goal is to machine the components of a pocket watch and assemble the watch as a means to demonstrate the capability of the MicroMAX for precision micromachining.

As the first step to reach the above goal, we acquired online the DXF of a wood clock "Genesis" by Clayton Boyle [12]. The clock was designed for hobbyists with the components cut manually with a scroll saw or a router. High-quality plywood was recommended for making the main components such as the gears. This is an ideal case to demonstrate the gear and clock making capability of waterjet in terms of fast turnaround and precision. The DXF files of the Genesis components were imported to LAYOUT and compiled in **MAKE**.

Figure 11. Cycloidal gear set (a) Top view (b) Side view.

All the components of the Genesis clock were then cut on a MAXIEM waterjet system in the OMAX Demo Lab in just hours as opposed to days using the scroll saw. **Figure 12** illustrates the assembled wood clock. The faces of the hour (lower left), minute (middle), and second (right) gears were cut from a thin stainless steel sheet. The clock is controlled by the adjustable length of the pendulum. The clock is driven by a 3.2 kg stainless steel bar that turns a click wheel attached to the back of the minute gear via a fish line. A small aluminum bar serves as the counter balance to straighten the fish line as the clock runs. Refer to Reference 12 for a detailed description of the clock.

For large bevels and countersinks, the A-Jet with a range of tilt angles from 0 to 60° to the vertical can be used. **Figure 13** illustrates a pair of beveled titanium honeycomb parts with 65 and 45° edge bevel angles, respectively; both the facesheet and the core were made of titanium. Note that cutting titanium honeycomb presents a considerable challenge to most machine tools. CNC hard tools tend to deform the thin core material whereas lasers and EDM must cut slowly to minimize the HAZ.

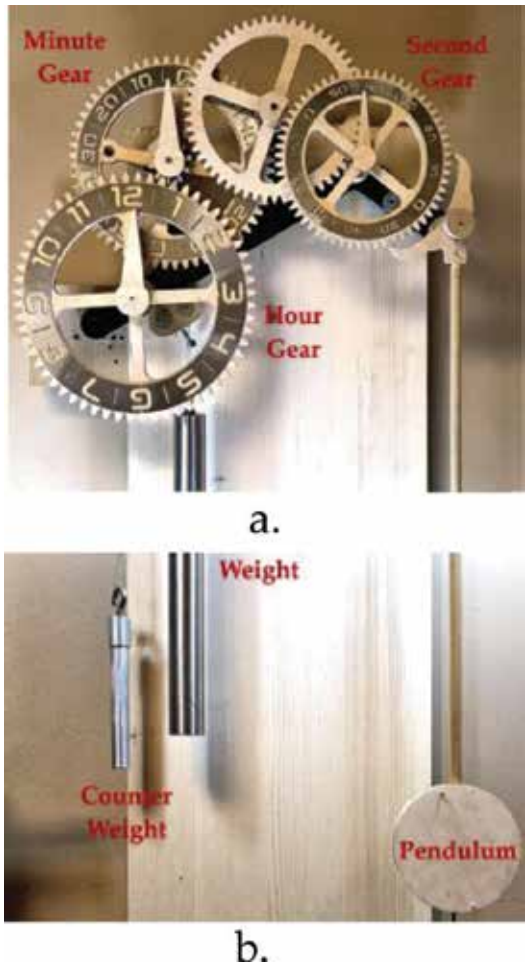

Figure 12. "Genesis" wood clock [12] (a) Top half (b) Lower half.

By combining the operations of the Rotary Axis and the A-Jet, complex 3D parts can be readily machined. One of the useful applications is to machine "fish mouth" weld joints for metal pipes, large and small, as illustrated in **Figure 14**. The joints are often cut with plasma cutting machines that leave a large HAZ on the cut edges. Removal of the HAZ often is done manually, leading to high labor costs and slow turnaround. The Intelli-MAX Software Suite has built-in programs to prepare tool paths for weld joints that can be cut with one of the JMCs. The as-cut joints are weld ready without the need of any secondary processing.

Another application is to machine inclined holes such as those used in aircraft engines [3]. For modern aircraft engines operating at very high temperature, there is a need for drilling inclined and shaped air breathing holes to achieve maximum cooling. The current practice requires a two-step process to drill inclined and shaped holes on TBC coated metal. First, the nonconductive TBC is removed with a laser and the hole in the substrate is drilled with an

Figure 13. Beveled titanium honeycomb parts (a) Top view (b) Side view.

EDM process. The EDM process is very slow in order to minimize the HAZ damage. The AWJ was applied successfully to drill such holes on refractory metals with and without thermal barrier coating, as illustrated in **Figure 15**. In the absence of the HAZ, the AWJ drills holes much faster than CNC tools. By mounting the workpiece on the Rotary Axis, any inclined angle of holes can be drilled. The geometries of the holes were drilled by controlling the tilting of the A-Jet. Within certain limitations, the inclined angle and the shape can vary simultaneously along the hole axis. The AWJ nozzle consisted of a 0.18-mm ID diamond orifice and a 0.38-mm ID mixing tube. Garnet of 220 mesh with a flow rate of 45 gr/min was used. Seven hole geometries were drilled with a single nozzle on these samples to demonstrate the versatility of the AWJ in hole drilling. Most important, there was no delamination between the coatings and substrates and no HAZ on the hole edges on the substrates.

Figure 14. AWJ-cut "Fish mouth" weld joints.

4.3.2. Milling of glass mirrors

One of the more interesting applications for abrasive waterjets is controlled depth milling. Instead of cutting through the workpiece, the abrasive waterjet is traversed at a high speed across the part's surface. This causes the jet's kerf to change from a through cutting cross section to a grooving and then to an etching cross section. As the relative traverse rates increase between the nozzle and workpiece's surface, the penetration depth decreases. Precise depth control is achieved through a multi-pass process when, like with traditional milling operations, the final depth is achieved by walking the milled surface down to the final target depth. This is achieved by choosing a process where the amount of material removed per milling pass is less than the target depth tolerance. Depth control on the order of 0.03 mm can be achieved with the correct combination of process parameters.

When milling glass materials, the goal is to diffuse or reduce the power being applied to the surface of the part from a glass fracturing risk perspective. It is well known that cutting glass without abrasive results in fracturing the glass. Milling is no different, except that the fracturing tends to have more of a spalling damage. The key is choosing a set of process parameters where if the abrasive feed was interrupted, then glass will not break. This is achieved by using higher standoff distances on the order of 150–300 mm, orifice diameters less than 0.2 mm, mixing tube diameter to orifice diameter ratio's on the order of 10:1, and mixing tube lengths 100–300 mm, with jet pressures in the 70–200 MPa. The abrasive mass flow rate to waterjet mass flow rate ratio ranges from 25–100%. One of the keys is the traverse rates from 0.02 m/s to over 8 m/s. The higher the traverse rate, the more precise the depth control. The higher traverse rates are easier to achieve by spinning the work piece on a turntable.

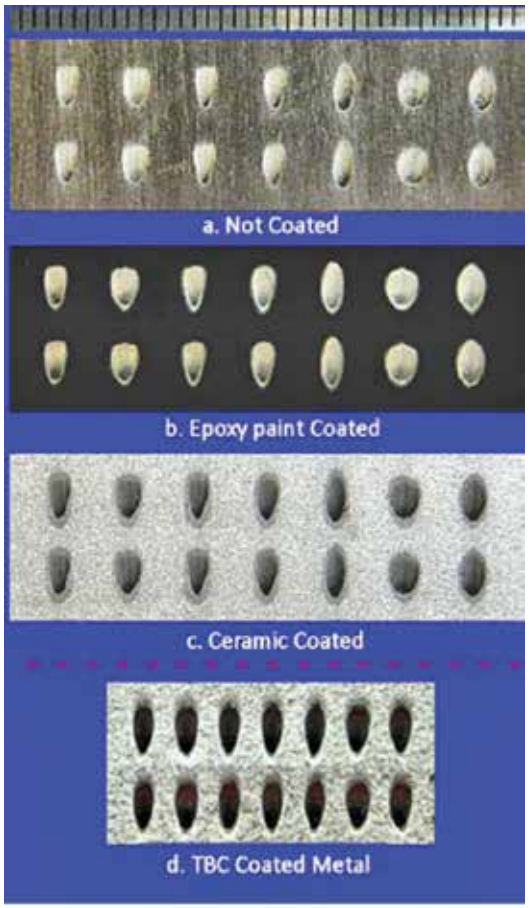

Figure 15. Inclined shaped holes on refractory metals.

One of the applications that the abrasive waterjet milling process has been successfully applied to is reducing weight in glass materials for ultralight-weight mirrors [13]. Samples include a 250 mm (major axis) elliptical mirror with pockets milled to a depth of 9.5 mm (**Figure 16**) and a 305 mm wide mirror made from 5.3 mm thick Ultra Low Expansion (ULE) glass with pockets milled to a depth of 3.6 mm (**Figure 17**). This mirror design was for testing of the active bending concept to change its focal point for phasing together multiple mirrors together for the James Webb telescope program.

These mirrors were milled with a milling process where the relative traverse rates were about 8 m/s. At these speeds, slowing the jet down to change directions without causing the jet to mill deeper as the jet speed decreased is mechanically impossible to accomplish. To solve this problem a mask with the lightweighting Isogrid pattern was placed on top of the glass, and the abrasive waterjet milling process is rastered across the entire surface of the mask. The mask was made from steel, and the relative erosion rate between the glass and steel is about 40 to 1. This allows for the mask to be reused on multiple parts before needing to be replaced.

Figure 18 shows an artistic milled pocket pattern that can be easily replicated dozens of times using the same milling mask.

Figure 19 illustrates how the jet rasters across the mask's surface. The glass is milled where all of the openings in the masks are located. Very intricate patterns can be milled into the glass surface. As a side note, one of the other advantages the abrasive waterjet machine has, is that the very same tool used to mill the glass can be used to cut the mask pattern. After each pass of the abrasive waterjet, the centerline of the jet is laterally indexed, as shown in **Figure 20**. When the index distance is approximately 70% of the mixing tube diameter, the milled surface produced is smooth and flat.

Figure 16. 250 mm (major axis) elliptical mirror with pockets milled to 9.5 mm deep.

Figure 17. 305 mm wide mirror made from 5.3 mm thick ultra-low expansion glass with pockets milled to 3.6 mm deep.

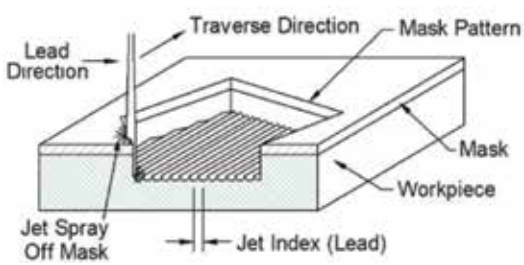

Figure 18. Masking the pattern.

4.3.3. Machining glass artworks

Glass that is often used as a comparison material for industrial comparative testing is a great material to demonstrate the versatility of AWJ. Known as a strong and brittle material, glass has a variety of applications across industries, including the creative sector. Exploration to generate artworks that investigate the waterjet process in the medium of glass was conducted. Working in a variety of scales the process remains the same with slight considerations regarding the delicacy, intricacy and complexity of the design [14]. **Figure 21** illustrates two artwork examples by assembling multiple layers of AWJ-machined pieces.

The design process can start in a variety of different ways, such as importing a vector file from any software capable of saving a drawing as a vector file (e.g., Rhino, AutoCAD, Illustrator and SolidWorks). The process of cutting is a two dimensional process and therefore requires a single outline. The initial programming is undertaken in various softwares and nested into the machine's software before cutting. The files are made and saved as a vector such as a DWG or DXF file. In work such as the "Scrutiny" handwriting was photographed and saved as a

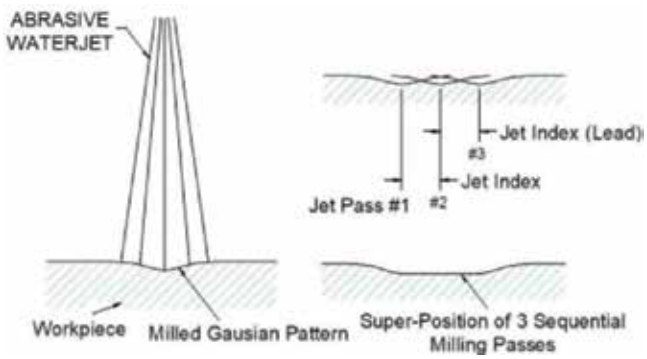

Figure 19. Superimposing successive milling passes to generate flat surfaces.

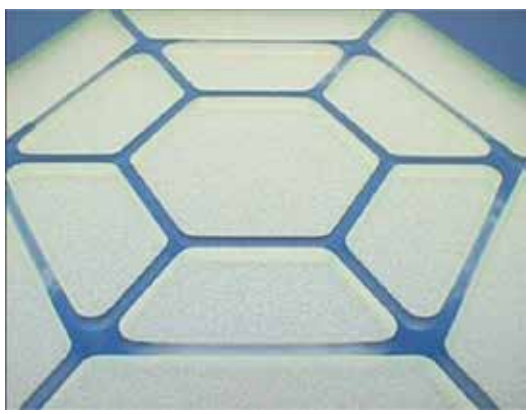

Figure 20. Artistic masked milling.

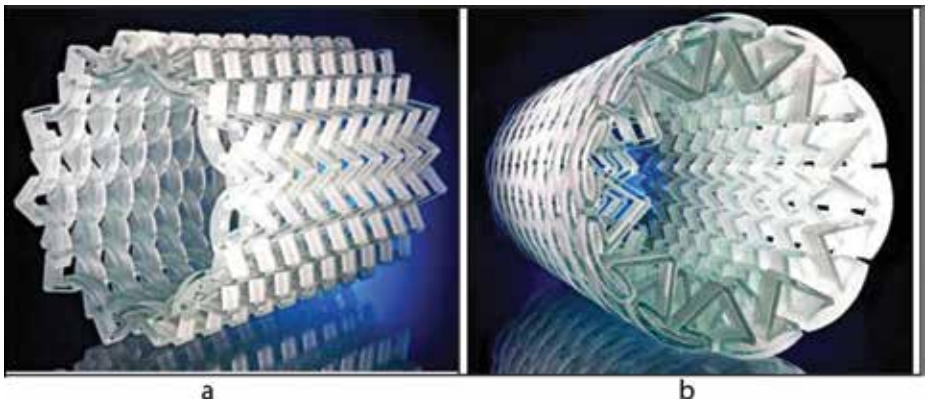

Figure 21. AWJ-machined artwork examples (a) Multi-layers of AWJ-cut glass (b) "Intertwine" glass sculpture.

JPEG and imported into the OMAX Intelli-TRACE software, where the writing was adapted within the software to fit within a given surface area [15].

The process is able to capture detail and work to tight tolerances and variable angles to effectively capture the handwriting. The AWJ can cut through stacks, working with glass thicknesses from 1 mm to over 65 mm using a variety of soda-lime, clear float glass and various artist glass stacks such as Bulleye.[4]

A variation in speed of abrasive flow, standoff distance, and how the machine is set up along with the order and direction of cutting can have effect on obtaining a successful outcome. Optimum pump pressures depending on the work undertaken varies between 11,000 and 58,000 psi. Higher pressure pumps have been used but with the application of multiple pierce points and variation of pressure from high to low, a lower pressure pump has proved more suitable due having to ramp from low to high pressure multiple times. Maintaining a consistency of pressure and abrasive is crucial in cutting glass. In cutting the handwriting, rhino board was used for the more delicate forms with water not covering the head in case a splash fractured the glass. Other handwriting at 2 mm thickness and not as complex, the work was cut underwater. **Figure 22a–c** illustrates the processes for machining handwriting on glass.[5]

For 5-axis cutting, the consideration with glass is how the material is held in place, as well as the order and priority of cutting. Most work is cut sitting on a surface tilled to reduce the residual wastes falling away. Another consideration is "taper lock," which can trap the form within the waste material. There is a lot more risk with a brittle material such as glass; residual stress within the material can causing internal fracturing especially in thicker glass material. Cutting a form in glass can have different programming to that of a metal form and its set up is crucial to a successful outcome.

[4]A brand of fusing glass that allows various colored glass to be used together that have the same coefficient that make the glass compatible with each other.
[5]Photography credit: Simon Bruntnell

Figure 22. Processes for AWJ-machining of handwriting on glass [15] (a) Initial drawing sketch (b) Tool paths and (c) Micro glass handwriting.

4.3.4. Piercing of composites

Composites, laminates, and brittle materials have long been difficult materials to process by conventional machine tools such as mills and lathes as well as abrasive water jets and other beam cutting technologies. Most of the issues involved in shaping involve either peculiarities with the materials' heat sensitivity, brittleness, low tensile strength or its abrasive nature. Rapid wearing of alloy drills has been one of the main concerns that degraded the precision and repeatability of machined features. Early tests revealed similar damage took place during the initial hole piercing process with AWJ. Considerable efforts were subsequently made in an attempt to understand and mitigate such damage [3, 16–17]. It was discovered that damage occurred whenever the buildup of stagnating pressure inside blind holes exceeds the tensile/adhesive strength of composites/ laminates' binder. Based on the above understanding, novel processes to minimize the stagnating pressure were developed for piercing composites/ laminates without inducing damage. The Turbo (patented) and Mini Piercers were developed for AWJ drilling of large and small holes, respectively. **Figure 23** illustrates AWJ-machined internal features that require piercing on composite (G10), laminate (aluminum), brittle materials (glass and silicon wafer) with no damage.

Another advantage of using AWJ to machine composites is that the nozzle, unlike drill bits, does not come in direct contact with the workpiece. In other words, the nozzle wear is independent of the property of composite workpiece. For certain composites that are highly abrasive, excessive and rapid wear was experienced by the drill bits. Such rapid wearing of the drill bits and cutting tools tends to degrade the precision and repeatability of the machined features [18]. On the other hand, the AWJ nozzle wears considerably slower than the drill bits do. For extremely precise parts, AWJ can be readily used as a near-net shaping tool. The part can then be finished by light trimming with a precision hard tool. As such, the tool life can be greatly extended.

4.3.5. Patient-specific orthopedics and prosthetics

At present, most orthopedic and prosthetic implants are mass produced with limited sizes to achieve an average fit for individual patients. Since the implants are not tailored to the specific patient, it is not possible to optimize the implant operation for an optimum match. Recently,

http://dx.doi.org/10.5772/intechopen.75313

there has been strong advocacy for manufacturing patient specific implants for optimum fitting, with a slogan of "one patent, one implant." Waterjet technology with its technological and manufacturing merits is most suitable for manufacturing such implants cost effectively with fast turnaround.

Waterjets are expected to lower the manufacturing cost of implants because of its no tooling requirement. As a cold cutting tool, all parts can be machined including secondary processes,

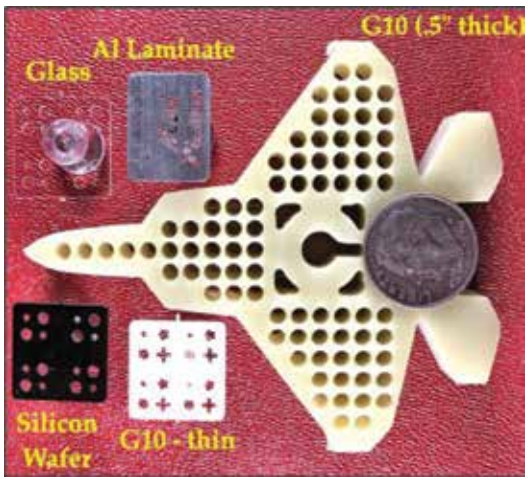

Figure 23. Piercing with Turbo and mini piercers.

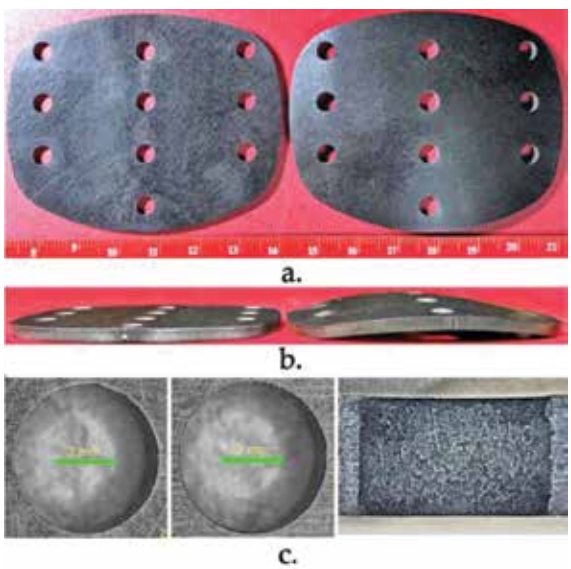

Figure 24. AWJ-machined cranial implants made from PEEK with fiber reinforcement (a) Top view (b) Side view and (c) Top, bottom, and side view.

if needed, in a matter of minutes or hours, depending on the complexity of the parts. Such fast turnaround is a must for in-situ implant operations. Furthermore, a mobile waterjet system has been applied successfully in remote areas such as the battlefield for rapid response repair [19]. The ruggedness of the system would facilitate setting up waterjet systems in remote areas for machining implants to broaden the reach of quality healthcare to underprivileged populations.

The applications of AWJ machining of biomedical components made of biocompatible metals such as titanium and stainless steel have been given elsewhere [11, 20]. An example of an AWJ-machined titanium mesh cage is illustrated in **Figure 8**. A relatively new biocompatible material, Polyether-Ether-Ketone (PEEK), has been shown to be a superior replacement of titanium implants in terms of avoidance of allergic tissue reaction to metallic ion and transparency to X-rays [21]. Success in applying waterjet for machining PEEK implants would greatly reduce the manufacturing costs together with fast turnaround. **Figure 24** illustrates AWJ-machined internal features that require piercing on the PEEK material with carbon fiber reinforcement. On the right of **Figure 24a** and **b**, the curved implant was thermally shaped at 316°C. **Figure 24c** shows the micrographs of the top, bottom and side views of one of the holes. Note that the hole edges were cut cleanly with no fiber hanging out loosely.

5. Conclusion

With the commercialization of micro abrasive waterjet or μAWJ technology, the full capability has established for precision multimode machining of most materials from macro to micro scales for a wide range of part size and thickness. This "7 M" advantage of waterjet technology, together with cost effectiveness and fast turnaround, has greatly broadened manufacturing applications from R&D, prototyping, to 24–7 production of both small and large lots. The technological and manufacturing merits of waterjet technology have elevated it as one of most versatile machine tools unmatched by others. Specifically, the material independence and low side force exertion on workpieces are two most outstanding technological merits. A collection of AWJ-machined samples, made from a wide range of materials from metal, nonmetal, and anything in between, were presented to demonstrate the versatility of waterjet technology for a broad range of applications. In particular, machining many such examples presents considerable challenge to other machine tools in terms of material property, part geometry, tool performance, equipment/production costs, and machining/turnaround time.

It is concluded that recent advancement has elevated waterjet as a mainstream machine tool, often competing with lasers, EDM, and others on equal footings. For certain applications, waterjet out performs its competitors. For cutting heat sensitive materials with low tolerance in heat damage, waterjet is at least 10 times faster than lasers and EDM.

Acknowledgements

This work was supported by an OMAX IR&D fund and NSF SBIR Phase I and II Grants #1058278. Any opinions, findings, and conclusions or recommendations expressed in this

material are those of the authors and do not necessarily reflect the NSF's views. The authors wish to thank the technicians in the Demonstration Laboratory for assistance in machining some of the parts illustrated in this article.

Author details

H.-T. (Peter) Liu[1]*, Vanessa Cutler[2], Chidambaram Raghavan[1], Peter Miles[1], Ernst Schubert[1] and Nathan Webers [1]

*Address all correspondence to: peter.liu@omax.com

1 OMAX Corporation, Kent, Washington, United States

2 Independent Waterjet Specialist and Glass Artist, Hampshire, United Kingdom

References

[1] Liu H-T, Schubert E. Micro abrasive-waterjet technology. In: Kahrizi M, editor. Micromachining Techniques for Fabrication of Micro and Nano Structures. INTECH Open Access Publisher; 2012. pp. 205-234. DOI: 10.5772/1364

[2] Liu PH-T. Mint: Precision machining of advanced materials with abrasive waterjets. IOP Conf. Series: Materials Science and Engineering, 164, 2017. 012008 DOI:10.1088/1757-899X/164/1/012008 (5th Global Conference on materials Science and Engineering, 8-11 November 2016, Tunghai University, Taiwan)

[3] Liu H-T. "7M" advantage of abrasive waterjet for machining advanced materials. Mint: Journal of Manufacturing and Materials Processing. 2017; **1**(11): 1-19 MDPI, Basel, Switzerland. DOI: 10.3390/jmmp1010011. http://www.mdpi.com/2504-4494/1/1/11/pdf

[4] (Peter) Liu H-T. (2015) Abrasive-waterjet machining of most materials from macro to micro scales, In: Proceedings 2015 TechConnect World Innovation Conference and Expo; 14-17 June 2015; Washington DC. pp. 39-42

[5] Liu H-T. Versatility of micro abrasive waterjet technology for machining nanomaterials. Dekker Encyclopedia of Nanoscience and Nanotechnology, 3rd ed. 2017. pp. 1-18. DOI: 10.1081/E-ENN3-120054064

[6] Watanoa S, Imada Y, Hamadab K, Wakamatsub Y, Tanabeb Y, Davec RN, Pfefferc R. Mint: Microgranulation of fine powders by a novel rotating fluidized bed granulator. Mint: Powder Technology. 2003;**131**:250-255

[7] Liu PH-T. Roles of abrasives in AWJ meso-micro machining. In: Proceedings of 22nd International Conference on Water Jetting; 3–5 September 2014; the Netherland. pp. 151-165

[8] Liu PH-T. Roles of taper compensation in AWJ precision machining. In: Proceedings of the. 23rd International Conference on Water Jetting; 16-18 November 2016. Washington: Seattle. pp. 33-46

[9] Kluger JM, Slocum AH, Sapsis TP. Beam-based Nonlinear US Patent No. 9599180 B2; 2016

[10] Kluger JM, Sapsis TP, Slocum AH. High-resolution and large force-range load cell by means of nonlinear cantilever beams. Precision Engineering, 43, 2016. 241-256 (http://dx.doi.org/10.1016/j.precisioneng.2015.08.003)

[11] Liu H-T, Olsen JH. Application of AWJ for 3D machining. In: Proceedings of the 2013 WJTA-ICMA Conference and Expo; 9-11 September 2013; Houston, Texas

[12] Boyle C. Genesis [Internet] 2018. Available from: http://lisaboyer.com/Claytonsite/Genesispage1.htm [Accessed: January 07, 2018]

[13] Miles P. Lightweighting large optics with abrasive Waterjets. In: Proceedings of SPIE, Novel Optical Systems and Large Aperture Imaging, 3430; 1998

[14] Cutler V. New Technologies in Glass. London: Bloomsbury; 2012. 128 p. ISBN 978-1-4081395-4-7

[15] Webers N, Cutler V. Interpreting handwritten scrawl. In: Proceedings of 23rd International Conference on Water Jetting; 16-18 November 2016; Seattle, Washington. pp. 99-109

[16] Liu H-T, Schubert E. Piercing in delicate materials with abrasive-waterjets. Mint: The International Journal of Advanced Manufacturing Technology. 2009;**42**(3-4):263-279. DOI: 10.1007/s00170-008-1583-5

[17] Liu H-T, Schubert E, McNiel D, Soo, K. Applications of abrasive-waterjets for precision machining of composites. In: Proceedings of SAMPE 2010 Conference and Exhibition, 17-20 May 2010; Seattle, Washington; 2010

[18] Khashaba UA. Drilling of polymer matrix composites: A review. Mint: Journal of Composite Materials. 2013;**47**(15):1817-1832. DOI: 10.1177/0021998312451609

[19] Anderson M, editor. Watercutting in Wartime [Internet]. 2013. Available from: http://sme.org/MEMagazine/Article.aspx [Accessed: Decemeber 29, 2017]

[20] Liu H-T. Abrasive-waterjet technology for biomedical applications, In: Proceedings 21st Internal Conference on Water Jetting; 19-21 September 2012; Ottawa, Canada. pp. 99-112

[21] Kurt SM, Devine JN. PEEK biomaterials in trauma, orthopedic, and spinal implants. Mint: Biomaterials. 2007;**28**(32):4845-4869

Chapter 4

Grinding Force of Cylindrical and Creep-Feed Grinding Modeling

Pavel Kovač and Marin Gostimirović

Additional information is available at the end of the chapter

http://dx.doi.org/10.5772/intechopen.76968

Abstract

This chapter presents an experimental study of grinding forces as relationship of workpiece speed v, feed rate s_a and depth of cut a. For the modeling of cylindrical grinding used was response surface methodology and genetic algorithms. Modeled was the tangential force F_t and the normal force F_n in cylindrical grinding. The process included measurement of cutting forces during cylindrical grinding and later calculating their values using abovementioned techniques and determined adequate models. This chapter also examines the value and character of cutting forces in the creep-feed grinding. In order to identify the impact of cutting forces on the state of the process of creep-feed grinding, according to the elements of the machining experimental tests, relationship of the tangential and normal components of the grinding force and ratio of grinding force were determined. In comparison with the traditional multi-pass grinding results, the occurrence of higher cutting forces in creep-feed grinding, especially normal components, is shown.

Keywords: cutting force, cylindrical grinding, modeling, genetic algorithms, creep-feed grinding

1. Introduction

Knowledge about machinability of materials parameters, tool wear, quality of machined surface, cutting temperature, cutting forces, and so on, is beneficial not only for cutting process but also for designing the machine tools, fixtures, tools and process management. This was the goal of many researches especially in cutting, but there are only few data regarding grinding [1].

Research in grinding is performed with the purpose to define machining parameters, roughness of machined surface, grinding forces and grinding temperatures [2, 3]. Forces in surface grinding are measured with dynamometer Kistler, and they are increasing with increase of the material removal rate. Cutting forces measurements, during cylindrical grinding, are realized with dynamometer Kistler and are shown in [4].

Mathematical models of grinding force and grinding temperature for three wheels were established in [3]. Then, the role of chip formation force and friction force in grinding was investigated, and the thermal distribution in contact zone between workpiece and wheel was analyzed based on the mathematical model.

Grinding process is generally used to improve the tolerance integrity and surface integrity of a workpiece. It is crucial to know process forces since they are necessary to identify the conditions for surface burn. In [5], a new semi-analytical force model for grinding process was developed by modeling abrasive grits and their interaction with the workpiece material. Semi-analytical equations for normal and tangential force components as well as average force per grit are established by using the micro milling analogy. The model can then be used in prediction of the forces for different cases involving the same material and the abrasive grain however with different conditions.

In [6], a new grinding force model was developed by incorporating the effects of variable coefficient of friction and ploughing force. This is based on the fact that chip formation during grinding consists of three stages: ploughing, cutting and rubbing. Equations for the total normal and tangential force components per unit width of the grinding during these three stages were established. These components were expressed in terms of the experimental coefficients and process parameters like wheel speed, table feed and depth of cut. All the coefficients were determined experimentally by performing grinding tests at specified conditions according to the experimental trifactorial central composition plan.

Investigation of grinding force and grinding temperature of ultra-high-strength steel Aermet 100 in conventional surface grinding using a single alumina wheel, a white alumina wheel and a cubic boron nitride wheel was done in [7]. First, mathematical models of grinding force and grinding temperature for three wheels were determined. Then, the role of chip formation force and friction force in grinding force was investigated and thermal distribution in contact zone between workpiece and grinding wheel was analyzed based on the mathematical model. The experimental result indicated that the ratio of minimum grinding force to the maximum grinding force under the same grinding parameters can be achieved when using a CBN wheel and a single alumina wheel, respectively.

Proper understanding of the grinding forces can be useful in designing grinding machine tools and fixtures. Additionally, information on specific energy helps in selecting process parameters for achieving optimum output [8]. In this chapter, analysis of the effects of process parameters, tribology, work material and auxiliary equipment on grinding forces and specific energy, has been carried out. Existing models have been critically analyzed, and Werner's specific force model was found to be quite promising for advanced grinding processes. It was found that under specific boundary conditions and environment similar to advanced grinding processes, this model estimates grinding forces with acceptable accuracy [9].

Optimal control of workpiece thermal state in creep-feed grinding using inverse heat conduction analysis was done in [10] and surface layer properties of the workpiece material in high-performance grinding were analyzed in [11]. An inverse heat transfer problem for optimization of the thermal process in machining was done in [12].

For determination of dependence between cutting forces and machining parameters, firstly the full factorial experiment second-order design is used by [13]. With this approach, it is possible to determine the dependence of machining parameters and the results with minimal number of experiments.

This chapter analyzes the cutting forces in the creep-feed grinding and experimentally determined mean values of cutting force of abrasive grains that are currently in the grip with the workpiece as well. Cutting forces are determined depending on the treatment regime for two types of corresponding wheels.

As a second option for modeling, the dependence functions are genetic algorithms. They are extensively described in [14], and the same principle is implemented in this chapter.

1.1. Genetic algorithms

Genetic algorithms (GA) mimic the process of natural evolution by incorporating the "survival of the fittest" philosophy. In GA, a point in search space (binary or decimal numbers) is known as chromosome. A set of chromosomes is called population. A population is operated by three fundamental operations as follows:

1. reproduction (to replace the population with large number of good strings having high-fitness values)
2. crossover (for producing new chromosomes by combining the various pairs of chromosomes in the population).
3. mutation (for slight random modification of chromosomes).

At the very beginning, an initial population of 50 individuals is created. They are randomly generated from interval 0–1 using uniform distribution for creation of population. This indicates that real number coding was used. As a fitness scaling function, rank method was used. Most fit individual with the best raw score is assigned as first on the scaling list. Next to fittest is ranked number 2 and so on. This method is ranking every individual in generation as compared to the best individual in that same generation, no matter how good or bad fitness value is. And It was selected because it allowed the fastest convergence toward the best solution.

Selection of individuals for presence in mating pool was executed by roulette wheel method. Size of area on wheel occupied by a single individual is defined by rank score—the better the score, the bigger the area. Wheel is then spun and individual with the largest area has the most chances to be assigned a slot in mating pool. This action is repeated until all slots in mating pool are assigned. In each generation, two of the best individuals are automatically transferred to next generation. This act is called elitism and it guarantees that best genetic material is passed onto next generation. By setting this parameter high, the genetic diversity

is quickly reduced which leads to prolonged convergence time. On the other hand, setting it low, elite genetic material of every generation may be lost and algorithm stuck in local minimum. Number of individuals created by heuristic crossover is, in this case, 43. Heuristic crossover is carried out by creating children that randomly lie on the line containing the two parents, a small distance away from the parent with the better fitness value and in the direction away from the parent with the worse fitness value. After transferring two elite individuals from previous generation and creating 43 by crossover to complete a full population with 50 members last 5 individuals are created by mutating 5 of their predecessors.

With the process of mutation, a completely new genetic material is introduced into the population which helps in expanding genetic diversity and search space. It also prevents jamming an algorithm in a local minimum of the function. Uniform mutation is selected with the rate of 0.2. This type of mutation is basically a two-step process. In the first step, the algorithm selects a gene of an individual for mutation where each gene has the same probability as the mutation rate of being mutated. In the second step, the algorithm replaces each selected entry by a random number selected uniformly from the range for that entry. This whole process of selection, recombination and mutation lasted 500 generations.

2. Experimental investigation

2.1. Mathematical model

The abovementioned methodology of trifactorial central composition plan design was used during investigation in cylindrical grinding. Input parameters during modeling were machining parameters:

- Workpiece speed v (m/min)
- Feed rate s_a (mm/rev)
- Depth of cut a (mm)

Output parameters were:

- Tangential force F_t (N)
- Normal force F_n (N)

Other parameters were kept constant: tool geometry, tool wear, cooling and lubricating fluid, dynamical system machine-tool-workpiece.

Chosen mathematical model for grinding forces has the form:

$$F_i = C.v_r^{x}.s_a^{y}.a^{z}. \quad (1)$$

2.1.1. Creep-feed grinding

In the case of surface grinding, where there is no lateral movement of the table, usually resulting force has been divided into tangential (extensive) component F_t and normal (radial) component F_n [6, 15].

Tangential component acts in the direction of the tangent to the surface of the grinding wheel and workpiece contact, that is, in the direction of cutting speeds. The normal component acts normally to the surface of the wheels and workpiece. As the diameter of the wheel is far greater than the depth of cut, it can be assumed that the tangential and normal component supine in a horizontal or vertical plane, **Figure 1**.

The relationship of normal and tangential components of the grinding forces is defined as the grinding force ratio:

$$\lambda = \frac{F_n}{F_t} = \frac{F_n'}{F_t'} \tag{2}$$

In the previous equation, the components of the grinding forces are reduced per unit width of grinding b, referred to as the specific grinding force:

$$\begin{aligned} F_t' &= \frac{F_t}{b} \\ F_n' &= \frac{F_n}{b} \end{aligned} \tag{3}$$

Grinding force can be expressed by specific grinding energy, which shows how much energy is consumed per unit volume of material removed:

$$u = \frac{P'}{Q'} = \frac{F_t' \cdot v_s}{a \cdot v_w} = \frac{F_t'}{h_m} \tag{4}$$

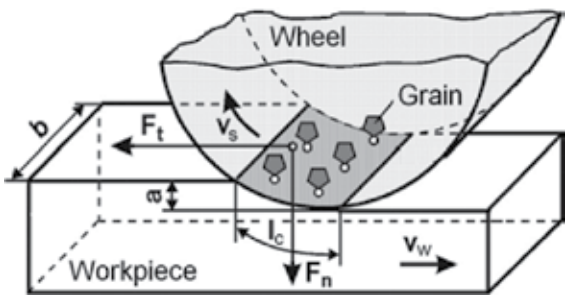

Figure 1. Components of the cutting force during creep-feed grinding.

2.2. Conditions during the experiment

2.2.1. Cylindrical grinding

Workpieces were cylindrical shaped Ø 60 × 150 mm and were made from two types of steel:

- Steel EN 34Cr4. with mechanical properties R_{p02} = 460 MPa; R_m = (690–840) MPa
- Steel EN 18CrNi8. with mechanical properties $R_{p0.2}$ = 485 MPa; R_m = (1080–1330) MPa

Tool was cylindrical grinding wheel Ø 350 × 40 × 127 mm, type B60L6V. Machining was performed on cylindrical grinder by manufacturer LŽTK Kikinda type UB, with dimensions of the workplace 1000 × 400 mm and power was rated 4 kW. Cutting speed was kept constant at v_s = 3.65 m/s. Varied machining regime parameter values: work speed v_r, feed rate s_a and depth of cut a are shown in **Table 1**.

2.2.2. Creep-feed grinding

Workpiece material used in the experimental setup was the molybdenum high-speed steel (HSS), which is widely used in the industry of cutting tools. Designation of the selected speed steel is DIN S 2-10-1-8. This steel belongs to a group of ledeburite steel with a microstructure consisting of martensite and fine mixtures of primary and secondary ledeburite cementite. The chemical composition of the test material was: 1.08% C; 0.22% Si; 0.23% Mn; 0.014% P; 0.019% S; 4.1% Cr; 1.5% W; 9% Mo; 1.1% V and 8% Co. Measured hardness on all samples ranged 66 ± 1 HRC. Experimental samples consisted of tiles measuring 40 × 20 × 16 mm.

Based on the recommendations, the chosen material of the workpiece and set the conditions of processing were selected two wheels similar characteristics: wheels "Norton" type 32A54 FV BEP and size 400 × 80 × 127 mm, respectively "Winterthur" type 53A80 F15 V PMF and size 400 × 50 × 127 mm. The wheels are with high-quality abrasive grain, medium grain size, hardness soft, open structure with ceramic binder. All experiments were conducted with sharp wheels, and sharpening is done with a diamond planer alignment with a depth of 0.01 mm/ speed and displacement of 0.1 mm/rev.

The machining conditions included variable depths of cut and workpiece speed. The depth of cut was a = 0.05; 0.1; 0.25; 0.5; 1 mm and the workpiece speed was v_w = 2.5; 5; 10; 25; 50 mm/s. The adopted mean value of specific material removal rate is Q' = 2.5 mm^3/mm·s. The grinding wheel speed was constant v_s = 30 m/s.

2.3. Measurement of grinding force components

2.3.1. Cylindrical grinding

Resulting grinding force can be divided into three components (**Figure 2**):

- Tangential component F_t (acts in vertical direction)
- Normal component F_n (acts horizontally)
- Axial force F_a (acts in the direction of workpiece axis-feed)

No.	Machining factor			Experimentally measured values				Calculated values by response surface methodology			
				EN 18CrNi8		EN 34Cr4		EN 18CrNi8		EN 34Cr4	
	v_r [m/min]	s_a [mm/rev]	a [mm]	F_t [N]	F_n [N]	F_t [N]	F_n [N]	F_t [N]	F_n [N]	F_t [N]	F_n [N]
1	18.4	20	0.01	11.8	17	10.9	17.8	12.31	20.36	11.87	20.48
2	36.8	20	0.01	12.4	17.8	11.8	19.8	12.67	21.43	12.39	21.71
3	18.4	30	0.01	12.3	18.4	13	18.9	12.56	21.40	12.42	20.97
4	36.8	30	0.01	12.9	19.8	13.2	21.1	12.92	22.53	12.97	22.23
5	18.4	20	0.02	16.1	29	17.4	29	15.37	28.23	15.64	27.51
6	36.8	20	0.02	16.6	31.5	17.9	31.2	15.81	29.71	16.33	29.16
7	18.4	30	0.02	17.2	31.2	18.8	33.1	15.68	29.66	16.36	28.16
8	36.8	30	0.02	17.5	33.3	20	33.6	16.13	31.22	17.09	29.86
9	26	25	0.014	12.1	25.4	12.3	24.8	14.06	25.16	14.22	24.65
10	26	25	0.014	12	25.3	13.5	24.7	14.06	25.16	14.22	24.65
11	26	25	0.014	12.6	24.5	12.2	24	14.06	25.16	14.22	24.65
12	26	25	0.014	12.8	24.3	14	24.1	14.06	25.16	14.22	24.65
13	16	25	0.014	13.6	23.1	12.6	22.8	13.79	24.27	13.79	23.66
14	42.4	25	0.014	14.2	25.6	13.6	25.6	14.35	26.08	14.66	25.69
15	26	18.4	0.014	14.4	22.1	12.4	23.1	13.85	24.23	13.74	24.21
16	26	32.6	0.014	15.5	28.2	14.1	24.3	14.25	25.99	14.64	25.03
17	26	25	0.0086	11	19.2	10.8	19	12.03	20.00	11.71	20.03
18	26	25	0.023	17.1	33.2	18.1	31.1	16.48	31.78	17.32	30.45
19	16	25	0.014	13.4	23	12.1	22.5	13.79	24.27	13.79	23.66
20	42.4	25	0.014	14.5	25.8	13.9	25.7	14.35	26.08	14.66	25.69
21	26	18.4	0.014	14.2	22.9	12.6	23.3	13.85	24.23	13.74	24.21
22	26	32.6	0.014	15	28.1	14.6	24.1	14.25	25.99	14.64	25.03
23	26	25	0.0086	11.1	19.2	11	19.6	12.03	20.00	11.71	20.03
24	26	25	0.023	17.6	33.3	18.5	31.8	16.48	31.78	17.32	30.45

Table 1. Measured and calculated values of cutting forces.

During cylindrical grinding, axial force component F_a can be neglected because it is minor in comparison with F_t, which allows a much simpler dynamometer design.

Until now, two-component dynamometer with strain gauges was used for cylindrical grinding force monitoring. The same will be used in this experiment. Strain gauges were placed on both centers which enable reliable and accurate measurement of both components of cutting force on whole length of the workpiece.

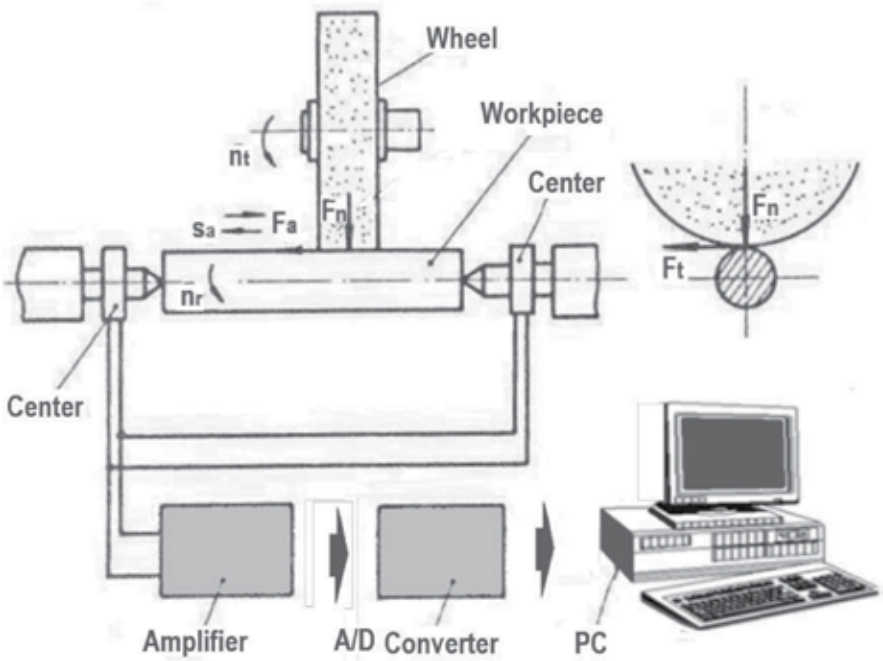

Figure 2. Information system for monitoring and processing cutting forces during cylindrical grinding.

Dynamometers were constructed in the manner that four strain gauges were taped onto cylindrical part of the center. In this way, two of the strain gauges are in the horizontal direction and two are in the vertical direction. All strain gauges are connected to bridge, so every component can be measured independently.

During grinding, under the influence of cutting forces, centers are deformed in the vertical and horizontal planes which are measured by strain gauges. Deformation of the strain gauge is proportional to load and signals coming from them have to be amplified and registered. To determine the cutting resistance values, dependence between measured signal (voltage on bridge) and load, $F_i = f(U)$, is determined with the use of lever and weight.

Mentioned measurement technique is accurate enough, but some things have to be considered:

- Quality of the glue used to stick strain gauges onto revolving centers
- Possible differences between electrical properties of strain gauges
- Accuracy of strain gauges positioning into vertical and horizontal planes
- Protecting the strain gauges from environmental influence
- Quality of the acquisition system
- Length of the cables to transfer measured signal

During the experiment, standard cemented carbide revolving centers are used.

Signals from dynamometers on centers were amplified with Kistler CA 5001 amplifier. Afterward, those signals were transformed by A/D converter to PC computer for further processing and analysis of measured data, **Figure 2**.

2.3.2. Creep-feed grinding

Measuring the forces that occur during creep-feed grinding was done using three-component dynamometers "Kistler Instrument AG," type 9257. The used dynamometer works on the piezoelectric principle, which is reflected in the emergence of electricity on the surface of the crystal plate embedded in the dynamometer when the same force exerted pressure. Electricity is amplified by means of amplifiers capacitive "Kistler," type CA 5001 and then is converted into DC voltage in the range from 0 to 10 V.

Measurement, analysis and control of the grinding force were performed using the information of the measuring system [10], where data acquisition is implemented by AD cards and cash integrated software package, **Figure 3**. The set information measurement data acquisition system is characterized by a high degree of accuracy, reliability, speed of response and the ability to reproduce measurement results. It allows real-time measurements, timely intervention if they appear illogical results, as well as comprehensive and rapid processing and analysis of results.

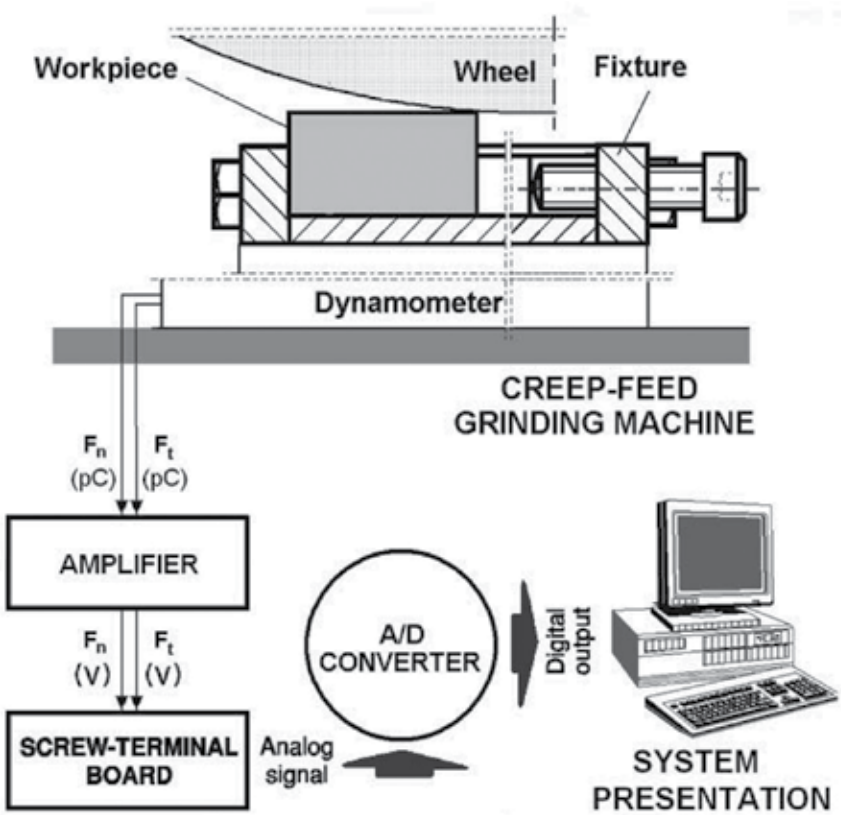

Figure 3. Information system for measuring and processing cutting forces during creep-feed grinding.

3. Analysis of experimental data

3.1. Cylindrical grinding

Based on the experimental plan and with the use of experimental devices, grinding forces values F_t and F_n are measured and recorded. Measured and calculated values for different machining parameters are shown in **Table 1**. On each sample of the material used for machining, for every experimental point, three repetitions were done, and the mean value of the repetitions was used in calculation of models.

Processing of the experimental data is performed with full factorial second-order design [9]. Side by side comparison of modeling with the genetic algorithms that were used to generate four coefficients from Eq. (1) while keeping the overall average error minimal is performed.

Table 2 contains values of regression coefficients [Eq. (1)]. It also shows the results and grades from model adequacy F_a and significance of mathematical model coefficients. Values of the coefficients which can be neglected with probability of $\alpha = 0.05$ are marked with *.

In **Table 3**, are results of modeled cutting forces with genetic algorithms are shown. **Table 4** contains exponents which are generated by genetic algorithms according the Eq. (1). Process of generating the coefficients was carried out during 5000 generations with 50 individuals. From which 5 were elite individuals and rest were created by 0.6 crossover fractions and the rest of the generation was created by mutation.

Table 5 features the comparison of success rate of these two methods of coefficients determination. Average errors in deviation of calculated resp. modeled values from experimentally obtained values are shown. It can be seen that genetic algorithms generated more suitable coefficients and thus produced smaller error for most of the forces and materials except for tangential force F_r and for steel EN 34Cr4.

From **Table 5**, it can be concluded that both techniques can be used for cutting forces modeling but genetic algorithms having a slight advantage.

Influence of cutting conditions on grinding forces $F_{t,}$ and $F_{n,}$ for both workpiece material (EN 18CrNi8 and EN 34Cr4) is shown in **Figure 4** for workpiece speed, in **Figure 5** for the feed rate and for the depth of cut in **Figure 6**.

	EN 18CrNi8		**EN 34Cr4**	
	F_t	**F_n**	**F_t**	**F_n**
C	125.3	229.8	52.03	296.1
x	0.016*	0.232	0.104	0.270
y	0.073*	0.236	0.038*	0.273
z	0.590	0.850	0.654	0.945
F_a	3.069	0.740	1.775	5.389

Table 2. Coefficients in Eq. (1), calculated by response surface methodology.

No.	Machining factor			Experimentally measured values				Modeled values by genetic algorithms			
				EN 18CrNi8		EN 34Cr4		EN 18CrNi8		EN 34Cr4	
	v_r [m/min]	s_a [mm/rev]	a [mm]	F_t [N]	F_n [N]	F_t [N]	F_n [N]	F_t [N]	F_n [N]	F_t [N]	F_n [N]
1	18.4	20	0.01	11.8	17	10.9	17.8	10.64	17.35	10.19	17.60
2	36.8	20	0.01	12.4	17.8	11.8	19.8	11.28	18.81	11.65	19.79
3	18.4	30	0.01	12.3	18.4	13	18.9	12.31	22.08	11.54	21.37
4	36.8	30	0.01	12.9	19.8	13.2	21.1	13.06	23.94	13.19	24.03
5	18.4	20	0.02	16.1	29	17.4	29	14.41	24.51	14.49	24.60
6	36.8	20	0.02	16.6	31.5	17.9	31.2	15.28	26.57	16.57	27.67
7	18.4	30	0.02	17.2	31.2	18.8	33.1	16.68	31.20	16.40	29.87
8	36.8	30	0.02	17.5	33.3	20	33.6	17.69	33.82	18.75	33.60
9	26	25	0.014	12.1	25.4	12.3	24.8	13.76	24.39	13.84	24.43
10	26	25	0.014	12	25.3	13.5	24.7	13.76	24.39	13.84	24.43
11	26	25	0.014	12.6	24.5	12.2	24	13.76	24.39	13.84	24.43
12	26	25	0.014	12.8	24.3	14	24.1	13.76	24.39	13.84	24.43
13	16	25	0.014	13.6	23.1	12.6	22.8	13.2	23.05	12.60	22.50
14	42.4	25	0.014	14.2	25.6	13.6	25.6	14.34	25.82	15.21	26.54
15	26	18.4	0.014	14.4	22.1	12.4	23.1	12.31	20.32	12.60	21.09
16	26	32.6	0.014	15.5	28.2	14.1	24.3	15.14	28.57	15.01	27.74
17	26	25	0.0086	11	19.2	10.8	19	11.11	19.13	10.80	19.31
18	26	25	0.023	17.1	33.2	18.1	31.1	17.1	31.24	17.81	31.06
19	16	25	0.014	13.4	23	12.1	22.5	13.2	23.05	12.60	22.50
20	42.4	25	0.014	14.5	25.8	13.9	25.7	14.34	25.82	15.21	26.54
21	26	18.4	0.014	14.2	22.9	12.6	23.3	12.31	20.32	12.60	21.09
22	26	32.6	0.014	15	28.1	14.6	24.1	15.14	28.57	15.01	27.74
23	26	25	0.0086	11.1	19.2	11	19.6	11.11	19.13	10.80	19.31
24	26	25	0.023	17.6	33.3	18.5	31.8	17.1	31.24	17.81	31.06

Table 3. Measured and modeled values of cutting forces.

	EN 18CrNi8		EN 34Cr4	
	F_t	F_n	F_t	F_n
C	21.165	20.637	24.130	23.674
x	0.085	0.116	0.193	0.169
y	0.361	0.595	0.306	0.479
z	0.438	0.498	0.508	0.483

Table 4. Coefficients in Eq. (1), generated with genetic algorithms.

	Response surface methodology				Genetic algorithms			
	EN 18CrNi8		EN 34Cr4		EN 18CrNi8		EN 34Cr4	
	F_t	F_r	F_t	F_r	F_t	F_r	F_t	F_r
Average error %	5.96	6.63	7.98	5.14	5.39	5.25	5.63	5.48

Table 5. Comparison of the average errors made by response surface methodology and genetic algorithms.

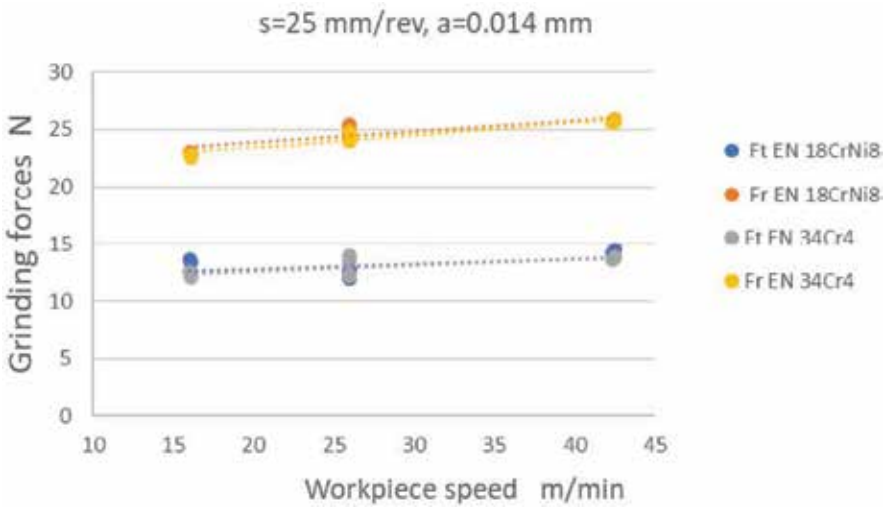

Figure 4. Influence of the workpiece speed on grinding forces.

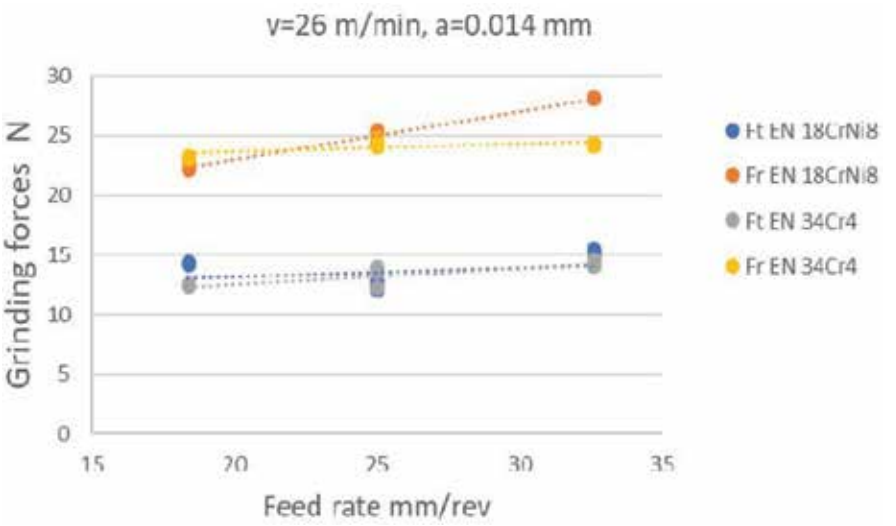

Figure 5. Influence of the feed rate on grinding forces.

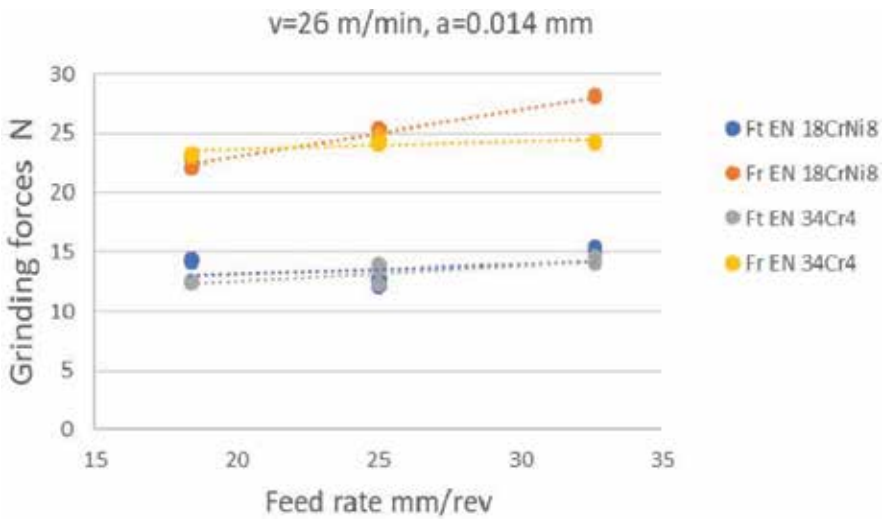

Figure 6. Influence of the depth of cut on grinding forces.

From **Figures 4–6**, it can be noticed that all input parameters, significantly influence increasing of cutting forces during cylindrical grinding process. Depth of cut has the highest influence on grinding forces followed by workpiece speed and then feed rate. This conclusion is valid for both study materials in study.

3.2. Creep-feed grinding

An example of measurement results of the cutting force during creep-feed grinding, two wheels with similar characteristics but different manufacturers, is shown in **Figure 7**. It can be concluded that for the same processing conditions obtained different values of force components sanding, or about the same dynamic character.

Figures 8 and **9** are given depending on the specific components of cutting forces, as well as their relationship F'_n/F'_t, depending on the cutting depth and the workpiece speed for both selected wheels. With diagrams shown it can be concluded that with increased cutting depth grinding forces are increasing and decrease with increasing the workpiece speed, because of cutting depth is decreasing.

Relationship of cutting force in grinding depends on the elements of the cutting regime, and a constant specific productivity of grinding, is shown in **Figure 10**. The diagram shows that compared to conventional grinding, in creep-feed grinding cutting forces appear higher for both grinding wheels.

The ratio of normal and tangential grinding forces moved to within 2–4, except that higher values related to creep-feed grinding for both grinding wheels versus the workpiece speed.

Input parameters significantly influence increase in specific cutting forces during creep-feed grinding process. Depth of cut has the highest influence on grinding forces have depth of cut,

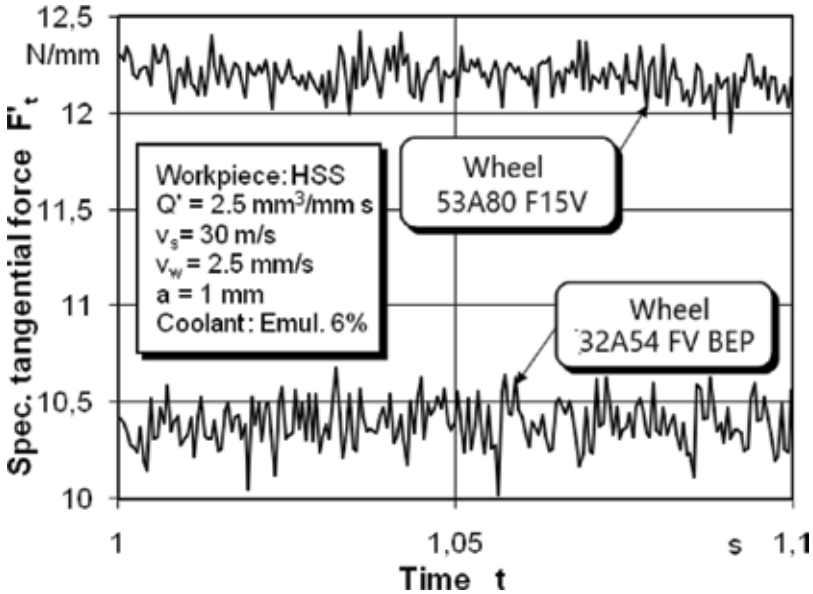

Figure 7. Value and character of the measured tangential grinding force components.

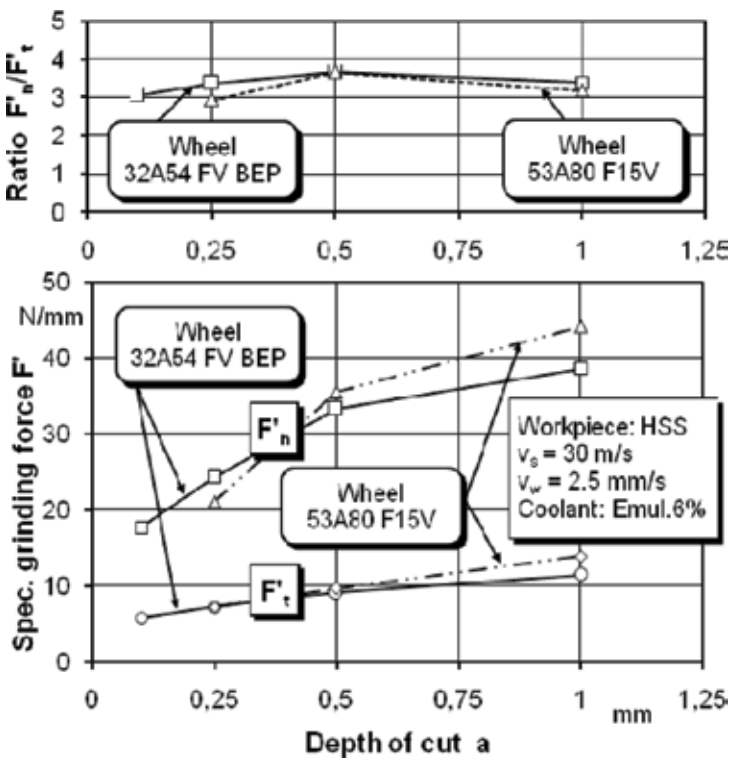

Figure 8. The grinding forces versus the depth of cut.

http://dx.doi.org/10.5772/intechopen.76968

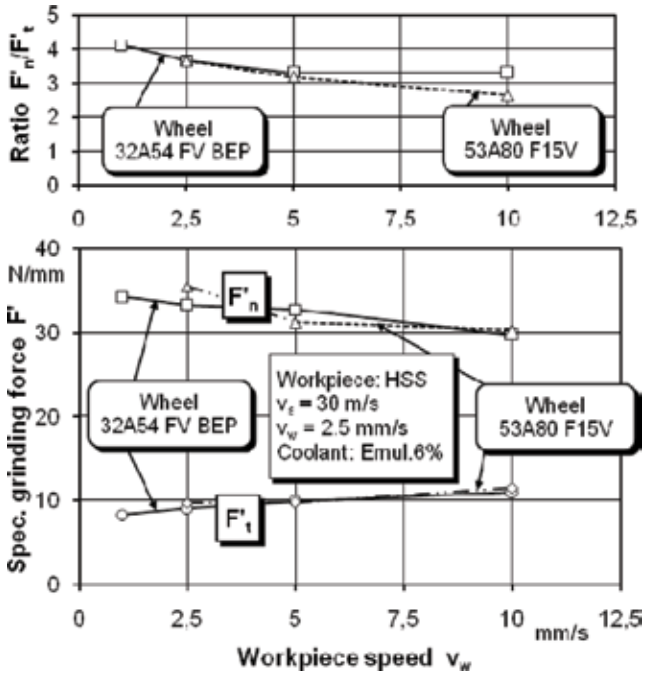

Figure 9. The grinding forces versus the workpiece speed.

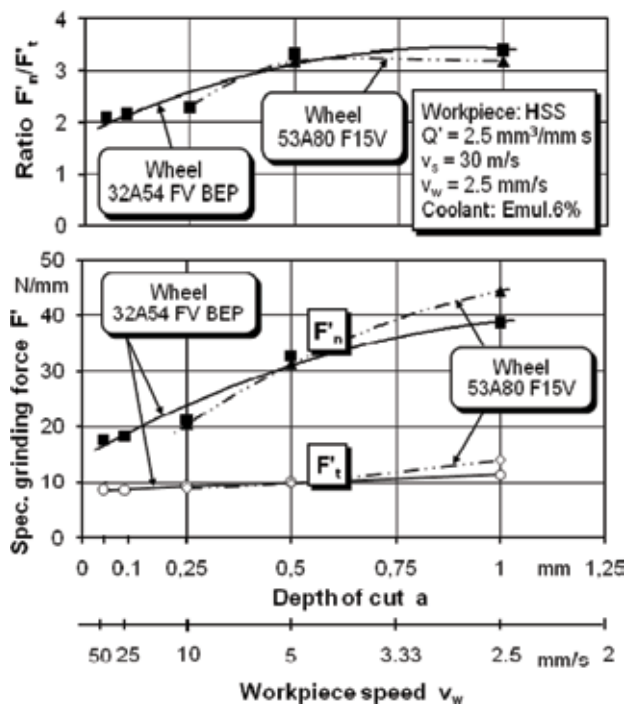

Figure 10. Specific grinding force versus the cutting regime for creep-feed grinding.

while workpiece speed has low influence on grinding forces. Increasing workpiece speed decreases specific grinding forces for both used grinding wheels.

4. Conclusions

Based on stated earlier, following can be concluded:

- Presented dynamometers can be successfully used for measurement of cutting forces during cylindrical grinding.
- Defined mathematical model of cutting forces F_t and F_r are adequate
- Influential elements of machining parameters on cutting forces are determined.
- Genetic algorithms are suitable for generating the coefficients for cutting force modeling.
- Creep-feed grinding reduces processing time, but also increases the cutting force
- Cutting forces primarily depend on the type of workpiece material and elements of its process
- Cutting forces during creep-feed grinding, due to a greater number of active abrasive grains into engagement with the workpiece material, are significantly higher compared to conventional grinding
- The grinding forces, the increasing length of contact of the grinding wheel and workpiece material, with increasing depth of cut;
- Increase the speed of the workpiece grinding forces decrease because it reduces the cross-section of the affected layers of material by grinding grain;
- Greater grinding force ratio can be observed in creep-feed;
- Cutting forces during creep-feed grinding allow identification of the energy balance of machine tools and estimation of the level of accuracy for different machining conditions

Acknowledgements

The Technological Development program Republic of Serbia, supported this TR 35015 project. For their support authors show great appreciation.

Nomenclature

v_r (m/min)	workpiece speed
s_a (mm/rev)	feed rate

a (mm)	depth of cut a (mm)
v_w (m/min)	workpiece speed creep-feed grinding
v_s (m/s)	grinding wheel speed
F_t (N)	tangential force
F_n (N)	normal force
F_a (N)	axial force
λ	grinding ratio
b	(mm) width of grinding
F_t', F_n' (N/mm)	specific grinding force:
u (n/mm^2)	specific grinding energy
h_m (mm)	grinding depth
Q′ (mm^3/mm·s)	specific material removal rate is
P′ (W/mm)	specific grinding power

Author details

Pavel Kovač* and Marin Gostimirović

*Address all correspondence to: pkovac@uns.ac.rs

Faculty of Technical Sciences, University of Novi Sad, Novi Sad, Serbia

References

[1] Rowe WB. Principles of Modern Grinding Technology. Boston: William Andrew Publishing; 2009

[2] Chang HC, Wang JJ. A new model for grinding force prediction and analysis. International Journal of Machine Tools & Manufacture. 2008;**48**:1335-1344

[3] Guo C, Campomanes M, Mcintosh D, Becze C, Green T, Malkin S. Optimization of continuous dress creep-feed form grinding process. CIRP Annals – Manufacturing Technology. 2003;**52**(1):259-262

[4] Holešovski F, Hrala M, Stančik L. Measurement of cutting forces in the centre grinder. Manufacturing Technology Journal. 2005;**5**

[5] Aslan D, Budak E. Semi-analytical force model for grinding operations. Procedia CIRP. 2014;**14**:7-12. DOI: 10.1016/j.procir.2014.03.073

[6] Patnaik Durgumahanti US, Singh V, Venkateswara Ra P. A new model for grinding force prediction and analysis. International Journal of Machine Tools and Manufacture. 2010;**50**(3):231-240

[7] Yao C, Wang T, Xiao W, Huang X, Ren J. Experimental study on grinding force and grinding temperature of Aermet 100 steel in surface grinding. Journal of Materials Processing Technology. 2014;**214**:2191-2199

[8] Kopač J, Krajnik P. High-performance grindig – A review. Journal of Materials Processing Technology. 2006;**175**(1-3):278-284

[9] Liu Q, Chenb X, Wangc Y, Gindy N. Empirical modelling of grinding force based on multivariate analysis. Journal of Materials Processing Technology. 2008;**203**:420-430

[10] Gostimirovic M, Sekulic M, Kopac J, Kovac P. Optimal control of workpiece thermal state in creep-feed grinding using inverse heat conduction analysis. Strojniški vestnik – Journal of Mechanical Engineering. 2011;**57**(10):730-738

[11] Gostimirovic M, Kovac P, Jesic D, Skoric B, Savkovic B. Surface layer properties of the workpiece material in high performance grinding. Meta. 2012;**51**(1):105-108

[12] Gostimirovic M, Kovac P, Sekulic M. An inverse heat transfer problem for optimization of the thermal process in machining. Sadhana. 2011;**36**(4):489-504

[13] Kovač P. Modeling of Machining Process- Factorial Experimental Plans (in Serbian). Novi Sad: FTS; 2006

[14] Pucovski V, Kovač P, Tolnay M, Savković B, Rodić D. The adequate type of function for modeling tool life selection by the use of genetic algorithms. Journal of Production Engineering. 2012;**15**(1):25-28

[15] Mishra VK, Salonitis K. Empirical estimation of grinding specific forces and energy based on a modified Werner grinding model. Procedia CIRP. 2013;**8**:287-292

Chapter 5

HyDRa: Vortex Polishing with a Deterministic Hydrodynamic Radial Polishing Tool

Erika Sohn, Esteban Luna, Elfego Ruiz, Luis Salas and Joel Herrera

Additional information is available at the end of the chapter

http://dx.doi.org/10.5772/intechopen.75524

Abstract

This work presents the deterministic hydrodynamic polishing system (HyDRa (HyDRa-dynamic Radial Polishing Tool) based on a polishing tool developed at the Instituto de Astronomía, UNAM. HyDRa is one of several modern deterministic polishing techniques that allow for computer controlled finishing of complex optical surfaces. The HyDRa system is based on a hydrodynamic polishing tool that generates a variable-density abrasive flow that makes possible the production of high-quality optical surfaces of diverse materials. The tool comprises several stacked operational stages that generate a grazwing abrasive flow with a predictable, zero-force erosion footprint on the workpiece that removes material. A recent innovation to the hydrodynamic polishing tool adds a switching capacity to the tool that allows the polishing action to be interrupted at will, without losing the stability of the operating parameters. This further increases the versatility and performance of the tool, since it is now possible to polish only the areas where the surface needs correction. Pulsed polishing also adds several techniques to this polishing method that further increase the system's versatility.

Keywords: deterministic polishing, fluid jet polishing, vortex polishing, pulsed polishing, simultaneous polishing with multiple tools

1. Introduction

As the demand to fabricate larger and increasingly complex aspheric optics becomes more common, the need for deterministic polishing tools which can meet these demands has motivated the development of the hydrodynamic, polishing tool (HyDRa).

The HyDRa polishing tool [1, 2] is a non-contact, zero-force hydrodynamic tool that rotationally accelerates a slurry and air mixture and expels it tangentially onto the workpiece. It consists of several operational stages: an abrasive suspension (water and polishing grit) is fed to the tool's first operational stage, where it is mixed with air at a controlled pressure in order to produce a variable-density abrasive foam. This foam then enters the rotational acceleration chamber, where it is sped up to high revolutions per minute (RPM). The rotational energy of the flow then turns into radial velocity in a nozzle that forms between the tool's divergent output and the workpiece. In this way, the abrasive particles graze the workpiece in closely tangential trajectories. Thus, the polishing particles generate a shearing action that removes material in a ductile removal process, as described in [3]. The drag generated by this radial flow forms a central low-pressure zone (vacuum) surrounded by a high-pressure ring. As a result, the tool floats over the workpiece, exerting no net force onto it [4], since these regions cancel each other out. This poses many advantages in modern deterministic polishing, in particular the capability of polishing ultra-thin surfaces, such as semiconductor wafers and optical membranes.

The HyDRa tool belongs to the fluid jet polishing (FJP) family, originally developed by Fähnle et al. [5]. Although HyDRa also expels an abrasive suspension onto the surface to be polished, there are several basic operational principles that differ from the classic FJP technique. The FJP method, and most other polishing techniques, needs to apply pressure onto the workpiece, in order to remove material. In some cases, as in the classic FJP technique, the force that is exerted onto the material can be minimized by using a small contact area; see for example [6], where the force on the workpiece is less than 1 N. This however, could represent a trade-off between footprint size and removal rate; removal rates of <0.01 mm^3/h are common for 1–2 μm Cerium oxide polisher [6]. Other deterministic methods, such as ion beam figuring (IBF), are non-contact, zero-force processes that present removal rates of up to 50 mm^3/min [7] without degrading the initial micro-roughness.

2. Polishing with HyDRa

This section describes the generalities of polishing with the HyDRa system. A typical static removal footprint is shown in **Figure 1**.

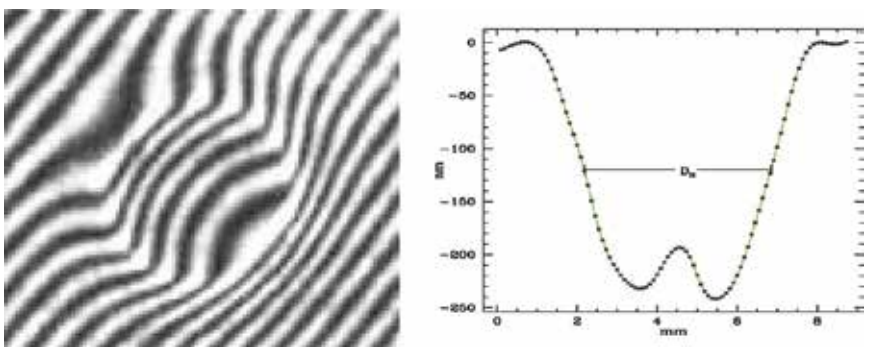

Figure 1. Tool influence function. The image to the right shows the removal function profile extracted from the interferogram to the left. This profile was obtained by operating the tool for 2 s on a fixed position over the workpiece. D_H is the full width at half maximum (FWHM) of the removal function. Tool footprint diameters typically range between 3 and 10 mm, depending on the particular tool.

http://dx.doi.org/10.5772/intechopen.75524

As can be seen, the removal takes place in a ~5 mm diameter region that has an M-shaped geometry. Removal in the central region is about 20% lower than the peripheral region. Removal is a function of slurry density (ρ) and accelerating air pressure (P_T), slurry flow, i.e., flow rate (F_1), and is a linear function of dwell-time. In order to attain deterministic polishing, all tool parameters are controlled with high precision, as described in Section 4.

2.1. The HyDRa polishing rig

The HyDRa tool is part of a complex polishing robot, consisting of a CNC positioning device; a fluid and compressed air control system; a slurry management unit, which stirs the slurry and controls its density; and a software package that obtains error maps from a series of interferometers, and generates dwell-time/constant-velocity PWM trajectories. These trajectories correct the workpiece figure, depending on the selected method (pulsed or continuous operation), as the block-diagram of **Figure 2** illustrates.

The HyDRa tool is attached to a five degree of freedom (DOF) polishing machine with force feedback, based on a 2.4 × 2.4 m Cartesian CNC, with two additional DOF (tip and tilt), implemented by means of a 3-actuator hexapod. This configuration allows the generation and polishing of any surface geometry. Since feedback control keeps all polishing parameters constant, removal is exclusively a function of dwell-time. In this way, figure correction depends on the trajectory followed by the tool and the velocity at each point along it, which requires that the CNC be capable of following five-dimensional, controlled-velocity trajectories. Simultaneously, z-axis movement is controlled so that the tool can accurately follow the surface contour with zero-force. Although the machine's repeatability is around 10 μm, the removal is accomplished with nanometric accuracy due to a load cell that regulates tool height over the workpiece, as reported in [4]. The slurry conditioning unit (SCU) supplies a

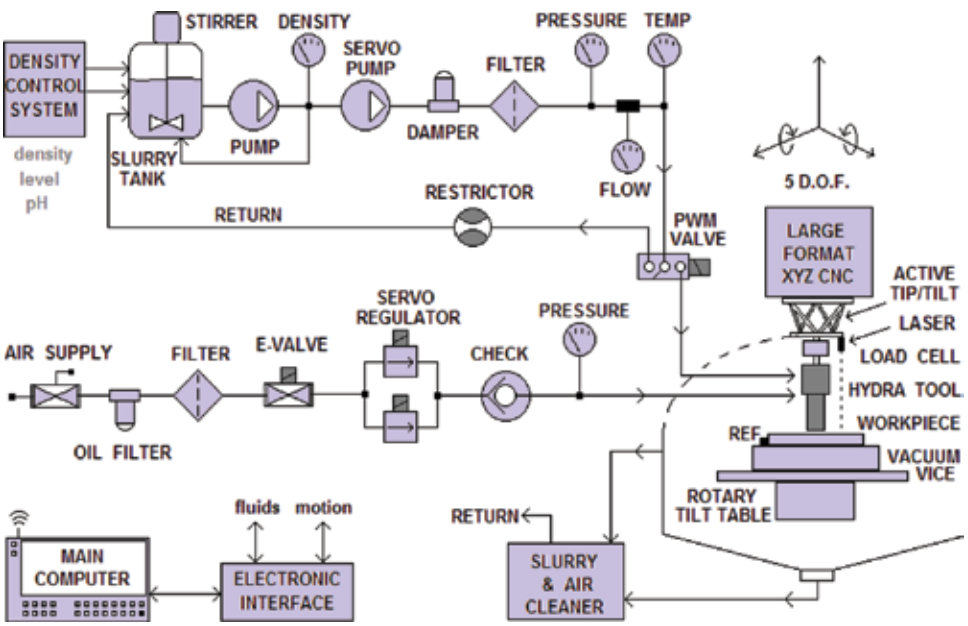

Figure 2. HyDRa polishing process setup, (see text).

density controlled polishing suspension to the HyDRa slurry supply system. It also captures and reincorporates the liquid and atomized slurry that is expelled from the tool. The density is continuously monitored by means of a photodensitometer and controlled by means of polishing-paste and water supply systems. The expelled slurry is captured by the return system, which consists of a blower that reincorporates this slurry and air into the SCU container, forcing the mixture through a washed-air system.

A pump is continually recirculating the polisher in the container, and a derivation supplies filtered slurry to the HyDRa slurry control system. The slurry that flows into the tool is fed by means of a damped-diaphragm DC pump that is feedback-controlled by means of either a flow meter or a pressure sensor. In order to reduce air contamination, the HyDRa system polishes in shallow immersion so that an air-lock for the return system is formed. The HyDRa tool accelerates an abrasive foam, composed of a variable-density suspension of slurry and air created by means of an air control system that regulates the foaming and propelling air pressures using electromechanic air regulators, pressure sensors and control electronics. All polishing parameters are acquired with a data acquisition card, and controlled and visualized in LabView®. The surface is fixed onto the CNC platform as the tool is swept over the surface in a pattern chosen by the user. Pulsed operation of the tool sweeps the tool(s) along the workpiece at a constant velocity, switching the polishing action on and off depending on how much material needs to be removed. The slurry is fed to the tool at controlled pressures and flow rates. The tool is supplied with compressed air to operate the foaming and acceleration stages. The abrasive foam is radially expelled through the tool nozzle onto the surface to be polished, as described above. Tool height is controlled by the feedback variable provided by the load cell, so that the CNC can adjust tool height in order to polish with zero force, as is discussed below.

2.2. Zero-force polishing

One of the central advantages of the HyDRa tool resides in that it can be adjusted to exert zero force on the work surface, while maintaining considerable removal rates (~10 mm^3/h). The flotation effect is described in more depth in this section.

As the HyDRa tool expels the slurry through its nozzle, the rotational energy of the flow is converted to radial velocity. The drag generated by this radial flow produces a central low-pressure zone that is surrounded by a vortex which is in turn confined by a ring shaped, positive thrust zone. This effect differs from the linear jet polishing technique [3, 8] in that, in normal-incidence, classic jets, the pressure profile is represented by a Gaussian distribution, where the maximum is located at the jet's center. In contrast, the pressure distribution of HyDRa on the workpiece presents negative values at the footprint's center and is circumscribed by an annular, positive-pressure region. With this, the force on the workpiece can be adjusted to net zero-force. In **Figure 3a**, footprint pressure vs. distance from the center of the tool is plotted. This was obtained by means of a 0.46 mm diameter orifice connected to a pressure sensor over which the tool footprint was radially scanned. As can be seen, a low pressure zone forms at the central part of the footprint and, as the radius increases, the gauge pressure increases to a maximum. It then falls again as the orifice approaches the tool's outer radius.

http://dx.doi.org/10.5772/intechopen.75524

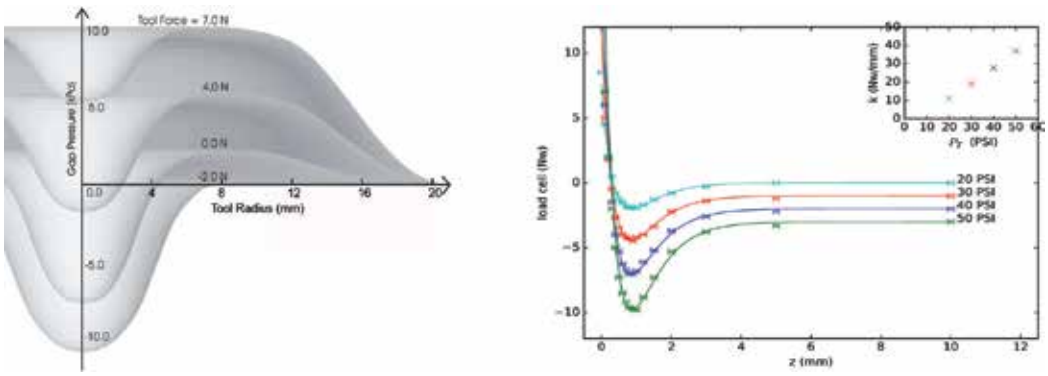

Figure 3. (a) (left) Pressure distribution as a function of tool radius for different operating pressures. (b) (right) Force applied by the HyDRa tool as a function of distance Z from the work surface for accelerating pressures P_T = 20, 30, 40 and 50 PSI. For clarity, a constant offset has been added to the 30, 40 and 50 cases. Typical error bars are 0.1 N for the load cell and 20 μm for the Z position. The solid lines are an analytical function fit derived from a Morse potential. In the upper right inset, the restitution spring constant is shown to be related to P_T. When an external holding force F_h is applied to the tool and pushes it against the workpiece, the vacuum force F_v has a tendency to decrease as the thrust force F_e is increased.

As the tool moves away from the workpiece, the vacuum has a tendency to increase, as the thrust force tends to decrease; in consequence, the balance of these two forces is a function of the tool's distance from the surface to be polished. With this, several operational modes can be achieved, one of them allowing the tool to freely float over the surface without the need to rigidly attach it to a positioning device. In this case, the tool's weight is counterbalanced by the thrust and vacuum forces. When the HyDRa tool is mounted onto a passive hexapod through a load cell, the support force F_h counterbalances the tool weight mg and the remaining forces to zero, while maintaining the tool in a static position.

The load cell value F_h is then used as feedback for the control system to maintain zero force on the workpiece. This is done by adjusting the z-axis of the CNC/hexapod.

We measured the tool and workpiece force interactions as a function of separation. In **Figure 3b**, the overall behavior of this interaction is shown in experiments where slurry accelerating pressures of 20 to 50 PSI and a polishing slurry flow of 5 ml/s were used. The distance over the workpiece was modified from several millimeters, down to a few hundred microns. The values of the load cell F_h were used to obtain the substrate force F_x, as explained above.

When the tool exceeds a certain distance, the workpiece experiences no force (see **Figure 3**). As the tool approaches the substrate, a negative force (attraction) is produced by a vacuum that develops between the workpiece and the HyDRa tool. As the tool further approaches the workpiece, a positive repulsion force is experienced, caused by the thrust force. At a few hundred μm from the workpiece, the vacuum and thrust forces balance each other out to zero. Here the surface can be polished without being deformed by the tool.

The combination of attractive and repulsive forces commonly arises in physical problems. One of such is given by the empirical Morse potential of diatomic molecules $U(z) = B\,(1 - e^{(-\alpha(z-z_m))})^2 - B$, where B is the dissociation potential and z_m is the separation at which the minimum of the potential is

P_T (PSI)	B (N mm)	α (1/mm)	z_m (mm)	k (N/mm)
50	10	1.36	0.36	40
40	7.5	1.36	0.34	27.7
30	5.1	1.36	0.34	18.9
20	3	1.36	0.34	11.1

Table 1. Fitting curve parameters.

reached, which constitutes a stable equilibrium separation. A force can be readily obtained from this potential by calculating its gradient: $F(z) = -\frac{d}{dz}U(z)$. We have plotted this force along the data of the figure by least-squares fitting the three parameters, B, α and z_m; their resulting values are listed in **Table 1**. A reasonable fit is obtained, and some insights may be derived from this exercise. It can be noted that, as the accelerating pressure P_T increases, so does the depth of the potential well and thus the amplitude of the forces involved, as given by the parameter B. However, the minimum of the potential is found roughly at a constant separation z_m of around 340 μm. At this distance, the force derived from the potential is zero (since the derivative of the potential is zero) and the tool floats over the work surface in stable equilibrium. If we approximate the minimum of the potential by a square law (Hooke's law) a restitution spring constant $k = 2\alpha B$ can be obtained, which measures the force with which the stable position is restituted. The values of k are also given in **Table 1**. As indicated in the inset in **Figure 3b**, k is a linear function of the accelerating pressure P_T.

2.3. Tool influence function and removal rates

Several tools have been developed to accommodate for different removal rates that range from 1 to 600 mm^3/h. This section presents measurements of static and volumetric removal rates for a medium removal-rate tool with a nozzle diameter of 3.8 mm. Several polisher grits have been tested: Cerium oxide (Opaline) with a particle size of 1 μm, and aluminum oxide (μ-grit) with particle sizes of 5 and 12 μm, suspended in water at a constant relative density of 1.09. Samples of different materials were polished: standard window glass, water-free fused silica (Infrasil®-302), BK-7 borosilicate, and Ohara's CLEARCERAM-Z® vitroceramic.

The measurements were performed by scan-sliding the tool over the sample at a constant speed and a corresponding zero-force tool height. The resulting cavity was measured interferometrically, and both the volume of removed material and the depth of the cavity were calculated. With these measurements the static removal rate D_S (depth/time) and the volumetric removal rate D_V were then calculated. We performed these measurements at different operational conditions of accelerating pressure (P_T) and slurry flow (f_p). In all cases, the relative density of the slurry was kept at 1.09. In **Figure 4**, the test results are shown. In all three panels, the left vertical axis D_V is related to D_S as $D_V = D_S * A$, where A is the tool footprint area. Each plot indicates the dependence of removal on the accelerating pressure P_T. The top left panel, where Cerium oxide was used, slurry flow f_p values of 3, 5 and 7 ml/s on window glass were tested. These are indicated as numbers on the curve.

http://dx.doi.org/10.5772/intechopen.75524

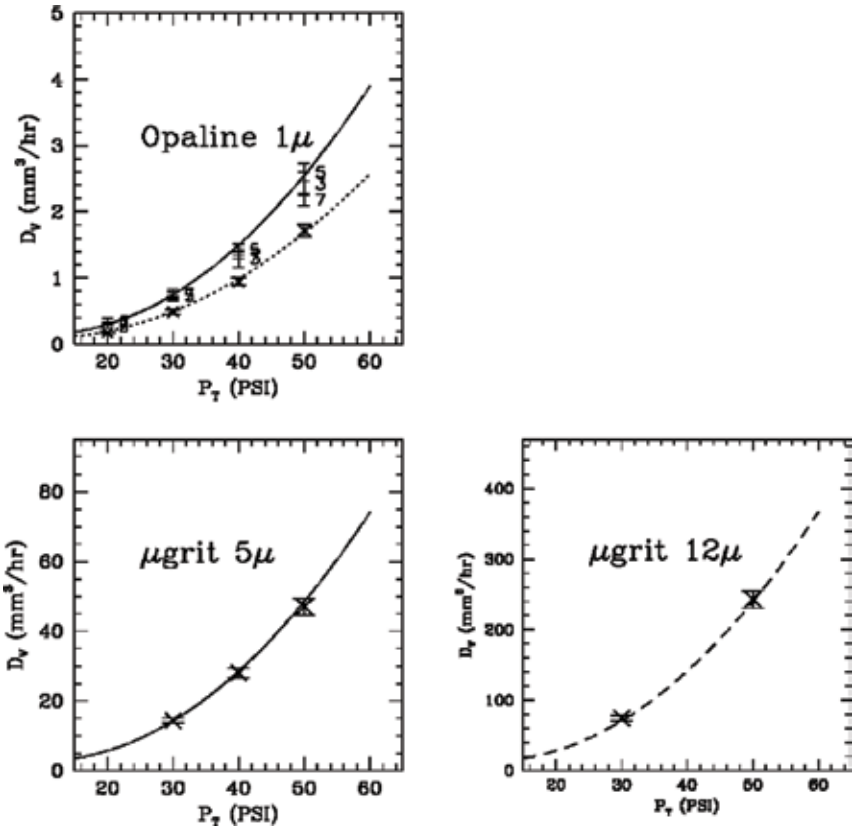

Figure 4. Volumetric removal rate D_V as a function of accelerating pressure (P_T) for various polisher types: 1 μm cerium oxide (Opaline), 5 μm aluminum oxide (μgrit) and 12 μm aluminum oxide. Opaline removal rates are presented for window glass (solid line), fused silica, and borosilicate (dotted line). Removal of μ-grit is shown for window glass and CLEARCERAM®-Z vitroceramic. All fitted curves are versions of the same second order polynomial law, scaled by a factor that is a function of substrate material and particle size (see text). Zero-force polishing was achieved at the corresponding tool height for this effect.

As can be noted, the highest removal rate for this tool is achieved with a slurry flow of 5 ml/s, thus this flow was employed for all consecutive experiments. Removal rates up to 2.5 mm^3/h at 50 PSI are obtained for this polisher. The $f_p = 5$ points are well fitted by a second order polynomial. In the first panel we also show the results of polishing a fused silica sample (crosses). In this case the hardness of the material causes the removal rate to decrease to 66% compared to window glass. The dotted line that fits these values is obtained by multiplying the same D_S polynomial by a small factor. In the lower left panel we tested the removal rate of 5 μm aluminum oxide grit on glass (crosses). The volumetric removal rate rises to ~50 mm^3/h at an accelerating pressure of 50 PSI. The solid line is the D_S polynomial obtained previously, multiplied by 19. Again, a very good fit can be seen. Lastly, in the lower-right panel, the removal rate of aluminum oxide grit (12 μm particle size) on Ohara CLEARCERAM® vitroceramic is shown. Removal was so large that it was impossible to measure it reliably with an interferometer, so the resulting cavity was measured by means of a needle profilometer. Only two points were

taken in this experiment (crosses in the last graph). If the same polynomial D_S were to be fitted (dashed line), it would have to be multiplied by 94. For all cases, the removed volume per abrasive particle is 3 to 5 orders of magnitude lower than the particle's volume. The kinetic energy as well as the grazing incidence associated with both the cerium and alumina particles, creates stresses that are not large enough to produce permanent dents. Resulting typical micro-roughnesses of 2, 24, and 31 nm, for grit sizes of 1, 5, and 12 μm, respectively, are around three orders of magnitude smaller than the particle sizes. These tests demonstrate that independently of grit size and material, as well as substrate hardness, behavior of removal as a function of accelerating tool pressure is comparable, which indicates that the same material removal process discussed above is taking place. The scaling parameter is an indicator of how efficiently a particular abrasive removes material from a surface of a given hardness. All HyDRa tools present this same relationship of removal as a function of P_T and grit size for pressures of up to 90 PSI. Currently, typical removal rates of ~15 mm^3/h @ 90 PSI, using 1 μm Opaline on borosilicate glass, are common.

2.4. Software

The HyDRa trajectory planning tool (HyTPT) is a software package developed specifically for the HyDRa tool [9]. It feeds machining code to a CNC or any computer-controlled positioning device, based on the error map that has been obtained interferometrically. When only one HyDRa tool is available, the amount of material that is removed at each specific position is proportional to the dwell time. This dwell time can be controlled either by the speed of the tool along a given trajectory when the tool is operated in continuous mode, or by the width of the pulses when operated in pulsed mode.

In HyTPT (**Figure 5**) a main window presents the project name and grants the user the ability to go from error maps to machine coordinates in four steps:

1. **Error Map alignment:** This allows the easy alignment of the error map, and the determination of its center, orientation and pixel size. The basic shapes are rectangular, circular, and annular surfaces.
2. **Base trajector:** It is possible to select the base trajectory from a series of curves: from simple raster patterns to more complex curves, such as trochoids and rotating triangles. It is possible to define and analyze each curve from the point of view of trajectory density, total polishing time, and speed at each point, among several others.
3. **Surface shape:** The shape of the surface, currently any on- or off-axis conic section, is defined in this window. The 2-D base trajectory is projected onto this 3-D surface. In addition to the 3-D trajectory the normal vector to the surface at each position is calculated, so that the CNC may orient the HyDRa tool normal to the surface along the trajectory.
4. **Machine coordinates:** A set of alignment tools facilitates the transformation of surface coordinates to machine coordinates. These routines communicate with the CNC machine and are developed for each particular CNC or robot arm to which the HyDRa tool is attached.

http://dx.doi.org/10.5772/intechopen.75524

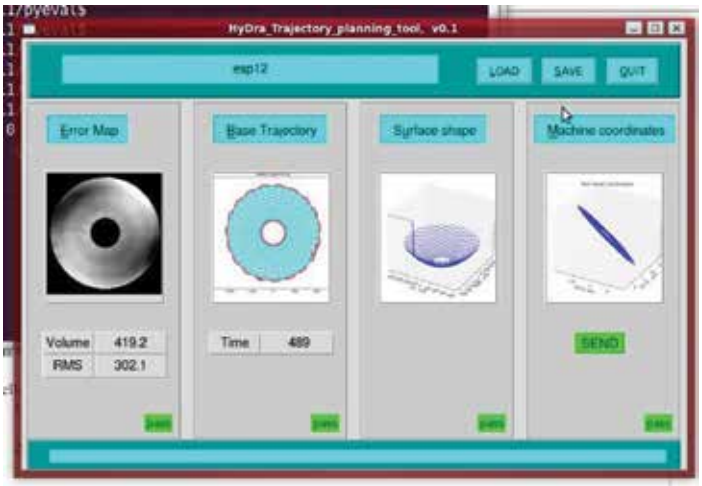

Figure 5. HyTPT software main interface showing all four steps.

Finally, the centering and orientation parameters, nine in total, are determined in order to properly align the system. Once each of these parameters has been calculated, the trajectory is delivered to the CNC machine, or robot arm so it can be executed there.

3. Pulsed polishing

Due to its hydrodynamic properties, the original HyDRa tool [1] does not allow the modification or switching of any of its operational parameters during operation. Therefore, in order to control the removal, dwell time is modified by means of tool velocity. However, there is a maximum tool velocity imposed by CNC limitations, that fixes a minimum, non-zero amount of material that can be removed with the tool. This poses problems for several operational applications, such as zonal corrections, multi-head or tessellated polishing, and edge problems. A new HyDRa tool design (patent pending) [2] overcomes these problems, by switching one of the operational parameters (polisher flow). This enables the pulsing of the abrasive action at will, without affecting tool bias. The ability to operate the HyDRa tool in a switched manner widens its overall performance and efficiency, adding new applications. It is not simple to switch most of the tool's operational parameters during use, since this causes a loss of tool bias, which affects the flotation capability. Restoring these parameters on the fly takes time and produces unwanted effects such as cavitation. This has limited the polishing strategy to making full sweeps of the entire surface. When needing to polish only a small section, the region must be approached with the tool biased, leaving behind an unwanted track and approach and exit marks. A new HyDRa tool design has been developed which allows switching slurry flow without losing tool bias. Switching frequencies of up to 10 Hz, and pulses as narrow as 10 ms, can be achieved with this new tool. This is accomplished by means

of an overdriven electro-valve which is installed in, or close to, the tool. This allows the use of polishing pulses that can be applied on a per-pixel basis or in a continuous scan using pulse width modulation (PWM) techniques. With this feature, dwell time can be controlled below the minimum attainable by a continuous action at the maximum CNC speed.

3.1. Linearity

A pulsed HyDRa tool with a 7 mm footprint has been developed and tested for linearity. **Figure 6a** shows the results of erosion vs. dwell-time. Pulse width was varied at constant increments, starting from 10 ms to a maximum of 500 ms, as the tool was moved at 0.2 mm increments, overlapping 35 times at each tool footprint diameter. The erosion was measured using a Fizeau interferometer and the result was normalized, so that removal corresponded to a single pass of the tool over each point along the line that was polished. Error bars are primarily due to errors produced by the subtraction of the base reference during interferogram reduction. A removal resolution of 0.1 nm/ms can be seen from the data. Noticeable polishing effects were observed at 25 ms. We attribute this effect to the electro-valve response time, which can be improved by using faster actuators.

3.2. Pulsing the polishing process

3.2.1. Pulse width modulation polishing (PWM)

It is now possible to control the duration of a pulse as a fraction of the time it takes the tool to travel a distance of one footprint diameter.

The depth of removed material for a raster scan pattern h, can be given by:

$$h = D_V Y / VS$$

where D_V is the volumetric removal rate, Y is the PWM duty cycle (ON time divided by the period T), V is the CNC velocity, and S is the raster step size. The period of the switching

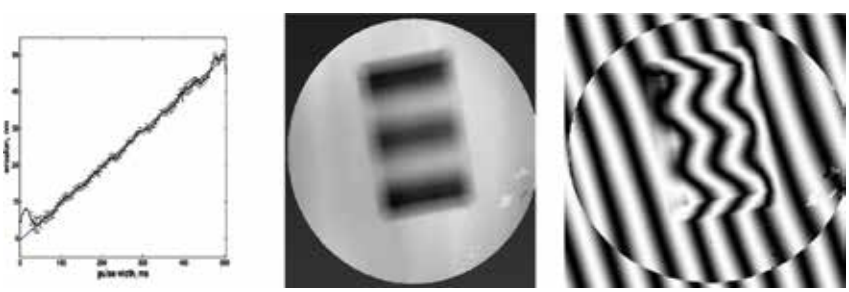

Figure 6. (a) Erosion vs. pulse-width in a linearity test. (b) Response function of the tool for pulsed operation at constant tool velocity. The tool was switched in a PWM mode, with a 50% duty cycle and 100 ms on/off switching times. The raster pattern used to generate this surface is perpendicular to the surface produced in the figure. Pixel size is limited by footprint size. Tool velocity was chosen so the pulses could be resolved independently.

signal is $T = D/V$, where D is the tool footprint diameter. In the time it takes to cross a tool footprint, there is a single pulse whose width can be varied from zero to the entire footprint diameter. The depth of the removed material $h = \beta\tau$ is proportional to the dwell time τ, defined by $\tau = \Upsilon D/V$, with a proportionality constant $\beta = D_V/SD$. When $\Upsilon = 1$, which is the continuous mode, tool removal (dwell time) h is controlled by CNC velocity. When $\Upsilon < 1$, which is the pulsed mode, h is controlled by means of switching the slurry supply and keeping the tool velocity constant. The continuous mode is limited to removals greater than $h_{\{min\}} = D_V\, \Upsilon/V_{\{max\}}S$. In order to obtain a lower removal, the pulsed mode must be employed.

For a tool footprint diameter of 7 mm and a maximum CNC velocity of 2000 mm/min, the minimum period of the switching signal will be 0.2 seg, or 5 HZ, which is within the 10 Hz switching frequency range. In an extreme case, where the duty cycle is switched between 0 and 1 while maintaining a constant velocity, it is possible to create a pixelated pattern that is useful for determining the response function of the pulsed tool (**Figure 6b**). A fringed pattern can be observed where the interface between the regions presents a slope that corresponds to the tool footprint diameter, which is the limiting polishing element size (*poxel*, or polishing element).

3.2.2. Zonal polishing

When only a small section of the surface needs to be polished, this region must be approached with the tool turned on, leaving behind unwanted tracks, as well as approach and exit marks. This is solved by using the pulsed mode of the HyDRa tool. When an isolated region that needs further polishing is identified, a dampening band of constant width surrounding it is defined. Assuming a raster pattern is used, the region is approached with the HyDRa tool fully operational with $\Upsilon = 0$, until it enters the dampening region. Here velocity is smoothly incremented to the value needed inside the region while at the same time, the desired dwell time is controlled by means of PWM. The width of the dampening region is determined by the CNC acceleration and deceleration capabilities. Inside the region to be corrected, either a pulsed or continuous polishing can be used in order to maximize efficiency.

3.2.3. Pixel polishing

In the constant velocity PWM polishing case, the resulting response function in the sweep direction is different from the response function of the transverse, raster direction. When a symmetrical finishing is needed, it is possible to employ the pixel polishing method, which consists of stepping the tool at discrete positions with respect to each other, covering the region of interest with the same step increments in both axes. The tool is then switched on for the necessary time in order to achieve the desired removal for each position. This method can also be useful when very localized zonal polishing is needed. This allows the tool to either follow a raster pattern, or any other trajectory or set of discrete positions over the region of interest. An example of this method was used in Section 3.1 for the linearity test, where it was shown that a removal resolution of 0.1 nm can be attained.

3.2.4. Tessellated polishing

In the polishing of meter-class surfaces, efficiency is limited due to HyDRa's small footprint size and volumetric removal rate. Efficiency, however, can be improved by simultaneously polishing the surface with several HyDRa tools. These tools can be mounted on independent polishing robots, where each robot tackles a certain section of the surface. Alternatively, several tools can be mounted on a single robot arm, as described below. This method poses several problems, such as obtaining smooth seams between sections, approaching each section without leaving marks, and avoiding collisions as two tools concurrently approach the boundary between sections. In order to obtain a seamless interface between two independent sections, it is necessary to approach the boundary following special trajectories, such as the wedge pattern shown in **Figure 7** (bottom). This trajectory avoids duplicating dwell time at the seam, such as would happen if a rectangular pattern were used (top of **Figure 7**).

3.2.5. Polishing run interrupt

When the polishing process needs to be interrupted, it is now possible to stop at any point on the surface and continue polishing at a later time.

3.2.6. Edge problem

As in other polishing methods, the HyDRa tool tends to leave a small (one footprint diameter) fallen edge. In order to overcome this with the unmodified HyDRa tool, tool velocity is

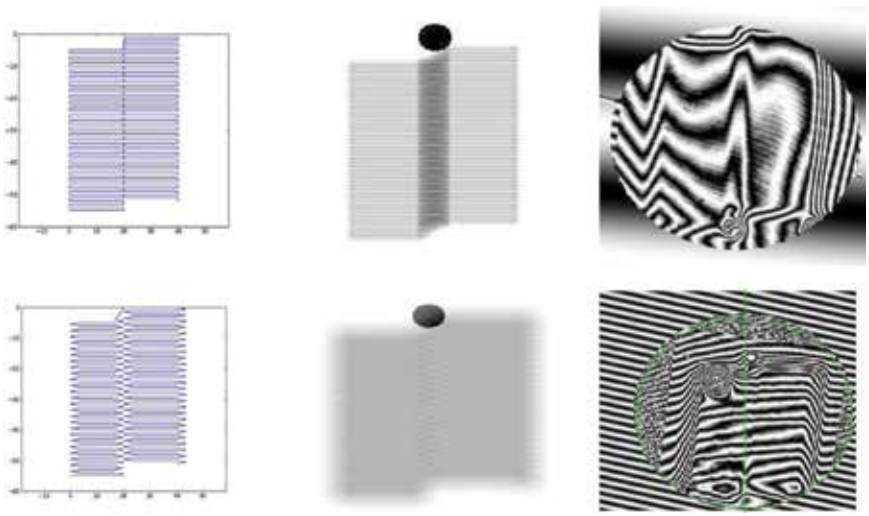

Figure 7. Tessellated polishing showing two different trajectory approaches. The figures to the left show the region of the interface between two raster patterns that use a rectangular (upper) and wedge (lower) seam at the boundary. The middle figures show a simulation of the resulting removal with the tool moving at a constant velocity and without PWM. Note the approach/exit tool mark at the beginning/end of the trajectory due to not switching the tool off. The interferograms to the right are actual polishing experiments. As can be seen, the raster pattern using rectangular trajectories duplicates removal at the seam, whereas the wedge trajectory produces a seamless interface. Another possible solution is to vary the pulse width at the seam, in order to match the dwell time between adjacent polishing sections.

incremented as the tool approaches the edge, reducing dwell-time. This is counterintuitive and can present CNC control problems, since the tool is accelerated in a region where it should be preparing for a raster direction change. The on–off capability of the new tool can alleviate this problem, since dwell-time can be controlled without having to increment tool velocity at the edge region. In fact, this method allows for decelerating the CNC in order to prepare for a direction change.

3.2.7. Convergence

Another advantage of being able to pulse the tool is a quicker convergence towards the desired surface [10]. As pointed out in [11], the existence of a minimum amount that will be removed due to not being able to turn the tool off (h_{min}), limits the amount of material that can be removed in each run, whereas, by being able to pulse the tool, h_{min} can be made zero, allowing for a maximum value of f, further increasing the polishing convergence rate.

3.3. Multiple-head polishing

Since HyDRa tools can now be pulsed, several polishing heads can be mounted onto a common arm which moves at a constant velocity over the surface. Dwell time is then controlled using PWM for each tool, as required by the error map. We can also take advantage of the self-conforming capabilities of HyDRa, in that it is not necessary to employ a positioning device to conform the parallelism of the tool to the surface. Only one degree of freedom (DOF) per tool is required. Each loop is closed with a load cell signal and implemented by means of a linear stage, which permits zero-force polishing while freely following the local sag and tilt of the surface. Another advantage of this type of polishing is that one single slurry supply system can be used for all the tools, simplifying the system and considerably reducing the costs. Polishing efficiency becomes a function of the number of tools, and in the case of a matrix configuration, several polishing runs can be implemented into a single sweep, reducing polishing time.

By polishing with several tools, each tool is essentially given a section of the surface and the boundaries between sections are finished seamlessly, either by employing wedged joints, or by using PWM. Among the possible multi-tool configurations are matrix, linear and spiral layouts:

3.3.1. Linear

By mounting several HyDRa tools onto a single polishing arm, attached to a Cartesian CNC machine, it is possible to cover an area by sweeping the arm in the x and y directions. Each tool is separated from the next by a fixed distance δ in the x axis. The sweeping action in the x axis is done by moving the arm by δ, and then advancing with the selected raster step in the y axis. The overlap between the sections assigned to each tool is managed by either using tessellated or the PWM techniques, as described above. There are certain considerations to be taken into account for this method, particularly due to the edge problem that arises when polishing circular or non-rectangular surfaces. There will always be a tool that needs to either enter or exit the surface, while others are already polishing. Additionally, since these tools need to take advantage of their self-conforming capability, as they approach the edge of the workpiece, they loose floatability. These problems can be dealt with by adequate trajectory programming.

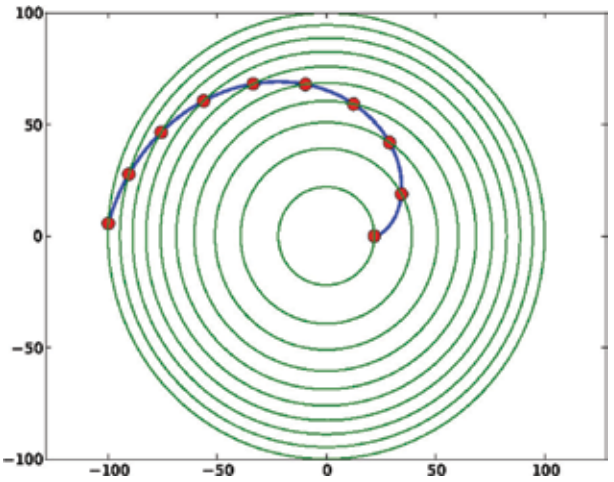

Figure 8. Hydra tools mounted on a spiral arm (see text).

3.3.2. Matrix

The linear configuration can be expanded by creating a matrix of tightly packed HyDRa tools maximizing tool number in order to minimize polishing time. The working principle is the same as the linear case, but adding *M* rows. This is equivalent to carrying out M polishing runs in a single iteration.

3.3.3. Spiral

In the case of large circular mirrors, it may be more efficient to polish the mirror by placing it on a rotary table. If we seek to fix as many HyDRa tools as possible onto a single arm, two conditions must be met. First, the number of tools should increase as r^2, so that each tool covers the same mirror area. Secondly, tools must be packed at the maximum allowable density, so that each tool sits next to the following one. Therefore, the shape of the arm must be a kind of spiral which is possible to solve for. By calculus of variations a spiral curve parameterized by the (increasing) radial coordinate, given in polar coordinates (r, θ) results in: $\theta(r) = \sqrt{4k^2 - 1/r^2} - \arctan\left(\sqrt{4(kr)^2 - 1}\right), r > 1/2k$. An example of this is shown in **Figure 8**, where HyDRa tools are mounted at equal separations along a spiral arm and may move along it to span equal areas, as the surface under it rotates.

4. Polishing parameters

Of the multiple finishing techniques currently in use, the ones based on sub-aperture polishing may be candidates for deterministic polishing, provided that the uncertainty of key polishing parameters is minimized. Deterministic polishing relies on a stable and predictable tool influence function; thus it is imperative that it is fully characterized for each material that will be

http://dx.doi.org/10.5772/intechopen.75524

polished. Simultaneously, metrology is a determining factor of the final quality of the surface, since it limits the precision of the error maps that can be obtained. This requires the knowledge of a series of polishing parameters such as tool velocity, pressure and height as well as slurry type, temperature, etc. Most of these parameters remain constant during the time periods required for polishing small optics, i.e. a few minutes. If larger, meter-class surfaces need to be polished, it is important to control and keep all parameters constant during an entire polishing run, which can represent over 10 h. Thus, a very stable and precise process control of the process is required.

The HyDRa tool removal function is based mainly on four independent operating parameters: propelling air pressure, grit mass concentration, height of the tool over the surface to be polished, and slurry flow and/or slurry pressure. In order to ensure deterministically polished surfaces, the errors contributed by each of these factors must be taken into account and precisely controlled to 1% for the entire length of the polishing run (over 100 h). Simultaneously, metrology is crucial for determining the surface's final quality, since it dictates the limit of the precision of the error maps that can be obtained.

4.1. Deterministic polishing

To maximize polishing performance, an abrasive foam is created in the tool's first stage. This raises the velocity of the polishing particles, improving the removal of material. This foam is produced by combining a constant flow f (a few ml/s) slurry, with air that is kept at a constant pressure P_p. This fluid is then accelerated with pressurized air at a propelling pressure P_T, in one or more cylindrical cavities. The resulting abrasive foam is then expelled through the tool's nozzle, where a vortex is produced that develops into a radial flow, and generates a grazing, uniform removal footprint. A relation of slurry flow f to slurry pressure P_p exists for each value of accelerating pressure P_T. This, in addition, depends on the tool's physical characteristics, such as its overall dimensions, the geometry of the acceleration chamber(s), as well as the nozzle shape. This relation establishes an operational diagram that defines tool bias. In this section, the control of f is chosen, although it is possible to select to control for either f or P_p. The removal D of HyDRa mainly depends on four independent operating parameters: propelling air pressure P_T, grit mass concentration ρ_i, slurry flow f, and distance of the tool over the workpiece Z. In order for deterministically polished surfaces to be obtained, the errors contributed by each of these parameters must be taken into account and controlled.

The removal rates, as determined by a series of independent experiments, where the polishing parameters varied, are shown in **Figure 9**.

To generalize the analysis, all parameters X are normalized around their operational values as x/x^-. With this, the relative variation of each parameter, defined as $\delta X = \frac{\Delta X}{X^-} = \Delta\left(\frac{X}{X^-}\right)$, is computed. The ratio between the relative variations of removal rate and the relative variations of each polishing parameter is given in the upper-left corner of the graphs. Here the operational value for the relative density is 80 g/l. As can be seen, removal rate varies as 1.18 times the fluctuations in the concentration. The relationship between the removal rate and the rest of the parameters can be determined similarly, where the fluctuations around the operation point of each parameter are taken into account. The sensitivities on

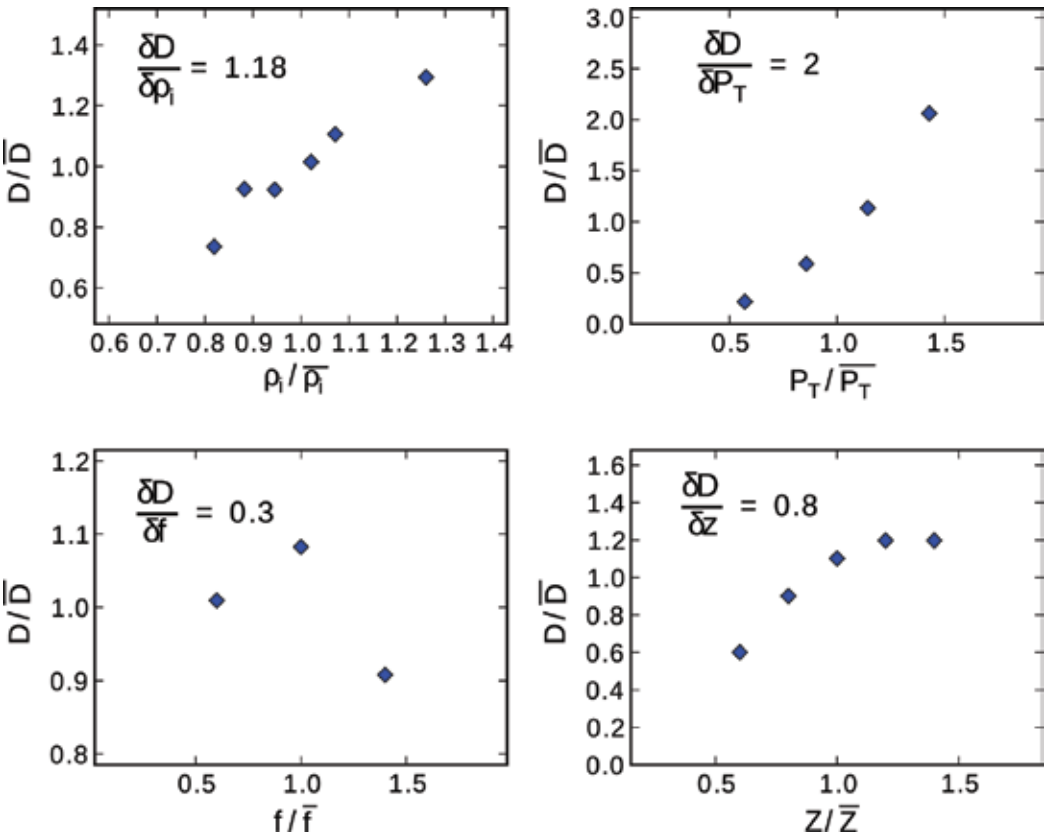

Figure 9. Normalized removal rate $D/\bar{D}$ (dimensionless) with reference to the normalized value of certain polishing parameters (mass concentration ϱ_i, propelling pressure P_T, slurry flow f and tool height z). The sensitivity of removal to each parameter is indicated in the upper left corner of each graph.

propelling pressure P_T (upper-right), slurry flow f (lower-left) and tool height z (lower-right) are 2, 0.3 and 0.8, respectively. In this test, the operation points were 40 PSI, 5 ml/s and 400 μm, respectively. An optimum value of slurry flow (around 5 ml/s), for which the removal rate is maximized and which is chosen to operate the HyDRa tools, can be found. Removal only decreases slightly for higher or lower flow rates around this value. This is shown in the lower left panel of **Figure 9**.

In the case of tool height z, load cell force F_c can be used instead, since, as shown in [4] tool force is an approximate linear function of distance when close to the operation point, given that $z + K F_c$, with $K \sim 10$ μm/N, and hence $\delta z = \delta F_c$.

If we assume that each of these four variables is statistically independent, the total error can be added in quadrature. For example, if each parameter is controlled to ~1% precision, then the total error δD_T is $\delta D_T = \sqrt{(1.18 * \delta\rho)^2 + (2 * \delta P_T)^2 + (0.3 * \delta f)^2 + (0.8 * \delta z)^2}$, which amounts to 2.5% for this case. This means that if 500 nm of material are removed in one polishing run, considering that the parameters are controlled to 1%, the total surface error results in 12.5 nm RMS (λ/50). This constitutes a 2.5% level of nondeterminism (i.e., 97.5% determinism).

http://dx.doi.org/10.5772/intechopen.75524

4.2. Polishing example: polishing of an 84 cm mirror

As mentioned before, in order to deterministically polish large surfaces it is imperative that removal rate remains stable over extended time periods. We polished an 84-cm hyperbolic primary mirror to $\lambda/10$ RMS, 0.7 λ PV in order to prove that HyDRa could deterministically tackle meter-class optics. The polishing process is described in [12]. From the error maps that were acquired during the iterations, the level of determinism of the process could be calculated. From each map we computed a tool trajectory with distinct dwell times. The amount of removed material was calculated by subtracting the previous error map from the measured one. Then, from the obtained result after polishing, the removed material for each iteration was determined and plotted as a function of dwell time. Refer to **Figure 10**. A linear relation is expected and the deviation from this represents the level of determinism, **Figure 11**. This experiment was useful to evaluate the importance of the stability of each parameter in the level of determinism for prolonged time periods. In the figure, a larger error can be noticed for shorter dwell-times than for longer ones. This is due to CNC errors when the tool has to be quickly accelerated to obtain short dwell-times. As the mirror is progressively corrected, the surface is smoother and these changes tend to decrease.

4.3. Polishing example: PSD and polishing of Fabry-Perot etalons

Three components in the power spectral density (PSD) of the residual surface errors that are related to the footprint diameter of the tool D_H exist for any given polishing method. In the low frequency domain ($L >> D_H$), the surface errors (optical figure) are a function of the stability of the polishing parameters during the polishing run, while at the high-frequency domain ($L << D_H$), the physics of the polishing process determine surface quality (micro-roughness). In the case of mid-spatial frequencies ($L \sim D_H$) surface quality depends on the geometry and overlap of the polishing trajectories. We obtained PSD measurements as described in [4] and references therein.

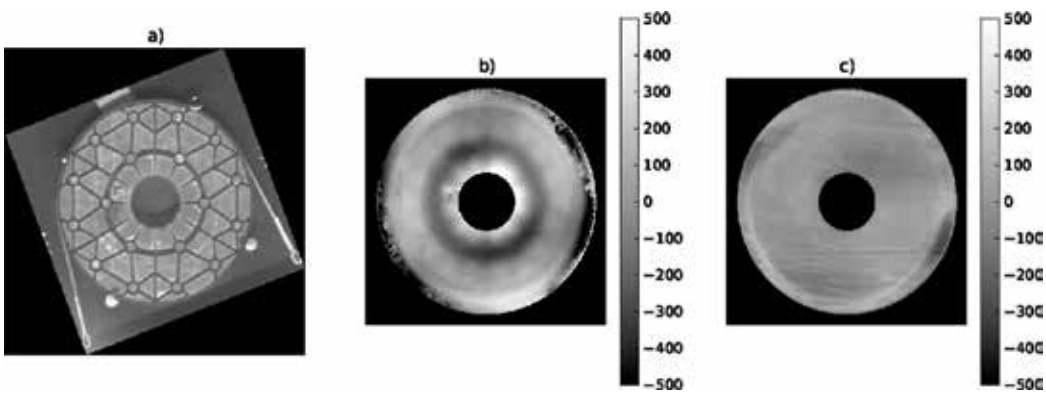

Figure 10. An 84 cm mirror with a 1 cm thick faceplate that was polished using the HyDRa system. (a) Picture of the mirror's internal back-structure. (b) Mirror prior to HyDRa finishing. The print-through left by the original lap-polishing process can be noted. (c) Mirror surface after HyDRa polishing. The polishing process entirely removed the print-through by polishing with the zero-force, error-map based process described in this chapter. Low-order Zernikes have been removed so this effect is highlighted. Z-scales are the same and are shown as vertical bars in nm.

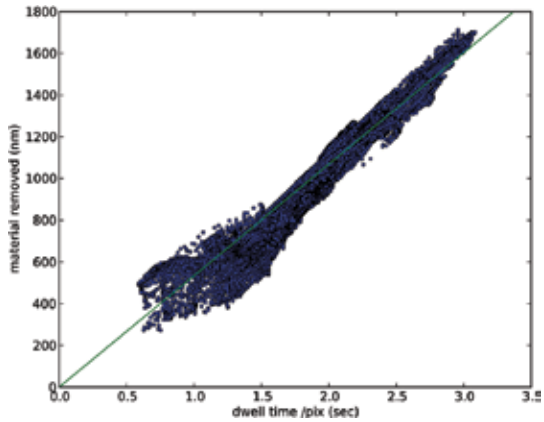

Figure 11. Total amount of material removed in the final iteration (3 runs = 30 h), as a function of dwell time in each area element of 2.6 × 2.6 mm^2 (pixel size). A linear relation at a removal rate of 13 mm^3/h (shown as a solid line) is expected for an entirely deterministic process. The true deviations from this behavior amount to 10.6%, which is the attained level of non-determinism and represents the standard deviation of the points with respect to the best-fit line.

The PSD is discussed using the results obtained while polishing four 50 mm etalon plates to better than $\lambda/100$. These 50 mm diameter water-free fused silica plates are used in an NIR scanning Fabry-Perot interferometer. These surfaces were polished using the HyDRa tool discussed in Section 4. Surface measurements were taken with a phase-shifting (PS) Fizeau interferometer in order to quantify the figure with a 180 μm pixel size projected onto the surface. A PS Linnik interferometer with 2× and 50× objectives (equivalent pixel sizes of 7.6 and 0.16 μm) was used to determine mid- and high-spatial frequencies, respectively. In **Figure 11a**, the 2-dimensional power spectrum PSD_2 vs. spatial frequency is plotted. It can be noted that three overlapping regimes exist that correspond to the series of instruments that were used to evaluate the surface quality. The integrated RMS values for each regime are 3.8, 1.5 and 2.9 nm for low-, mid- and high-spatial frequencies, respectively. The overall slope is approximately described as $f^{-2.5}$. Since in this section the physics of the HyDRa tool are described, emphasis will be made on the PSD high spatial-frequencies (micro-roughness). For lower frequencies, i.e. meter-class optics, where it is crucial to achieve a very high stability of the operational parameters, refer to [13]. **Figure 12b** shows one of four etalon plates that were polished.

Interferograms [10] showed initial figure errors that ranged between 27 and 83 nm. Using these measurements, we calculated the error maps to compute a dwell-time based raster pattern trajectory for the CNC polishing machine. An acceleration pressure of 40 PSI was chosen and tool height was controlled to achieve zero-force on the workpiece. RMS surface qualities between 3.6 and 6.8 nm were obtained after two 15 min polishing runs. The low frequency interval of the PSD shows an overall RMS fit to the desired figure of 3.8 nm, which is in accordance with the results presented in the previous section: a final surface figure quality of $>>\lambda/100$ for visible wavelengths. Sub-aperture polishing can introduce unwanted patterns associated with the polishing trajectories [14] which can occur in HyDRa polishing with a 7 mm footprint on a 40 mm sample. To minimize these mid-spatial frequencies, the tool was raster-scanned with 0.25 mm steps, which corresponds to 1/20th of the tool's footprint size.

http://dx.doi.org/10.5772/intechopen.75524

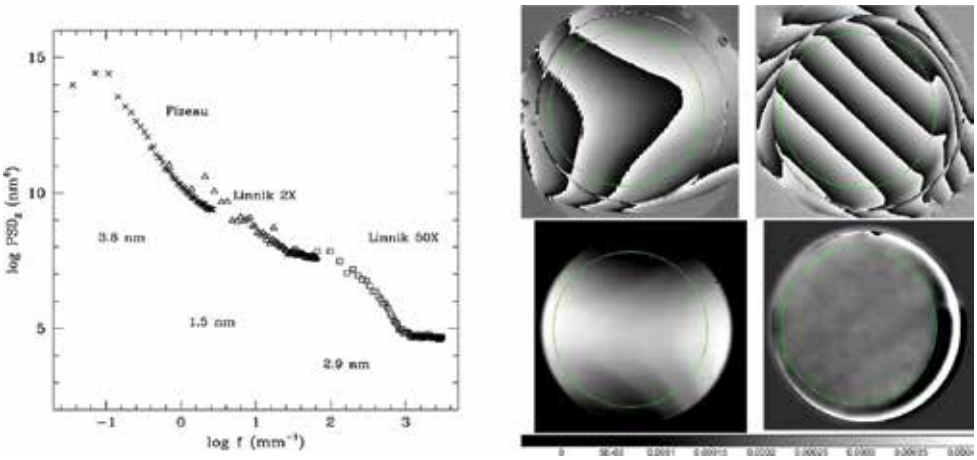

Figure 12. (a) 2-D power spectral density PSD_2 as a function of linear spatial frequency obtained with HyDRa on an etalon plate. (b) One of four etalon plates prior and after HyDRa polishing. The wrapped phase of the surface before (left) and after (right) polishing is shown in the upper images. Unwrapped phases of the original and polished surface, respectively (lower images). The inscribed green circle delimits the plate's usable region. Of the 50 mm plate diameter, only the central 40 mm were polished, since the exterior ring is used for mounting the plates. This area is indicated within the light-colored circle.

Traces of this raster pattern should have been visible in the 0.14–4 mm^{-1} frequency range on the PSD. However, no evident peaks that could have been related to grooves left by a raster pattern could be observed, and only a tiny peak corresponding to about 100 μm could be noted. This peak adds a very small fraction of a nm to the total 1.5 nm RMS of the mid-frequency band, demonstrating that "over-rastering" can be effective in minimizing mid-spatial frequencies. This represents an alternative to the approach proposed by Fähnle [15], using only one tool. A comparatively large footprint has the extra advantage of making our process insensitive to CNC positioning errors, which are two orders of magnitude smaller than the footprint size. Finally, the high-spatial frequency domain shows an RMS of close to 3 nm. Although the PSD decreases in this region, it apparently stabilizes at frequencies $>10^3$ mm^{-1} or sizes smaller than 1 μm. This number is related to the grit size that was used in this test. To sustain a decreasing PSD tendency and thus, smaller values of the high-frequency RMS, the use of smaller grit sizes is suggested. Integrating the high-frequency domain of the PSD to obtain the RMS is also equivalent to calculating the RMS directly from a 50 × 50 μm area of the micro-interferogram, according to a standard definition of micro-roughness [16]. This micro-roughness obtained with the HyDRa process (3 nm) is comparable to the roughness reported in current FJP literature [5].

Acknowledgements

This work was funded by Universidad Nacional Autónoma de México DGAPA-PAPIIT grants IN112505, IN115509, IT100216 and IT100118, as well as by Instituto de Astronomía, UNAM.

Author details

Erika Sohn*, Esteban Luna, Elfego Ruiz, Luis Salas and Joel Herrera

*Address all correspondence to: sohn@astro.unam.mx

National Autonomous University of Mexico (Universidad Nacional Autónoma de México), Institute for Astronomy, Ensenada, BC, México

References

[1] Ruiz E, Sohn E, Salas L, Luna E. Hydrodynamic radial flux tool for polishing and grinding optical and semiconductor surfaces. 2007. US Patent 7169012

[2] Ruiz E, Sohn E, Salas L, Luna E. Modulo mezclador para una herramienta hidrodinamica deterministica para el pulido pulsado de superficies opticas, y metodo para llevar a cabo el pulido pulsado. PCT Patent Application. UNAM.REG.OMPIPCT/MX/a/2016/016317

[3] Li Z, Li S, Dai Y, Peng X. Optimization and application of influence function in abrasive jet polishing. Applied Optics. 2010;**49**:2947-2953

[4] Sohn E, Ruiz E, Salas L, Luna E, Herrera J. HyDRa: Polishing with a vortex. Applied Optics. 2013;**52**:6146-6152

[5] Fähnle OW, van Brug H, Frankena H. Fluid jet polishing of optical surfaces. Applied Optics. 1998;**37**:6771-6773

[6] Shi C, Yuan J, Wu F, Wan Y. Ultra-precision figuring using submerged jet polishing. 2011. COL 092201

[7] Arnold T, Böhm G, Fechner R, Meister J, Nickel A, Frost F, Hänsel T, Schindler A. Ultra-precision surface finishing by ion beam and plasma jet techniques-status and outlook. Nuclear Instruments and Methods in Physics Research A. 2010;**616**:147-156

[8] Guo P, Fang H, Yu J. Edge effect in fluid jet polishing. Applied Optics. 2006;**45**:6729-6735

[9] Joel HV, Esteban Antolin LA, Fernando QP, Elfego Guillermo RS, Luis SC, Erika SL. Programa de Computo de Evaluacion de Error Ygeneracionde Trayectorias HYTPT. Software Copyright, Universidad Nacional Autonoma de Mexico, 03-2012-120612154800-01. Mexico: INDAUTOR; 2012

[10] Luna E, Salas L, Sohn E, Ruiz E, Nunez JM, Herrera J. Deterministic convergence in iterative phase shifting. Applied Optics. 2009;**48**:1494-1501

[11] Salas L, Luna E, Sohn E, Ruiz E, Herrera J. HyDRa: Polishing process convergence rate optimization. Applied Optics. 2013;**52**:7007-7010

[12] Sohn E, Ruiz E, Salas L, Luna E, Herrera J, Quiros F, Nunez M, Lopez E. Polishing results of an 84 cm primary mirror with HyDRa. In: Proceedings of the SPIE Optifab, TD07-17; 2011

[13] Ruiz E, Salas L, Sohn E, Luna E, Herrera J, Quiros F. HyDRa: Control of parameters for deterministic polishing. Optics Express. 2013;**21**:20334-20345

[14] Dunn CR, Walker DD. Pseudo-random tool paths for CNC sub-aperture polishing and other applications. Optics Express. 2008;**16**:18942-18949

[15] Fähnle O, Mourad S, Hauser K, Meeder M. Detection and removal of spatial mid-frequencies in sub-aperture finishing. In: OSA IODC OFT, OWE4; 2010

[16] Nunez M, Salinas J, Luna E, Salas L, Ruiz E, Sohn E, Nava A, Cruz-Gonzalez I, Martinez B. Surface roughness results using a hydrodynamic polishing tool (HyDra). SPIE. 2004;**5494**: 459-467

Section 2

Characteristics of Abrasive Tools, Materials and Machines

Chapter 6

Additives for Abrasive Materials

Artur Jamrozik, Łukasz Klapiszewski,
Beata Strzemiecka, Adam Voelkel and
Teofil Jesionowski

Additional information is available at the end of the chapter

http://dx.doi.org/10.5772/intechopen.74822

Abstract

The overarching objective of the chapter is to acquaint the readers with the topic associated with the production of abrasive tools and presentation of the most significant research results regarding the determination of the most important functional properties of selected additives (described in the literature and established on the basis of authors' own scientific experiences). The studies regarding various additives, which were characterized in detail in the literature, were mainly based on thorough physicochemical and microstructural analysis as well as the determination of basic strength and thermos-mechanic parameters. The attempt to implement alternative cross-linking agents, which would result in the limited release of volatile organic compounds, is also of great importance in terms of production of environmentally friendly final products. A subsequent aim is to attract the attention of a wide range of readers and popularize the topic associated with conventional abrasive materials and next-generation abrasive compositions.

Keywords: abrasive machining, abrasive tools, binders, functional fillers, biopolymers

1. Introduction

Modern abrasive tools used in industry are required to fulfill a number of conditions relating to quality, durability and performance. Progress in a wide range of areas related to materials engineering has made it possible to use abrasive machining in place of complex specialized processes. Recent work on the development of abrasive tools has been focused on the search for functional additives, above all to improve the functional properties of the product through the addition of fillers that primarily increase adhesion between the grains and binder. Another key issue is to obtain more environmentally friendly final products by reducing the quantities

of harmful compounds released, which can be done by using alternative cross-linking agents. In this chapter, the authors focus above all on the aforementioned questions, describing both the current state of knowledge and likely directions of future development in these areas.

2. The basics of abrasive machining

Abrasive machining is the most popular method of finishing, in which an abrasive tool (usually in the form of a grinding wheel or disk) rotating at high speed is used to remove the surface layer of a softer material. In modern industry, grinding technology is constantly being developed, in line with specific requirements applicable to a wide range of products and processes. Grinding is a key stage in the technology of production for advanced products and surface treatment in many fields of industry. The technique has many advantages over other surfacing methods.

A grinding process can be used for precise operations in the production of high-quality parts, with high accuracy and small dimensional tolerance [1]. It can be used to produce both very large machine parts and small objects such as optical instruments, elements of electronic devices, silicon wafers and rolling bearings. Another invaluable feature is the possibility of adjusting the abrasive machining process to remove large quantities of material in a short time. High grinding performance is necessary when it is required to remove a significant quantity of the machined material in a single fast operation. This applies, for example, in the cleaning of castings in foundries. Abrasive machining is also a technique used in working with very hard materials and hardened surfaces. In many cases, it is the only feasible method of finishing the surface of hard materials. The increasingly popular use of inorganic materials composed of ceramics and hard minerals with a crystalline structure enables the elimination of problems related to the finishing of surface layers. Such operations are applied, for instance, in the aerospace industry.

Figure 1 shows the grinding process in diagram form. Six basic elements may be identified: the grinding wheel, the worked material, the coolant or cutting fluid, the machine tool, the surroundings (air) and material chips.

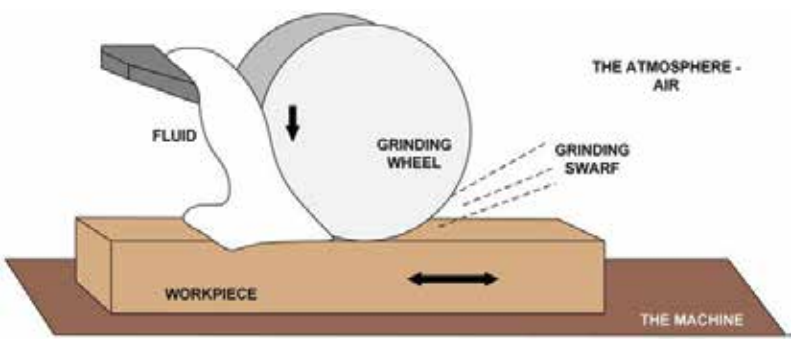

Figure 1. Simplified diagram of the grinding process, adapted from [2].

The most important elements playing a role in the process are the abrasive tool and the processed material. It is their properties that have a decisive impact on the course and effect of abrasive machining. Parameters of the grinding wheel, such the grain size and type, hardness, rigidity, and physical and chemical properties, determine its suitability for the machining of a given material. The choice of an appropriate tool is also dependent on the shape, hardness and physicochemical properties of the worked surface, and it is therefore essential to perform a full analysis of the material being processed [2, 3]. The process is also influenced by chemical factors. Atmospheric oxygen and high temperature favor the formation of oxides on the metal surface, which improves lubrication. Often, however, a coolant or cutting fluid is additionally used; this draws excess heat from the worked material and the tool, as well as reducing friction and extending the lifetime of the grinding wheel. Because of the greater stability of a cooled process, its accuracy can be improved and heat damage can be prevented. The technical condition of the machine tool is also important. Its purpose is to provide static and dynamic restriction of displacements between the tool and the worked object. The high quality and stability of the machine tool are therefore of key importance for achieving the desired tolerance in terms of geometry, dimensions and roughness. Unwanted vibrations of the machine may cause cracking and accelerated wear of the abrasive grains [4].

3. Abrasive tools

An abrasive tool is a composite material in which the continuous phase (matrix) consists of a binder, while the dispersed phase is an abrasive grain. Apart from these two basic components, additives are used in the form of fillers—active and inactive—which serve either to improve the technical parameters (active fillers) or to reduce the production cost of the tool (inactive fillers). A diagram of the structure of an abrasive tool is shown in **Figure 2**.

The industrial process of production of abrasive tools with an organic binder comprises three principal stages: mixing of components, molding, and firing (annealing) to provide cross-linking of the binder [5, 6].

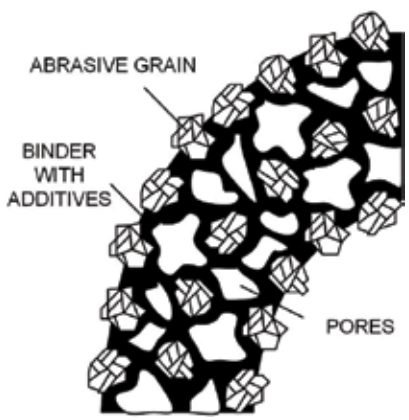

Figure 2. Simplified diagram of the structure of an abrasive tool, adapted from [2].

The mixing of the components of the tool begins with covering of the surface of the grains with liquid resin or a solvent (such as furfuryl alcohol). The uniformly moistened grains are then mixed with powdered resin, with the addition of fillers. The resulting mixture is sieved to remove lumps or agglomerates. The mixing of the components is a very important process: too loose a consistency may cause inhomogeneity of the final product, while excessive wetness will lead to difficulties in further processing.

The next important stage of the preparation of abrasive materials is molding, which may be hot or cold. Cold molding is applied in the case of tools in which pores account for at least 10% of the volume, and the pressing time does not usually exceed 1 min. Hot molding is used in the production of non-porous grinding wheels of high density. In this case, the pressing time is longer, between 20 and 60 min, and the temperature may be as high as 150°C.

The final process is the firing of the molded prefabricated elements. This is done in industrial furnaces, according to a strictly defined temperature program. The length of the program depends on the size of the tool—with larger tools, the increase in temperature should be slower and the duration of the program as a whole should be longer. In most cases, the cross-linking process lasts between 18 and 35 h, and the temperature does not exceed 200°C (or usually 180°C).

4. Abrasive materials

Abrasives are natural or synthetic materials which are used in a highly fragmented state (usually in the form of grains) as a basic component for the production of abrasive tools. Synthetic abrasive materials may be obtained by:

- electrothermal melting processes (synthetic corundums);
- in-furnace processes between solid and gas phases (silicon carbide);
- high-pressure processes (superhard materials such as synthetic diamond and cubic boron nitride);
- sintering processes (sintered corundums).

For a material to serve as an abrasive, at least one basic condition must be fulfilled. If a layer of material is to be removed by abrasion, the ratio of the hardness of the abrasive H_s to the hardness of the worked material H_m must exceed a certain minimum value. In the great majority of cases the H_s/H_m ratio is in the range 1.5–2.0. The hardness parameter is therefore the principal criterion determining whether or not a material can be classed as an abrasive. Another very important parameter is the material's melting point. Even in the early 1960s it was shown that during the grinding of metals the temperature may rise high enough to cause the metals to melt. This implies that abrasive materials should not have melting points below 1600°C. Due to this criterion, all known organic substances and almost 99% of inorganic substances are excluded from use as abrasive grains. A further surprising fact is that there is no known hard material containing more than four atoms. The most commonly used abrasives

http://dx.doi.org/10.5772/intechopen.74822

are boron carbide, silicon carbide, synthetic corundums (standard, noble and modified), diamond (mainly synthetic) and cubic boron nitride. A classification scheme for natural and synthetic abrasive materials is shown in **Figure 3**.

4.1. Silicon carbide

Silicon carbide, also known as carborundum, is a compound of carbon and silicon with the condensed formula SiC, composed of 70.045% silicon and 29.955% carbon. It was the first abrasive material to be obtained by synthesis. The compound was discovered by the Cowles brothers in 1885, when they were attempting to melt quartz in an electric arc between carbon electrodes. It was first produced industrially in 1891 in the United States, by the Carborundum Company founded by Edward G. Acheson, who was officially recognized as the originator of the method of production of SiC. Silicon carbide may crystallize either in a hexagonal arrangement (α-SiC) or in a cubic arrangement (β-SiC) [7]. The atoms in the SiC crystal lattice form two interpenetrating tetrahedral structures. SiC is resistant to the action of molten metals such as Al, Cu, Pb, Sn, Zn, Cd, although it is sensitive to Fe, Ni, Cr, Co, Mn, since these metals are capable of forming alloys with SiC. It is not damaged by acidic slags or salts, although damage

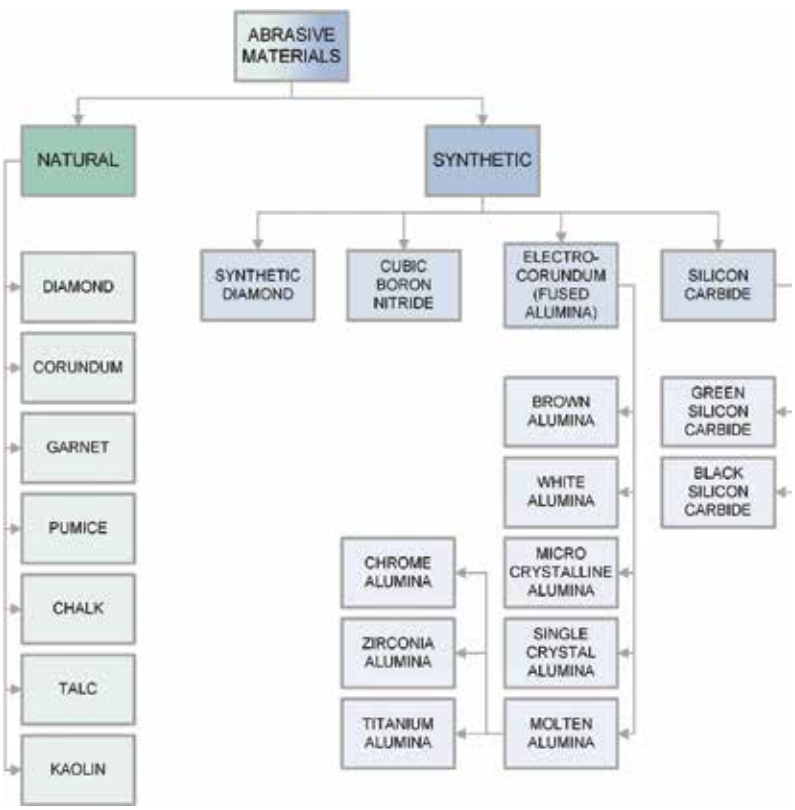

Figure 3. Classification scheme for natural and synthetic abrasive materials, based on [4].

is caused by molten alkaline compounds, including certain hydroxides and salts. Sample reactions with such compounds are given below in Eqs. (1) and (2):

$$SiC + Na_2CO_3 + 2O_2 \rightarrow Na_2SiO_3 + 2CO_2 \quad (1)$$

$$SiC + 2KOH + 2O_2 \rightarrow K_2SiO_3 + H_2O + CO_2 \quad (2)$$

At high temperatures, SiC is able to react with certain oxides (above 800°C), including CuO and PbO, and with oxides of magnesium and calcium (above 1000°C). Up to 900°C, its stability is not significantly affected by oxygen, but above that temperature, the surface is fairly strongly oxidized. The products of this reaction may be compounds such as CO, CO_2, SiO and SiO_2. The role of oxidizing agent may also be played by steam or carbon(II) oxide [8].

Silicon carbide has found many applications in various branches of industry. Because of its high mechanical strength, hardness, and ability to form relatively thick crystals, it is used chiefly as an abrasive material in abrasive tools. Somewhat less frequently, it is also used to produce fire-resistant materials such as retorts, crucibles, furnace linings, bricks, and pipes in heating systems. This is possible because of its very high thermal conductivity, resistance to sudden temperature changes, and high decomposition temperature. Silicon carbide also offers high electrical conductivity, and can thus be used in electrical engineering to produce heating elements, resistors, diodes and transistors [8, 9].

4.2. Synthetic corundum

Synthetic corundum is a material whose principal component is crystalline α-Al_2O_3 (corundum). It also contains other compounds, chiefly oxides of silicon, titanium, iron, calcium and magnesium. It can be produced in a Higgins electric arc furnace. The main raw material used to obtain ordinary synthetic corundum is bauxite. Synthetic corundum is highly resistant to the action of practically all acids and bases, both organic and inorganic. Only at high temperatures (above 900°C) does it react with molten salts of alkaline metals, producing aluminosilicates. Hydrogen causes the reduction of corundum to suboxides of aluminum, although this occurs only above 1400°C. Carbon in large excess is able to reduce Al_2O_3 at temperatures above 2000°C [10].

Synthetic corundum is used practically exclusively for the manufacture of abrasive tools. Its abrasive ability is largely dependent on the quantity of additives. Apart from standard synthetic corundum, which is produced in the largest quantities, there are also other varieties, such as [11]:

- White alumina—this material contains significantly fewer impurities than standard synthetic corundum. It is generally laid down that noble synthetic corundum should not contain less than 98.5% aluminum oxide. The principal feature of this material is the possibility of self-sharpening of the abrasive grains during operation of the tool. Synthetic corundum grains have slightly lower mechanical strength, and so when the cutting edge of the crystal becomes blunted it is chipped off the tool, thus uncovering fresh, unblunted layers. This property is particularly desirable when very accurate working is required and when the tool is to apply a low pressure on the worked material.

- Modified synthetic corundums—these are materials based on aluminum oxide, produced with the addition of compounds that are able to become incorporated into the corundum crystal lattice and form solid solutions with it. The parameters of the final product can be controlled by varying the quantity and type of modifier used. The most commonly encountered modifiers are:
  - chromium oxide (Cr_2O_3)—this modifier is used to produce pink alumina, a material that has a greater quantity of crystals than white alumina, better abrasive ability, unchanged microhardness, but slightly lower mechanical strength;
  - titania (Ti_2O_3)—this modifier produces a material with high abrasive ability and greater microhardness than white alumina;
  - zirconia (ZrO_2)—this produces a material with high ductility and mechanical strength.
- Monocorundum—this is a variety of synthetic corundum with greater grain isometry and smoother faces. It has higher microhardness and mechanical strength than other varieties of synthetic corundum. Like white alumina, it has self-sharpening capacity. Because of the lower power of grinding when monocorundum is used, the worked surface heats up to a lesser degree, and this helps to prevent defects such as cracks and burn.

4.3. Synthetic diamond

Diamond is one of the allotropic varieties of carbon, and is unquestionably the hardest mineral occurring on Earth (with a hardness of 10 on the Mohs scale). Since the quantity of mined diamond is insufficient to meet supply, leading to very high prices, it has proved necessary to develop a method for synthesizing diamond. This was achieved for the first time by the Swedish company ASEA in 1953. Since that time, annual production of artificial diamonds has been continuously increasing.

Diamond has a density of 3.5 g/cm^3. Its crystal lattice has the form of a cube containing 18 carbon atoms [12]. All of the carbon atoms in diamond are joined by high-energy covalent bonds, which give the material its exceptional hardness. Another important property is its very good thermal conductivity, which enables heat to be removed efficiently during grinding. It also has a small thermal expansion coefficient, which reduces thermal deformation of tools with diamond grains. Another very important feature is anisotropy of hardness and grindability. These parameters vary not only between different planes, but also depending on the direction in which the force acts in a given plane. The material is resistant to the action of very strong acids and their mixtures, but dissolves in molten hydroxides and salts such as $NaNO_3$ and KNO_3. It also dissolves in molten iron and its alloys above a temperature of approximately 800°C. In the presence of air it combusts at a temperature from 850 to 1000°C. Synthetic diamonds also have several features that distinguish them from natural diamonds. They are usually smaller (with an average size between 0.2 and 0.4 mm) and have different grain shapes and a rougher surface. Surface roughness, and crystal vertices with smaller angles and smaller radii of curvature are desirable features for abrasive machining. Since the content of impurities in synthetic diamonds is higher than in natural diamonds, parameters such as

mechanical strength and brittleness are somewhat inferior. Processes for synthesizing diamond are carried out at high pressures (reaching 10 GPa) and high temperatures (up to 3000°C) [13, 14].

Because of its properties, diamond is used successfully for the machining of cemented carbides and ceramic sinters, for cutting glass panels, for the working of optical glass, and for making measurements of hardness and smoothness of surfaces.

4.4. Boron nitride

Cubic boron nitride (borazon) is, like diamond, a member of the group of superhard abrasive materials. Due to the similarity of the hexagonal form of boron nitride (α-BN) to the structure of graphite, it was predicted by analogy that the compound must also exist in a diamond-like form (β-BN). This was proved in 1957 by Robert H. Wentorf, who became the first to successfully synthesize cubic boron nitride [15]. Its crystal lattice has a similar structure to diamond. Of the 18 atoms contained in a cube, four are boron atoms and the remainder nitrogen. Unlike diamond, in which all bonds are covalent, in cubic boron nitride 75% are covalent bonds and 25% ionic. This fact is significant for the mechanical properties of Borazon: its hardness and mechanical strength are lower than those of diamond. The material is exceptionally thermally stable in atmospheric air (up to 2000°C at normal pressure), being transformed back to the hexagonal form only above 2500°C. However, it is sensitive to the action of water, which at high temperature causes its decomposition into boric acid (H_3BO_3) and ammonia. This needs to be taken into account when selecting a filler whose decomposition products include H_2O. Synthesis of β-BN is carried out in the presence of catalysts (such as metallic potassium) at pressures of 6.5–9.0 GPa and temperatures of 1500–2000°C [16, 17].

Borazon is not used for the machining of such hard and brittle materials as glass, ceramics and granite, for which the use of tools based on synthetic diamonds is recommended. Nevertheless, it offers excellent performance in the working of tool steels, as well as other metals and alloys. Tools containing β-BN can produce a ground surface of high quality, thanks to low grinding power and lower temperatures of abrasive machining.

4.5. Modification of abrasive grains

Conventional abrasive materials that perform well in typical abrasive machining may prove insufficiently effective in a chemically aggressive environment or when high temperatures and grinding pressures are used. To improve the functional properties of the abrasive grain and the tools based on it, one of two routes may be selected—modification of conventional abrasives to improve their functional parameters, or the development of new methods of producing superhard materials (or improvement of existing methods) with the aim of reducing costs. Conventional abrasive materials are usually subjected to thermal or thermal-chemical processing, although more and more research is being done into the surface modification of abrasive grains.

Thermal processing is among the oldest and most popular methods of modifying raw abrasive grains. It enables reduction of the brittleness of grains, particularly those of synthetic corundum, by means of roasting at temperatures up to 2000°C. This results in the creation on the grain

surface of a fine crystalline structure, which increases its operational durability and the stability of its machining properties. Roasting is carried out to eliminate undesirable impurities: sodium and potassium 11-aluminates, described as β-Al_2O_3. The presence of aluminates in the grain may also reduce the mechanical strength of a single grain by as much as 30%. As a result of thermal processing, β-Al_2O_3 corundums in the form $K_2O{\cdot}11Al_2O_3$ transform completely into α-Al_2O_3 at a temperature of around 1520°C, while $Na_2O{\cdot}11Al_2O_3$ transforms at 1700°C. The roasting temperature may be reduced to 1300°C if gaseous hydrogen is used [18].

Abrasive grains are also modified to reduce the adverse impact of water-based coolants, which usually shorten the tool's lifetime. The reason for the reduced durability is the tendency of resins to crack under the influence of water, causing the grains to become loose and fall out. A way of preventing this may be to cover the grains with a layer of modifier containing hydrophilic and/or hydrophobic components. Hydrophilic components used include silanes containing amine, ureide, isocyanide, acetoxy and chloride groups. Hydrophobic silanes contain mainly phenyl, vinyl, methacrylic or epoxide groups. Surface modification using a dual-component silane-based modifier brings several undoubted benefits. The hydrophilic component covers the entire surface well, at the same time facilitating its moistening. The hydrophobic component may be applied together with the first component or as a separate layer, demonstrating the ability to bond with both the covered grains and the resin binder. Such modification prevents water-based coolants from penetrating to the interior of the tool, and thereby extends the tool lifetime, improves the material removal rate (MRR) and enhances the overall quality of the finished surface [19].

The development of innovative abrasives involves not only the modification of conventional materials but also the creation of new methods for producing superhard materials (superabrasives). The production of such materials, primarily synthetic diamond and cubic boron nitride, originally required high temperatures and very high pressures. To convert graphite to diamond, a pressure of around 13 GPa and a temperature of 3000°C are required. In view of the difficulty of providing such extreme conditions, other methods are used, such as solvent catalyst synthesis. This method makes it possible to reduce the high activation energy and the required pressure and temperature by a half [20]. The catalysts used in the process dissolve graphite, enabling the carbon atoms to move and to adopt the positions appropriate to diamond. Commonly used metal catalysts include nickel, iron and cobalt, as well as rhodium, palladium, platinum and others [21]. Diamond may also be obtained using non-metal catalysts, such as hydroxides and carbonate salts [22].

Of increasing importance, however, are metastable processes of diamond synthesis. An undoubted advantage of these is the relatively simple equipment required to produce diamond film and the high purity and homogeneity of the product [23]. In such processes, carbon in the form of diamond is precipitated from a mixture of hydrocarbon and hydrogen [24]. Several techniques of chemical vapor deposition (CVD) are currently applied, using microwave plasma [25], plasma jet [26], arc discharge [27] and laminar and turbulent oxy-acetylene combustion [28, 29] (see **Figure 4**). These methods require the use of high pressures and gases of relatively high purity. The gas mixture may consist of hydrogen, argon, oxygen and methane—the composition depends on the desired size of the diamond grains [30–32]. Methods have also been developed which reduce the use of harmful and expensive gases, including a

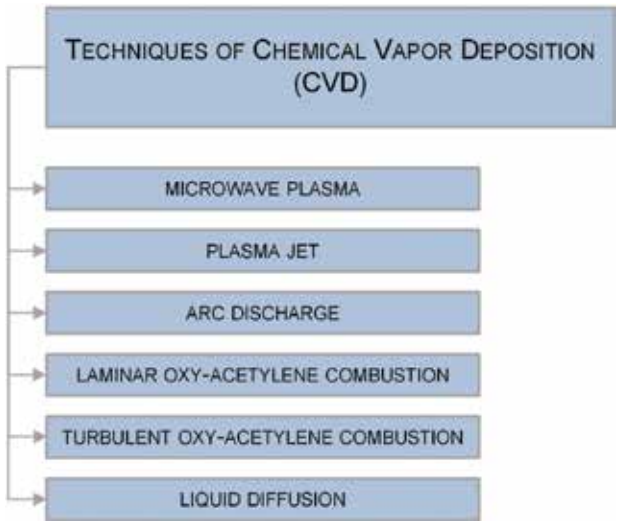

Figure 4. Techniques of chemical vapor deposition (CVD).

liquid diffusion method with methanol as a source of carbon, carried out in an argon atmosphere under microwave energy. This method can produce a film with a diamond content of approximately 75%, while reducing the risk associated with the use of explosive gases such as hydrogen and methane [33].

Another interesting study concerns the obtaining of single-phase nano-polycrystalline diamonds using direct conversion from graphite under high temperature and ultra-high pressure. This product offers very high mechanical strength, and does not exhibit anisotropy of its mechanical properties. Moreover, such a material does not require any additional binders, and this fact also has a positive effect on its thermal stability [34].

5. Binders

In terms of quantity, the binder is the second most significant component of an abrasive tool. It serves as a continuous phase that binds the single grains into a compact, strong composite. Abrasive composites may be based on organic binders (such as rubber, organic resins and polyurethanes) or inorganic binders (ceramics, magnesite, sintered and galvanic metals). Inorganic bonds with glass-like or vitreous structures are mostly used in grinding wheels with fine grain sizes for precision operations, while resin-bonded tools are applied in heavy metal removal processes. Ceramic and resin binders are the most commonly used types. Ceramic binders are thermally and chemically resistant and also ensure the repeatability of grinding processes. Disadvantages include their brittleness and the need to apply very high temperatures when making tools from them. Technologies for producing ceramic abrasive tools are being constantly improved. A recently introduced technology is used to obtain tools bonded with Vitrium 3 [35], which enables a smaller quantity of binder to be used, increasing the tool's

http://dx.doi.org/10.5772/intechopen.74822

performance and also making it more porous, which enables better cooling and thus less likelihood of burning of the machined surface. Ceramic binders are used to bond superhard abrasives such as diamond and cBN. For corundum abrasives, the less expensive resin binders are more often used. These are produced with the consumption of much less energy than in the case of ceramic binders: the semi-finished product is heated at 200°C, compared with 1200°C for ceramic binders. Resin binders also offer high strength and elasticity, and give the abrasive tool good properties for polishing the ground surface. Grinding wheels with resin binders are used primarily for the cutting of materials and for rough grinding operations at high machining speeds (45–100 m/s).

A disadvantage of binders of this type is their sensitivity to the action of coolants containing bases, and to high temperature. Resin binders are most commonly based on phenol formaldehyde resins.

Phenolic resins, also called phenoplasts, have a range of properties that enable them to be used in a fairly wide range of applications. They are formed by a polycondensation reaction of phenols with formaldehyde. There are two distinct types of phenol formaldehyde resins: novolacs and resoles. The processes by which they are obtained are depicted in **Figure 5**. They differ in terms of the molar ratios of reactants and the environment in which the reaction takes place. Hardening is also carried out by a different method in each case: resole is heat-hardened, whereas novolac is a thermoplastic and must be hardened using a cross-linking agent—most commonly hexamethylenetetramine (urotropine), with the further addition of HCHO (usually in the form of paraformaldehyde).

Due to the harmful properties of formaldehyde and of the ammonia emitted when novolac is cross-linked using urotropine, new hardening agents are being sought (although up to date urotropine is still the cross-linking agent most commonly used in industry). By means of modification of novolac, for example by the introduction of epoxide and amine groups [36], it is possible to obtain resins with lower levels of emission of low-molecular-weight compounds and resulting binders with greater strength and chemical and thermal resistance.

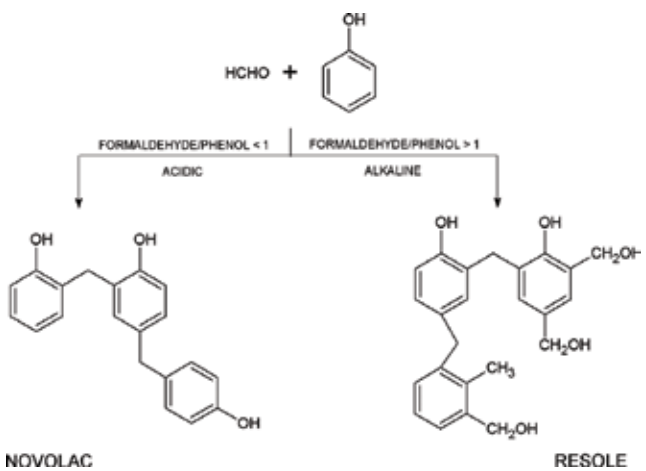

Figure 5. Reactions leading to phenol formaldehyde resins in novolac and resole form, adapted from [5].

There has been increasing interest in recent years in the use of natural raw materials to produce phenolic resins [37, 38]. However, there is still only a limited number of reports on industrial applications of abrasives containing phenolic resins based on natural materials such as lignin, which currently represents a new trend in the abrasive tools industry [39]. There would therefore appear to be a need for continued intensive research to achieve further improvements in this area, related to elimination of the existing defects of binders based on resins with the partial use of phenols of natural origin. These defects include the low reactivity of derivatives of phenol from natural sources, processing problems with abrasive articles made using them, and the inferior mechanical properties compared with tools based on traditional phenolic resins. Lignin-based resins have already been successfully used in certain demanding applications, including brake blocks [40].

A very interesting alternative to binders based on phenolic resins are benzoxazine resins. These products have a wide range of mechanical and physical properties that can be tailored to various needs. Their main advantage is the absence of emissions of low-molecular-weight compounds during their cross-linking. There is also no need to add cross-linking agents. It is also noteworthy that they are produced using phenol and its derivatives, which provides the possibility of alternative use of products of natural origin. However, it was only in 2016 that benzoxazine resins were first synthesized from lignin [41]. This area of research thus remains ripe for development.

6. Fillers

Fillers are used as an auxiliary materials in the production of abrasive tools. They are usually inorganic compounds that demonstrate affinity toward both the abrasive grains and the binder holding the grains together in the substance of the tool [42]. There are several kinds of fillers, and they can be classified according to the mechanism of their action (see **Table 1**) [43].

Possible mechanism	A description of the action
I	The first mechanism involves thermal decomposition of the filler, which leads to the emission of low-molecular-weight products (such as H_2O, HF or HCl). These reactions are endothermic, which means that the tool can operate at a lower temperature
II	In the second mechanism, the action of the filler results from its reaction with the worked surface, which causes corrosion of freshly removed fragments of metal. This prevents the chips from reacting with the abrasive and fusing back onto the worked object
III	The third mechanism is explained by the melting of the auxiliary material due to the heat produced by grinding, which leads to reduced friction (self-lubrication of the tool) and thus allows the tool to operate at a lower temperature
IV	In the final mechanism, fillers react with the machined surface. The reaction causes cracks to appear on the metal surface, making machining easier

Table 1. Examples of the mechanisms of action of different kinds of fillers.

Fillers used in a tool perform several extremely important functions:

- they increase the tool's mechanical strength by improving the adhesion of grains to the binder;
- they protect the abrasive grains from the harmful atmosphere existing in the furnace during firing;
- they prevent thermal degradation of the resin on the contact surface between grain and binder;
- they cool the tool while it is operating.

Fillers are added to abrasive composites for several reasons. Most commonly, they serve merely to reduce the production cost of the tool, through the addition of an inactive filler, usually soot, cooper slag or iron oxide. It is preferable, however, to use active fillers, which serve above all to draw heat from the process, as a result of which they undergo thermal decomposition and prevent melting of the resin binder [44, 45]. Conventional active fillers have certain drawbacks, the chief of which is the emission of harmful gases due to their decomposition. Popular fillers such as pyrite (FeS_2) and lithopone ($ZnS + BaSO_4$) emit sulfur when they decompose, while potassium fluoroborate (KBF_4), cryolite (Na_3AlF_6) and potassium hexafluoroaluminate (K_3AlF_6) emit fluorine and its compounds. Hence, at the present time, fillers are being sought that will combine desirable properties with limited adverse impact on the environment. The division into active and inactive fillers is shown in **Figure 6**.

It is worth mentioning that aluminosilicates such as natural zeolite have been successfully used as functional and ecological fillers [46, 47]. This is a cheap and environmentally friendly raw material, which also has a favorable effect on the thermomechanical properties of prototypical

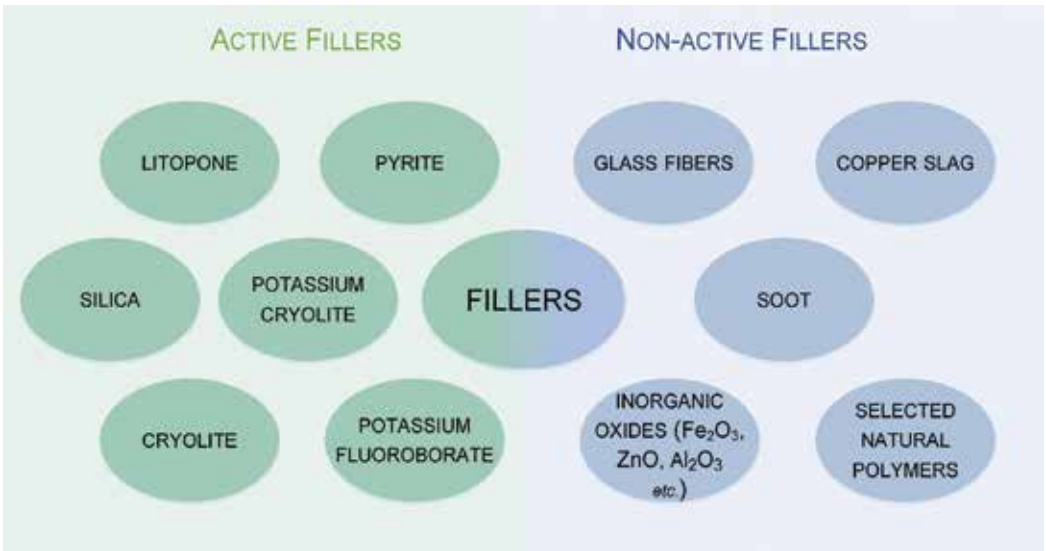

Figure 6. The division into active and inactive fillers.

resin composites used in the production of bonded abrasive tools [48]. Moreover, zeolites may accelerate the cross-linking of phenol resins [48]. Since they retain a large quantity of water in their structure [49], they should not be used for superhard abrasive tools based on cBN; since at the high working temperature of such a tool and in the presence of water emitted by the zeolites, decomposition of cBN may occur.

An interesting raw material that may be used as a filler is lignin, which offers many advantages—it is of natural origin, it is renewable, and it is produced in large quantities as a by-product of the process of delignification of wood [50]. Unfortunately, due to its characteristic structure, lignin in raw state is not able to provide the required properties [51]. Its properties can be improved in two ways. One is the activation of raw lignin via its oxidation, which enables the formation of new, more active functional groups capable of reacting with the resin binder [52]. Another way to improve the thermal stability of lignin preparations is to combine them with appropriate inorganic oxides, so as to form an organic-inorganic hybrid material [53]. Addition of these innovative materials makes it possible, above all, to improve the mechanical strength and thermal stability of the final abrasive composite.

The search for new, functional fillers, which increasingly often are hybrid materials, is intensifying at the present time. The primary goal is to produce systems with improved properties, having a decisive impact on the abrasive tool that is the final product. The combination of organic polymers or biopolymers with inorganic oxides makes it possible to obtain modern additives with previously unencountered properties. Another important factor is the cost associated with the production of abrasive materials. These can be kept relatively low by using waste products for this purpose, including wastes of natural origin.

7. Conclusions

Abrasive technology has been developed for centuries, but there still exists a wide range of opportunities for its continued improvement. In view of the development of manufacturing industry and the dynamic state of the global economy, modern abrasive tools are becoming subject to ever more rigorous requirements as regards quality, performance, durability, cost, and impact on the environment. Future development will involve further work on each of the main components of abrasive composites, as all of these have a significant effect on the functional properties of the final product. Present trends indicate that the search will continue for new, cost-effective ways of obtaining polycrystalline abrasive materials on the nanoscale, with previously unobtainable strength properties. Attempts will also no doubt be made to modify the surface of grains with organic compounds to produce on the surface functional groups capable of reacting with the groups present in resin binders. The development of binders, in turn, will be focused on reducing their toxicity by limiting the quantities of compounds emitted during the manufacture and operation of tools, while at the same time improving their mechanical properties. An excellent alternative to traditional resin binders would appear to be benzoxazine resins, which offer very interesting physicochemical parameters, low toxicity and wide possibilities of molecular design. It is equally important to seek new functional fillers for abrasive tools, especially organic-inorganic hybrid materials. This

vision is particularly attractive in view of the possibility of producing and using many different systems combining inorganic oxides with natural polymers, which in many respects appears to be an innovative and beneficial solution. In short, the further development of abrasive composites will be driven by the concept of sustainable development, involving the improvement of functional properties while at the same time caring for the environment.

Acknowledgements

This work was supported by the National Science Centre Poland under research project no. UMO-2017/25/N/ST8/00401 and PUT research grant no. 03/32/DSPB/0806.

Conflict of interest

The authors declare no conflict of interest.

Author details

Artur Jamrozik, Łukasz Klapiszewski*, Beata Strzemiecka, Adam Voelkel and Teofil Jesionowski

*Address all correspondence to: lukasz.klapiszewski@put.poznan.pl

Faculty of Chemical Technology, Institute of Chemical Technology and Engineering, Poznan University of Technology, Poznan, Poland

References

[1] Malkin S, Guo C. Grinding Technology: Theory and Application of Machining with Abrasives. 2nd ed. New York: Industrial Press Inc.; 2008. ISBN-13: 978-0831132477

[2] Marinescu ID, Hitchiner M, Uhlmann E, Rowe WB, Inasaki I. Handbook of Machining with Grinding Wheels. 2nd ed. Boca Raton: CRC Press; 2016. ISBN: 9781482206685

[3] Bhushan B. Modern Tribology Handbook. Boca Raton: CRC Press; 2000. ISBN: 978084938 4035

[4] Jackson MJ, Davim JP. Machining with Abrasives. New York: Springer; 2011. ISBN: 978-1-4419-7302-3

[5] Gardziella A, Pilato LA, Knop A. Phenolic Resins: Chemistry, Applications, Standardization, Safety and Ecology. 2nd ed. Berlin: Springer; 2000. ISBN: 978-3-662-04101-7

[6] Jacobs FB. Abrasives and Abrasive Wheels, Their Nature, Manufacture and Use: A Complete Treatise on the Manufacture and Practical Use of Abrasives, Abrasive Wheels and Grinding Operations. London: Forgotten Books; 2017. ISBN-13: 978-0331571110

[7] Harris GL. Properties of Silicon Carbide. London: Inst of Engineering & Technology; 1995. ISBN-13: 978-0863415548

[8] Jayant Baliga B. Silicon Carbide Power Devices. London: World Scientific Pub. Co. Inc.; 2006. ISBN-13: 978-9812566058

[9] Yang D, Yu Y, Zhao X, Song Y, Lopez-Honorato E, Xiao P, Lai D. Fabrication of silicon carbide (SiC) coatings from pyrolysis of polycarbosilane/aluminum. Journal of Inorganic and Organometallic Polymers. 2011;**21**:534-540. DOI: 10.1007/s10904-011-9481-y

[10] Wellborn W. Modern abrasive recipes. Cutting Tool Engineering. 1994;**4**:42-47

[11] Linke B. Life Cycle and Sustainability of Abrasive Tools. Cham: Springer International Publishing; 2016. DOI: 10.1007/978-3-319-28346-3

[12] Field JE. The Properties of Diamond. London, New York: Academic Press; 1979. ISBN: 0122553500 9780122553509

[13] Field JE. Diamond—Properties and Definitions. Cambridge: Cavendish Laboratory; 1983

[14] Zaitsev AM. Optical Properties of Diamond—A Data Handbook. Berlin Heidelberg: Springer-Verlag; 2001. DOI: 10.1007/978-3-662-04548-0

[15] Bello I. Diamond and Cubic boron nitride: Synthesis and electronic applications. In: Proceedings of the Fourth International Conference on Advanced Semiconductor Devices and Microsystem "ASDAM '02"; 14–16 October 2002; Smolnice Castle, Slovakia: IEEE; 2002, p. 1-11

[16] Hitchiner MP, Wilks J. Some remarks on the chemical wear of diamond and CBN during turning and grinding. Wear. 1987;**114**:327-338. DOI: 10.1016/0043-1648(87)90120-7

[17] Bello I, Chong YM, Leung KM, Chan CY, Ma KL, Zhang WJ, Lee ST, Layyous A. Cubic boron nitride films for industrial applications. Diamond and Related Materials. 2005;**14**: 1784-1790. DOI: 10.1016/j.diamond.2005.09.003

[18] Souza Santos P, Souza Santos H, Toledo SP. Standard transition aluminas. Electron microscopy studies. Materials Research. 2000;**3**:104-114. DOI: 10.1590/S1516-14392000000400003

[19] US Patent US 80214492011

[20] Davies G. Charge states of the vacancy in diamond. Nature. 1977;**269**:498-500. DOI: 10.1038/269498a0

[21] Wakatsuki M. New catalysts for synthesis of diamond. Japanese Journal of Applied Physics. 1966;**5**:337-340. DOI: 10.1143/JJAP.5.337

[22] Akaishi M. New non metallic catalysts for the synthesis of high pressure, high temperature diamond. Diamond and Related Materials. 1993;**2**:183-189. DOI: 10.1016/0925-9635(93)90050-C

[23] Tong SL, Lin Z, Jiang X. CVD diamond films: Nucleation and growth. Materials Science & Engineering R: Reports. 1999;**25**:123-154. DOI: 10.1016/S0927-796X(99)00003-0

[24] Das D, Singh RN. A review of nucleation, growth and low temperature synthesis of diamond thin films. International Materials Review. 2007;**52**:29-64. DOI: 10.1179/174328007X160245

[25] Kamo M, Sato Y, Matsumoto S, Setaka N. Diamond synthesis from gas phase by decomposition of methane in microwave plasma. Journal of Crystal Growth. 1983;**62**:642-644. DOI: 10.1016/0022-0248(83)90411-6

[26] Kurihara K, Sasaki M, Kawanda M, Koshino N. High rate of synthesis of diamond by dc plasma jet chemical vapour deposition. Applied Physics Letters. 1988;**52**:437-438. DOI: 10.1063/1.99435

[27] Akatsuka F, Hirose Y, Komaki K. Rapid growth of diamond films using arc discharge technique. Japanese Journal of Applied Physics. 1988;**27**:L1600-L1602. DOI: 10.1143/JJAP.27.L1600

[28] Snail KA, Freitas JA, Vold CL, Hanssen LM. In: Proceedings of the 2nd International Symposium on Diamond Materials; May 1991; Washington, USA. Electrochemical Society; 1991. p. 91

[29] Snail KA, Vold CL, Marks CM, Freitas JA. High temperature epitaxy of diamond in turbulent flame. Diamond and Related Materials. 1992;**1**:180-186. DOI: 10.1016/0925-9635(92)90021-F

[30] Lin CR, Liao WH, Wei DH. Improvement on the synthesis technique of ultrananocrystalline diamond films by using microwave plasma jet chemical vapor deposition. Journal of Crystal Growth. 2011;**326**:212-217. DOI: 10.1016/j.jcrysgro.2011.01.100

[31] Vaitkuviene A, McDonald M, Vahidpour F. Impact of differently modified nanocrystalline diamond on the growth of neuroblastoma cells. New Biotechnology. 2015;**32**:7-12. DOI: 10.1016/j.nbt.2014.06.008

[32] Vikharev AL, Gorbachev AM, Kozlov AV. Microcrystalline diamond growth in presence of argon in millimeter-wave plasma-assisted CVD reactor. Diamond and Related Materials. 2008;**17**:1055-1061. DOI: 10.1016/j.diamond.2008.01.050

[33] Yang L, Jiang C, Guo S, Zhang L, Gao J, Peng J, Hu T, Wang L. Novel diamond films synthesis strategy: Methanol and argon atmosphere by microwave plasma CVD method without hydrogen. Nanoscale Research Letters. 2016;**11**:415-420. DOI: 10.1186/s11671-016-1628-x

[34] Sumiza H. Novel development of high-pressure synthetic diamonds "ultra-hard nanopolycrystalline diamonds". SEI Technical Review. 2012;**74**:15-22

[35] Vitrium3—White Paper [Internet]. 2016. Available from: http://www.saint-gobain-abrasives.com/en-us/resources/expertise/vitrium3-white-paper [Accessed: 2018-01-24]

[36] EPON™ Resin 160 produced by HexionTM, Technical Data Sheet [Internet]. Available from: http://www.hexion.com/en-US/product/epon-resin-160 [Accessed: 2018-01-13]

[37] Yoshida C, Okabe K, Yao T, Shiraishi N, Oya A. Preparation of carbon fibers from biomass-based phenol-formaldehyde resin. Journal of Materials Science. 2005;**40**:335-339. DOI: 10.1007/s10853-005-6087-1

[38] Srivastava R, Srivastava D. Studies on the synthesis and curing of thermosetting novolac resin using renewable resource material. International Journal of ChemTech Research. 2013;**5**:2575-2581

[39] Pilato LA. Phenolic Resins: A Century of Progress. Berlin: Springer; 2010. ISBN: 978-3-642-04714-5

[40] Silveira JVW, Bittencourt E, Aguila ZJ. Thermal and dynamic investigations on brake pad composites produced with lignin-phenolformaldehyde resin. Materials Science Forum. 2013;**730–732**:390-394. DOI: 10.4028/www.scientific.net/MSF.730-732.390

[41] Abarro GJ, Saake B, Lehnen R, Podschun J, Ishida H. Benzoxazines with enhanced thermal stability from phenolated organosolv lignin. RSC Advances. 2016;**6**:107689-107698. DOI: 10.1039/C6RA22334F

[42] Wypych G. Handbook of Fillers. 4th ed. Toronto: ChemTec Publishing; 2016 978-1-895198-91-1

[43] European Patent EP 2177318

[44] Jurga J, Voelkel A, Strzemiecka B. Application of different analytical methods used in the study of the cross-linking of resins in intermediate-product used in manufacturing of abrasive articles. Journal of Applied Polymer Science. 2009;**112**:3305-3312. DOI: 10.1002/app.29840

[45] Laza JM, Alonso J, Vilas JL, Rodríguez M, León LM, Gondra K. Influence of fillers on the properties of a phenolic resin cured in acidic medium. Journal of Applied Polymer Science. 2008;**108**:387-392. DOI: 10.1002/app.26816

[46] Strzemiecka B, Heberger K, Voelkel A. Similarity and grouping of perlite and zeolite abrasive fillers: A replacement test. Journal of Applied Polymer Science. 2013;**127**:3839-3847. DOI: 10.1002/app.37695

[47] Strzemiecka B, Voelkel A, Chmielewska D, Sterzyński T. Influence of different fillers on phenolic resin abrasive composites. Comparison of inverse gas chromatographic and dynamic mechanical-thermal analysis characteristics. International Journal of Adhesion and Adhesives. 2014;**51**:81-86. DOI: 10.1016/j.ijadhadh.2014.02.013

[48] Strzemiecka B, Voelkel A, Hinz M, Rogozik M. Application of inverse gas chromatography in physicochemical characterization of phenolic resin adhesives. Journal of Chromatography. A. 2014;**1368**:199-203. DOI: 10.1016/j.chroma.2014.09.069

[49] Strzemiecka B, Kołodziejek J, Kasperkowiak M, Voelkel A. Influence of relative humidity on the properties of examined materials by means of inverse gas chromatography. Journal of Chromatography. A. 2013;**1271**:201-206. DOI: 10.1016/j.chroma.2012.11.037

[50] Biermann CJ. Handbook of Pulping and Papermaking. 2nd ed. London: Academic Press; 1996. ISBN: 978-0-12-097362-0

[51] El Mansouri N-E, Pizzi A, Salvado J. Lignin-based wood panel adhesives without formaldehyde. Holz als Roh- und Werkstoff. 2007;**65**:65-70. DOI: 10.1007/s00107-006-0130-z

[52] Klapiszewski Ł, Jamrozik A, Strzemiecka B, Matykiewicz D, Voelkel A, Jesionowski T. Activation of magnesium lignosulfonate and kraft lignin: Influence on the properties of phenolic resin-based composites for potential applications in abrasive materials. International Journal of Molecular Sciences. 2017;**18**:1224-1243. DOI: 10.3390/ijms18061224

[53] Klapiszewski Ł, Jamrozik A, Strzemiecka B, Borek B, Matykiewicz D, Voelkel A, Koltsov I, Jesionowski T. Characteristics of multifunctional, eco-friendly lignin-Al_2O_3 hybrid fillers and their influence on the properties of composites for abrasive tools. Molecules. 2017;**22**:1920-1939. DOI: 10.3390/molecules22111920

Chapter 7

Tuning the Morphology and Surface Property of Mineral Particles by Grinding Media

Zhiyong Gao and Chengwei Li

Additional information is available at the end of the chapter

http://dx.doi.org/10.5772/intechopen.74836

Abstract

Grinding of minerals for particle size reduction and liberation is a prerequisite for successful mineral flotation separation and powder modification. Different grinding media produce mineral particles with different physical morphology and surface chemistry properties. Different mill particles expose different proportions of cleavage surfaces which lead to different shape indexes and different surface reactivities to organics, such as collector. Rod mill produces scheelite particles with a higher exposure of more reactive {101} surface that are beneficial for a stronger interaction with collector. More exposure of {101} surface also causes the rod mill particles to possess such values as larger elongation and flatness that are essential for particles attachment to air bubbles by shortening the induction time. The rod mill particles have a lower critical surface tension, greater hydrophobicity and a better flotation recovery when treated with the collector. In addition, the rod mill particles with a narrow particle size distribution have a smaller specific surface area, so the full monolayer adsorption of the collector on their surfaces can be achieved at a relatively lower concentration. These findings will help establish the relation between the particle surface physicochemistry and wettability, hence providing valuable guidance for the optimization of flotation separation and powder modification technology.

Keywords: grinding media, morphology, wettability, reactivity, flotation, surface modification, scheelite

1. Introduction

Size reduction by mechanical comminution (i.e., crushing and grinding) is an indispensable process in many fields, such as the field of mineral processing, metallurgical, power and chemical industries [1], etc. However, this process consumes such a considerable amount of energy that it becomes the heaviest energy consumption unit in many industries [2]. For

example, in the field of mineral processing, comminution of run-of-mine consumes 70% of the total energy [3]. Therefore, optimizing the process of crushing and grinding is of great significance for achieving energy-saving and cost-reducing in minerals processing.

Mineral processing is a predominant technology used to fulfill the enrichment of valuable minerals from coexisted (undesired) gangue minerals and then, provides raw materials for the following metallurgical operation [4]. During this process, minerals first go through crushing and grinding for particle size reduction and sufficient mineral liberation before separation operations [5, 6]. Conventionally speaking, there are primarily two ways for separation: gravity separation and flotation separation. Gravity separation is used when both the valuable minerals and gangues are coarsely grained in ore deposits and the density between them features a significant distinction. In this process, the rod mill is commonly employed to break preferentially coarser particles, produce more uniform particle products and avoid overgrinding [7–9]. In gravity separation, the valuable minerals and gangues have different movement speeds and trajectories in the equipment, such as jigging, dense medium cyclone and centrifuge, thus leading to the successful separation. But with the ever increasing demands for processing the low-grade, fine-grained and disseminated ores, the flotation separation has been increasingly employed as a complementary or substitute method for gravity separation [10]. Flotation is a separation method based on the differences in wettability at particle surfaces after being treated with surfactants, during which sufficient liberation of the fine-grained minerals is the key factor for a successful separation. Compared with the rod mill under the same energy consumption, the ball mill is more beneficial for the production of finer particle products [11].

Different grinding methods possess different breakage mechanisms and accordingly, produce particles with different shapes or morphologies [12]. For the rod mill, line loads are exerted on the mineral particles, and the predominant breaking forces are the impact which can produce particles with sharp edges [13]. In contrast, the ball mill imposes point loads on the particles, so that the main forces are abrasion and chipping which can trim off the corners and sharp edges of particles efficiently [14, 15]. Mill particles with different shapes always exhibit different gravity or flotation behavior. The research group led by Yekeler from Cumhuriyet University found that compared with the ball mill particles, the rod mill ones provide a more elongated and smoother surface, thus performing a better floatability [16–19]. This phenomenon can be explained by the higher attachment efficiency of the elongated particle to the air bubbles through accelerating the rupture of the surrounding liquid film and shortening the induction time [20, 21]. Recently, Xia [22] has systematically reviewed the role of particle shape in mineral floatability, and concluded that the particles with shape far away from sphere own an increasing surface hydrophobicity and floatability. Moreover, the coverage of collector on irregular particle surface is conducive to the stability of the three-phrase contact line and hence increasing the flotation recovery.

The grinding environments also play a considerable role on the surface properties and flotation behavior of the ground particles. Feng and Alrichv [23] indicated that more micro - structural defects found in the dry ground samples can serve as the active sites to accelerate the adsorption of collector, while smoother and cleaner surfaces are found in the wet mill particles. Recently, the spodumene samples were also ground using dry and wet mills by Zhu

et al. [24] and Xu et al. [25]. The separate research groups independently found that more {110} and {100} surfaces are exposed for the wet mill particles while more {010} exposed for the dry mill ones. The wet mill particles are more hydrophobic when treated with collector and accordingly, obtain a better flotation recovery.

Scheelite $CaWO_4$ is the most prominent mineral source for tungsten which is of great importance in many other fields like electronic information, aerospace and military [26]. The above two separation methods have been used to enrich the scheelite from gangue minerals for a long time [27–29]. In Xingluokeng Tungsten Ore (Fujian, China), the ore deposit mainly belongs to the scheelite-feldspar-quartz type. Because of the coarsely grained characteristics and distinct density differences between scheelite and gangues, the rod mill has been employed to achieve mineral liberation prior to the gravity separation. However, with the continuous consumption of the high-grade ore, the scheelite has become much more fine-grained. Thus, the gravity separation was proved to be less efficient in recent years, and a regrinding-flotation process after gravity separation was investigated to improve the comprehensive recovery of scheelite.

Unlike the Xingluokeng ore, the scheelite deposit in Shizhuyuan Ore (Hunan, China) mainly belongs to the scheelite-calcite-fluorite-grossularite type with a very fine-grained characteristic. Furthermore, due to the similar specific gravity between sheelite and grossularite, and similar physicochemical properties between scheelite and calcite and fluorite [30], the flotation method is therefore, the dominant process to recover the sheelite. Naturally, the ball mill is used to liberate the scheelite particles [31].

In the past 2 years, our group prepared a novel metal-organic complex, i.e., lead- benzohydroxamic acid (BHA) complex. This complex, as a collector, was successfully applied to the selective flotation of scheelite from gangues in Shizhuyuan Ore, leading to a significant increase in the comprehensive recovery of WO_3 by 8-10% [32, 33]. However, when we used this complex in Xingluokeng Ore, some obvious differences in the flotation behavior and recovery of scheelite were observed compared with those in Shizhuyuan Ore. We thought that the differences were mainly caused by the different mill media and ore type.

In this chapter, the surface properties and flotation behavior of scheelite particles produced by ball and rod mills were studied through single mineral flotation experiment, scanning electron microscopy (SEM) observation, wettability measurement, and X-ray diffraction (XRD) test. These results will help establish the relation between the particle surface properties and the grinding media, hence providing guidance for optimizing flotation separation.

2. Experimental procedures

2.1. Materials and reagents

Representative samples of pure scheelite crystals were collected from the Huili mine, Sichuan, China. The chemical analysis of samples confirmed that the scheelite samples were over 98% pure.

Chemically pure benzohydroxamic acid (BHA) (above 98% purity) was purchased from Tokyo Chemical Industry. Lead nitrate with 99% purity was purchased from Tianjin Kermil Chemical Reagents. The pH of solution was adjusted with sodium hydroxide (NaOH) or hydrochloric acid (HCl) stock solutions. Deionized (DI) water with a resistivity of over 18 MΩ × cm was used throughout the experiments.

2.2. Methods

2.2.1. Grinding tests

Representative samples of pure scheelite crystal samples (**Figure 1a**) were first crushed from a diameter of 40–5 mm using the JC6 jaw crusher (Beijing Grinder Instrument Equipment Co., Ltd.). Then the crushed samples were ground by ball and rod mills. The grinding tests were operated using the 146 × 200 mm laboratory size mill (**Figure 1b**).

For the ball mill, corundum balls with diameters of 21, 16 and 12 mm were used as grinding media. For the rod mill, corundum rods of 15 and 11 mm in diameter and 15 cm in length were used. Scheelite samples with a total mass of 200 g were fed into the mill and ground for 30 s each run to prevent over-grinding. After a run, the ground products were sieved by a standard screen with a pore size of 74 μm (200 mesh). The oversize particles were returned to the mill for

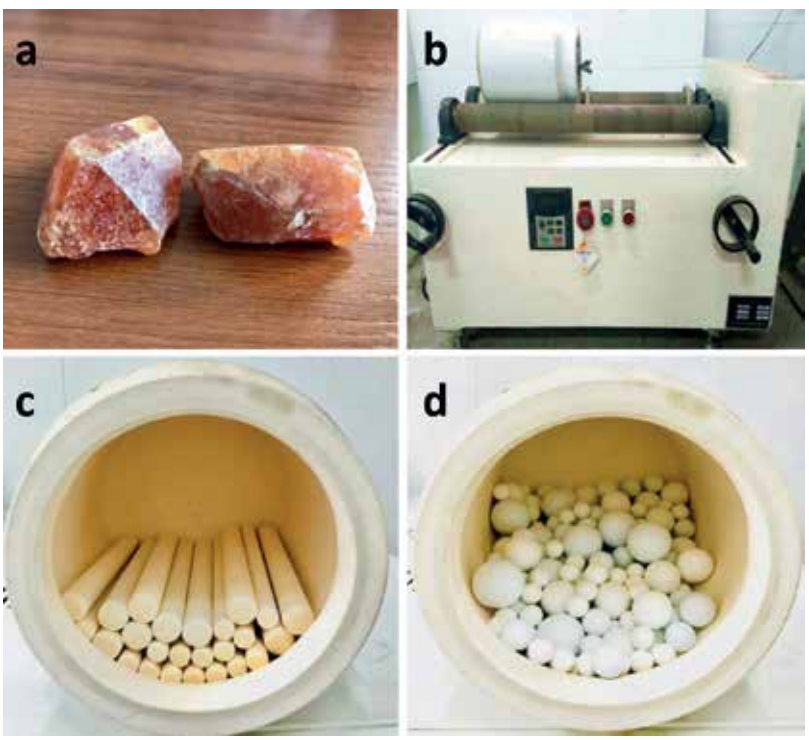

Figure 1. (a) Pure scheelite crystal samples, (b) grinder, (c) corundum rod media, and (d) corundum ball media used in the grinding tests.

the next run, while the products under the screen were collected for further sieving to obtain particles in the size fraction of −74 + 38 μm (the size of the particle is between 38 and 74 μm). The samples with required size were rinsed with Deionized (DI) water and dried at the temperature of 60°C. The surface area measurement (BET) indicated that the special surface areas of the ball and rod mill particles are 0.040 and 0.027 m^2/g, respectively.

2.2.2. Particle shape characterization by SEM

The shape characterization of milled particles was imaged by the JSM-6490LV SEM instrument. Assuming that the projection of the particles had the ellipse-like shape [17], the imaged micrographs were analyzed using CorelDraw×4 software to measure the length (L) and width (W) of the particles. As shown in **Figure 2**, the particles without overlapping nor border out of the picture were chosen. For each particle, the mean value of the five liner lengths and widths were taken as the real length (L) and width (W), respectively [16, 17]. Then more than 200 particles were measured and the L and W of the particle groups were calculated by averaging all value of the chosen particles.

Based on the ellipse-like shape assumption, Eqs. (1) and (2) were used to calculate the area (A) and perimeter (P), respectively.

$$A \approx \frac{\pi LW}{4} \tag{1}$$

$$P \approx \frac{1}{2}\pi\left[\frac{3}{2}(L+W) - (LW)^{1/2}\right] \tag{2}$$

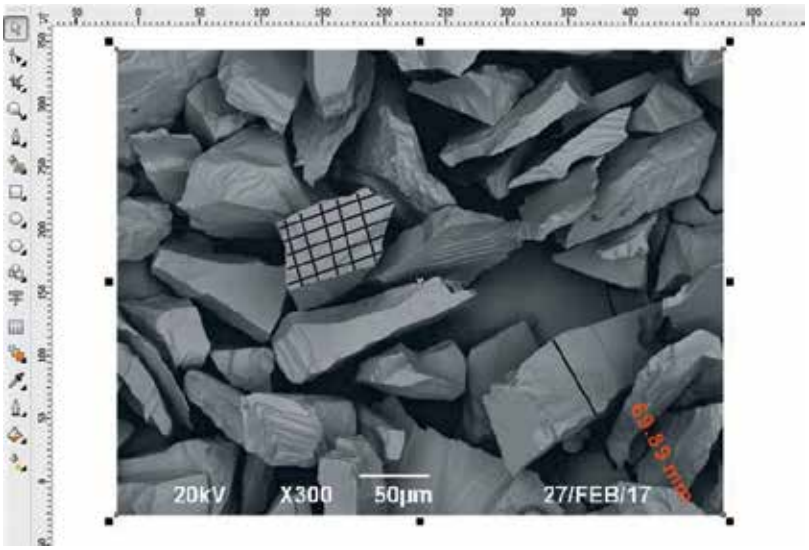

Figure 2. Measurements of the length (L) and width (W) of a particle projection exported from an SEM micrograph on CorelDraw software.

With the values of L, W, A and P, the four shape factors, namely the roundness (Ro), flatness (F), elongation (E) and relative width (RW), were calculated using Eqs. (3)–(6).

$$\mathrm{Ro} = \frac{4\pi \mathrm{A}}{\mathrm{P}^2} \tag{3}$$

$$\mathrm{F} = \frac{\mathrm{P}^2}{4\pi \mathrm{A}} \tag{4}$$

$$\mathrm{E} = \frac{\mathrm{L}}{\mathrm{W}} \tag{5}$$

$$\mathrm{RW} = \frac{\mathrm{W}}{\mathrm{L}} \tag{6}$$

It should be noted that the maximum value of the roundness is 1.0 for a circle, while the flatness has a minimum of 1.0 for a circle.

2.2.3. X-ray diffraction (XRD) measurement

X-ray diffractometer (D8-ADVANCE Bruker-AKS) was run in the reflection mode with Cu Kαradiation (λ = 1.5406, tube potential of 40 mV, and tube current of 40 mA), and at a goniometer speed of 4°/min. It is important that the samples were randomly oriented during the sample preparation process.

2.2.4. Wettability measurement

To measure the wettability of nubby samples, the sessile drop technique [34] and the captive bubble method [35] have been widely used, while as for powder samples, the Washburn method [36] and the flotation method [37] were employed. In this study, the flotation method was employed to investigate the wettability of the milled particles treated by the activator and collector. This method is based on the assumption that the flotation recovery of the minerals decreases with the decrease in the surface tension (γ) of the solution [38]. Therefore, methanol solution with different concentrations were used as the flotation media and 2.0 g of samples was conditioned by 1×10^{-4} mol/L lead nitrate and 1×10^{-4} mol/L BHA. After 3 min of flotation at pH 9 (an industrially preferred pH for effective scheelite flotation), the froth concentrates and tailings were filtered, dried and weighted to calculate the flotation recovery.

Moreover, the advancing contact angle of the commonly exposed cleavage surfaces of scheelite (the {101} and {001} surfaces) was measured by the sessile-drop technology using a goniometer (GBX, France) at 20°C and ambient relative humidity of about 50%. The accuracy of the measurements was approximately ±2°. Firstly, and the prepared sample surfaces were immersed in the surfactant solution with desired concentration under gentle agitation for 30 min, then gently washed with distilled water and vacuum dried at 50°C for 15 min. Then a water drop of about 3.5 μL was placed on the sample surface and the readings of contact angles were taken automatically on the left and right sides of the water droplet profile by computer software. The height of the drop is dependent on the wettability of the scheelite

sample surface. Ten readings of contact angle were taken on each drop within 1 min after placing the drop, and the contact angle commonly reaches a stationary value (the equilibrium contact angle) after 30 s. At least three drops were measured and the mean value was taken as the real advancing contact angel for each crystal surface after treated with a certain concentration of collector [39–41].

2.2.5. Micro-flotation test

Micro-flotation tests were carried out in an XFG flotation machine with a 40 mL plexiglass cell, at an impeller speed of 1650 rpm. The mineral suspension was prepared by adding 2.0 g of minerals and 36 mL DI water into the flotation cell and agitated for 2 min, followed by the adjustment of pH using NaOH or HCl for 2 min. Then the reagents were added in following orders: (1) the lead nitrate as the activator (2) the BHA as the collector; (3) 25 μL/L (i.e., adding 25 μL frother into 1 L mineral suspension) terpineol as the frother. Once the desired reagent was added, the suspension was agitated for 3 min. The stable pH value was recorded before the flotation. The flotation process lasted for 3 min before the flotation products were collected, filtered, dried and weighted. The flotation recovery was calculated using the weight of the dry products.

3. Results and discussions

3.1. Shape indexes of scheelite particles by different mills

The shape characterization of both the ball and rod mill particles was determined using 2D shape analysis (SEM method), and the mean values of the main shape indexes calculated according to Eqs. (1)–(6) are listed in **Table 1**. In addition, the distribution of the roundness and the elongation were calculated and shown in **Figure 3**.

Furthermore, the Statistical Product and Service Solutions (SPSS) software and the "two-sample t-test" were applied to the study of shape index (flatness, roundness, elongation and relative width) differences of the products produced by the ball and rod mills. The values of the shape indexes were compared pair-wise for any statistically significant differences at the 95% confidence interval with the results listed in **Table 1**.

As shown in **Table 1**, the rod mill particles have higher values of elongation (E) and flatness (F), while the ball mill particles possess larger values of roundness (R) and relative width (RW). Since all values at the column of "Sig. (2-side)" listed in **Table 2** are less than 0.05, a significant difference between the ball and rod mill scheelite products with a confidence interval of 95% is

Mill products	Particle number	L(μm)	W(μm)	A(μm^2)	P(μm)	E	F	Ro	RW
Ball	240	96.140	63.830	4817.244	253.741	1.505	1.069	0.935	0.664
Rod	240	108.867	67.412	5796.279	281.199	1.615	1.097	0.916	0.623

Table 1. Mean values of the shape indexes of both the ball and rod mill products of the scheelite mineral.

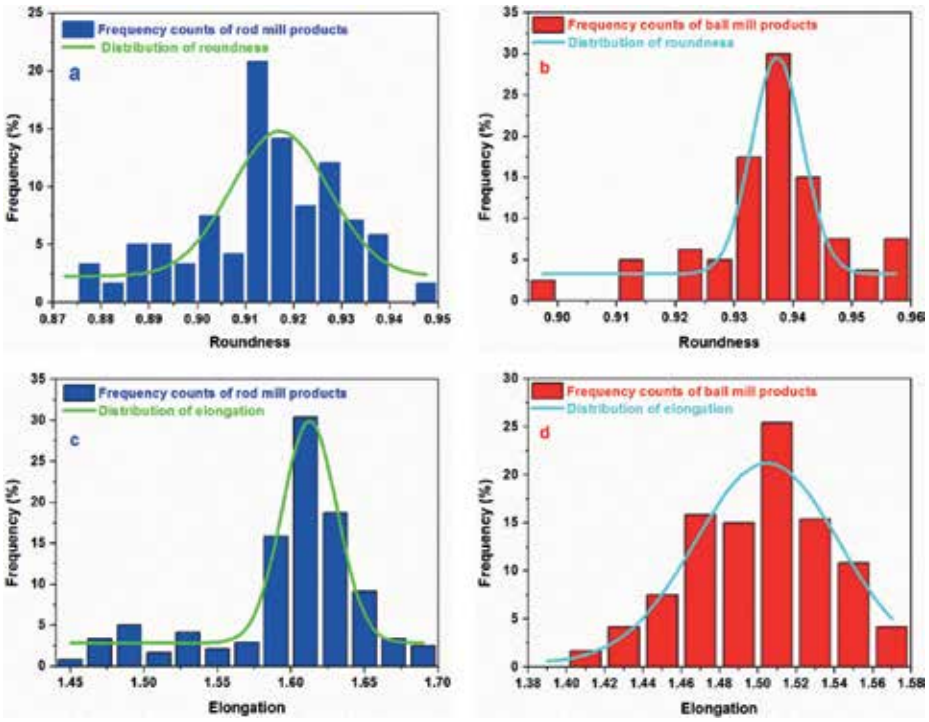

Figure 3. The distribution of shape indexes: The roundness of the (a) rod mill and (b) ball mill products, the elongation of the (c) rod mill and (d) ball mill products.

Parameter	Pair differences							
	Mean	Standard deviation	Standard error of mean	95% Confidence interval of the difference		t	df	Sig.(2-side)
				Lower	Upper			
F_d	0.02648	0.02363	0.00673	0.01614	0.03873	17.359	239	0.000
R_d	−0.02291	0.01986	0.00464	−0.0301	−0.0118	−17.555	239	0.000
E_d	0.10053	0.02021	0.00483	0.05160	0.14945	76.444	239	0.000
RW_d	−0.04127	0.00750	0.00222	−0.04910	−0.00886	−85.232	239	0.005

L_d, W_d, F_d, R_d, E_d and RW_d represent the shape differences of the scheelite particles produced by rod and ball mills.

Table 2. The statistical shape differences of the ball and rod mill products determined by the two-sample t-test.

inferred [42]. It was noted from the literature that the 2D shape data is used to reproduce the crucial shape characteristics of the real 3D shape indexes when the measured particles number is greater than 200 [43–47]. Therefore it is worth mentioning here that the shape indexes obtained in this study are reliable.

http://dx.doi.org/10.5772/intechopen.74836

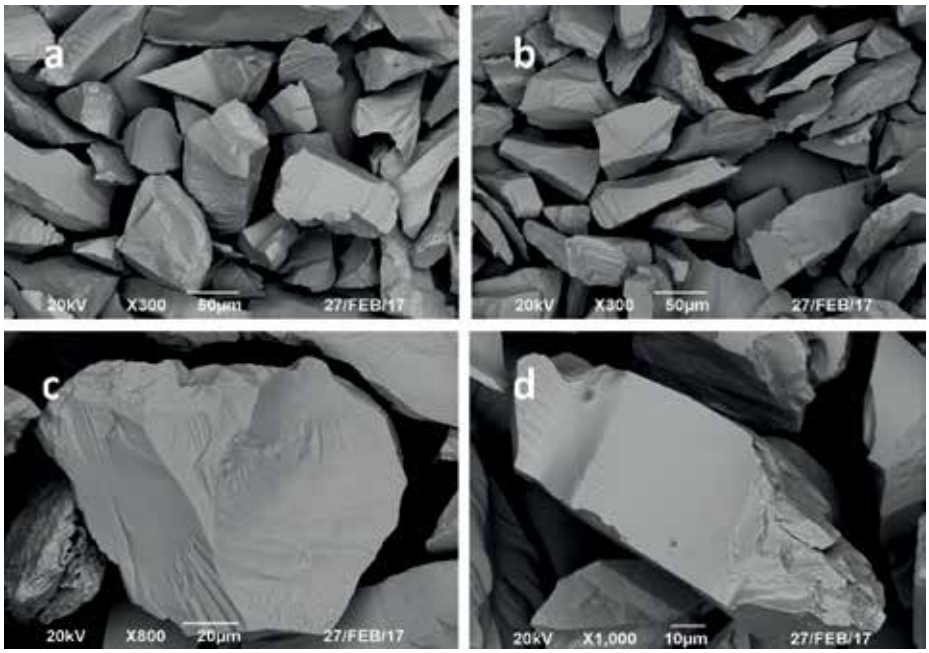

Figure 4. SEM pictures of the ball (a,c) and rod (b,d) mill particles of scheelite mineral.

SEM pictures in **Figure 4** show that the ball mill particles are more rounded while the rod mill particles are more elongated with more sharp edges. Those differences in the shape indexes between the ball and rod mill particles could be explained by the fact that breakage mechanism determines particle shape in all comminution equipment. The rod mill exercises line loads on the particles and the dominant breakage mechanism is the impact, during which the sharp edges are created, turning the particle to become more elongated [13]. Whereas the ball mill exerts point loads on the particles, and the predominant breaking forces are abrasion and chipping, which could eliminate the corners and sharp edges of the particles, turning them to become more rounded [14, 15].

3.2. XRD measurement results

Previous literatures reported that the relative exposure proportion of different crystal surfaces changes when the grinding environment varied [24, 25]. Previous publications revealed that the exposure of crystal surfaces of scheelite particles follows the order {112}, {101} and {001} [48–51]. The schematic of the commonly exposed surfaces of scheelite crystal particles can be found in **Figure 5**. In this work, the XRD measurements were conducted to investigate the exposure of different crystal surfaces in the two mill products, and the results are shown in **Figure 6**.

The relative intensity of a maxima (or peak) in the spectrum is believed to represent the relative exposure proportion of the crystal surfaces in the particulate samples [52, 53]. **Figure 6**

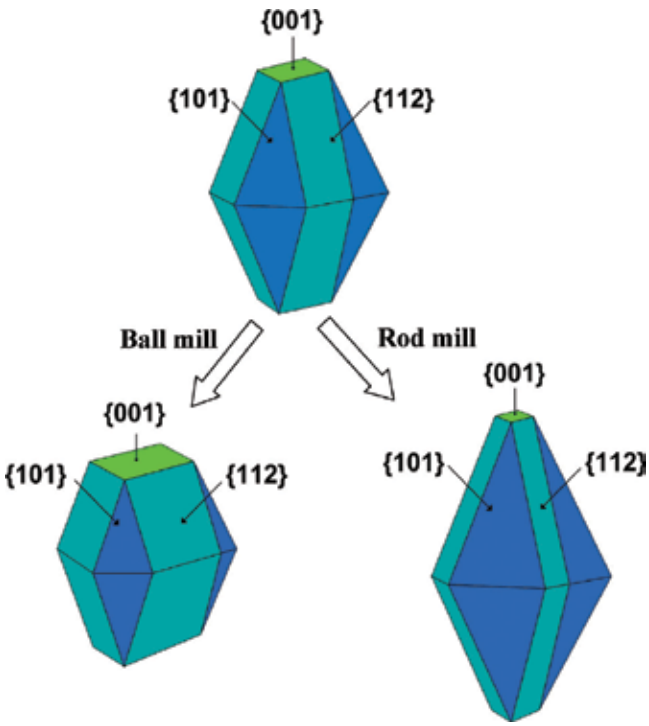

Figure 5. The schematic of the commonly exposed surfaces of original, ball and rod milled scheelite particles.

shows the same trend of the exposure of three main crystal surfaces of scheelite as **Figure 5**. Moreover, the {112} surface is the most abundant plane, and the intensity of the {112} surface is nearly the same for both mill products. In this case, the exposure proportion of {112} surface in the mill products is assumed as 100%. Accordingly, the relative proportions of the {101} plane in ball and rod mill samples are calculated to be 71.9% and 87.7%, respectively, while for the {001} planes, 44.4% and 33.8% respectively. The ball mill samples expose more {001} surfaces while the rod mill samples show more {101} surfaces. It is also interesting to mention that, from the **Figure 5**, more exposure of {001} surfaces will lead to the decrease in the elongation and the increase in the roundness of scheelite particles, while more exposure of {101} surface will increase the elongation and reduce the roundness of scheelite particles. That is to say, ball mill particles with more {001} surfaces are of a higher Ro value smaller E value which was verified by the results in **Table 1**.

It has been reported that every Ca atom on the scheelite {101} surface is fivefold-coordinated, while Ca on the {001} surface is sixfold-coordinated, as shown in **Figure 7**. The Ca atom in bulk scheelite crystal is eightfold-coordinated to surrounding oxygens. Based on our early findings [40, 54] that the atom with more dangling bonds is more active, the Ca atom on the {101} surface is more active than that on {001} surface, and has a higher interaction strength with organics, such as oleate. The atomic simulation results showed that a larger adsorption energy

http://dx.doi.org/10.5772/intechopen.74836

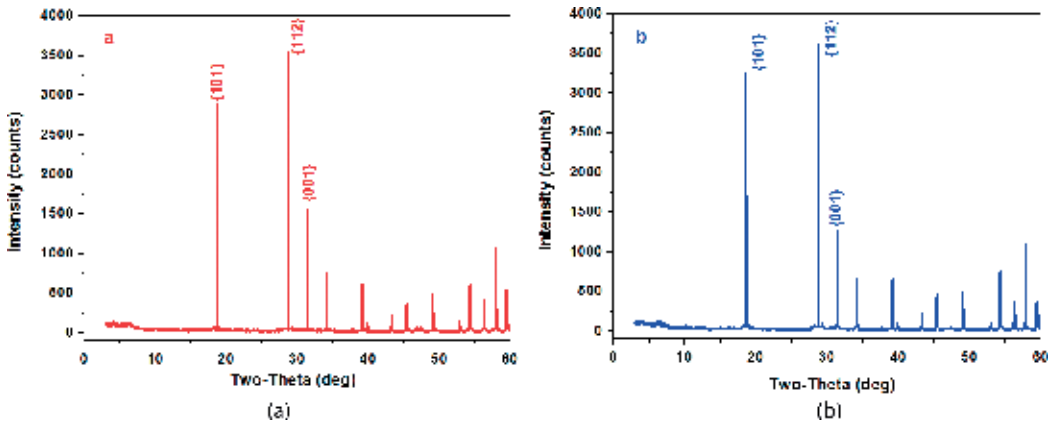

Figure 6. The XRD spectrums of the (a) ball and (b) rod mill products of scheelite minerals.

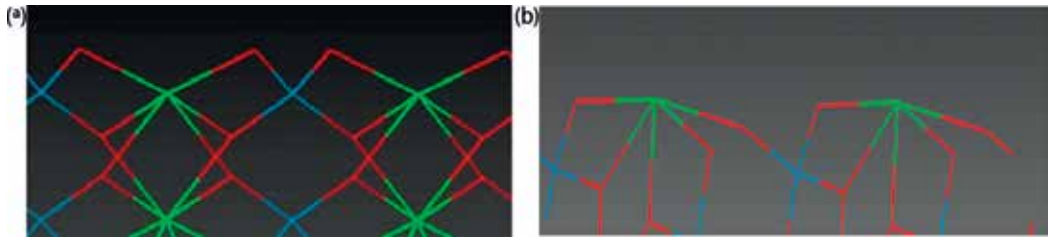

Figure 7. The bonding state of the top layer of scheelite (a) {001} and (b) {101} surfaces (green-Ca, red-O, and blue-W).

(−102 kJ/mol) of the oleate on the {101} surface was calculated while the adsorption energy was −93 kJ/mol for the oleate on the {001} surface [10]. Thus, it is tenable to infer that the rod mill products with relatively more {101} surface have stronger interaction with the collector and may possess a higher flotation recovery.

3.3. Wettability test results

The flotation method was used to investigate the wettability of both ball and rod mill particles. The experiments were conducted at pH 9 using 1×10^{-4} mol/L lead nitrate as the activator and 1×10^{-4} mol/L BHA as the collector at different concentration of the methanol solution. The critical surface tension (γ_c) of wetting was determined by plotting the percent recovery (R%) versus the surface tension of the methanol - water solutions (γ_{LA}), which gives a recovery R % = 0 at $\gamma_c = \gamma_{LA}$. The particles are wetted and cannot float when $\gamma_{LA} < \gamma_c$, indicating that the mineral with a lower γ_c is more hydrophobic [55]. The γ_{LA} of the methanol solution was measured by the Automatic Surface Tensiometer and the results are provided in **Figure 8**. And the flotation results are shown in **Figure 9**. It shows that the γ_c of the ball and rod mill

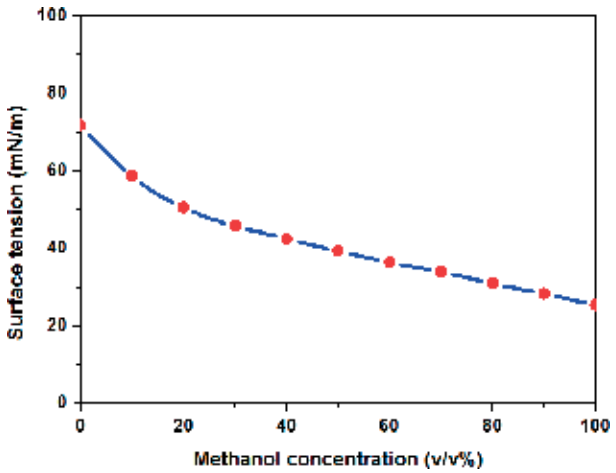

Figure 8. Variation of the surface tension of the methanol – water solutions (γ_{LA}) with the increase of mechanol concentration.

particles are approximately 43 and 41 mN/m, respectively, indicating that the ball mill ones are more likely to be wetted while the rod mill ones are more hydrophobic, which may result in a higher floatability.

According to the XRD measurement results, in addition to {112} surface, the ball mill samples expose more {001} surfaces while the rod mill samples show more {101} surfaces, which means that the wettability of the ground particles may be influenced by the proportion of the exposed surfaces. Then the advancing contact angles of both the {001} and {101} crystal planes treated by the lead nitrate and the BHA were measured, and the results are shown in **Figure 10**. It demonstrates that the scheelite {101} surface has higher contact angles after being treated with the surfactants, meaning that {101} is more hydrophobic than {001} surface.

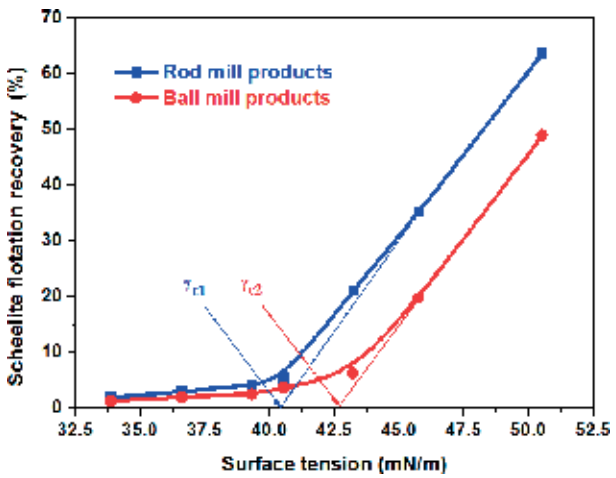

Figure 9. Flotation recoveries of the ball and rod mill products as a function of the methanol surface tension. ($C_{Lead\ nitrate} = 1 \times 10^{-4}$ mol/L; $C_{BHA} = 1 \times 10^{-4}$ mol/L; $C_{Terpineol} = 25$ μL/L; pH = 9 ± 0.2).

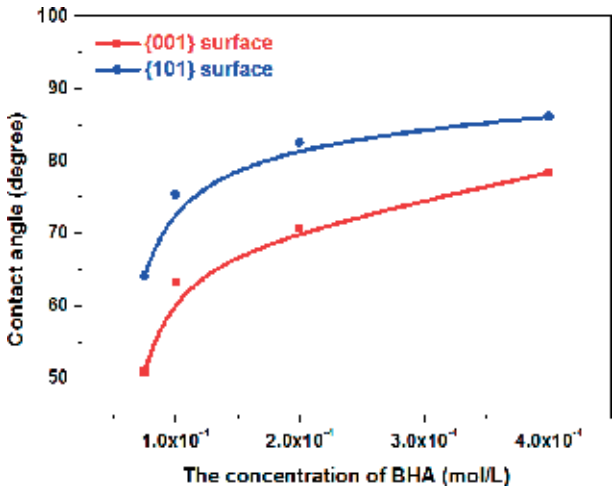

Figure 10. Contact angles of the scheelite (a) {101} and (b) {001} crystal surfaces. ($C_{Lead\ nitrate} = 1 \times 10^{-4}$ mol/L; pH = 9 ± 0.2).

From the above measurements, it can be concluded that the rod mill particles with more {101} surfaces exposed and a lower critical surface tension were more hydrophobic. As a result, the differences in wettability could influence the flotation behavior of these two different mill particles.

3.4. Micro-flotation experiment results

Micro-flotation experiments were conducted to study the flotability of the particles in the fraction of −74 + 38 μm that ground by the ball and rod mills. The flotation results, using different concentrations of BHA as collector at a pH of 9 ± 0.2, are provided in **Figure 11**. **Figure 11** shows that both the ball and rod mill particles have a similar trend of flotation

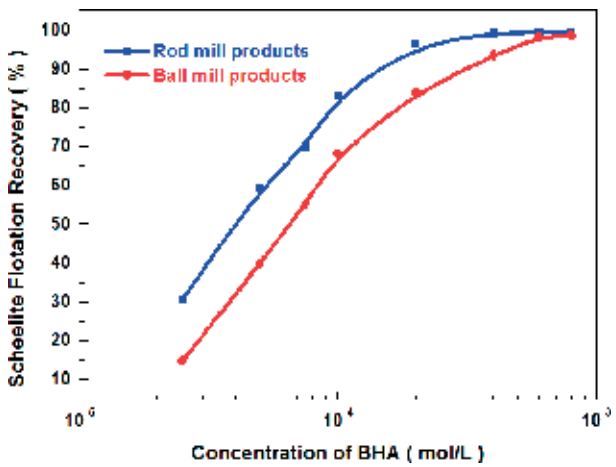

Figure 11. Flotation recoveries of the ball and rod mill products as a function of the BHA concentration. ($C_{Lead\ nitrate} = 1 \times 10^{-4}$ mol/L; $C_{Terpineol} = 25$ μL/L; pH = 9 ± 0.2).

recovery. The flotation recovery increases steadily with the increasing of BHA concentration till it reaches 4×10^{-4} mol/L for the rod mill particles and 6×10^{-4} mol/L for the ball mill ones, where the maximum recovery for both two samples are obtained at given concentrations of BHA, respectively. The maximum recovery may be caused by the monolayer adsorption of collector on the scheelite surfaces [56]. For the rod mill samples, it is easier to reach the monolayer adsorption because of the smaller specific surface area of 0.027 m^2/g compared with that of 0.040 m^2/g for the ball mill ones. Moreover, the flotation results, obtained at a pH of 6–11 are demonstrated in **Figure 12**. **Figure 12** shows that the recoveries of both milled particles follow a similar trend, but a higher recovery for the rod mill particles was observed. It was also observed that the flotation recovery increases with the increasing pH of solution until it reaches the value of 9, where the maximum recovery is achieved for both milled particles [32].

Therefore, it can be inferred from the micro-flotation results that the flotation behavior of the ball and rod mill particles is similar, while the rod mill ones have a better flotation performance than the ball mill ones. And the reason could be explained by the shape and the surface chemistry differences of scheelite particles ground by ball and rod mills. To begin with, the rod mill particles expose more {101} surfaces, on which the Ca sites are more reactive, resulting in a stronger interaction of collector with the rod mill particles and a better floatation performance. In addition, the wettability measurements show that the ball mill scheelite, with higher critical surface tension and more {001} surfaces, may have relatively lower contact angles and may be more likely to get wetted during the flotation process. Secondly, the rod mill particles, with a lower specific area and larger elongation, are more easily attached to the air bubbles than the rounded ones. This can be attributed to the sharp edges of elongated particles, which are conducive for rupturing the water film at the mineral/solution interface and help shorten the attachment time, leading to the improvement of the collision efficiency and flotation recovery.

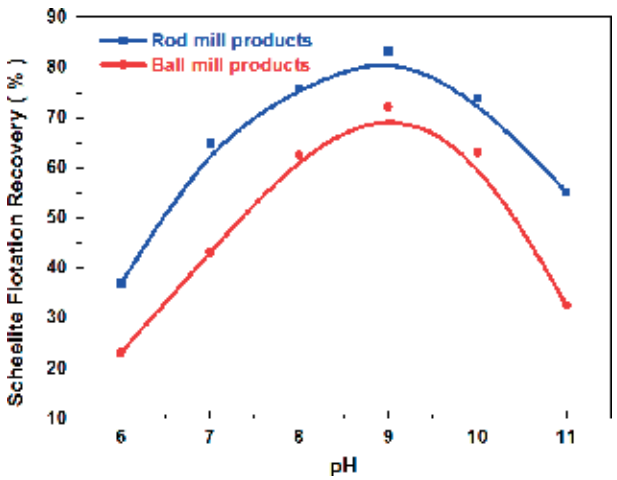

Figure 12. Flotation recoveries of the ball and rod mill products as a function of the solution pH. ($C_{Lead\ nitrate} = 1 \times 10^{-4}$ mol/L; $C_{BHA} = 1 \times 10^{-4}$ mol/L; $C_{Terpineol} = 25$ μl/L).

4. Conclusions

In this work, the morphology and the surface properties of the scheelite particles with a size of −74 + 38 μm produced by ball and rod mills were studied through SEM observation, XRD analysis, wettability measurement, and single mineral flotation experiment. The flotation results revealed that the rod mill particles are much easier to achieve a monolayer adsorption of collector and hence have a higher flotation recovery compared to the ball mill ones which can be explained from both physical and chemical points of view. The XRD spectrums showed that minerals particles obtained from ball and rod mill have similar expose intensity of abundant {112} surface. However, the rod mill particles have more {101} surface exposed with more reactive Ca atoms while more {001} surface is exposed for the ball mill particles. Moreover, more exposure of {001} surfaces will lead to the decrease in the elongation and the increase in the roundness of scheelite ball mill particles, while more exposure of {101} surface will increase the elongation and reduce the roundness of scheelite rod mill particles. Those discussions were verified by the SEM observations and shape indexes distribution calculation. The contact angles of {101} surface are larger than that of the {001} surface after being treated with the collector, indicating that the rod mill particles with more exposed {101} surfaces possess a higher hydrophobicity. The wettability measurements indicated that the values of the critical surface tension (γ_c, a measure of surface tension) are 41 and 43 mN/m for the rod and ball mill particles treated with collector, respectively. The rod mill particles with more exposure of reactive {101} surfaces and higher elongation have stronger attachment to collectors and air bubbles, and hence a higher hydrophobicity and flotation recovery in the presence of collector.

Acknowledgements

The authors acknowledge the financial support from the National Natural Science Foundation of China (51774328, 51404300), the Young Elite Scientists Sponsorship Program by CAST(2017QNRC001), the Innovation-driven Program of Central South University of China (2017CX007), the Key Program for International S & T Cooperation Projects of China (2016YFE0101300), and the National 111 Project (B14034), the Innovation Program for Postgraduate Students of Central South University (2017zzts576). Natural Science Foundation of Hunan Province of China (2018JJ2520).

Author details

Zhiyong Gao* and Chengwei Li

*Address all correspondence to: zhiyong.gao@csu.edu.cn

School of Mineral Processing and Bioengineering, Central South University, Changsha, Hunan, China

References

[1] Kursun H, Ulusoy U. Influence of shape characteristics of talc mineral on the column flotation behavior. International Journal of Mineral Processing. 2006;**78**:262-268. DOI: 10.1016/j.minpro.2005.11.003

[2] Ballantyne GR, Powell MS. Benchmarking comminution energy consumption for the processing of copper and gold ores. Minerals Engineering. 2014;**65**:109-114. DOI: 10.1016/j.mineng.2014.05.017

[3] Curry JA, Ismay MJL, Jameson GJ. Mine operating costs and the potential impacts of energy and grinding. Minerals Engineering. 2014;**56**:70-80. DOI: 10.1016/j.mineng.2013.10.020

[4] Austin LG, Trass O. Size reduction of solids crushing and grinding equipment. In: Fayed ME, Otten L, editors. Handbook of Powder Science & Technology. Boston, MA: Springer US; 1997. pp. 586-634

[5] Leroy S, Dislaire G, Bastin D, Pirard E. Optical analysis of particle size and chromite liberation from pulp samples of a UG2 ore regrinding circuit. Minerals Engineering. 2011;**24**:1340-1347. DOI: 10.1016/j.mineng.2011.06.006

[6] Bournival G, Ata S, Wanless EJ. The roles of particles in multiphase processes: Particles on bubble surfaces. Advances in Colloid and Interface Science. 2015;**225**:114-133. DOI: 10.1016/j.cis.2015.08.008

[7] Abouzeid AZM, Fuerstenau DW. Flow of materials in rod mills as compared to ball mills in dry systems. International Journal of Mineral Processing. 2012;**102**:51-57. DOI: 10.1016/j.minpro.2011.09.013

[8] Heyes GW, Kelsall DF, Stewart PSB. Continuous grinding in a small wet rod mill part I. Comparison with a small ball mill. Powder Technology. 1973;**7**:319-325. DOI: 10.1016/0032-5910(73)80043-9

[9] Tavares LM, de Carvalho RM, Guerrero JC. Simulating the bond rod mill grindability test. Minerals Engineering. 2012;**26**:99-101. DOI: 10.1016/j.mineng.2011.10.015

[10] Cooper TG, de Leeuw NH. A computer modeling study of the competitive adsorption of water and organic surfactants at surfaces of the mineral scheelite. Langmuir. 2004;**20**:3984-3994. DOI: 10.1021/la049796w

[11] Oja M, Tuunila R. The influence of comminution method to particle shape. In: Massacci P, editor. Developments in Mineral Processing. Elsevier; 2000. p. C4-64-C64-70. DOI: 10.1016/S0167-4528(00)80028-9

[12] Moosakazemi F, Mohammadi MRT, Mohseni M, Karamoozian M, Zakeri M. Effect of design and operational parameters on particle morphology in ball mills. International Journal of Mineral Processing. 2017;**165**:41-49. DOI: 10.1016/j.minpro.2017.06.001

[13] Ulusoy U, Yekeler M. Correlation of the surface roughness of some industrial minerals with their wettability parameters. Chemical Engineering and Processing. 2005;**44**:557-565. DOI: 10.1016/j.cep.2004.08.001

[14] Vizcarra TG, Wightman EM, Johnson NW, Manlapig EV. The effect of breakage method on the shape properties of an iron-oxide hosted copper-gold ore. Minerals Engineering. 2011;**24**:1454-1458. DOI: 10.1016/j.mineng.2011.07.007

[15] Francioli D. Effect of operational variables on ball milling. Tijdschrift Voor Theologie. 2015;**52**:180-180

[16] Hicyilmaz C, Ulusoy U, Yekeler M. Effects of the shape properties of talc and quartz particles on the wettability based separation processes. Applied Surface Science. 2004;**233**: 204-212. DOI: 10.1016/j.apsusc..2004.03.209

[17] Yekeler M, Ulusoy U, Hicyilmaz C. Effect of particle shape and roughness of talc mineral ground by different mills on the wettability and floatability. Powder Technology. 2004; **140**:68-78. DOI: 10.1016/j.powtec.2003.12.012

[18] Ulusoy U, Hicyilmaz C, Yekeler M. Role of shape properties of calcite and barite particles on apparent hydrophobicity. Chemical Engineering and Processing. 2004;**43**:1047-1053. DOI: 10.1016/j.cep.2003.10.003

[19] Ulusoy U, Yekeler M, Hicyilmaz C. Determination of the shape, morphological and wettability properties of quartz and their correlations. Minerals Engineering. 2003;**16**: 951-964. DOI: 10.1016/j.mineng.2003.07.002

[20] Koh PTL, Hao FP, Smith LK, Chau TT, Bruckard WJ. The effect of particle shape and hydrophobicity in flotation. International Journal of Mineral Processing. 2009;**93**:128-134. DOI: 10.1016/j.minpro.2009.07.007

[21] Verrelli DI, Bruckard WJ, Koh PTL, Schwarz MP, Follink B. Particle shape effects in flotation. Part 1: Microscale experimental observations. Minerals Engineering. 2014;**58**: 80-89. DOI: 10.1016/j.mineng.2014.01.004

[22] Xia WC. Role of particle shape in the floatability of mineral particle: An overview of recent advances. Powder Technology. 2017;**317**:104-116. DOI: 10.1016/j.powtec.2017.04.050

[23] Feng D, Aldrich C. A comparison of the flotation of ore from the Merensky reef after wet and dry grinding. International Journal of Mineral Processing. 2000;**60**:115-129. DOI: 10.1016/S0301-7516(00)00010-7

[24] Zhu GL, Wang YH, Liu XW, Yu FS, Lu DF. The cleavage and surface properties of wet and dry ground spodumene and their flotation behavior. Applied Surface Science. 2015; **357**:333-339. DOI: 10.1016/j.apsusc.2015.08.257

[25] Xu LH, Hu YH, Wu HQ, Tian J, Liu J, Gao ZY, Wang L. Surface crystal chemistry of spodumene with different size fractions and implications for flotation. Separation and Purification Technology. 2016;**169**:33-42. DOI: 10.1016/j.seppur.2016.06.005

[26] Ilhan S, Kalpakli AO, Kahruman C, Yusufoglu I. The investigation of dissolution behavior of gangue materials during the dissolution of scheelite concentrate in oxalic acid solution. Hydrometallurgy. 2013;**136**:15-26. DOI: 10.1016/j.hydromet.2013.02.013

[27] Gao ZY, Bai D, Sun W, Cao XF, Hu YH. Selective flotation of scheelite from calcite and fluorite using a collector mixture. Minerals Engineering. 2015;**72**:23-26. DOI: 10.1016/j.mineng.2014.12.025

[28] Gao ZY, Sun W, Hu YH. New insights into the dodecylamine adsorption on scheelite and calcite: An adsorption model. Minerals Engineering. 2015;**79**:54-61. DOI: 10.1016/j.mineng.2015.05.011

[29] Cooper TG, de Leeuw NH. A combined ab initio and atomistic simulation study of the surface and interfacial structures and energies of hydrated scheelite: Introducing a CaWO4 potential model. Surface Science. 2003;**531**:159-176. DOI: 10.1016/S00039-6028(03)00362-5

[30] Deng LQ, Zhao G, Zhong H, Wang S, Liu GY. Investigation on the selectivity of N-((hydroxyamino)-alkyl) alkylamide surfactants for scheelite/calcite flotation separation. Journal of Industrial and Engineering Chemistry. 2016;**33**:131-141. DOI: 10.1016/j.jiec.2015.09.027

[31] Wang JJ, Gao ZY, Gao YS, Hu YH, Sun W. Flotation separation of scheelite from calcite using mixed cationic/anionic collectors. Minerals Engineering. 2016;**98**:261-263. DOI: 10.1016/j.mineng.2016.09.006

[32] Han HS, Hu YH, Sun W, Li XD, Cao CG, Liu RQ, Yue T, Meng XS, Guo YZ, Wang JJ, Gao ZY, Chen P, Huang WS, Liu J, Xie JW, Chen YL. Fatty acid flotation versus BHA flotation of tungsten minerals and their performance in flotation practice. International Journal of Mineral Processing. 2017;**159**:22-29. DOI: 10.1016/j.minpro.2016.12.006

[33] Yue T, Han HS, Hu YH, Sun W, Li XD, Liu RQ, Gao ZY, Wang L, Chen P, Zhang CY, Tian MJ. New insights into the role of Pb-BHA complexes in the flotation of tungsten minerals. Journal of Metals. 2017;**69**:2345-2351. DOI: 10.1007/s11837-017-2531-3

[34] Rupp F, Gittens RA, Scheideler L, Marmur A, Boyan BD, Schwartz Z, Geis-Gerstorfer J. A review on the wettability of dental implant surfaces I: Theoretical and experimental aspects. Acta Biomaterialia. 2014;**10**:2894-2906. DOI: 10.1016/j.actbio.2014.02.040

[35] Baek Y, Kang J, Theato P, Yoon J. Measuring hydrophilicity of RO membranes by contact angles via sessile drop and captive bubble method: A comparative study. Desalination. 2012;**303**:23-28. DOI: 10.1016/j.desal.2012.07.006

[36] Galet L, Patry S, Dodds J. Determination of the wettability of powders by the Washburn capillary rise method with bed preparation by a centrifugal packing technique. Journal of Colloid and Interface Science. 2010;**346**:470-475. DOI: 10.1016/j.jcis.2010.02.051

[37] Williams M, Fuerstenau D. A simple flotation method for rapidly assessing the hydrophobicity of coal particles. International Journal of Mineral Processing. 1987;**20**:153-157

[38] Yarar B, Kaoma J. Estimation of the critical surface tension of wetting of hydrophobic solids by flotation. Colloids and Surfaces. 1984;**11**:429-436

[39] Hu YH, Gao ZY, Sun W, Liu XW. Anisotropic surface energies and adsorption behaviors of scheelite crystal. Colloid Surface A. 2012;**415**:439-448. DOI: 10.1016/j.colsurfa.2012.09.038

[40] Gao ZY, Sun W, Hu YH. Mineral cleavage nature and surface energy: Anisotropic surface broken bonds consideration. Transactions of Nonferrous Metals Society of China. 2014;**24**:2930-2937. DOI: 10.1016/S1003-6326(14)63428-2

[41] Han HS, Liu WL, Hu YH, Sun W, Li XD. A novel flotation scheme: Selective flotation of tungsten minerals from calcium minerals using Pb-BHA complexes in Shizhuyuan. Rare Metals. 2017;**36**:533-540. DOI: 10.1007/s12598-017-0907-8

[42] Ulusoy U, Kursun I. Comparison of different 2D image analysis measurement techniques for the shape of talc particles produced by different media milling. Minerals Engineering. 2011;**24**:91-97. DOI: 10.1016/j.mineng.2010.05.011

[43] Ulusoy U, Yekeler M. Dynamic image analysis of calcite particles created by different mills. International Journal Of Mineral Processing. 2014;**133**:83-90. DOI: 10.1016/j.minpro.2014.10.006

[44] Morgan DJ, Jerram DA. On estimating crystal shape for crystal size distribution analysis. Journal of Volcanology and Geothermal Research. 2006;**154**:1-7. DOI: 10.1016/j.jvolgeores.2005.09.016

[45] Mock A, Jerram DA. Crystal size distributions (CSD) in three dimensions: Insights from the 3D reconstruction of a highly porphyritic rhyolite. Journal of Petrology. 2005;**46**:1525-1541. DOI: 10.1093/petrology/egi024

[46] Berger A, Herwegh M, Schwarz JO, Putlitz B. Quantitative analysis of crystal/grain sizes and their distributions in 2D and 3D. Journal of Structural Geology. 2011;**33**:1751-1763. DOI: 10.1016/j.jsg.2011.07.002

[47] Jerram DA, Mock A, Davis GR, Field M, Brown RJ. 3D crystal size distributions: A case study on quantifying olivine populations in kimberlites. Lithos. 2009;**112**:223-235. DOI: 10.1016/j.lithos.2009.05.042

[48] Gao ZY, Sun W, Hu YH, Liu XW. Surface energies and appearances of commonly exposed surfaces of scheelite crystal. Transactions of Nonferrous Metals Society of China. 2013;**23**:2147-2152. DOI: 10.1016/S1003-6326(13)62710-7

[49] Mogilevsky P, Parthasarathy TA, Petry MD. Anisotropy in room temperature microhardness and fracture of CaWo(4) scheelite. Acta Materialia. 2004;**52**:5529-5537. DOI: 10.1016/j.actamat.2004.08.022

[50] Mogilevsky P. Identification of slip systems in CaWO4 scheelite. Philosophical Magazine. 2005;**85**:3511-3539. DOI: 10.1080/14786430500227996

[51] Longo VM, Gracia L, Stroppa DG, Cavalcante LS, Orlandi M, Ramirez AJ, Leite ER, Andres J, Beltran A, Varela JA, Longo E. A joint experimental and theoretical study on the nanomorphology of $CaWO_4$ crystals. Journal of Physical Chemistry C. 2011;**115**: 20113-20119. DOI: 10.1021/jp205764s

[52] Li HL, Li TD, Liu HX, Huang BB, Zhang Q. Hierarchical flower-like nanostructures of anatase TiO_2 nanosheets dominated by {001} facets. Journal of Alloys and Compounds. 2016;**657**:1-7. DOI: 10.1016/j.jallcom.2015.09.257

[53] Gao ZY, Li CW, Sun W, Hu YH. Anisotropic surface properties of calcite: A consideration of surface broken bonds. Colloid Surface A. 2017;**520**:53-61. DOI: 10.1016/j.colsurfa.2017.01.061

[54] Gao Z, Hu Y, Sun W, Drelich JW. Surface-charge anisotropy of scheelite crystals. Langmuir. 2016;**32**:6282-6288. DOI: 10.1021/acs.langmuir.6b01252

[55] Cebeci Y, Sonmez I. A study on the relationship between critical surface tension of wetting and oil agglomeration recovery of calcite. Journal of Colloid and Interface Science. 2004;**273**:300-305. DOI: 10.1016/j.jcis.2004.01.032

[56] Gao YS, Gao ZY, Sun W, Hu YH. Selective flotation of scheelite from calcite: A novel reagent scheme. International Journal of Mineral Processing. 2016;**154**:10-15. DOI: 10.1016/j.minpro.2016.06.010

Chapter 8

Recycling and Recharging of Supreme Garnet in Abrasive Waterjet Machining

Vu Ngoc Pi and Tran Quoc Hung

Additional information is available at the end of the chapter

http://dx.doi.org/10.5772/intechopen.75180

Abstract

Abrasive waterjet (AWJ) technology is widely used for cutting technical materials, cleaning contaminated surfaces, polishing hard-to-machine materials, etc. However, its main disadvantage is high cutting cost. Therefore, recycling and recharging abrasives used in the AWJ cutting process have been subject to many studies. This chapter presents a study on the recycling and recharging of Supreme garnet (or IMC garnet) in abrasive waterjet machining. In this study, the reusability of the recycled and recharged garnet was explored. Also, the cutting performance and the cutting quality of the recycled and recharged abrasive were investigated. Finally, the optimum particle size for recycling and recharging was found.

Keywords: abrasive waterjet (AWJ), abrasive recycling, abrasive recharging

1. Introduction

Abrasive waterjet (AWJ) technology is a recent non-traditional machining process. In this technology, a very high-pressure beam of water and abrasives is used for cutting difficult-to-machine materials, milling slots, cleaning contaminated surfaces, etc. In practice, AWJ machining has been developed from waterjet machining. The earliest use of the water beam in coal mining started in the former Soviet Union and New Zealand [1]. Then, waterjet beam was used for cutting wood in the 1950s [4]. Nevertheless, it was not until 1971 that the first waterjet cutting machine was applied [2]. After that, the abrasive waterjet cutting method was invented by adding abrasives into a beam of pure waterjet. Since then, abrasive waterjet was first used to cut glass, steel, and concrete in 1980. The invention of AWJ [3] led to a huge expansion of applications of cutting a wide variety of materials.

AWJ machining has many advantages over other nonconventional techniques [4]:

- It can cut a wide range of materials including titanium, stainless steel, aerospace alloys, glass, plastics, ceramics, and so on.
- It can cut net-shaped parts and near net-shaped parts.
- There are no heat-affected areas; thus, no structural changes in work materials occur because no heat is generated in the cutting process.
- It is particularly environmentally friendly as it does not cause any cutting dust or chemical air pollutants.
- Only one nozzle is needed to machine various types of work materials and workpiece shapes.
- AWJ machining can be easily automated, and therefore it can be run with unmanned shifts.

2. Abrasive waterjet system

Figure 1 shows a typical AWJ entrainment system. There are four main parts in the system. They are the water preparation system, the pressure generation system, the jet former, and

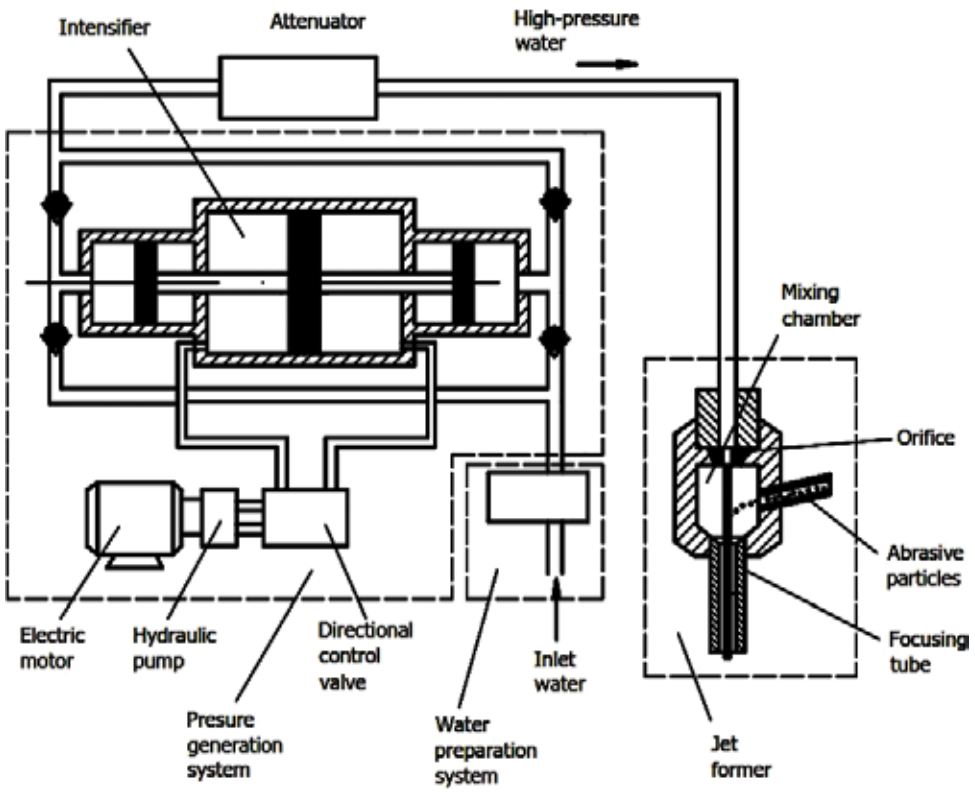

Figure 1. Schema of an AWJ machining system [4].

http://dx.doi.org/10.5772/intechopen.75180

the abrasive supply system. An abrasive waterjet entrainment system mixes abrasives with the waterjet in a mixing chamber. The abrasive particles are accelerated by the high-velocity water stream and then leave the focusing tube (or the nozzle) with the stream. The high-velocity beam of water and abrasives is used for cutting harder materials such as stainless steel, glass, ceramics, titanium alloys, composite materials, and so forth.

3. Challenges in abrasive waterjet technology

Although AWJ machining has a number of advantages as described in Section 1, a considerable disadvantage of this technology is its relatively high cutting cost. Therefore, the reduction of the machining cost is a significant challenge in this technology.

In order to reduce AWJ machining cost, there are two possible solutions including optimization of the machining process and abrasive recycling. For the first solution, until now, there have been many studies in optimizing AWJ's factors that include jet parameters (e.g., water pressure, orifice diameter, focusing tube diameter, focusing tube length, abrasive mass flow rate, abrasive size, abrasive shape, and abrasive type) and cutting parameters (e.g., the standoff distance, the work material, and the feed speed).

For optimum selection of focusing tube and orifice diameters, H. Blickwedel [5] introduced an optimum ratio between the focusing tube diameter and the orifice diameter. Zeng and Munoz [6] also reported the optimum combination of focusing tube/orifice for the highest AWJ cutting performance. The optimum focusing tube length for maximum depth of cut was proposed by Blickwedel [5]. Hashish [7] noted that the depth of cut and the kerf width both depend on the length of the focusing tube. In addition, a new way for using the focusing tube in order to get the minimum cutting cost was proposed [8].

Numerous studies have been carried out on optimum abrasive mass flow rate. The optimum abrasive mass flow rate for the maximum cutting performance (or for the maximum depth of cut) depends on many parameters including the water pressure [9–11], the orifice diameter [9, 11], the focusing tube diameter [9, 10, 12], and the focusing tube length [10].

The effects of other parameters on the depth of cut have also been investigated. Those are the abrasive particle sizes [13] and the standoff distance [5, 14]. For getting the minimum cutting time, the minimum cutting cost, and the maximum profit rate, Vu Ngoc Pi [4] carried out a study on AWJ optimization. In the study, models for determination of the optimum abrasive mass flow rate and the optimum nozzle exchanged diameter were proposed.

The other solution to enhance AWJ cutting cost is abrasive recycling. So far, there were several studies on this area. Labus et al. [15] presented a fundamental research on the influence of the process parameters on the particle size distribution after the mixing process and after the cutting process. The authors found that the water pressure from 0 to 205 MPa had more influences on the fraction of abrasive particles than the pressure from 274 to 342 MPa. Furthermore, the geometry of the mixing chamber affected the distribution of abrasive particle size. It was also noted that the particle fraction was not connected to the length of the mixing tube.

Louis et al. [16] explored the influences of cutting parameters on the fragmentation of abrasive particles after penetration to the workpiece. It was mentioned that after the workpiece, the average size of particles was smaller than that after the focusing tube. In addition, the authors found that the particle fragmentation depended on the workpiece materials. For instance, the particle size after cutting stainless steel was smaller than after cutting aluminum. Furthermore, the fragmentation after workpiece of different abrasive materials was inspected. The authors reported that olivine produced a slightly smaller average particle size than garnet [16].

For evaluation of the fragmentation of abrasive particles, Ohlsen [13] introduced a "disintegration number" in a systematic study on the recycling of Barton garnet. In the study, the effects of different process parameters on the magnitude of the disintegration number were investigated, such as the water pressure, the abrasive mass flow rate, the abrasive particle diameter, the focusing tube diameter, and the focusing tube length.

Another study on the abrasive recycling was performed for a local garnet from India [17]. In this study, the reusability of the garnet was investigated with four recycling cycles. It was found that the recycling capacity (or the reusability) of the first, the second, the third, and the fourth recycling was 81, 49, 26, and 15%, respectively. In addition, the influences of recycled abrasives on the cutting performance and the cutting quality were explored.

In order to increase and preserve the cutting performance of recycled abrasives, new abrasives are added into recycled abrasives. This process is called recharging of abrasives. Kantha Babu and Krishnaiah Chetty [18] announced the results of an abrasive recharging study. It was reported that an increase of the added new abrasives up to 40% led to a significant increase of the depth of cut and a slight increase thereafter. Subsequently, in order to get the maximum depth of cut, the recharging at 40% of the recycled abrasive mass was recommended. Besides, the percentage of added abrasives as well as the cutting performance and the cutting quality of recharged abrasives was examined.

Vu Ngoc Pi et al. [19] carried out a study on the recycling and recharging of GMA abrasive. In the research, the reusability of GMA abrasive after the first cut and second cut was explored. In addition, the reusability of the recharged abrasives was explored. Furthermore, the cutting performance and the cutting quality of both recycled abrasive and recharged abrasive were investigated. The optimal particle sizes for the recycling and the recharging of GMA garnet were also proposed.

The cutting performance and the economics when using recycled and recharged GMA abrasives were evaluated in another study of Vu Ngoc Pi [4]. It was concluded that the cutting performance when cutting with recycled and recharged abrasives is higher than that when cutting with the new abrasive (about 17% when cutting with recycled abrasives and 10% when cutting with recharged abrasive). Also, cutting with those abrasives can reduce the total cutting cost and increase the profit rate significantly [4].

4. Recycling and recharging of supreme garnet

In this chapter, the recycling and recharging of Supreme garnet are investigated. In the study, the reusability of the garnet, the cutting performance, and the cutting quality of the recycled

and recharged abrasive are explored. Also, the optimum particle size for getting the maximum cutting performance for both recycling and recharging of Supreme garnet is determined.

4.1. Reusability of supreme garnet

4.1.1. Experimental setup

Figure 2 describes the experimental setup for determination of the reusability of the garnet. The cutting system consists of a M23120B Flow Waterjet machine and a cutting head with a focusing tube diameter of 1.02 mm and an orifice diameter of 0.33 mm. The workpiece material is SUS 304, the abrasive is IMC garnet #80, and the cutting regime is as follows: the water pressure of 350 MPa, the abrasive mass flow rate of 300 g/min, and the feed speed of 90 mm/min. For abrasive sieving, a sieve shaker and 11 sieves (ISO3310-1) are used. The nominal aperture sizes of the sieves are 63, 75, 90, 106, 125, 150, 180, 212, 250, 300, and 355 μm, respectively. To investigate the reusability of the first recycling, the abrasives after cutting are collected, washed, dried, chips separated, sieved, and sorted.

In AWJ cutting process, the fragmentation (or the breaking) of abrasive particles occurs in two stages [4]: during mixing process (due to the interactions between particles and the mixing chamber walls and focusing tube and between particles with each other) and during the cutting process (due to the interactions between particles with the workpiece and particles

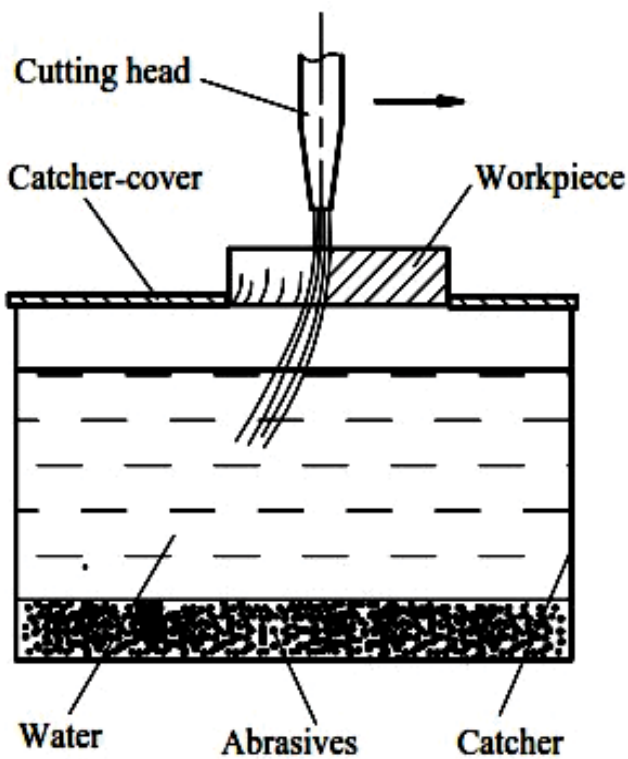

Figure 2. Experimental setup for collecting abrasives [4].

with each other). Therefore, studying the abrasive recycling needs an understanding of the fragmentation of abrasive particle in both above stages.

The experiment for investigating the abrasive fragmentation after focusing tube is the same as in **Figure 2**. However, in this experiment, no workpiece was used. After coming into water tank, the abrasives were collected and dried. After that, they were sieved and sorted into different sizes. The experiment was performed with four recycled abrasive samples (with particle sizes larger than 90, 106, 125, and 150 μm) and a new Supreme garnet sample.

4.1.2. Results and discussions

Table 1 presents the reusability of the garnet after the first cut. Similar to GMA garnet [19], the reusability of Supreme garnet decreases with the increase of the recycled particle size. It is noted that Supreme garnet can be reused better than GMA garnet. As it can be seen in **Table 1**, the reusability of Supreme garnet (with particles larger 90 μm) is 58.86%, while it is 53.64% with GMA garnet [19].

Figure 3 describes the relation between retained particle mass and the particle size after the mixing process. It is found that, with all abrasive samples, the retained particle mass with the size larger than 150 μm is nearly the same. Nevertheless, with the size smaller than 150 μm, the retained particle mass is significantly different from each other. Also, the retained particle mass of all recycled abrasive samples with the size smaller 150 μm is higher than that of the new ones.

Sieve size (μm)	**>90**	**>106**	**>125**	**>150**	**>180**	**>212**	**>250**
Reusability (%)	58.86	53.4	47.0	38.7	27.4	16.4	4.6

Table 1. Reusability after the first cut.

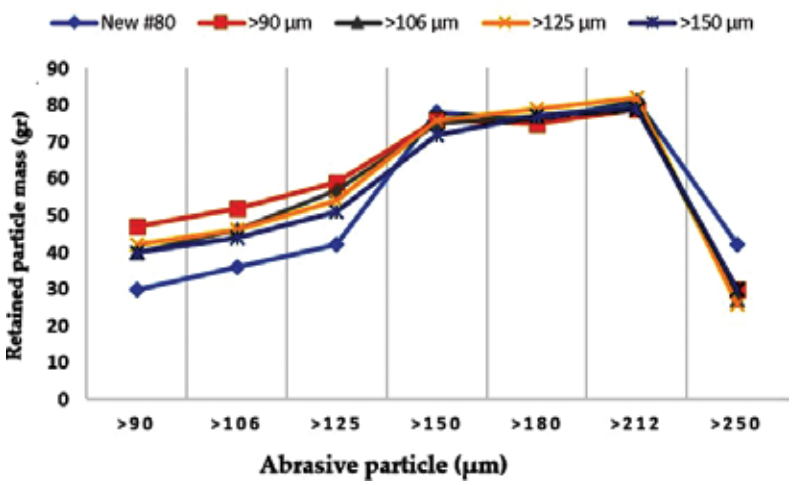

Figure 3. Retained particle mass versus recycled particle size after mixing process.

http://dx.doi.org/10.5772/intechopen.75180

4.2. Cutting performance and cutting quality of recycled abrasives

4.2.1. Experimental setup

Figure 4 shows the experiment setup for comparison of the cutting performance (or the maximum depth of cut) between the new and recycled abrasives. The workpiece in this experiment is described on **Figure 5**, and its material is SUS304. In the experiment, four samples of recycled abrasives (with particles larger than 90, 106, 125, and 150 μm) and a sample of new Supreme garnet #80 are used for the test. Each abrasive sample is tested with five cuts and with two replications. The AWJ cutting parameters used in the experiment include the water pressure of 350 MPa, the abrasive mass flow rate of 540 g/min, the orifice diameter of 0.33 mm, the nozzle diameter of 1.02 mm, and the feed speed of 100, 125, 150, 175, and 200 mm/min.

In order to investigate the effects of the recycled abrasives on the surface roughness, four recycled abrasive samples (as mentioned above) and a new Supreme garnet #80 are tested (with two replications) with the following cutting regime: the workpiece material of SUS304,

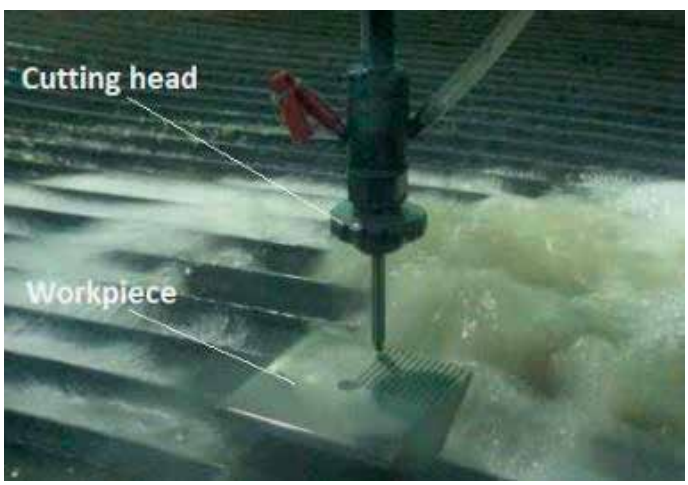

Figure 4. Experimental setup for determination of maximum depth of cut.

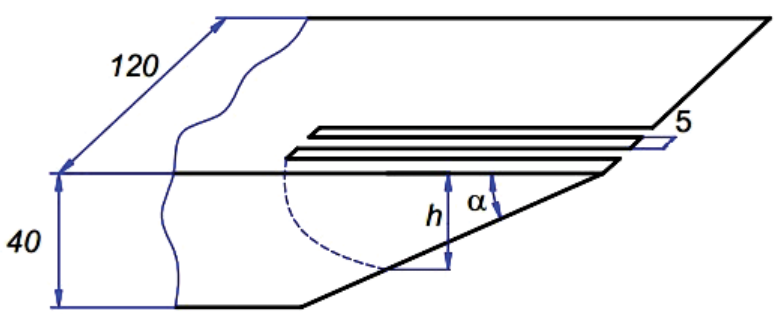

Figure 5. Workpiece used in experiment for determination of maximum depth of cut [20].

the water pressure of 350 MPa, the abrasive mass flow rate of 540 g/min, the feed speed of 125, 150, 175 and 200 mm/min, the focusing tube diameter of 1.02 mm, and the orifice diameter of 0.33 mm.

4.2.2. Results and discussions

Figure 6 shows the cutting performance of the recycled abrasives. It is noticed that the cutting performance of all recycled samples is slightly higher than that of the new Supreme garnet #80. This can be explained that after mixing process, with the new sample, the mass of retained particles with the size <150 μm is less than that of all recycled samples (**Figure 3**). Consequently, the number of recycled particles involved in the cutting process is higher than that of the new sample. Hence, the removed workpiece volume and therefore the cutting performance grow. It is also found that there is an optimum value of the recycled abrasive size (particle size larger than 90 μm) with which the cutting performance is maximum.

To evaluate the influence of recycled abrasives on the cutting quality, the surface roughness (Ra) is measured (**Figure 7**) at six values of the depth from 5 to 30 mm. **Figure 8** describes the average of the surface roughness of three replications of tests. It is detected that the surface roughness of the recycled abrasive is slightly lower than that of the new. The reason is that although the recycled particles are smaller than the new ones, they are sharper. As a result, the influences of the recycled abrasive size and shape on the surface roughness can be considered equivalent.

4.3. Cutting performance and cutting quality of recharged abrasives

4.3.1. Experimental setup

In order to find the optimum particle size of recharged abrasives, four samples of the first recycled abrasives (with the particle size larger than 90, 106, 125, and 150 μm) are recharged

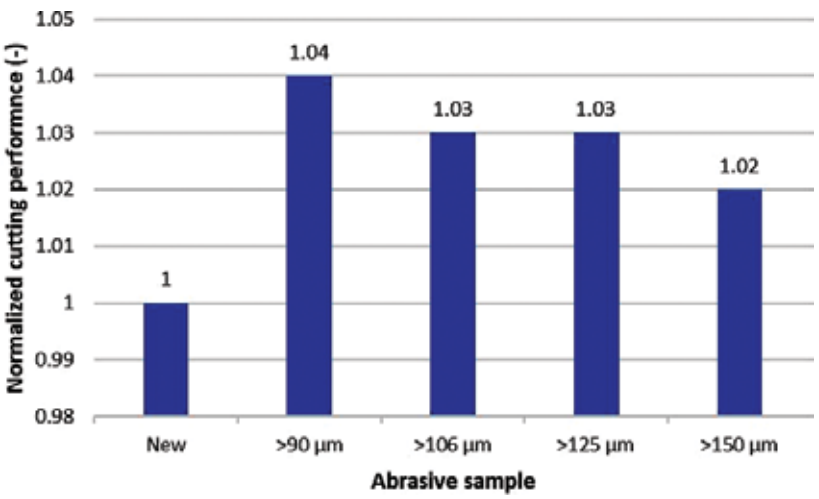

Figure 6. Cutting performance of recycled abrasives.

http://dx.doi.org/10.5772/intechopen.75180

Figure 7. Measurement of surface roughness.

with the new abrasive (Supreme garnet #80) for getting the same amount of abrasives (100%) (**Table 2**). To investigate the cutting performances of these recharged samples, experiments with the same setup as that for the cutting performance of the recycled abrasives (**Figure 4**) are carried out.

To investigate the effects of the recharged abrasives on the cutting performance and cutting quality, four recharged abrasive samples (as mentioned above) and a new Supreme garnet #80 are tested (with two replications). The cutting regime of these experiments consists of the

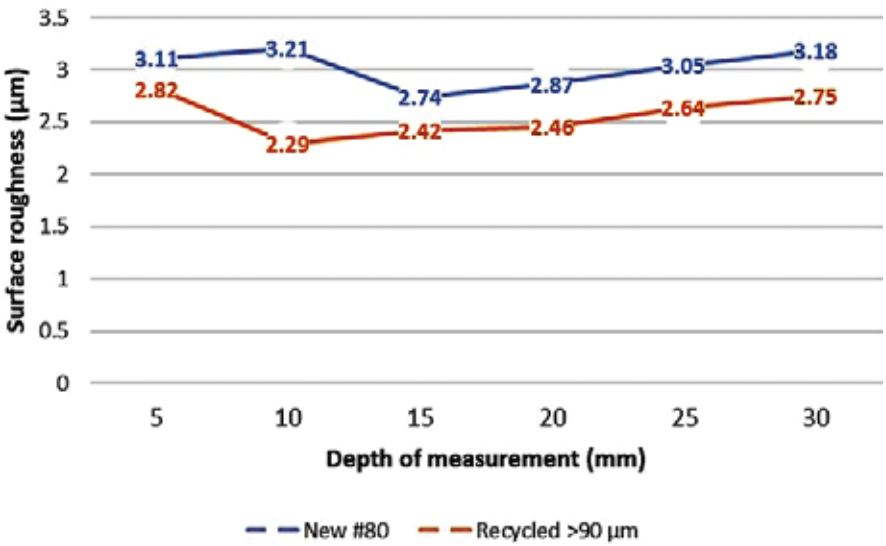

Figure 8. Surface roughness when cutting with recycled abrasives.

Sample	Sieve nominal aperture size (μm)	Reusability (%)	Recharged abrasive (%)
1	150	58.8	41.2
2	125	53.4	46.6
3	106	47.0	53.0
4	90	38.7	61.3

Table 2. Recharging abrasives.

workpiece material of SUS304; the water pressure of 350 MPa; the abrasive mass flow rate of 540 g/min; the feed speed of 125, 150, 175, and 200 mm/min; the focusing tube diameter of 1.02 mm; and the orifice diameter of 0.33 mm.

4.3.2. Results and discussions

Figure 9 presents the cutting performance of the recharged abrasives. It is observed that the cutting performance of all recharged samples is higher than that of the new Supreme garnet #80. The reason of that is the same with recycled samples (see Section 4.2.2): with all recharged samples, the mass of retained particles with the size smaller than 150 μm is higher than that of the new (see **Figure 10**). Hence, the particle in the recharged samples and then the particle number taking part in the cutting process increase. Consequently, the volume of removed work material growth and therefore the cutting performance increase. It is also detected that the particle size larger than 90 μm is the optimum value with which the cutting performance is maximum.

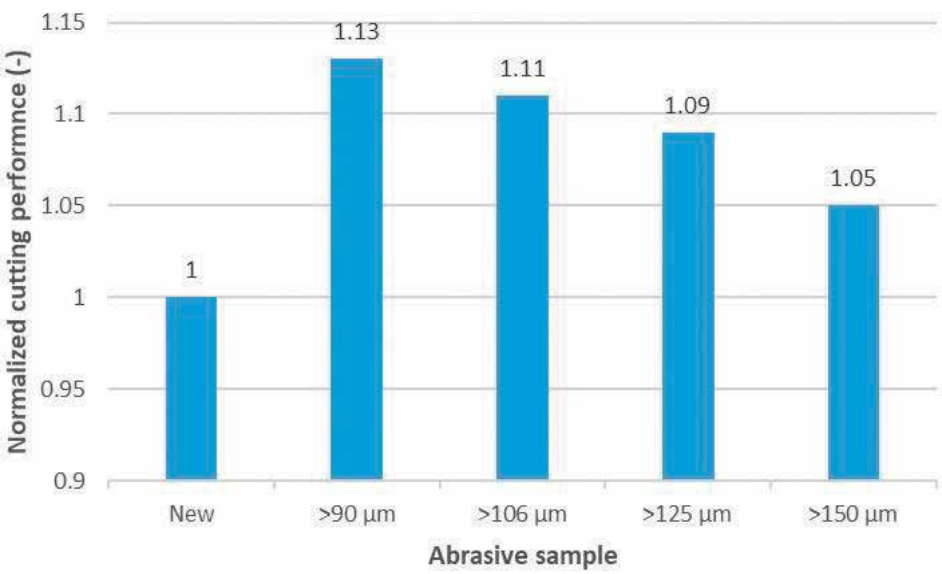

Figure 9. Cutting performance of recharged abrasives.

http://dx.doi.org/10.5772/intechopen.75180

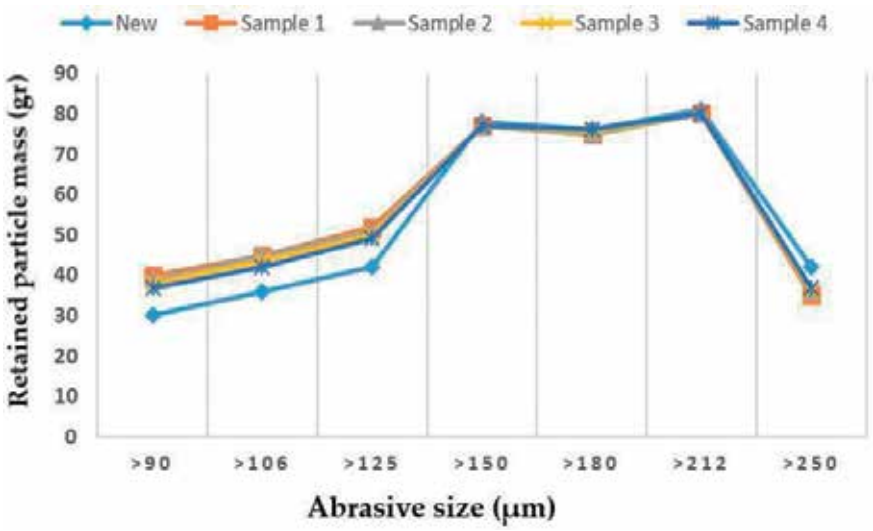

Figure 10. Retained particle mass versus recharged particle size after mixing process.

In order to evaluate the effect of recharged abrasives on the cutting quality, the surface roughness (Ra) is measured at six values of the depth from 5 to 30 mm. **Figure 11** shows the average of the surface roughness of three replications of tests. It is found that the surface roughness when cutting with recharged abrasive is slightly lower than that when cutting with new Supreme garnet #80. As it was explained above (in Section 4.2.2), in spite of the fact that the recharged particles are smaller than the new ones, they are sharper. Hence, the effects of the recharged abrasive size and shape on the surface roughness are considered equivalent.

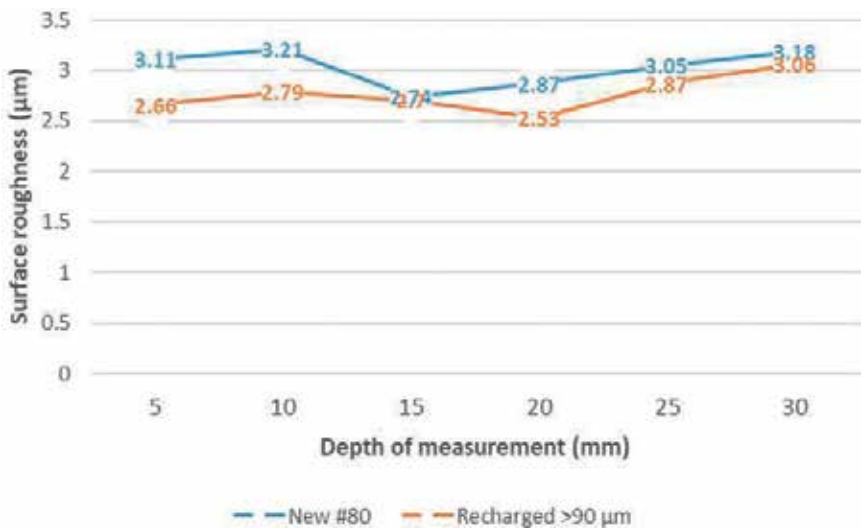

Figure 11. Surface roughness when cutting with recharged abrasives.

5. Conclusions

In this chapter, the investigation of recycling and recharging of Supreme garnet, including the reusability of the abrasive, the cutting performance, and the cutting quality of the recycled and recharged abrasives, has been carried out. Several conclusions can be obtained from the investigation as follows:

- The reusability of Supreme garnet is higher than that of GMA garnet. For example, with the particle size of >90 μm, the reusability of Supreme garnet is 58.86%, while it is only 53.64% for GMA garnet.
- The cutting performance of recycled and recharged Supreme abrasives is slightly higher than that of the new Supreme garnet #80.
- The optimum particle size for the cutting performance is larger than 90 μm for both the recycling and the recharging.

Author details

Vu Ngoc Pi[1]* and Tran Quoc Hung[2]

*Address all correspondence to: vungocpi@tnut.edu.vn

1 Thai Nguyen University of Technology, Thai Nguyen City, Vietnam

2 Hanoi University of Industry, Ha Noi City, Vietnam

References

[1] Summers DA. Waterjet Technology. Chapman & Hall; UK. 1995

[2] Tikhomirov RA, Babanin VF, Petukhov EN, Starikov ID, Kovaleb VA. High-Pressure Jetcutting. ASME Press; USA. 1992

[3] Hashish M, Kirby M, Pao Y-H. Method and apparatus for forming a high velocity liquid abrasive jet. United States Patent No. 4,648,215. Filed October 7, 1985, Issued March 10, 1987

[4] Vu Ngoc Pi. Performance enhancement of abrasive waterjet cutting [PhD thesis]. Delft University of Technology; 2008

[5] Blickwedel H. Erzeugung und Wirkung von Hochdruck-Abrasivstrahlen. VDI Fortschritt – Berichte. Reihe 2, Nr. 206, 1990

[6] Zeng J, Munoz J. Optimization of abrasive waterjet cutting- the abrasive issues. SME Techincal Paper. 1994:MR94-M247

[7] Hashish M. Optimization factors in abrasive-waterjet machining. Journal of Engineering for Industry. 1991;**113**:29-37

[8] Vu Ngoc Pi, Hoogstrate MA, Karpuschewski B. Cost optimization and a new and effective way of using AWJ nozzles. In: 5th International Conference of PhD Students; Hungary. 2005. pp. 153-165

[9] Chalmers EJ. Effect of parameter selection on abrasive waterjet performance. In: 6th American Water Jet Conference; August 24-27, 1991; Houston, Texas. pp. 345-354

[10] Guo NS. Schneidprozeß und Schnittqualitat beim Wasserabrasivstrahlschneiden, VDI-Fortschritt-Berichte, Reihe 2, Nr. 328. 1994

[11] Guo NS, Louis H, Meier G, Ohlsen J. Abrasive water jet cutting—Methods to calculate cutting performance and cutting efficiency. In: Rakowski, editor. Geomechanics 93. Balkema, Rotterdam; 1994. pp. 291-299

[12] Hoogstrate AM, Susuzlu T, Karpuschewski B. Abrasive waterjet cutting beyond 400 MPa. In: 2005 WJTA American Waterjet Conference; August 21-23, 2005; Houston, Texas

[13] Ohlsen J. Recycling von Feststoffen beim Wasserabrasivestrahlverfahren. VDI Fortschritt-Berichte, Reihe 15, Nr. 175; 1997

[14] Barton RE. A safe method of cutting steel and rock. In: 6th International Symposium on Jet Cutting Technology; BHRA Fluid Engineering, Cranfield; 1982. pp. 503-518

[15] Labus TJ, Neusen KF, Alberts DG, Gores TJ. Factors influencing the particle size distribution in an abrasive waterjet. Journal of Engineering for Industry. 1991;**113**:402-411

[16] Louis H, Meier G, Ohlsen J. Analysis of the process output in abrasive water jet cutting. In: 8th American Water Jet Conference; August 26-29, 1995; Houston, Texas. pp. 137-151

[17] Kantha Babu M, Krishnaiah Chetty OV. A study on recycling of abrasives in abrasive water jet machining. Wear. 2003;**254**:763-773

[18] Kantha Babu M, Krishnaiah Chetty OV. Studies on recharging of abrasives in abrasive water jet machining. International Journal of Advanced Manufacturing Technology. 2002;**19**:697-703

[19] Ngoc Pi V, Gonfiotti P, Hoogstrate AM, Karpuschewski B. A study on abrasive recycling and recharging in Abrasive Waterjet (AWJ) Machining. International Journal of Machining and Machinability. 2009;**6**(3/4). DOI: 10.1504/IJMMM.2009.027325

[20] Pi VN, Chau HV, Hung TQ. A study on recycling of supreme garnet in abrasive waterjet machining. Applied Mechanics and Materials. 2013;**248**:499-503. DOI: 10.4028/www.scientific.net/AMM.248.499

Chapter 9

Nanostructural Deformation in Brittle-Ductile Compounds and Its Application in Fabricating Ductile Nanoparticles

Babak Alinejad and Yazdan Zare

Additional information is available at the end of the chapter

http://dx.doi.org/10.5772/intechopen.76787

Abstract

The ball-milling process involves both fracturing and welding of particles. Particles of ductile materials are very likely to attach to each other when entrapped between balls. Therefore, conventional milling methods fail to grind ductile materials into nanoparticles. However, using brittle particles together with the starting materials, one can fracture and highly activate ductile particles through planetary ball milling. During the milling process, brittle particles are easily fractured down, and their sharp edges chop the particles of the ductile materials incessantly into pieces until both ductile and brittle particles are nano-sized (a process which is unlikely, if not impossible, to accomplish by ball milling of ductile materials alone). In this chapter, the effects of ball milling of ductile materials (e.g., graphite, aluminum, and zinc) together with a brittle material (here, NaCl), for preparation of metal nanoparticles or metal oxide nanoparticles are investigated. A theoretical explanation of the mechanism is also presented based on the facts and practical measurements.

Keywords: ball milling, brittle, ductile, nanoparticle, nanochopper, graphene

1. Introduction

In every branch of material engineering, it happens very frequently that a bulk material is ground into very fine particles. Therefore, material engineers are quite acquainted with grinding process. Having basic principles in common, grinding methods may be slightly different depending on the characteristics of the material that is about to be ground, ultimate size of particles after grinding, energy- and time-consumption condensations (which may also be referred to as economy of the process), etc.

One of the most routine methods for grinding is planetary ball milling in which a given material is loaded in a jar that is partially filled with balls made of a harder material (e.g., stainless steel and zirconia). The jar is then sealed and rotates multi-directionally by means of electromotors. The bulk material is gradually ground as the balls exert large enough compressive and shear stresses on it to fracture it into fine particles. For most of the materials, the longer the ball-milling duration, the smaller the particle size. However, as we will see soon in this chapter, this is not always the case. Particles of ductile materials rejoin together to form larger particles when they are shoved into each other by the balls (this phenomenon is referred to as *cold-welding*). Hence, the ball milling does not necessarily lead to size reduction of the particles.

Introduced in this chapter is a new, simple method for ball milling of ductile materials (the method has already been examined for some ductile materials). When the materials to be ground are all ductile, then a brittle material should be added to the jar to serve as a chopper and prevent from cold-welding of the ductile materials. Using this method, one can obtain nanoparticles of ductile materials by ball milling [1–5]. The brittle choppers also undergo size reduction down to nano size during the ball milling. Thus, they are referred to as nanochoppers in this chapter.

Along with their brittle nature, the nanochoppers should also meet some other requirements. They, for example, must not react with the starting materials. They should be harder than the starting materials, nontoxic, abundant, and economic. However, nanochoppers must have another characteristic which is of great importance: they must be easy to remove from the product, leaving no vestige.

Consequently, the overall process of obtaining nano-sized powders of ductile materials consists of two steps. The first step is ball milling of the starting materials together with a brittle material, and the second step is removal of the brittle material from the product. The latter step, however, may be accomplished by different techniques depending on the characteristics of the brittle material and ultimate objective of producing the powder. The next three sections of this chapter consider the method according to the final purpose of the ball milling: production of metal nanoparticles, production of hydrogen by means of metal nanoparticles, and production of metal oxide nanoparticles.

2. Mass production of nanoparticles of ductile materials

When one's final objective is to produce nanoparticles of a ductile metal, conventional ball-milling procedure may not come in handy as it fails to downscale the ductile metal particles. At the beginning of ball-milling process, the bulk material is fractured into smaller pieces under the pressure of the balls. However, the rate of size reduction of particles decreases as the time passes and eventually approaches to zero [6]. That is, the further ball milling does not lead to smaller particles because the rate of fracture is very low and is almost equal to the rate of cold-welding. There are several reasons for low rate of size reduction after long time. Firstly, fine particles are very unlikely to be entrapped between two balls, and if they are, the stresses exerted from the balls do not break them into pieces. Instead, the ductile particles are

only kneaded and deformed or are thrusted into each other to make a larger particle. Also, the intersection of the balls is too large (compared to the size of the particles) to rip the particles apart. When the balls are rolling against each other, they buffet the particles about, making them more susceptible to agglomerate. Under such circumstances, one should add balls with radii comparable to the size of the particles. In practice, particles of a harder, brittle material can play the role of the tiny balls. If a brittle material is added to the jar at the beginning of the ball-milling process, then it is also ground into smaller pieces, and after adequately long time, the brittle particles are nano-sized and act as nanochoppers. These nanochoppers cut the ductile particles into pieces and reduce their sizes.

Some practical instances of application of this method are introduced here. First, we show how to prepare graphene nanoflakes, and then we report the experiment conducted to extend the methodology to mass production of aluminum nanoparticles.

2.1. Preparing graphene nanoflakes

Graphene has a two-dimensional, hexagonal lattice that is composed of sp2-bonded carbon atoms [1, 7, 8]. It was first invented through micromechanical cleavage of graphite in 2004 [9], and its extraordinary characteristics [10, 11] have drawn the scientists' and engineers' attentions toward its promising applications in different fields such as composite materials, transparent conductive films, ultrasensitive gas sensors, and solar cells [12–14]. Various methods for producing graphene flakes have so far been invented which are commonly categorized into two groups: bottom-up and top-down methods. In bottom-up methods, the hexagonal carbon structure is formed from molecular precursors (e.g., epitaxial growth of graphene on substrates) [15, 16] and thermal decomposition of SiC [17]. These production processes, however, are very energy-consuming, and their yield is low. They also need expensive equipment. In the methods classified as top-down group, on the other hand, graphene layers are peeled out or extracted off the graphitic microstructures such as carbon nanotubes, carbon fibers, and graphite (or graphite oxide) by chemical, electrochemical, or physical techniques [18–20]. These techniques typically include complicated syntheses, harsh oxidizers [21], or immoderate utilization of organic solvents for exfoliation [22–24]. To produce graphene flakes in larger quantities, one may also choose mechanical milling method because it is relatively convenient and economic. However, if graphite powder is solely ground in a planetary ball mill, then the milling process augments the stress in the graphite structure [25–27]. Wet environments, on the other hand, degrade the quality of the product because liquid solution in the jar may react with the balls and the jar leaves some impurities in the product [28]. Nevertheless, as explained above, there is a convenient method for reducing the size of graphite particles incessantly by addition of a brittle material to the planetary ball mill. Owing to its convenience and low cost of involved materials, this approach can be easily scaled up.

Sodium chloride (NaCl) is used as the brittle material for ball milling of natural graphite powder. NaCl is added directly to the jar with graphite and ball milled for 2–5 h. The ball-milling process specifications are listed in **Table 1**. The resultant powder is then leached with copious amount of water in ultrasonic bath and then dried at 80°C under vacuum.

NaCl to graphite molar ratio	3
Ball-to-powder weight ratio	20
Rotational speed of the planetary ball mill	350 rpm
Atmosphere	Argon
Atmosphere pressure	0.4 MPa
Ball-milling duration	2–5 h

Table 1. Ball-milling specification for preparing graphene nanoflakes.

The structural and morphological characteristics of a powder milled under abovementioned condition are reported to be as follow:

Figure 1 demonstrates the XRD pattern of the graphite powder milled together with NaCl (the salt is removed by water). The diffraction peak (002) at $2\theta = 26°$ corresponds to a d-spacing of 0.34 nm that approximately matches the graphite (JCPDS No. 75–1621). The width broadening of the peak may be attributed to the lattice strain and size reduction of the particles.

TEM image of the produced graphene is shown in **Figure 2**. One may easily recognize the distinct layers of graphene (with approximate size of 200 × 50 nm^2). As seen in the figure, the graphene flakes have ragged edges which are cut off by brittle salt particles.

Figure 3 shows the topology of the graphene powder obtained by AFM that, consistent with TEM image, confirms the ragged edges of the graphene layers.

Specific surface area of the graphene flakes produced by brittle-ductile milling technique is reported to be 524.4 m^2/g. This value is close to that of the graphene nanoflakes obtained using chemicals and microwave radiation, as reported by Sridhar et al. [29].

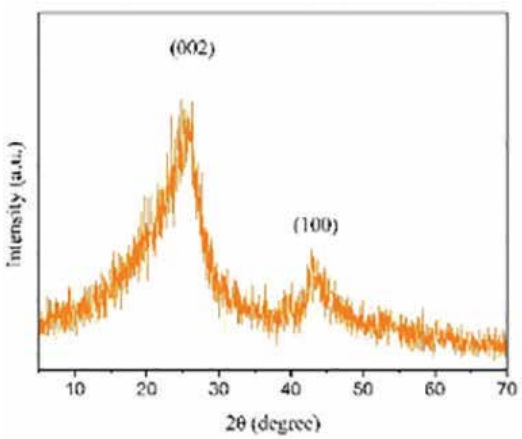

Figure 1. XRD pattern of graphite powder that is milled together with salt (salt is then washed away by water). Source: Ref. [1], Copyright @ 2017 Word Scientific.

http://dx.doi.org/10.5772/intechopen.76787

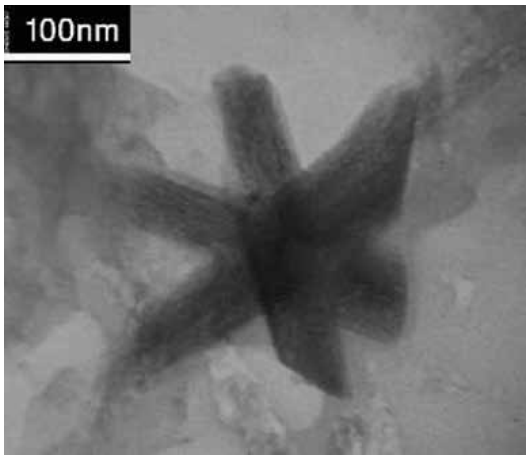

Figure 2. TEM image of graphene powder after 2 hours of milling with NaCl (salt is removed by water). Source: Ref. [1], Copyright @ 2017 Word Scientific.

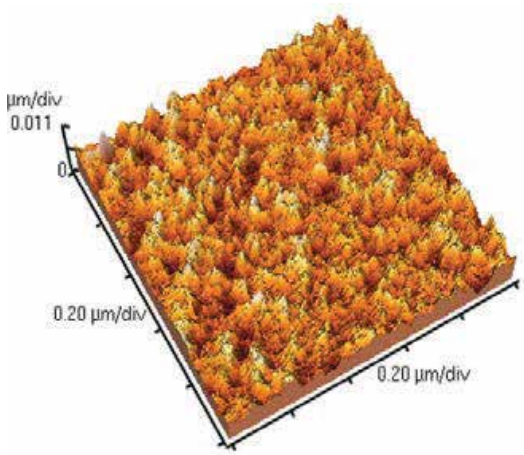

Figure 3. AFM image of the graphene flake. Source: Ref. [1], Copyright @ 2017 Word Scientific.

The average size of the particles reduces from 200 to 400 nm to about 50–150 nm as the ball-milling duration increases from 2 to 5 h. Size of salt particles also decreases during the ball milling [2] as shown in **Figure 4**. Average size of salt particles is reported to be about 150 nm after 5 h of ball milling. Owing to their brittle nature, salt particles fracture and take sharp edges by which they can cut graphite particles into smaller pieces. High salt-to-graphite molar ratio (3,1), on the other hand, retards the agglomeration of graphene flakes.

Moreover, graphene layers are exfoliated due to the sheer stress caused by random multiaxial collision of the balls which is also assisted by salt particles. Because of the random nature of the collisions and the random shape and position of the salt particles, they may exert either compressive forces that chop the graphene particles into smaller pieces or shear forces that exfoliate the layers (**Figure 5**).

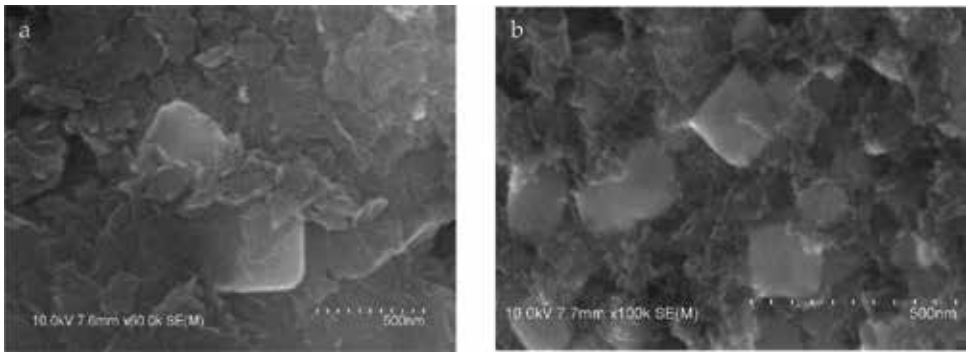

Figure 4. SEM images of graphite powder that is milled together with salt for (a) 2 h and (b) 5 h [1]. Source: Ref. [1], Copyright @ 2017 Word Scientific.

Figure 5. Exfoliation and fragmentation of graphene. Source: Ref. [1], Copyright @ 2017 Word Scientific.

As a nanochopper, salt meets almost all the requirements: it is not expensive, nor toxic; it is abundant and can be easily recycled; and, above all, it conveniently leaches out to water. Hence, this method can be employed for mass production of graphene nanoflakes because it is simple, eco-friendly, and economic.

2.2. Preparing nanoparticles of aluminum

The popularity and importance of aluminum nanoparticle are well understood by knowing its wide application in propellants and pyrotechnics. The methods of manufacturing aluminum nanoparticle are generally classified into two categories: methods involving vapor phase condensation and liquid phase chemistry. One of the vapor phase condensation methods is exploding electronically heated wires [30]. Aluminum nanoparticles, for example, are produced by condensing aluminum vapor generated by passing a strong electrical current through a thin aluminum wire. Some other techniques are occasionally used to prepare metal vapor, namely, radiative heaters, induction heaters or plasma, lasers, and electric arcs. All these techniques require a neutralized gaseous environment whose pressure strongly affects size distribution of resultant nanoparticles. At low pressures, condensation leads to formation of nano-scaled particles. The higher the pressure, the larger the particles. On the other hand, increasing the pressure increases the yield [31]. The effects of other experimental parameters, such as gaseous environment and electric pulse characteristics, are elaborately reported in [31].

All abovementioned techniques suffer from some disadvantages. Production rate is generally low in all of them. Moreover, distribution of particles size extends over a broad range from 10 nm to microns depending on the energy given to the metal. The higher the energy, the wider the distribution. On the other hand, higher energy is required for increasing the yield. This implies that there is a trade-off between the yield and size uniformity. Of course, a narrower range (i.e., uniform distribution of the particle sizes) is generally preferred.

Variations of the bulk aluminum heating technique are reported in [32] in which aluminum is ablated by an Nd-YAG laser.

The other methods of metal nanoparticle production (commonly referred to as liquid phase chemistry) are more chemical. Like all other liquid phase chemistry techniques, measured amount of starting solutions are mixed and stirred slowly, and then the product is dried. As the process is time-consuming, the methods are not appropriate for mass production. In practice, the methods require essential modifications to be qualified enough for producing nanoparticles in large quantities.

Inspired from the method introduced above for preparing graphene nanoflakes, we conducted series of experiments for preparing aluminum nanoparticles. Again, salt was used as the brittle material to serve as nanochopper. Following is the report of the experiments:

Elemental Al powder (99% purity, particle size <100 μm, Fluka) and NaCl (100–200 μm) were ground in a planetary ball mill. The jar of the ball mill was a 125 mL stainless-steel jar with radius of 15 cm. **Table 2** summarizes the specifications of the ball-milling process. The salt-to-aluminum molar ratio (hereafter denoted by η) was 2. To compare the effect of salt particles on size reduction of aluminum particles, the experiment was repeated without salt (η = 0).

After the milling process accomplished, the salt particles were washed away by immersing the powders in pure water. To prevent aluminum from reacting with water, the process of salt removal was performed using cold water at 1°C and as fast as possible. Resultant aluminum powders were characterized by scanning electron microscopy (SEM, Cambridge S 360) and X-ray diffraction (XRD, Philips 3710 W X-ray diffractometer with CuK α, λ = 1.54184 Å). The specific surface area of the powders was determined by means of nitrogen adsorption using Brunauer-Emmett-Teller method (BET-N_2 Micrometrics Gemini 2375).

As demonstrated in **Figure 6a**, ball-milling aluminum without salt (η = 0) has eventually reduced the size of particles to 10 μm. However, the morphology of particles is laminar and

NaCl to aluminum molar ratio (η)	0 and 2
Ball-to-powder-weight ratio	10
Rotational speed of the planetary ball mill	270 rpm
Atmosphere	Argon
Atmosphere pressure	0.4 MPa
Ball-milling duration	20 h

Table 2. Ball-milling specification for preparing aluminum nanoparticles.

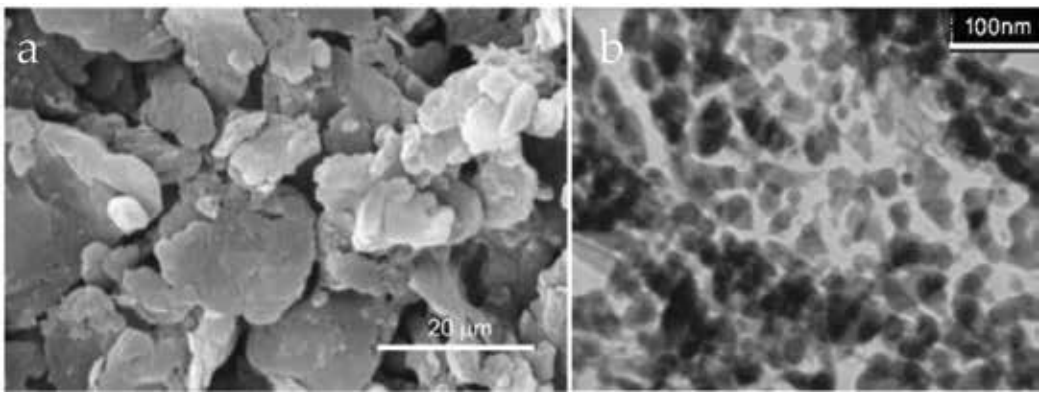

Figure 6. TEM image of ball-milled aluminum particles without (a) and with (b) salt, after removing the salt particles by cold water. Source: Reprinted from Ref. [5], Copyright 2009, with permission from Elsevier.

wrinkled. To reduce the size of the particles, aluminum was milled with high molar ratio of salt ($\eta = 2$). This helps aluminum particles to reach smaller sizes. Salt particles have sharp edges and are hard enough to chop aluminum particles. Due to their brittle nature, they fracture and break into smaller particles during the milling process and cut aluminum particles. Meantime, because of high η, there is a little chance for aluminum particles to meet and cold-weld. **Figure 6b** shows the micrograph of aluminum powder milled together with salt. The size of aluminum particles is decreased to less than 50 nm. Specific surface area of the powder is about 40.9 m^2/g.

Aluminum particles prepared by other methods have a hard aluminum oxide crust, while this method leads to nanoparticles with a soft aluminum hydroxide crust which is expected to show better mechanical, consolidation, and sintering behavior. Furthermore, nanoparticles produced by this method have higher lattice residual strain (cf. Section 3 of this chapter). Consequently, the aluminum nanoparticles are more active because mechanical milling causes various defects (dislocations, vacancies, grain boundaries, etc.) in them.

3. Production of hydrogen using metal nanoparticles

Environmental pollutions are one of the most serious challenges during the recent decades, and fossil fuels have the most contribution in the crisis [2]. On the other hand, fossil fuels are not renewable and will run out sooner or later. Consequently, the energy crisis has drawn scientists' attention to eco-friendly and recyclable fuels. One of the best candidates is hydrogen which is currently produced through various methods such as biological [33], water electrolysis [34], and chemical methods [35]. These methods suffer from some disadvantages: they are costly, they have typically low efficiency, and they consume fossil fuels which are neither clean nor recyclable [36, 37].

Another challenge with hydrogen as a fuel is its storage. Since the volumetric density of hydrogen is low, it needs very large storages (at 700 bars, volume of storage required for hydrogen is

about six times that for gasoline with the same energy content). The ignition energy of hydrogen, on the other hand, is 0.03 mJ, implying that it is extremely flammable [38], a fact that must be considered in designing hydrogen storage. Thus, it sounds quite reasonable idea to eliminate the need for the storage by producing hydrogen on demand. There are some hydrogen resources in the nature from which hydrogen may be extracted through a chemical process. Among all, water is the best candidate because its hydrogen content is relatively high (111 kg/m^3), it is abundant in nature, it is not costly, and it can be recycled by hydrogen combustion.

The chemical reaction through which hydrogen is obtained from water is simple: oxidation of the active metals. The only challenge is to find proper metal. According to Kravchenko et al., aluminum is the most eligible metal [39], because it is recyclable, it is the most abundant metal in the earth's crust, and its density is very low compared to other metals. The chemical reaction between aluminum and water is as follows:

$$Al + 2H_2O \rightarrow AlOOH + {}^3/_2\, H_2 \tag{1}$$

As seen, the byproduct of the reaction is aluminum oxide hydroxide which is eco-friendly and has many applications (e.g., water conditioning, papermaking, alumina production, fire prevention, and so on).

In normal condition, however, reaction (1) cannot proceed because there is a passive layer of aluminum oxide over the aluminum particles, preventing the inner aluminum atoms from reaction with water. Some solutions to the problem has been so far proposed, each of which having its own disadvantages. Immersing the aluminum in NaOH, for instance, removes the aluminum oxide layer; but it is intensely corrosive and may corrode the instruments [40–42]. Amalgamation of aluminum is another suggestion, but it involves dampening of aluminum surface with eutectic gallium-indium or mercury which are toxic and/or costly [43].

Another method for continuous hydrogen generation from aluminum is using aluminum powder with adequately small particles. This implies higher specific surface area of the powder and, consequently, more activity of the aluminum powder [44, 45]. As explained in the previous section, ordinary ball milling is unable to reduce the size of aluminum particles down to nano size because aluminum is a ductile metal. Even milling the aluminum particles together with brittle hydrides and salts (e.g., $MgCl_2$, KCl, NaCl, CaH_2, and MgH_2) with brittle-to-ductile molar ratios less than 0.1 has reportedly failed to decrease the size of the aluminum particles [46]. Also, grinding aluminum metallic composites (e.g., aluminum-bismuth) together with inorganic salts only leads to galvanic corrosion and ionic conductivity. This method provides the energy required for the reaction by the heat emerged from exothermic solution of salt. In spite the fact that the method is efficient in energy consumption, it is still ineffective in particle size reduction [46, 47], and moreover, the involved materials are costly, corrosive, and toxic.

As described in the previous section for preparing the aluminum nanoparticles, NaCl is added to the ball mill to serve as nanochopper because it is accessible, economic, easily soluble in water, nontoxic, and eco-friendly. However, η should be much higher than the reported values. Higher η (up to 15 times those reported in [46]) not only reduced the size of the aluminum particles but also increases defects in aluminum crystal by embedding salt gates [2].

As a result, specific surface area of the powder increases drastically, and reaction (1) can proceed until all aluminum content is consumed.

Since the method is simple and involves accessible materials (aluminum, salt, and water), it may be conveniently used for on-demand hydrogen generation:

For generating hydrogen from aluminum nanoparticles, one may start from elemental Al powder and ordinary salt, NaCl (100–200 μm). The mixture of aluminum and salt should be ball milled for 20 h. Ball-milling specifications are summarized in **Table 3**. The η may be selected to be as low as 0.2, but higher η leads to better result. After the milling process, about 150 mL water at a temperature of 70°C is added to the jar. Hydrogen is then released that should be condensed and dried for designated usage.

Figure 7 shows the yield of the reaction (1) as a function of time elapsed after adding water to the jar for different η's. As one may see in the figure, the efficiency of the samples with more

NaCl to aluminum molar ratio (η)	0.1, 0.2, 0.5, 1.0, and 1.5
Ball-to-powder weight ratio	20
Rotational speed of the planetary ball mill	270 rpm
Atmosphere	Argon
Atmosphere pressure	0.4 MPa

Table 3. Ball-milling specification for preparing aluminum nanoparticles for hydrogen generation.

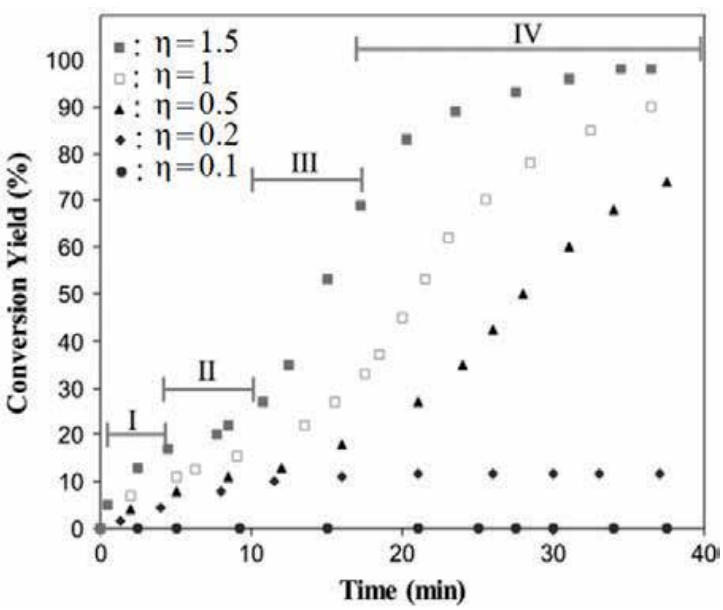

Figure 7. Conversion yield as a function of reaction time for samples with different η. Source: Reprinted from Ref. [2], Copyright 2009, with permission from Elsevier.

salt content is higher. The reaction time may be divided into four regions: In the first region, about the first 5 minutes of milling, hydrogen is mainly generated from the hydration of fresh surfaces. The higher the η in this region, the faster the reaction. This is mainly because smaller particles imply higher specific surface area. The reaction slows down as the passive AlOOH layer is formed over the surface of the particles (region II). The reaction accelerates again in region III when the salt gates dissolve, exposing fresh aluminum to water and letting water to penetrate to the core of the particles. The higher the η, the more surface of fresh aluminum and, hence, the more hydrogen generation. When all the fresh surfaces undergo the reaction, the passive AlOOH layer will eventually hinder the reaction (region IV). Almost all the aluminum atoms in the sample ball milled with $\eta = 1.5$ have undergone the reaction, while ball milling with $\eta = 0.1$ has no considerable effect on the yield. The highest rate of hydrogen generation happens in region III of the sample with $\eta = 1.5$ (75 mL/min per 1 gr of Al).

Unlike other methods (based on hydrogen generation using aluminum in which hydrogen generation is stopped when aluminum particles are covered by a layer of aluminum oxide), all the aluminum contents react with water when the particles are adequately small.

Continuous hydrogen generation may be explained as follows: Salt particles cut the aluminum particles and form local gates on the newly exposed surfaces. They also fracture into smaller particles during the ball milling due to their brittle nature. Salt particles have sharp edges and are harder than aluminum particles. During the ball milling, they rip through aluminum particles making local gates in them. When the salt particles are washed away, fresh surfaces are exposed to water.

Figure 8 is a SEM image of a salt particle among the aluminum particles for a sample with $\eta = 0.5$. Adding more salt to the jar in ball milling (i.e., higher η), of course, leads to development of more salt gates. Thus, higher η rises the kinetics of hydrolysis reaction by increasing the specific surface area of the aluminum particles in two ways: reducing the size of aluminum particles and developing salt gates in them.

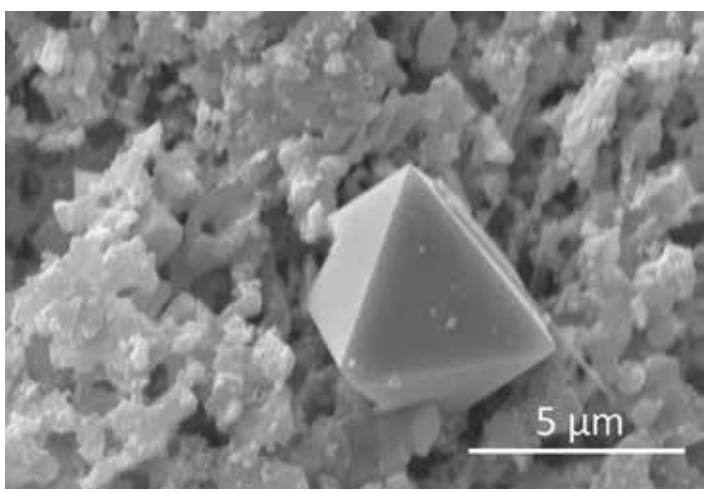

Figure 8. Salt nanochoppers in the context of aluminum nanoparticles. Source: Reprinted from Ref. [2], Copyright 2009, with permission from Elsevier.

It is worth mentioning that there are, of course, some inhibitors (e.g., stearic acid) that are assumed to prevent cold-wedding. However, they evaporate during the ball-milling process which relatively takes a long time. Therefore, they do not practically avoid the cold-welding in long-time ball milling. Furthermore, since the inhibitors are greasy, they prevent aluminum particle from reacting with water. Using salt brittle particles (with $\eta > 1.5$), one can obtain aluminum powder with particle size of about 50 nm and specific surface area of 40.9 m^2/g. This means that water can reach to the core of the particles and the reaction can proceed to release their innermost hydrogen contents. Moreover, mechanical milling gives rise to various defects in aluminum particles such as vacancies, dislocations, grain boundaries, etc.

Table 4 summarizes the lattice strain and crystallite size of the powders. The values are calculated by line broadening of XRD peaks and Williamson-Hall technique. This table suggests that adding salt to the ball mill increases the lattice strain, the fact that is also supported by XRD patterns of the samples milled with and without salt. **Figure 9** shows the XRD pattern of the samples ball milled with $\eta = 0$ (no salt) and $\eta = 1.5$. The inset in this figure magnifies the

η	Crystal structure (Å)	Crystalline size (nm)	Lattice strain (%)
0.0 (no salt)	Cubic (a = 4.046(2))	42.22(1)	0.61(4)
1.5	Cubic (a = 4.44(3))	43.13(3)	0.50(1)

Source: Reprinted from Ref. [2], Copyright 2009, with permission from Elsevier.

Table 4. Crystalline characteristics of aluminum powders milled with $\eta = 0$ (no salt) and $\eta = 1.5$.

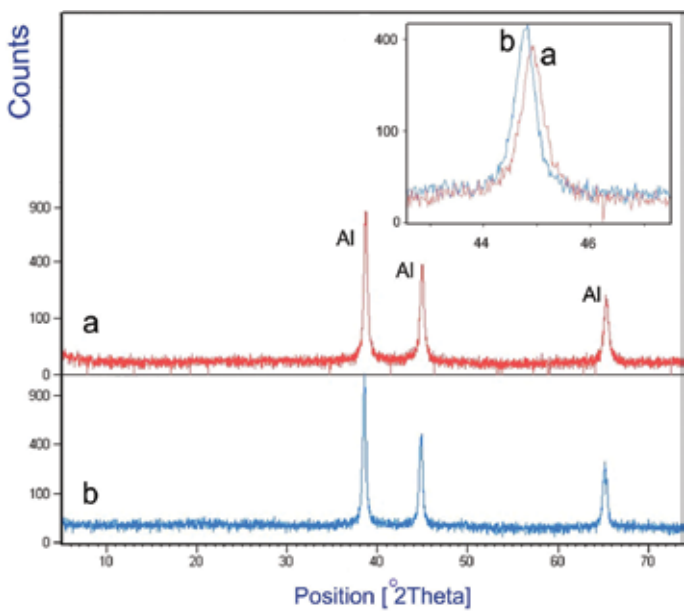

Figure 9. XRD pattern of the samples ball milled with $\eta = 1.5$ (a) and $\eta = 0$ (no salt) (b). The inset magnifies the shift of (200) peaks in the samples. Source: Reprinted from Ref. [2], Copyright 2009, with permission from Elsevier.

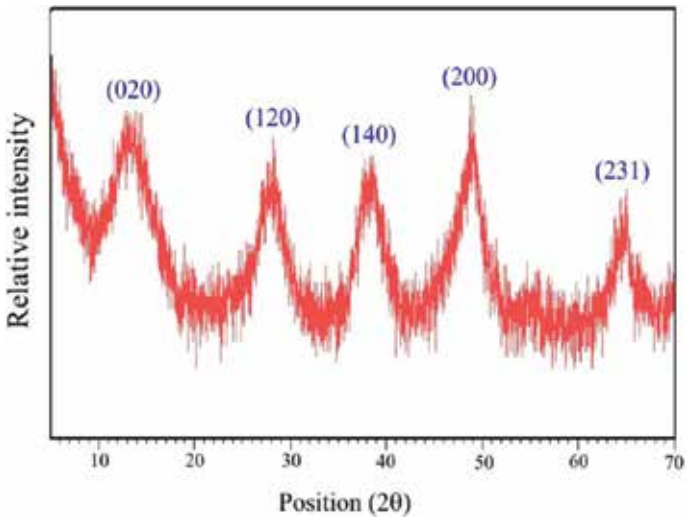

Figure 10. XRD pattern of the sample ball milled with η = 1.5 after reacting with hot water. The peaks correspond to AlOOH, and there is no evidence of aluminum. Source: Reprinted from Ref. [2], Copyright 2009, with permission from Elsevier.

XRD differences of the two samples. The lattice strain developed by ball milling provides a driving force that results in more corrosion or oxidation [14].

On the other hand, aluminum-water reaction is exothermic which helps the reaction proceed spontaneously. During hydrolysis, water temperature increases from 70°C to maximum of 74°C. Release of hydrogen in the interface of aluminum and aluminum hydroxide gel increases the porosity, letting water penetrate deep inside the aluminum particle and react with innermost atoms. X-ray diffraction pattern of the powder milled with η = 1.5 after reacting with hot water is shown in **Figure 10**, which is in good agreement with the characteristic spectrum of AlOOH crystal in the JCPDS database, except for the broader peaks due to a lower crystallinity. Aluminum is absent in the diffraction pattern, implying that reaction has reached the core of aluminum particles and entire aluminum powder has turned into AlOOH.

4. Production of metal oxide nanoparticles

The same method as explained above may be employed to prepare nanoparticles of ductile metal oxides. To examine the method for a different ductile metal, we selected a metal that its oxide is of great importance and has many applications: zinc oxide.

Even in its bulk state, zinc oxide has interesting properties: it is electrically stable with a direct band gap of 3.37 eV; it is transparent for visible light; it is abundant and nontoxic. Owing to its fabulous properties, it is widely used in various field of industry such as sensors, optoelectronic devices, solar cells, catalysts, field emission, data storage, etc. [48, 49]. On the other hand, due to its hexagonal Wurtzite structure and polar crystal surfaces, zinc oxide can take

on different nanostructures (e.g., nanorods, nanotubes, nanobelts, and nanosheets) only by restraining certain direction(s) from growing [50, 51]. The methods by which one can produce the different nanostructures are generally categorized into two groups: vapor phase process and solution phase route. The first group consists of physical vapor of the deposition, vapor phase transport and some other methods [52]. All these methods, however, have some disadvantages in common. They, for instance, require high temperatures to accomplish. Also, they need costly equipment and accomplish only when some strict conditions are all met. They sometimes employ metal catalysts (e.g., gold) to control the growth process [53]. Solution phase route group (including sol-gel and hydrothermal methods [54]) suffer from some disadvantages too: they are time-consuming and require costly chemicals. They also employ some toxic, dangerous and expensive organic solvents amine in solvothermal process.

The simplest method for producing zinc oxide is the direct reaction between zinc and water. However, as with aluminum, a thin layer of zinc oxide is formed all over the zinc particle, preventing from the reaction. Although some techniques have been proposed so far, none can synthesize zinc oxide incessantly. Using zinc foil as a substrate for growing zinc oxide, for instance, leads to formation of a thin layer of zinc oxide [55]. Another suggested method is oxidation of zinc nanoparticles. If average radius of particles is smaller than thickness of the zinc oxide layer (about 10 nm), then this method works; otherwise, the particle is coated with a zinc oxide layer hindering the core of particle from oxidation [56].

In our experiment, we tried to reduce the size of the particles (or, in other words, activate them). The activation may be performed by milling zinc powder with high molar fraction of salt (as described in previous sections). This not only reduces the size of zinc particles but also covers newly produced surfaces with salt particles that otherwise would be covered by zinc oxide layer. So, the product can be stored in the air needing no neutral gas. When the salt is leached, fresh surfaces of zinc are exposed to water. Then, all nanoparticles react with water, entirely. Instead of using zinc salts (e.g., $Zn(CH_3COO)_2.2H_2O$) and other chemicals (e.g., NaOH, KOH, etc.) or alcohol solutions (that are employed in preparing some metal oxides), only zinc, salt and water are utilized in this method. This method is highly efficient and eco-friendly and does not need costly, complex equipment. It can be employed to manufacture other metal oxide systems [5] and scaled up for mass production.

Following is the report of experiment:

Zn powder (99% purity, Mesh-325, Merck Art.No. 1.08789) and salt (100-200 μm) were ground in a planetary ball mill with the specification tabulated in **Table 5**. The ground powder was poured in 250 mL of water at 75°C and was stirred by a magnetic stirring machine at constant temperature for 5 h. The powder was then washed before being dried in an oven at 80°C and before being characterized by X-Ray Diffraction (XRD, using Philips 3710W X-Ray diffractometer with CuKα (λ = 1.54184 A°) radiation), Scanning Electron Microscopy (SEM, using Cambridge S 360) and Transmission Electron Microscopy (TEM, using Philips EM 208S). Specific surface area of the powder was determined through nitrogen adsorption by Brunauer-Emmett-Teller method (BET-N_2 adsorption, Micromeritics Gemini 2375).

Figure 11 shows X-ray diffraction profile of resultant zinc oxide powder. The peaks corresponding to hexagonal phase of ZnO (JCPDS 36-1451) are illustrated. Sharp peaks signify good crystallinity of zinc oxide powder. Lattice constants (a = 3.2543(1) Å and c = 5.2134(2) Å)

NaCl to zinc molar ratio	5
Ball-to-powder weight ratio	30
Rotational speed of the planetary ball mill	300 rpm
Atmosphere	Argon
Atmosphere pressure	0.4 MPa

Table 5. Ball-milling specification for preparing ZnO nanoparticles.

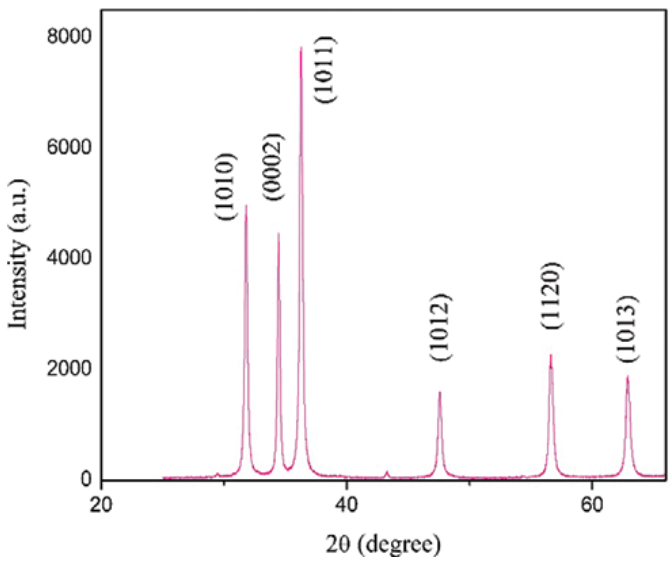

Figure 11. XRD pattern of zinc oxide powder obtained by reaction with water.

were slightly larger than those reported in corresponding JSPDS card number for bulk ZnO (a = 3.2498 Å and c = 5.2066 Å).

Zinc oxide particles obtained by this method are of two different morphologies: hexagonal flakes and rod structure. Depicted in **Figure 12a** is SEM of densely stacked hexagonal flakes. The average size of flakes is 200 nm. **Figure 12b** shows the TEM image of the second morphology (rod structure) with average length and diameter of 100 and 20 nm, respectively. Selected-Area Electron Diffraction (SAED) pattern of the powder is depicted just below **Figure 12b**. It can be indexed as hexagonal Wurtzite-structural ZnO, which is consistent with the analysis of XRD. The specific surface area of the powder obtained in our experiment was 18.25 m^2/g. It is, of course, a function of ball-milling specifications.

Theoretical explanation of the mechanism of synthesizing zinc oxide by abovementioned method may be represented as following: zinc atoms react with water to give zinc oxide. However, this happens only for the outermost atoms of a zinc particle because the zinc oxide (or zinc hydroxide) crust prevents water from diffusing into the particle, and consequently, inner atoms do not react with water. If the powder is milled together with brittle particles

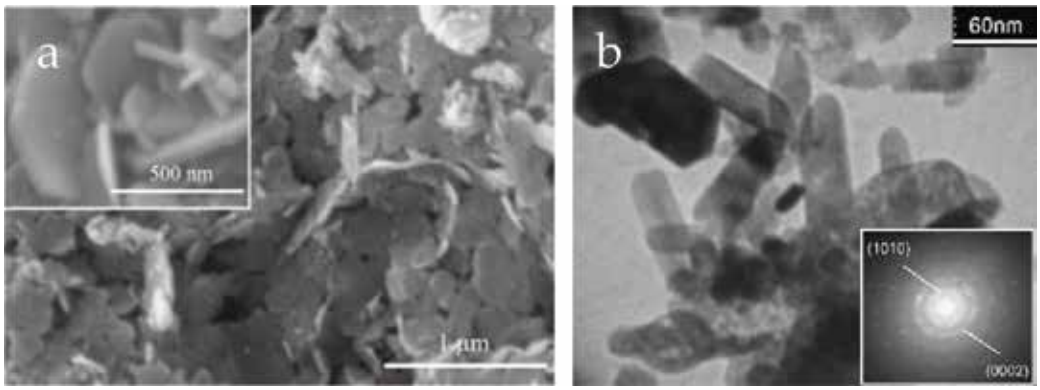

Figure 12. (a) SEM image of ZnO powder and (b) TEM image of ZnO powder and its corresponding SAED pattern (inset).

of salt, the oxide layer initially formed on the Zn particles is destroyed and newly produced surfaces are immediately covered by salt particles. Therefore, the activity of powder does not decrease after long-term storage in the air. When the powder is submerged by water, the salt is washed away, and zinc atoms are exposed to water and react with it:

$$Zn + 2H_2O \rightarrow Zn(OH)_2 + H_2 \tag{2}$$

Due to direct contact of zinc atoms with warm water, kinetics of reaction is rapid. Thus, a considerable amount of hydrogen is generated in each particle and in its way out, it burst open the zinc oxide or zinc hydroxide crust, exposing more fresh zinc to water. Hence, provided that zinc particles are small enough, all the contents of zinc is converted to zinc oxide. Zinc hydroxide contents are also hydrated to give zinc oxide as indicated by following reaction:

$$Zn(OH)_2 \rightarrow ZnO + H_2O \tag{3}$$

Unlike reaction (2) that is exothermic, reaction (3) is endothermic [57]. Warm water provides required energy for the reaction. The zinc oxide particles obtained from reaction (3) serve as seeds for agglomeration leading to a planar hexagonal nuclei. Zinc oxide lattice (as suggested by crystal habit of wurtzite ZnO) is composed of tetrahedrons with a zinc atom at the center and four oxygen atoms at the vertices. Hence, the (0001) planes in the hexagonal sheet is zinc-rich while the opposite plane (i.e., $(000\bar{1})(000\bar{1})$) is oxygen-rich. Li et al. put a rule forward according which the fastest growth rate of zinc oxide happens along $[000\bar{1}]$ direction and the rate of growth along other directions obey the following relation [58]:

$$V[0001] > V[01\bar{1}\bar{1}] > V[01\bar{1}0] > V[01\bar{1}1] > V[000\bar{1}] \tag{4}$$

Based on their rule, <0001> direction is the most preferable direction for zinc oxide nanoparticles to grow or aggregate. Two-dimensional hexagonal structures imply that the growth is hindered in this direction and the crystals grow along $<10\bar{1}010\bar{1}0>$ direction. This may be due to

resident Cl^- ions. Cl^- ions are adsorbed preferentially on the positive polar face of the (0001) surface, which limits the axis growth along the <0001> direction and accelerates the radial growth [59]. Thus, the morphology of synthesized particles can be controlled by manipulating the concentration of the ions in the media.

5. Conclusion

A simple method for preparing nanoparticles of ductile metals by means of ball milling was proposed based on the experiments reported by others and experiments conducted by the authors. The essential point of the method is using a brittle material as nanochopper during the ball milling. The method showed to be very useful and leads to good results. In all the cases represented in this chapter, salt was used as the brittle material (the nanochopper). However, other ductile materials may be employed according to the nature of the experiment and ultimate purpose of preparing the nanoparticles.

Author details

Babak Alinejad* and Yazdan Zare

*Address all correspondence to: 16nd114n@vc.ibaraki.ac.jp

Ibaraki University, Hitachi, Japan

References

[1] Alinejad B, Mahmoodi A. Synthesis of graphene nanoflakes by grinding natural graphite together with NaCl in a planetary ball mill. Functional Materials Letters. 2017;**10**(04):1750047. DOI: 10.1142/S1793604717500473

[2] Alinejad B, Mahmoodi K. A novel method for generating hydrogen by hydrolysis of highly activated aluminum nanoparticles in pure water. International Journal of Hydrogen Energy. 2009;**34**(19):7934-7938. DOI: 10.1016/j.ijhydene.2009.07.028

[3] Mahmoodi K, Alinejad B. Enhancement of hydrogen generation rate in reaction of aluminum with water. International Journal of Hydrogen Energy. 2010;**35**(11):5227-5232. DOI: 10.1016/j.ijhydene.2010.03.016

[4] Mahmoodi K, Alinejad B. Fast and facile synthesis of boehmite nanofibers, powder technology. 2010;**199**(3):289-292. DOI: 10.1016/j.powtec.2010.01.019

[5] Alinejad B, Mahmoodi K, Ahmadi K. A new route to mass production of metal hydroxide/oxide hydroxide nanoparticles. Materials Chemistry and Physics. 2009;**118**(2-3):473-476. DOI: 10.1016/j.matchemphys.2009.08.020

[6] Suryanarayana C. Mechanical alloying and milling. Marcel Dekker. 2004:87-89. DOI: 10.1080/10426910701416344

[7] Geim AK, Novoselov KS. The rise of graphene. Nature Materials. 2007;**6**:183. DOI: 10.1038/nmat1849

[8] Geim AK, MacDonald AH. Graphene: Exploring carbon flatland. Physics Today. 2007; **60**(8):35. DOI: 10.1063/1.2774096

[9] Novoselov KS, Geim AK, Morozov SV, Jiang D, Zhang Y, Dubonos SV, Grigorieva IV, Firsov AA. Electric field effect in atomically thin carbon films. Science. 2004;**306**(5696):666-669. DOI: 10.1126/science.1102896

[10] Wang F, Zhang Y, Tian C, Girit C, Zettl A, Crommie M, Ron Shen Y. Gate-variable optical transitions in graphene. Science. 2008;**320**(5873):206-209. DOI: 10.1126/science.1152793

[11] Lee C, Wei X, Kysar JW, Hone J. Measurement of the elastic properties and intrinsic strength of monolayer graphene. Science. 2008;**321**(5887):385-388. DOI: 10.1126/science.1157996

[12] Robinson JT, Keith Perkins F, Snow ES, Wei Z, Sheehan PE. Reduced graphene oxide molecular sensors. Nano Letters. 2008;**8**(10):3137-3140. DOI: 10.1021/nl8013007

[13] Blake P, Brimicombe PD, Nair RR, Booth TJ, Jiang D, Schedin F, Ponomarenko LA, Morozov SV, Gleeson HF, Hill EW, Geim AK, Novoselov KS. Graphene-based liquid crystal device. Nano Letters. 2008;**8**(6):1704-1708. DOI: 10.1021/nl080649i

[14] Ji Z, Shen X, Song Y, Zho G. In situ synthesis of graphene/cobalt nanocomposites and their magnetic properties. Materials Science and Engineering B. 2011;**176**(9):711-715. DOI: 10.1016/j.mseb.2011.02.026

[15] Reina A, Jia X, Ho J, Nezich D, Son H, Bulovic V, Dresselhaus MS, Kong J. Large area, few-layer graphene films on arbitrary substrates by chemical vapor deposition. Nano Letters. 2009;**9**(1):30-35. DOI: 10.1021/nl801827v

[16] Sutter PW, Flege J, Sutter EA. Epitaxial graphene on ruthenium. Nature Materials. 2008;**7**:406-411. DOI: 10.1038/nmat2166

[17] Berger C, Song Z, Li T, Li X, Ogbazghi AY, Feng R, Dai Z, Marchenkov AN, Conrad EH, First PN, de Heer WA. Ultrathin epitaxial graphite**:** 2D electron gas properties and a route toward graphene-based nanoelectronics. The Journal of Physical Chemistry B. 2004;**108**(52):19912-19916. DOI: 10.1021/jp040650f

[18] Park S, Ruoff RS. Chemical methods for the production of graphenes. Nature Nanotechnology. 2009;**4**:217-224. DOI: 10.1038/nnano.2009.58

[19] Kotov NA, Dékány I, Fendler JH. Ultrathin graphite oxide–polyelectrolyte composites prepared by self-assembly: Transition between conductive and non-conductive states. Advanced Materials. 1996;**8**:637-641. DOI: 10.1002/adma.19960080806

[20] Chandra S, Sahu S, Pramanik P. A novel synthesis of graphene by dichromate oxidation. Materials Science and Engineering B. 2010;**167**(3):133-136. ISSN:0921-5107. DOI: 10.1016/j.mseb.2010.01.029

[21] Zhamu A, Zhang B Z. Environmentally benign graphite intercalation compound composition for exfoliated graphite, flexible graphite, and nano-scaled graphene platelets. US patent claim 20090028778; 2009

[22] Geng Y, Wang SJ, Kim J. Preparation of graphite nanoplatelets and graphene sheets. Journal of Colloid and Interface Science. 2009;**336**(2):592-598. ISSN 0021-9797. DOI: 10.1016/j.jcis.2009.04.005

[23] Arsat R, Breedon M, Shafiei M, Spizziri PG, Gilje S, Kaner RB, Kalantar-zadeh K, Wlodarski W. Graphene-like nano-sheets for surface acoustic wave gas sensor applications. Chemical Physics Letters. 2009;**467**(4-6):344-347. ISSN 0009-2614. DOI: 10.1016/j.cplett.2008.11.039

[24] Drzal LT, Fukushima H. Graphite nanoplatelets as reinforcements for polymers. Polymer Preprints (American Chemical Society, Division of Polymer Chemistry). 2001;**42**(2):42-43

[25] Welham NJ, Berbenni V, Chapman PG. Effect of extended ball milling on graphite. Journal of Alloys and Compounds. 2003;**349**(1-2):255-263. ISSN:0925-8388

[26] Wakayama H, Mizuno J, Fukushima Y, Nagano K, Fukunaga T, Mizutani U. Structural defects in mechanically ground graphite. Carbon. 1999;**37**(6):947-952. ISSN:0008-6223

[27] Pierard N, Fonseca A, Colomer JF, Bossuot C, Benoit JM, Van Tendeloo G, Pirard JP, Nagy JB. Ball milling effect on the structure of single-wall carbon nanotubes. Carbon. 2004;**42**(8-9):1691-1697. ISSN:0008-6223. DOI: 10.1016/j.carbon.2004.02.031

[28] Knieke C, Berger A, Voigt M, Klupp Taylor RN, Röhrl J, Peukert W. Scalable production of graphene sheets by mechanical delamination. Carbon. 2010;**48**(11):3196-3204. ISSN:0008-6223. DOI: 10.1016/j.carbon.2010.05.003

[29] Sridhar V, Jeon J, Oh I. Synthesis of graphene nano-sheets using eco-friendly chemicals and microwave radiation. Carbon. 2010;**48**(10):2953-2957. ISSN:0008-6223. DOI: 10.1016/j.carbon.2010.04.034

[30] Sarathi R, Sindhu TK, Chakravarthy SR. Generation of nano aluminium powder through wire explosion process and its characterization. Materials Characterization. 2007; **58**(2):148-155. DOI: 10.1016/j.matchar.2006.04.014

[31] Meda L, Marra G, Galfetti L, Severini F, De Luca L. Nano-aluminum as energetic material for rocket propellants. Materials Science and Engineering C. 2007;**27**:1393-1396. DOI: 10.1016/j.msec.2006.09.030

[32] El S, Barberoglou M, Fotakis C, Viau G, Garcia C, Shafeev GA. Generation of Al nanoparticles via ablation of bulk Al in liquids with short laser pulses. Optics Express. 2009;**17**(15):12650-12659. DOI: 10.1364/OE.17.012650

[33] Kapdan IK, Kargi F, Oztekin R, Argun H. Bio-hydrogen production from acid hydrolyzed wheat starch by photo-fermentation using different Rhodobacter sp. International Journal of Hydrogen Energy. 2009;**34**:2201-2207. DOI: 10.1016/j.ijhydene.2009.01.017

[34] de Souza RF, Padilha JC, Gonçalves RS, de Souza MO, Berthelot JR. Electrochemical hydrogen production from water electrolysis using ionic liquid as electrolytes: Towards the best device. Journal of Power Sources. 2007;**164**:792-798. DOI: 10.1016/j.jpowsour.2006.11.049

[35] Kojima Y, Suzuki K, Fukumoto K, Sasaki M, Yamamoto T, Kawai Y, Hayashi H. Hydrogen generation using sodium borohydride solution and metal catalyst coated on metal oxide. International Journal of Hydrogen Energy. 2002;**27**:1029-1034. DOI: 10.1016/S0360-3199(02)00014-9

[36] Kotay SM, Das D. Biohydrogen as a renewable energy resource—Prospects and potentials. International Journal of Hydrogen Energy. 2008;**33**(1):258-263. DOI: 10.1016/j.ijhydene.2007.07.031

[37] U.S. Department of Energy. Office of fossil energy—Hydrogen Program Plan: Hydrogen from Natural Gas and Coal: the Road to a Sustainable Energy Future. Available from: https://www.netl.doe.gov/File%20Library/Research/Coal/ccbtl/fehydrogenplan2003.pdf [Accessed March 05, 2018]

[38] Tzimas E, Filiou C, Peteves SD, Veyret J B. Hydrogen storage: State of the art and future perspective, European Commission, Directorate General Joint Research Centre, Institute for Energy, Petten, the Netherlands. Available from: https://pdfs.semanticscholar.org/1fc0/398a56d147790df6b8af9aab677e1c04eeb6.pdf [Accessed: March 05, 2018]

[39] Kravchenko OV, Semenenko KN, Bulychev BM, Kalmykov KB. Activation of aluminum metal and its reaction with water. Journal of Alloys and Compounds. 2005;**397**:58-62. DOI: 10.1016/j.jallcom.2004.11.065

[40] Hiraki T, Takeuchi M, Hisa M, Akiyama T. Hydrogen production from waste aluminum at different temperatures with LCA. Materials Transactions. 2005;**46**(5):1052-1057. DOI: 10.2320/matertrans.46.1052

[41] Andersen ER, Andersen EJ. Method for producing hydrogen. US Patent 6506360; 2003

[42] Martínez SS, Sanchez LA, Alvarez Gallegos AA, Sebastian PJ. Coupling a PEM fuel cell and the hydrogen generation from aluminum waste cans. The International Journal of Hydrogen Energy. 2007;**32**:3159-3162. DOI: 10.1016/j.ijhydene.2006.03.015

[43] Parmuzina AV, Kravchenko OV. Activation of aluminum metal to evolve hydrogen from water. International Journal of Hydrogen Energy. 2008;**33**:3073-3076

[44] Ilyin AP, Gromov AA, Reshetov AA, Tihonov DV, Yablunowsky GV. Reactionary ability of aluminum ultrafine powders in various oxidation processes. In: The 4th Russian-Korean International Symposium on Science Technology KORUS Proceedings. Vol. 3; 2000. pp. 299-304

[45] Ivanov VG, Safronov MN, Gavrilyuk OV. Macrokinetics of oxidation of ultradisperse aluminum by water in the liquid phase. Combustion, Explosion, and Shock Waves. 2001;**37**(2):173-177

[46] Fan MQ, Xu F, Sun LX, Zhao JN, Jiang T, Li WX. Hydrolysis of ball milling Al–Bi–hydride and Al–Bi–salt mixture for hydrogen generation. Journal of Alloys and Compounds. 2008;**460**:125-129

[47] Fan MQ, Xu F, Sun LX. Studies on hydrogen generation characteristics of hydrolysis of the ball milling Al-based materials in pure water. International Journal of Hydrogen Energy. 2007;**32**:2809-2815

[48] Liu CH, Zapien JA, Yao Y, Meng XM, Lee CS, Fan SS, Lifshitz Y, Lee ST. High-density, ordered ultraviolet light-emitting ZnO nanowire arrays. Advanced Materials. 2003; **15**:838-841. DOI: 10.1002/adma.200304430

[49] Musić S, Dragčević Đ, Popović S, Ivanda M. Precipitation of ZnO particles and their properties. Materials Letters. 2005;**59**:2388-2393. DOI: 10.1016/j.matlet.2005.02.084

[50] Wang ZL. Nanostructures of zinc oxide. Materials Today. 2004;**7**(6):26-33. ISSN:1369-7021. DOI: 10.1016/S1369-7021(04)00286-X

[51] Kumar S, Kim YJ, Koo BH, Gautam S, Chae KH, Kumar R, Lee CG. Room temperature ferromagnetism in chemically synthesized ZnO rods. Materials Letters. 2009;**63**(2):194-196. ISSN:0167-577X. DOI: 10.1016/j.matlet.2008.09.057

[52] Ouyang W, Zhu J. Catalyst-free synthesis of macro-scale ZnO nanonail arrays on Si substrate by simple physical vapor deposition. Materials Letters. 2008;**62**(17-18):2557-2560. ISSN:0167-577X. DOI: 10.1016/j.matlet.2007.12.051

[53] Nagase M, Suhara M, Miyamoto Y, Furuya K. Peak width analysis of current–voltage characteristics of triple-barrier resonant tunneling diodes. Japanese Journal of Applied Physics. 2000;**39**:3314-3318 (Part 1, Number 6A)

[54] Lepot N, Van Bael MK, Van den Rul H, D'Haen J, Peeters R, Franco D, Mullens J. Synthesis of ZnO nanorods from aqueous solution. Materials Letters. 2007;**61**(13):2624-2627. ISSN:0167-577X. DOI: 10.1016/j.matlet.2006.10.025

[55] Chenglin Y, Dongfeng X. Solution growth of nano- to microscopic ZnO on Zn. Journal of Crystal Growth. 2008;**310**(7-8):1836-1840. ISSN:0022-0248. DOI: 10.1016/j.jcrysgro.2007.10.060

[56] Nakamura R, Lee JG, Tokozakura D, Mori H, Nakajima H. Formation of hollow ZnO through low-temperature oxidation of Zn nanoparticles. Materials Letters. 2007;**61**(4-5): 1060-1063. DOI: 10.1016/j.matlet.2006.06.039

[57] Ge J, Tang B, Zhuo L, Shi Z. A rapid hydrothermal route to sisal-like 3D ZnO nanostructures via the assembly of CTA+ and $Zn(OH)_4^{2-}$: Growth mechanism and photoluminescence properties. Nanotechnology. 2006;**17**(5):1316-1323

[58] Li W, Shi E, Zhong W, Yin Z. Growth mechanism and growth habit of oxide crystals. Journal of Crystal Growth. 1999;**203**(1-2):186-196. DOI: 10.1016/S0022-0248(99)00076-7

[59] Xu L, Guo Y, Liao Q, Zhang J, Xu JD. Morphological control of ZnO nanostructures by electrodeposition. Physical Chemistry B. 2005;**109**:13519-13522. DOI: 10.1021/jp051007b

Chapter 10

Abrasive for Chemical Mechanical Polishing

Hong Jin Kim

Additional information is available at the end of the chapter

http://dx.doi.org/10.5772/intechopen.75408

Abstract

Chemical mechanical polishing (CMP) is one of the most essential processes in semiconductor manufacturing. Its importance becomes highly underscored at the advanced device toward sub 14 nm scaling. The fundamental mechanism of CMP is to create soften surface layer by chemical reaction and then, mechanical force by abrasive particles remove soften layer. The role of CMP is not only material removal, but also planarization, surface smoothening, uniformity control, defect reduction and more. Moreover, semiconductor yield enhancement is sensitively influenced by CMP processing. Surface scratching, which is generated by CMP in nature, is considered as 'killer defect' in semiconductor manufacturing. Hence, to achieve proper CMP performance without surface scratching, understanding and development of abrasive particles are crucially important. In this chapter, CMP fundamentals, applications and challenges associated with abrasive particle technology including synthesis (up to nanoparticle scale), tribochemical reaction, abrasive surface zeta potential behavior, particle size and its distribution will be discussed.

Keywords: semiconductor manufacturing, chemical mechanical polishing (CMP), slurry, silica abrasive, ceria abrasive, alumina abrasive, advanced abrasive materials

1. Introduction

Chemical mechanical polishing (CMP) has been used for several decades in semiconductor manufacturing since its development at 1980s [1–5]. The original purpose of CMP is to planarize wafer surface both locally and globally, which enable subsequent lithographic patterning with proper depth of focus [1–5]. However, as device shrinkage continues, it has become critical process for device fabrication, and its applications play a pivotal role in semiconductor process since transistor scaling becomes beyond 14 nm [5–9]. The role of CMP and planarized wafer associated with lithography patterning is shown in **Figure 1** schematically [1, 4].

Surface topography hinders conformal deposition of photoresist, leading to distorted patterning. Furthermore, advantages of employment of CMP in semiconductor manufacturing are [4, 5]: (1) elimination of step coverage burden, (2) defect removal from prior process steps, (3) surface smoothening in wafer scale, and (4) enablement of metal gate formation at sub 14 nm device. The fundamental mechanism of CMP process is [1–4]: (1) Material surface becomes soften by chemical reaction with slurry, (2) Mechanical force by abrasive particle in the slurry removes soften layer and step height reduction, (3) Material surface reacts with slurry chemical to make surface soften layer again and repeat (1) – (3). Therefore, chemistry and abrasive particles in the slurry determines CMP performances. This procedure is given in **Figure 2**. With this process, fast material removal across the wafer with planarization can be achieved. From the abrasive perspective, abrasive-wafer contact model on removal rate has been published in many literatures which emphasize abrasive particle size (and size distribution) and shape, and abrasive hardness. Although CMP application had started from planarization of excessed dielectric materials, its utilization have been widely accepted in shallow trench isolation, contact and metal interconnection formation [1–10]. Recently, sub 14 nm semiconductor scaling has developed device integration scheme to 3-dimensional transistor formation such as fin field-effect transistor, therefore device process flow becomes much more complicated than previous device node [6–9, 11, 12]. Hence, application of CMP extends to transistor formation, and importance of CMP process becomes highly underscored.

Figure 3(a) shows polisher equipment and wafer polishing processing. Polishing head holds wafers by vacuum and it rotates on the polishing pad. Slurry is delivered by slurry arm and polishing pad conditioner refreshes polishing pad surface as each wafer processing, which results in global planarization and polishing. Whereas, in microscale observation, complicated interaction among pad asperity-slurry (abrasive and chemistry)-wafer surface occurs during CMP processing, which is depicted in **Figure 3**. According to semiconductor process development, CMP process itself has developed its equipment, consumables, polishing functions and slurries to improve performance.

CMP performances are defined by removal rate (throughput), selectivity, planarization (planarity), within wafer non-uniformity, surface topography (roughness), corrosion and post CMP defects. The definitions of them are:

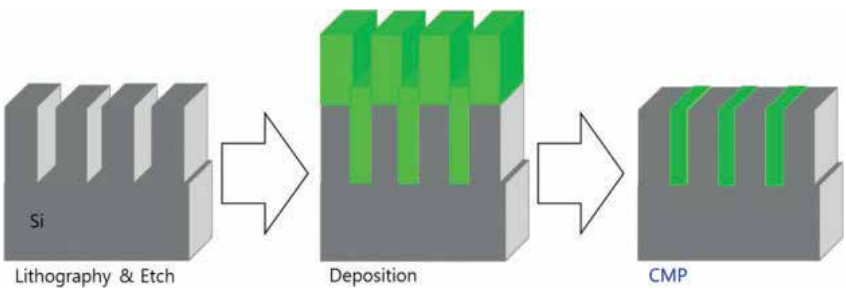

Figure 1. The concept of chemical mechanical polishing (CMP). Non-planarized topography becomes planarized surface by CMP.

http://dx.doi.org/10.5772/intechopen.75408

Figure 2. The schematic mechanism of material removal by CMP.

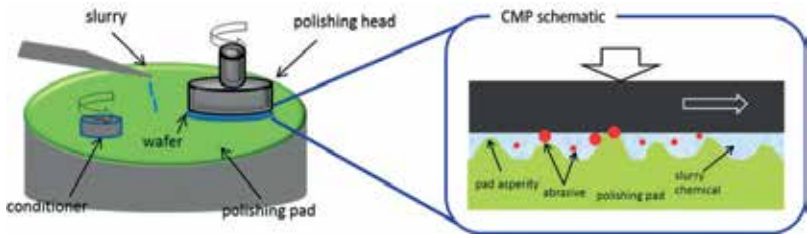

Figure 3. The schematic of conventional CMP equipment.

$$\text{Removal Rate (RR)} = (\text{pre CMP thickness} - \text{post CMP thickness})/(\text{polishing time})$$

$$\text{Within Wafer Uniformity} = \text{Film thickness sigma post CMP}/\text{Film mean thickness post CMP}$$

$$\text{Selectivity (A:B)} = \text{RR of A material}/\text{RR of B material}$$

Planarization is commonly measured by step height reduction rate. These performances are closely related with device yield and electrical performances. For example, CMP-induced microscratch defect (**Figure 4**) is detrimental to device yield [3, 5]; transistor resistance is strongly influenced by post CMP uniformity, and residual material blocks subsequent patterning. CMP performances are determined by multiple CMP process factors; however, CMP slurry is the most influencing parameter. CMP slurry consists of abrasive particles and chemical components such as pH adjuster, dispersant, polymeric additives, oxidizer, and passivation agent, depending on polishing purpose to provide proper surface modification of material.

As described in **Figure 3**, direct contact between abrasive particle and wafer surface removes material, thus, properties and characteristics of abrasive particle and their understanding are inevitable to optimize CMP process. Although a lot of different kinds of abrasives have been tried for CMP applications, three abrasives have been employed successfully until recent device manufacturing. They are silica-based abrasive, ceria-based abrasive, and alumina-based abrasive. However, CMP is indispensable process for future semiconductor fabrication and it needs development of new abrasives for the success of new designed device and matured manufacturing. **Figure 5** shows CMP abrasive market trend in semiconductor industry [14]. Its growth expectation for the next 4 years is about 30% increase from 2016. This chapter introduces abrasive particles and their applications to CMP process for semiconductor manufacturing.

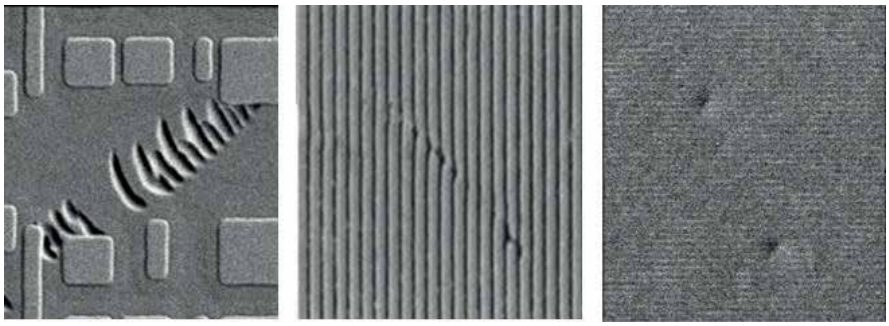

Figure 4. The examples of CMP-induced microscratch images [13].

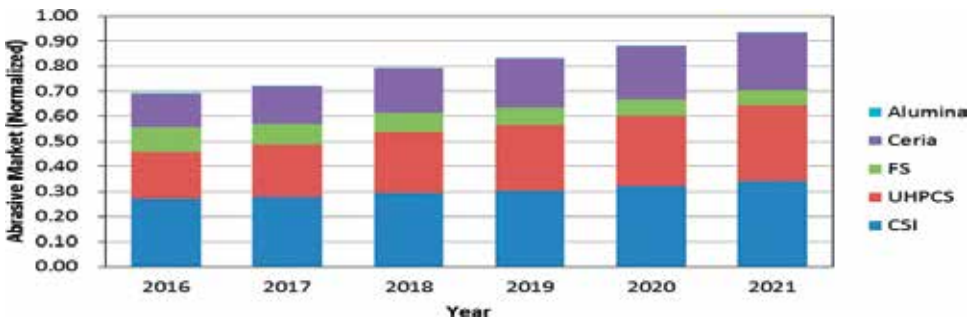

Figure 5. Slurry abrasive market trend (Reprinted from Ref. [14] with permission from author. Copyright Linx-consulting). FS is fumed silica, UHPCS is ultra-high purity colloidal silica and CSI is colloidal silica abrasive.

2. Abrasive for dielectric CMP

A dielectric material in semiconductor processing refers to insulating materials and mostly it indicates all kinds of silicon oxide materials [5]. Most dielectric CMP applications focus on transistor formation, which is called as front end of the line (FEOL) process. And dielectric CMP requires either oxide bulk CMP or CMP stop on 'stopper' material. For the stop on CMP case, oxide material is removed by CMP and CMP stops when stopper material is exposed. Shallow trench isolation (STI) CMP and interlayer dielectric (ILD) CMP are representative dielectric CMP applications. STI CMP process (stop on 'silicon nitride') is described in **Figure 6** [3] as an example of dielectric CMP. The stopper materials are mostly silicon nitride or poly-silicon in FEOL process. For dielectric CMP purpose, two – three major abrasives are used in the advanced node semiconductor manufacturing.

2.1. Silica-based slurry and silica abrasive

As briefly described in the introduction, CMP mechanism is soft layer removal by abrasive particle. This section introduces silica particle as slurry abrasive. During dielectric CMP process, silicon oxide surface reacts with OH^- from the slurry solution and forms silicon hydroxide, $Si(OH)_4$. The hydration reaction is.

$$(SiO_2)_x + 2H_2O \rightarrow (SiO_2)_{x-1} + Si(OH)_4$$

And this soften $Si(OH)_4$ is mechanically removed by silica abrasive [3, 15]. Then silicon oxide surface is exposed and hydration occurs again. This process is repeating until silicon oxide disappears. From **Figure 2**, soft layer can be considered as $Si(OH)_4$ in this case. The hydration rate is influenced by the concentration of OH^- ions in the solution, thus alkaline environment can accelerate surface hydration and make fast material removal by fast reaction [2, 15–16]. Therefore high pH silica-abrasive slurry is favorable to obtain high removal rate. Two common synthesizing methods of silica abrasives are commercially used in the semiconductor industry. One is fumed process and the other is colloidal process [5, 17–19]. The typical abrasive images

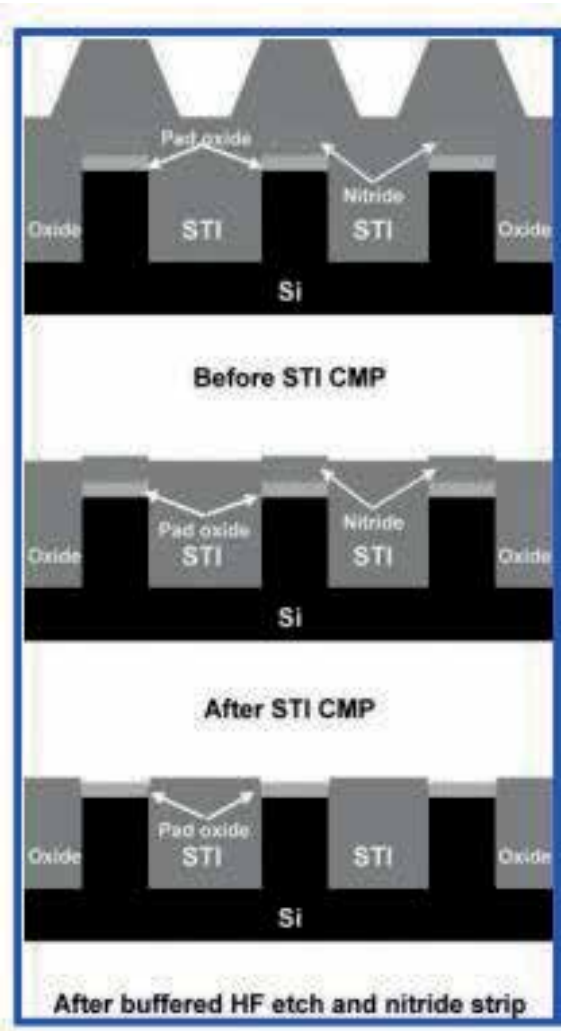

Figure 6. Procedure of shallow trench isolation (STI) CMP. Polishing stop on silicon nitride (Reprinted with permission from Ref. [3]. Copyright 2010 American Chemical Society).

of silica abrasive by each synthesis methods are shown in **Figure 7** [20, 21]. Fumed silica synthesis uses flame reaction of chlorosilane at high temperature, which is summarized at.

$$SiCl_4 + 2H_2 + O_2 \rightarrow SiO_2 + 4HCl$$

With this method, early development of silica abrasive particle size is larger than 300 Å, but development of filtration and post treatment enables to control the abrasive size below 150 Å. The commercial fumed silica abrasive slurry for dielectric CMP has high abrasive concentration to achieve enough removal rate. However, high abrasive concentration caused scratch defects, easy to agglomerate and clogging problem in slurry delivery system or filter.

Figure 8 shows example of clogged silica abrasive, which leads to significant defects on the wafer at post CMP. The whitish particles are silica abrasive in the slurry loop system. Therefore recent device manufacturing use high percentage of fumed silica abrasive slurry less and less, and forecast expects less usage of fumed silica abrasive as shown in **Figure 5**. Contrary to fumed method, colloidal abrasive is synthesized by liquid phase growth process via precursor [5, 16, 18–25]. Commonly, colloidal silica is made from sodium silicate (Na_2SiO_3) or sodium meta-silicate ($NaHSiO_3$). By ion exchange, sodium ion is eliminated and colloidal silica is formed to be used as CMP slurry abrasive. Colloidal silica abrasive slurry has much lower removal rate than fumed silica abrasive although it gives much lower scratch defect performance by its spherical shape and small size. To enhance removal rate of dielectric material by colloidal silica, organic cation is added as removal booster [16]. It changes colloidal silica abrasive surface charge from negative into positive and coulombic attraction force between abrasive and dielectric surface, which is negative, accelerates removal rate. As shown in **Figure 9(a)**, surface zeta potential behavior with respect to pH [26] can support this mechanism. Schematic of enhanced removal rate by colloidal silica abrasive is given in the same Figure. pH control is critical to this case. Recently, several attempts to new synthesis of silica abrasive to add

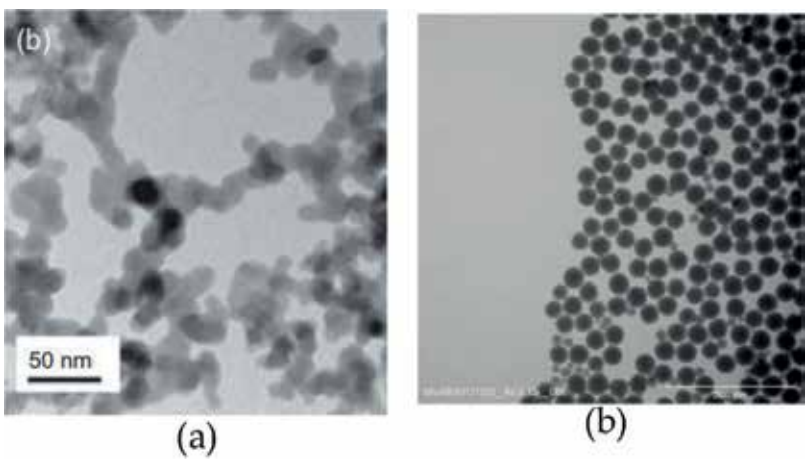

Figure 7. TEM images of (a) fumed (Reprinted by permission from [20], Copyright 2012 American Chemical Society) and (b) colloidal silica abrasive [21].

http://dx.doi.org/10.5772/intechopen.75408

Figure 8. The clogged silica abrasive in slurry delivery loop.

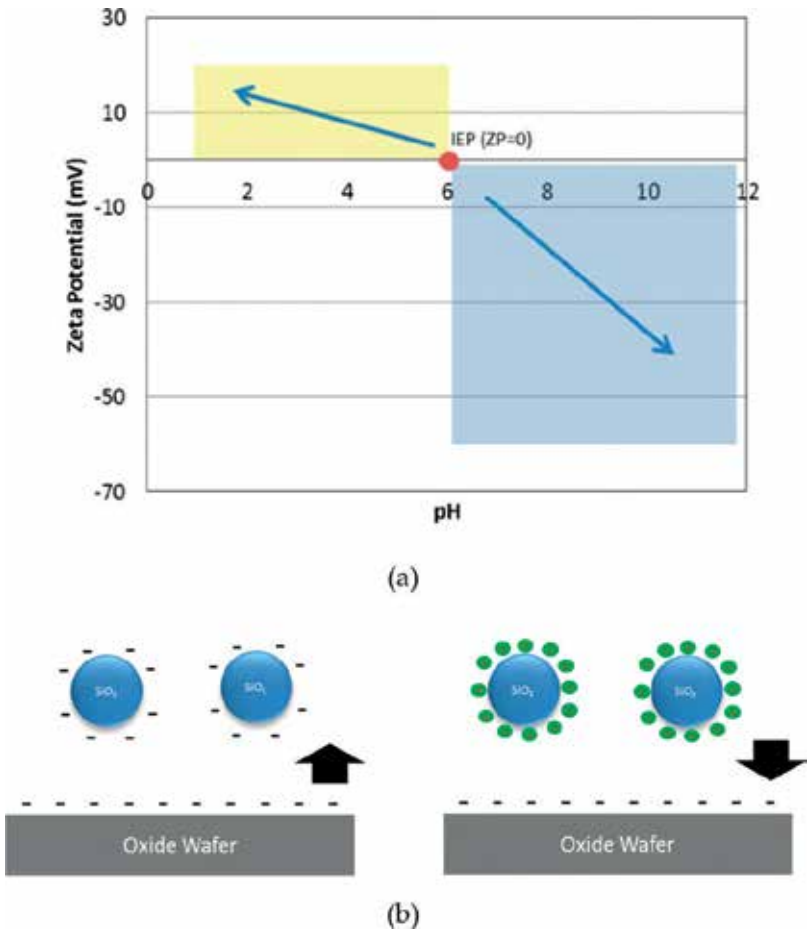

Figure 9. (a) Zeta potential of SiO_2, and (b) silica abrasive without surface treatment and with surface treatment with organic cation at acidic region.

more stable particle distribution have been reported [26–29]. For instance, Pan et al. presented silane modified silica abrasive particle preparation to mitigate gelation of colloidal silica due to high chemically active hydroxyl group from silica surface. The siloxane groups in silane and hydroxyl groups in silica surface generate hydrolysis condensation reaction, which results in surface zetapotential change to improve dispersion stability [27].

2.2. Ceria abrasive for dielectric CMP slurry

Although high removal rate, low cost of ownership and effective planarization are obtained by silica abrasive, selectivity control and low scratch defect requirements bring ceria-based abrasive to be universally used in dielectric CMP of advanced node semiconductor manufacturing. And recent dielectric CMP uses ceria-based slurry much more than before (refers to **Figure 5**). The CMP mechanism by ceria-based slurry is different from silica-based slurry. Instead of mechanical removal by silica abrasive, ceria abrasive uses surface interaction with silicon oxide dominantly, which is.

$$-Ce-OH+-SiO^{-} \rightarrow -Si-O-Ce+OH^{-}$$

Strong bonding between Ce and hydrated silicate detach silicon oxide and Si-O-Ce lump is removed from the surface [15, 30]. Ceria CMP process is shown in **Figure 10**.

Therefore, ceria abrasive surface charge control is important in determining CMP performance. The surface charge behavior can be indicated by ceria zeta potential property [31]. As shown in **Figure 11(a)**, isoelectric point (IEP) of ceria is ~pH 8 (at acidic: positive charge, at alkaline: negative charge) and surface potential is opposite to silicon oxide at acidic environment. Thus, most ceria-abrasive slurry pH is less than 8 to facilitate Si-O-Ce formation. Similar to silica abrasive synthesis, two types of ceria-base abrasive are commonly synthesized for CMP applications [5, 31, 32]. They are calcined ceria abrasive and wet (or colloidal) ceria abrasive. Calcined synthesis is based on solid-state oxidation process. Raw ceria material is oxidized followed by mechanical crushing to make them small particles. And filtration removes large particles. Depending on crushing condition and filtration, calcined ceria abrasive size can be controlled. On the other hand, wet process uses precipitation procedure in liquid state. Seed ceria nuclei in an aqueous cerium solution grows and forms ceria (or cerium hydroxide) particles. Ceria abrasive made by wet process has spherical shape and narrow particle size distribution compared with calcined process. These synthesis methods and typical ceria abrasive images from each method are shown in **Figure 11(b)–(d)** schematically

Figure 10. The schematic mechanism of oxide removal rate by ceria abrasive.

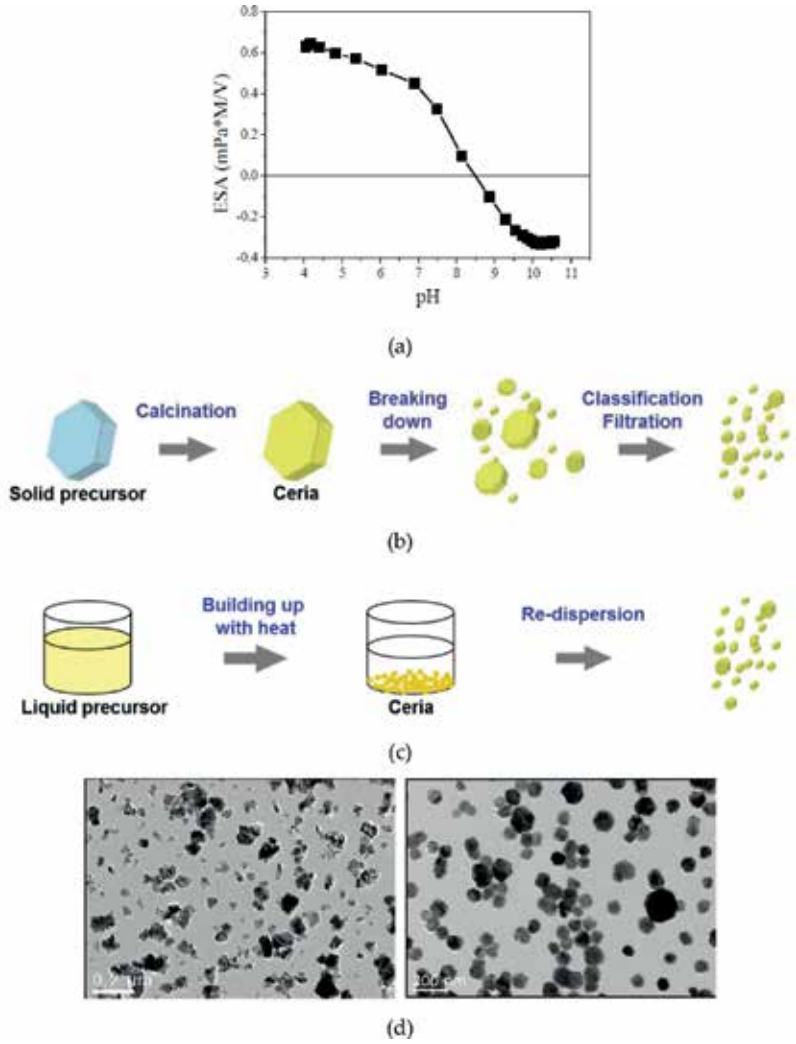

Figure 11. (a) Zeta potential curve of conventional ceria abrasive, (b) synthesis of calcined ceria abrasive, (c) synthesis of colloidal ceria abrasive, (d) TEM images of calcined (left) and colloidal (right) ceria abrasives ((a) & (d) reprinted by permission from mater. & interfaces, Jihoon Seo et al. [35], Copyright 2014 American Chemical Society) ((b)&(c) Reprinted from Ref. [34] with permission from authors)).

[31, 33–35]. The overall property comparison between calcined processed ceria abrasive and colloidal ceria abrasive is summarized in **Table 1** [31]. Calcined ceria abrasive slurry provides steady removal rate. Wet ceria abrasive slurry shows relatively lower removal rate than calcined ceria abrasive, however, the most critical advantage of wet ceria abrasive slurry is scratch defect improvement due to small and regular shape of abrasive particle. Recent study by Seo revealed Ce surface oxidation state had significant influence on the CeO_2 interaction to silicate and they investigated the effect of concentration of Ce^{3+} ions on the affinity to silicate ions and wet ceria particle size effect on the adsorption of silicate [35, 36]. Higher concentration of Ce^{3+} ions increased adsorption affinity with silicate ions and larger ceria abrasive has

Calcined CeO_2	Colloidal CeO_2
Mean particle size (nm): 150–500	Mean particle size (nm): 120–170
Relatively high oxide removal rate	Relatively low oxide removal rate
High crystallinity	Spherical shape
Tunable particle size	Uniform size distribution
Facet shape	High cost
Poor size distribution	Relatively low scratch
Mass production	
Relatively high scratch	

Table 1. Properties of calcined CeO_2 and colloidal CeO_2 (Reprinted from Ref. [31] with permission from author).

higher Ce^{3+} ions due to higher surface to volume ratio. In addition to calcined and wet process, flux method to synthesize ceria abrasive particle has proposed to overcome limitation of calcined or wet process [37]. It uses cerium nitrate hexahydrate ($Ce(NO_3)_3 \cdot 6H_2O$) and potassium hydroxide (KOH) as starting material and ethylene glycol ($C_2H_6O_2$)-DI mixture as solvent. Through precipitation, hydrothermal reaction and centrifuging process, narrow size distribution with desirable characteristics ceria abrasives synthesis are demonstrated [37]. Ceria or ceria-based slurry application in CMP is increasing and advanced slurries with ceria abrasive are emerging in the semiconductor industry. Ultrafine (or nano-sized) ceria abrasive and composite abrasive will be introduced in Section 5.

3. Abrasive for tungsten CMP

Tungsten has been used for metal interconnection and contact formation. Many candidate metals have been developed to replace tungsten; however, tungsten is still standard metal for sub 14 nm contact formation due to its excellent electromigration and diffusion barrier performance [3, 38]. The CMP mechanism of tungsten was proposed by Kaufmann firstly [39]. A pristine tungsten surface is oxidized by oxidizer at acidic condition and it transforms to tungsten oxide (WO_x). The formation of oxide depends on solution and chemistry. Tungsten oxide plays a role as passivation layer to protect subsurface tungsten from dissolution or corrosion. And tungsten oxide is easy to be removed by mechanical force of abrasive since its hardness is less than pure tungsten. This process is repeated until CMP stops. Therefore, role of chemistry (in particular oxidizer) is important in tungsten CMP. Among many kinds of oxidizer, ferric nitrate ($Fe(NO_3)_3$-) is the most successful one [3, 5]. The schematic description of tungsten CMP mechanism is given in **Figure 12**. The common and commercially available slurry for tungsten CMP has alumina-base and silica-base abrasives [3, 5]. At sub 14 nm logic device fabrication, tungsten CMP is the most important process to enable transistor formation. It requires superior planarity and extremely accurate uniformity control. For this purpose, alumina abrasive showed better planarity and selectivity performance. Hence its utilization for bulk tungsten CMP is commonly adopted in advanced device manufacturing.

http://dx.doi.org/10.5772/intechopen.75408

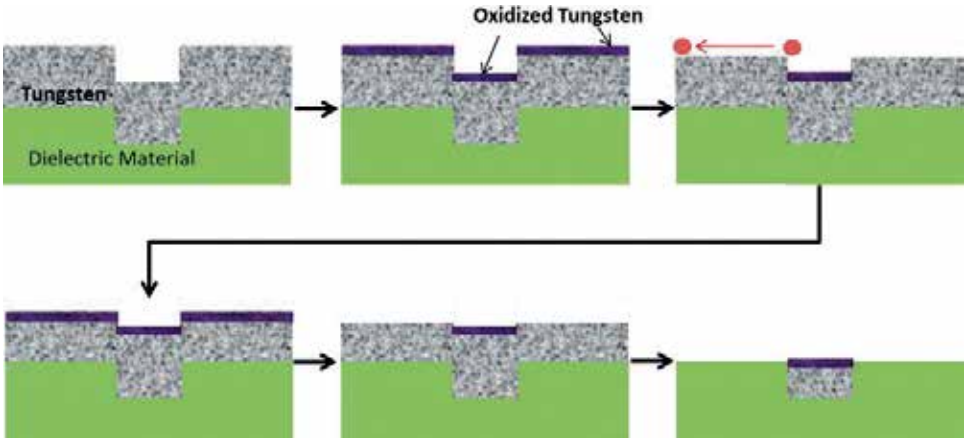

Figure 12. The mechanism of tungsten CMP.

Alumina abrasive has been synthesized by alum process and calcination [18]. For CMP application, alpha-alumina abrasive is commonly used. Hardness of alumina abrasive is much higher than tungsten and tungsten oxide, therefore it is easy to make scratch defect on the surface. Moreover, due to the surface charge difference between alumina and tungsten at acidic region, attractive force retains alumina abrasive on the wafer surface. Recently, composite alumina abrasive with polymeric material has been introduced in the industry due to defect concern at advanced node semiconductor [38]. Silica base slurry utilization on tungsten CMP is usually for non-selective CMP purpose (polishing both tungsten and dielectric material) because its selectivity with oxide is not as high as alumina abrasive slurry. Tungsten CMP is driven by chemical effect more than mechanical abrasion, removal rate strongly depends on chemical components (oxidizer, surfactant, and stabilizer) and activation condition (for example, process temperature) [39–41]. Therefore adequate combinations among them are essential to provide desired CMP performances. Although removal rate is linearly increasing with abrasive concentration in the slurry, loading effect (very low removal rate or non-linear removal rate behavior at the early stage of CMP) is more significant in tungsten CMP than dielectric CMP. Yttrium, ceria, zirconium and composite abrasives have been tried and under development for tungsten CMP applications [3].

4. Abrasive for copper CMP

Copper is introduced in semiconductor manufacturing for metal interconnection application mid-1990s and now it is standard metal for back end of the line interconnection [2–4, 10]. Accordingly, CMP for copper has been highlighted due to its process challenges. Like tungsten CMP, copper CMP mechanism is based on Kaufman's model. Chemical reaction from slurry produces oxidized copper and abrasive particle removes oxidized copper. The major components of copper CMP slurry are abrasive, oxidizer, inhibitor, surfactant and chelating agent. The challenges of copper CMP are scratch defects and copper corrosion. Corrosion is

mostly induced by chemical in the slurry and most of scratch defects are driven by abrasive particle. In particular, hardness of copper is lower than most abrasive particles. Therefore, smaller size of abrasive with spherical shape and less abrasive content are favorable to the slurry formulation. The common copper CMP abrasives are alumina and colloidal silica [3, 10]. However, at advanced semiconductor manufacturing, colloidal silica abrasive becomes prevalent because it has appreciable polish rate of barrier material (tantalum/tantalum nitride). The copper removal rate and CMP performances are sensitively influenced by chemistries and components in slurry in conjunction with silica abrasive characteristics. Most of copper CMP slurry researches have focused on chemistry perspective instead of abrasives.

5. Advanced abrasives for future CMP applications

One of the most important requirements of CMP process in semiconductor application is scratch defect reduction, which has mentioned in this chapter several times. For abrasive perspective, smaller size abrasive particle is favorable for scratch defect. Therefore, recent abrasive technology has focused on nano-sized abrasive synthesis with minimized agglomeration. For dielectric CMP, nano-sized cerium hydroxide (or ultrafine cerium hydroxide or nano-ceria) abrasive slurry has been introduced due to its potential scratch defect reduction [33–34, 42–43]. The synthesis procedure of nano-sized cerium hydroxide abrasive is given in **Figure 13**.

Transmission electron microscope image of calcined ceria abrasive and nano-sized abrasive is compared in **Figure 14** [44]. Single abrasive size becomes as small as 5 nm. Even agglomerated abrasive size is less than 20 nm. Tanaka et al., showed removal rate and selectivity control by changing additives [33–34]. However, CMP mechanism of nano-sized cerium hydroxide abrasive is not clearly understood yet. Han et al. reported polishing pad surface roughness control is critical to maintain removal rate stability with nano-sized cerium hydroxide abrasive [44]. Kim proposed particle coverage model on the wafer as material removal mechanism with nano-sized cerium hydroxide abrasive [43]. In order to apply nano-sized cerium hydroxide abrasive for dielectric CMP, role of chemistry to enhance removal rate with selectivity control needs to be further explored.

Composite abrasive has drawn attention to the semiconductor industry recently. Each abrasive has its own unique properties. Some of them are very attractive and some of them are not good for desired CMP performances. Tries to combine advantages only from different abrasives have triggered ceria-silica composite abrasive development [45–48]. Researchers have paid attention to ceria-coated silica as next generation CMP slurry abrasive. Zhao et al.

Figure 13. Synthesis of nano-sized cerium hydroxide abrasive (reprinted from Ref. [33] with permission from authors).

http://dx.doi.org/10.5772/intechopen.75408

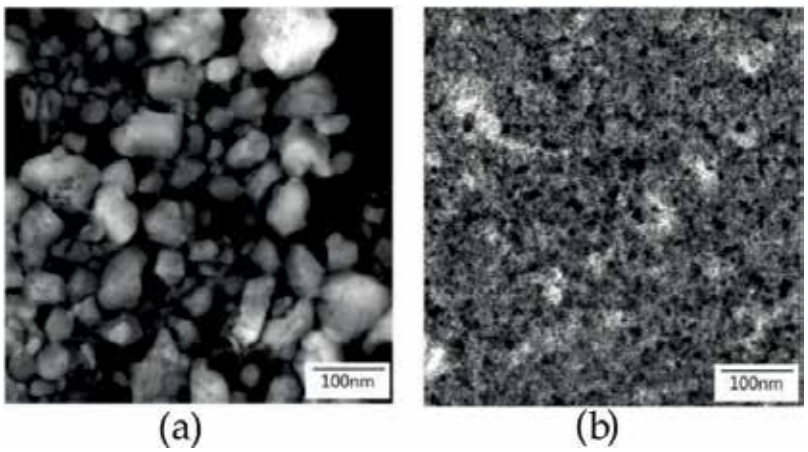

Figure 14. TEM images of (a) calcined ceria abrasive and (2) nano-sized cerium hydroxide abrasive (reprinted by permission from Ref. [44], Copyright 2013 Springer Nature).

uses sol–gel method to synthesize ceria-coated silica abrasive [48]. They prepared tetraethylorthosilicate and ammonia as raw materials, and composite nanoparticles are synthesized through precipitation procedure. About 150–200 nm spherical ceria-coated silica abrasives are successfully synthesized. Shell ceria size is 10 nm. Peedikakkandy et al. synthesized monodispersed ceria coated silica nanoparticles by micro-emulsion method and chemical precipitation process [46]. About~10 nm crystalline ceria over silica with spherical shape and overall particle size <100 nm abrasive is successfully obtained. Zhang et al. synthesized ceria-coated silica abrasive by precipitation process using ammonium cerium nitrate and urea as precipitant with poly(vinylpyrrolidone) (PVP) as assistant [45]. With optimized synthesis conditions, <200 nm ceria-coated silica abrasive is obtained. In their study, X-ray diffraction confirms face centered cubic CeO_2 nanoparticle encapsulate core silica. Scanning electron microscope (SEM) shows uniformly distributed particles with spherical shape. Transmission electron microscope (TEM) directly shows evidence of homogenous nucleation of ceria particles and heterogeneous nucleation of silica particle with uniform, distinctive and crystalline ceria shell. With ceria-coated silica composite abrasive, higher removal rate than pure silica abrasive and comparable surface roughness is demonstrated on glass substrate CMP. Likewise ceria-coated ceria abrasive, Chen et al. reported composite abrasive containing solid silica core with silica mesoporous shell structure [29]. The advantage of mesoporous silica is its significant elastic recovery ability combined with ductile behavior. Chen et al. synthesized solid silica core via conventional Stöber procedure and shell silica encapsulating the core by means of modified Stöber process. It uses vinyltrimethoxysilane (VTMS) as silica source and cetyltrimethylammonium bromide as structure directing agent. Well defined spherical shape abrasives are successfully achieved and it shows clearly core-shell structure. The thickness of mesoporous silica shell is controlled by VTMS amount during synthesis. With this abrasive, higher removal rate of thermal silicon dioxide film and lower surface roughness are exhibited. Polymeric composite has drawn attention to CMP society due to its potential scratch defect reduction. Chen et al. reported polymer based core-shell abrasive aiming to reduce scratch

defect by CMP. The core abrasive is spherical polystyrene (PS) and ceria is selected as shell abrasive [49]. The mechanism of low scratch and minimize wafer damage is cushion effect of soft polymer core abrasive. In-situ chemical precipitation with mixture of deionized water, PS spheres, cerium nitrate hexahydrate ($Ce(NO_3)_3 \cdot 6H_2O$), and hexamethyleneteramine is used for this hybrid abrasive synthesis. As shown in **Figure 15**, it is clearly observed uniformly distributed ceria particles on the PS core, indicating the formation of core/shell structured abrasive particle. The ceria particle size is about 10 nm and face centered cubic structure which is confirmed by XRD and SAED pattern. Based on CMP test with thermal oxide film, PS/ceria hybrid abrasive slurry demonstrates lower removal rate, fewer scratches, and lower surface roughness are compared with ceria abrasive slurry.

Nano-sized ceria abrasive is already used in the semiconductor manufacturing. Ceria-silica or silica-silica composite abrasive is still under development stage although several unique synthesizes are suggested and demonstrate promising CMP data. Most of literatures with composite abrasive focus on material removal rate and surface quality. However, CMP application needs more performances. In order to be utilized in the industry, composite abrasives have to avoid agglomeration, need to robust abrasive stability, require optimized chemistry, and more CMP performances such as selectivity and defectivity must be fulfilled.

New materials CMP has emerged along with new device introduction and device node shrinkage, from ultra-soft materials such as porous low-k and photoresist to highly non-reactive metal such as ruthenium (Ru) [3–5, 50, 51]. Ultra-soft material CMP needs very soft abrasive or even abrasive-free slurry development [5]. Ru is little chemical reactive metal with high hardness. And it relies more on mechanical force to remove Ru layer than chemical dissolution. Moreover, RuO_4, which can be produced by slurry chemistry, is toxical gas [50, 51]. Therefore Ru CMP has a lot of limitation to achieve enough removal rate by CMP. Cobalt (Co) is the most potential candidate metal for replacing tungsten as contact metal (or replacing Ta/TaN as barrier metal) and its CMP slurry abrasive development is upmost challenge for device fabrication [52–54]. Known issues by Co CMP are residual abrasive particle defects and Co corrosion. More difficulties on these materials are not only target material CMP but

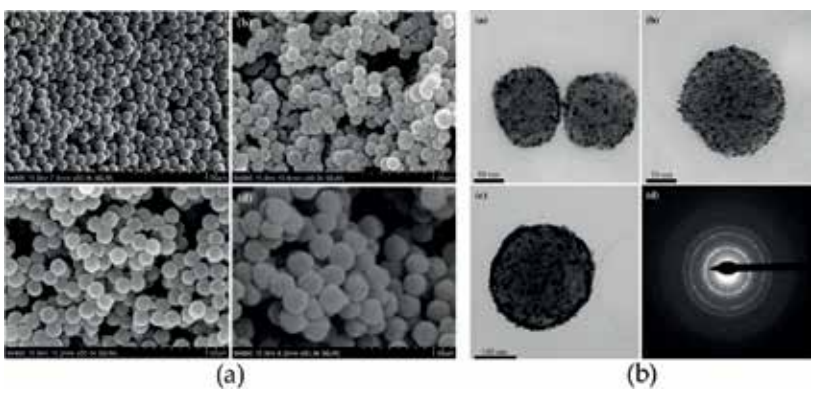

Figure 15. (a) SEM images and (b) TEM images of PS/ceria composite abrasive (Reprinted by permission from Ref. [49], Copyright 2016 Springer Nature).

also neighboring materials CMP for proper selectivity. Most of new materials CMP slurry is based on silica abrasive and chemistry optimization has been underscored. However, it still has a lot of opportunities to develop abrasives as well. Carbon based materials (either carbon nanotube or graphene) have drawn intense interests to the semiconductor industry for a long time. For CMP perspective, carbon-based material polishing, which has been rarely reported, is big challenge to abrasive development due to its high hardness.

6. Abrasive control in semiconductor fab

The role of abrasive in CMP application is to obtain enough material removal rate, desired selectivity and low defect (residual particle and scratch) performance. In addition to develop advanced abrasive material and synthesis, abrasive size distribution and dispersive ability in the solution has been developed to control large particle count. Particle size distribution is raw abrasive material nature resulting from synthesis, however, slurry distribution system and filtration can control large particles and agglomeration from the slurry without CMP performance degradation. In high volume semiconductor manufacturing fab, slurry distribution system is considered as infrastructure instead of equipment [18, 55]. It consists of (1) slurry drum, (2) agitation of drum (drum tumbling), (3) slurry blending and dispense, (4) daytank (or standby tank) with stirrer, (5) looping to tools. **Figure 16** shows simplified distribution system. Slurry is being circulated in the loop until it is used for CMP. Abrasive agglomeration is induced by shear stress, temperature change and chemistry variation if proper filtration is not implemented [56]. The location of filters from slurry distribution system is selected carefully. More filtration drops slurry flow pressure quickly by filter itself. Very fine filter will removes most abrasives, which results in low removal rate. Different slurry needs different type of filter and filtration at different locations; however global loop filtration and point of use (POU) filtration at polishing equipment are quite standard [18, 56, 57]. Global filter size is normally >10 μm, which is bigger than POU filter to avoid flow pressure drop. POU filter size is smaller than 1 μm. Yi Wei et al., showed agglomeration behavior of different slurries.

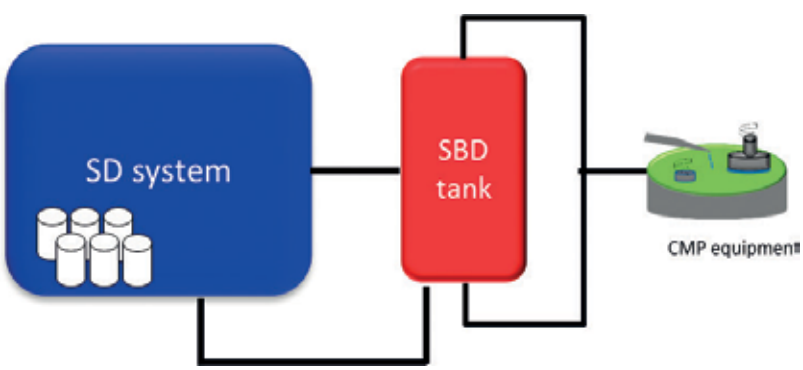

Figure 16. Slurry delivery facilities in semiconductor manufacturing fab. (SD = slurry dispense, SBD = standby distribution).

Colloidal silica abrasive agglomeration is more sensitive to shear stress than ceria abrasive. The most important challenge of filtration is plugging by abrasives. Three plugging mechanisms in filtration are well known, which are cake formation, gradual plugging, and complete plugging [58]. Cake formation is driven by particles build up on the filter surface, gradual plugging is induced by particles building up on the pore, and compete plugging indicates pore blocking by particles. Depending on particle size, deformability, and agglomeration, filtration procedure can be optimized. The most commonly used filter in CMP slurry is 'graded density depth' type. It has multi-layers of fibrous media and there is retention gradient along with flow direction. Commonly, large particles are captured first at outer layer and small particles are retained at inner layer. However, more advanced filter and filtration researches are reported recently. Nano-fiber based advanced filter to remove large abrasive as well as avoid agglomeration is reported. Morby et al., suggested composite/rigid structured filter which consists of thermally bonded polyolefin bi-component coarse fiber matrix and microfiber-glass web as next generation filter to retain slurry flow pressure and remove large abrasive effectively [59]. In addition to filtration, dispersant in the slurry prevents abrasive from agglomeration. For high abrasive content slurry case, abrasive particles are easy to sediment and agglomerate by particle charge interaction. Along with slurry abrasive development, advanced filter development and prevention of sediment of abrasive are required in slurry preparation.

7. Conclusion

This chapter reviews abrasives for CMP applications in semiconductor manufacturing. It includes abrasive types, abrasive synthesis, CMP mechanism and role of abrasives, and opportunities of new abrasive developments. Semiconductor business increases explosively and various semiconductor structures with high performance have been developed according to market requirement. In order to achieve mature semiconductor manufacturing, CMP process development is critical and abrasives in slurry play a pivotal role in determining CMP performances. The most common abrasive in dielectric CMP is either silica-based or ceria-based one. For metal CMP (tungsten and copper), silica is the most popular abrasive. Advanced synthesis for silica or ceria abrasives, new abrasive materials, and composite abrasives have studied for high performance CMP and new material CMP. Furthermore, the control of slurry abrasive in the looping is emphasized. Advanced filtration is critical to maintain abrasive size distribution. The applications of CMP are mostly focused on semiconductor industry; however its utilization expands to display industry, M/NEMs, automobile industry and biotechnology. The key of each application is noble abrasive development with proper chemistries.

Author details

Hong Jin Kim

Address all correspondence to: hongjin.kim@globalfoundries.com

Advanced Module Engineering, GLOBALFOUNDRIES, Malta, NY, USA

References

[1] Li Y, edited. Microelectronic Applications of Chemical Mechanical Planarization. USA: John Wiley & Sons Inc; 2008

[2] Steigerwald JM, SP Murarka, Gutmann RJ. Chemical Mechanical Planarization of Microelectronic Materials. USA: John Wiley & Sons Inc; 1997

[3] Krishnan M et al. Chemical Reviews. 2010;**110**:178-204

[4] Zantye PB, Kumar A, Sikder AK. Materials Science and Engineering R: Reports. 2004; **45**:89-220

[5] Babu S. Advances in chemical mechanical planarization (CMP). In: Woodhead Publishing Series in Electronic and Optical Materials. 2017

[6] Tsujimura M. Japanese Journal of Applied Physics. 2016;**55**:06JA01

[7] Hoffmann TY. Solid State Technology. 2010;**53**:20-23

[8] Feeney P. Solid State Technology. 2010;**53**(10):14

[9] Kim HJ et al. Proceedings of Advanced Metallization Conference: 27th Asian Session 2017. pp. 92-93

[10] Ein-Eli Y, Starosvetsky D. Electrochemica Acta. 2007;**52**:1825-1838

[11] Steigerwald JM. Proceedings of IEDM. 2008:37-40

[12] Chi M-h. Challenges in Manufacturing FinFET at 20nm node and beyond. Technology Development, GlobalFoundries; 2014. http://www.rit.edu/kgcoe/eme/sites/default/files/Min-hwa%20Chi%20-%20abstract_%20Challenges%20in%20Manufacturing%20FinFET.pdf

[13] Kim HJ. International Conference on Planarization/CMP Technology. AZ USA: Pheonix; 2010

[14] http://www.linx-consulting.com/

[15] Cook LM. Journal of Non-Crystalline Solids. 1990;**120**:152-171

[16] White ML, Jones L, Romine R. The mechanism of low pH silica based oxide slurries. Cabot Microelectronics Technical Paper (https://www.cabotcmp.com/cmp-research/cmp-technical-papers/)

[17] Tutorial, Planarization Processes for ULSI Fabrication to the Year 2002 (SEMICON WEST, July 16, 1997) p. 51

[18] Li SH, Miller RO. Chemical Mechanical Polishing in Silicon Processing. USA: Academic Press; 2000

[19] Doering R, Nishi Y. Handbook of Semiconductor Manufacturing Technology. 2nd ed. USA: CRC Press; 2008

[20] Zhant H et al. Journal of the American Chemical Society. 2012;**134**(38):15790-15804

[21] Gert Roebben et al. Frontier in Chemistry, Technical Report, Oct. 19, 2015 (https://www.researchgate.net/publication/283302479_Reference_materials_and_representative_test_materials_to_develop_nanoparticle_characterization_methods_The_NanoChOp_project_case)

[22] Zhang KL et al. Journal for Nanoscience and Nanotechnology. 2009;**9**(2):1054-1057

[23] Qin F, Liu W. Proceedings of 2015 International Conference on Planarization/CMP Technology (ICPT). pp. 119-122

[24] Kao MJ, Hsu FC, Peng DX. Advances in Materials Science and Engineering. 2014;**2014**:1-8

[25] Ming-ShyongTsai. Materials Science and Engineering: B. 15 January 2004;**106**(1):52-55

[26] Park K-W et al. Journal of the Korean Physical Society. 2007;**51**(1):214-223

[27] Shun G et al. Wear. 2011;**273**:100-104

[28] Posthumus W et al. Journal of Colloid and Interface Science. 2004;**269**:109-116

[29] Chen A et al. Journal of Alloys and Compounds. 2016;**663**:60-67

[30] Hoshino T et al. Journal of Non-Crystalline Solids. 2001;**283**:129-136

[31] Seo J. Surface Chemistry of Ceria Nanoparticles for CMP Applications. CAMP's 22th International Symposium on CMP; 2017

[32] Raghavan S, Keswani M, Jia R. Kona Powder and Particle Journal. 2008;**26**:94

[33] Tanaka T et al. Proceedings of 2014 International Conference on Planarization/CMP Technology (ICPT). pp. 22-24

[34] Minami H. Polishing Selectivity Control for Scratch Free Nano Size Cerium Hydroxide Slurry. CAMP's 19th International Symposium on CMP; 2014

[35] Seo J et al. ACS Applied Materials & Interfaces. 2014;**6**:7388-7394

[36] Seo J et al. Applied Surface Science. 2016;**389**:311-315

[37] Myoung-Hwan O et al. Powder Technology. 2011;**206**:239-245

[38] Broadbent EK et al. IEEE Transactions on Electron Devices. 1988;**35**:952-956

[39] Kaufman FB et al. Journal of the Electrochemical Society. 1991;**138**(11):3460-3464

[40] Kim HJ et al. ECS Journal of Solid State Science and Technology. 2014;**3**(10):P310-P314

[41] Palla BJ et al. IEEE/CPMT International Electronics Manufacturing Technology Symposium. 1998. 155-163

[42] Kim HJ, Qin L, Lee T. TechConnect World Innov. Conf. Washington DC, USA; 2015

[43] Kim HJ, Lee TH, Ryan A. ECS Transactions. 2016;**72**(18):27-36

[44] Han S et al. Electronic Materials Letters. 2013;**9**(2):155-159

[45] Zhang Z et al. Applied Surface Science. 2010;**257**:1750-1755

[46] Peedikakkandy L et al. Applied Surface Science. 2015;**357**:1306-1312

[47] Chen G et al. Applied Surface Science. 2015;**359**:664-668

[48] Zhao X et al. Microelectronic Engineering. 2010;**87**:1716-1720

[49] Chen A et al. Journal of Materials Science: Materials in Electronics. 2016;**27**:2919-2925

[50] Ruthenium CMP. Integration for Dual-Damascene Copper Interconnects. Cabot Microelectronics Technical Paper (https://www.cabotcmp.com/cmp-research/cmp-technical-papers/)

[51] Cheng J et al. Proceedings of 2016 International Conference on Planarization/CMP Technology (ICPT). pp. 195-198

[52] Alety SR et al. ECS Journal of Solid State Science and Technology. 2017;**6**(9):P671-P680

[53] Changhong W et al. ECS Transactions. 2017;**77**(5):93-97

[54] Turk MC et al. ECS Journal of Solid State Science and Technology. 2016;**5**(2):P88-P99

[55] Mason M. CMP metrics improved by undiluted slurry data. Solid State Technology (http://electroiq.com/blog/2011/06/cmp-metrics-improved-by-undiluted-cmp-slurry-data/)

[56] Lu Y et al. Proc. of 2014 International Conference on Planarization/CMP Technology (ICPT). pp. 291-295

[57] Wu M et al. Proceedings of 2017 International Conference on Planarization/CMP Technology (ICPT), pp. 323-328

[58] Yang HJ, et al. Semiconductor Technology International Conference (CSTIC), 2015. China: 2158-2297

[59] Morby J, Entezarian M, Gieger B. Proceedings of 2015 International Conference on Planarization/CMP Technology (ICPT). pp. 128-131

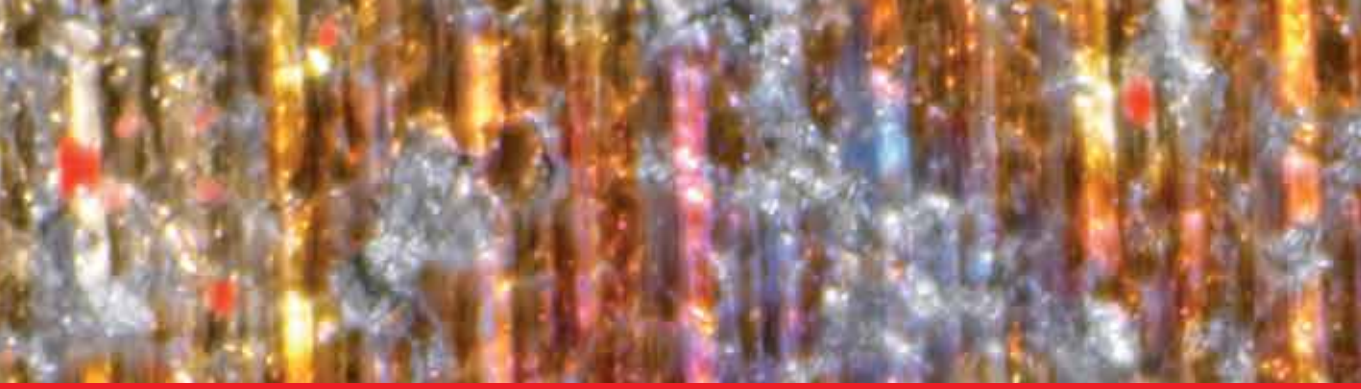

Edited by Anna Rudawska

The subject matter of this book is the information on the abrasive technology methods, the characteristics of the methods (for example, the technological parameters, tools, and machines), innovative methods, characteristics of surface structure and surface properties after this type of mechanical process, and application in various industrial branches and other technical and technological domains. Abrasive technology is very important, for example, in precision component manufacturing and nano-technology devices. The aim of this book is to present information on the characteristics and applications of abrasive technology, abrasive tools, tests, and also the innovative methods of this technology. This information enables scientists, engineers, and designers to ensure the soundness and integrity of the fabricated components and to develop new techniques effectively.

Published in London, UK

IntechOpen

ISBN 978-1-83881-680-3